

USING SPATIAL DATA FOR GEO-ENVIRONMENTAL STUDIES



A thesis submitted to the Faculty of Geosciences at Ludwig-Maximilians-University, Munich in partial fulfilment of the requirements for the Ph.D. degree.

By

Khaled Haider

From Damascus, Syria

September 2011

- 1. Referee: Prof. Dr. Wolfram Mauser**
- 2. Co-Referee: Prof. Dr. Ralf Ludwig**

Date of Disputation: 23 September 2011

***“The important thing is not to
stop questioning”***

-Albert Einstein

Acknowledgements

All praise is due to Almighty ALLAH (God) for granting me the health, strength, and time to complete this work. I would also like to express my deepest gratitude and appreciation to all those people who have directly or indirectly contributed to the successful completion of this study. First of all, I would like to thank my PhD supervisor Prof. Dr. Wolfram Mauser, not only for giving me the opportunity to do my PhD thesis at the Ludwig-Maximilian-University in Munich (one of the most prestigious universities in Europe), but also for having so much trust and confidence in me. He provided me with his model PROMET, which was essential for the successful fulfilment of this thesis. I did make much profit from his extensive knowledge and experience in the field of environmental modelling in general and in hydrological modelling in particular. For his continuous guidance, encouragement, support, fruitful suggestions, constructive criticism, and patience throughout the course of this study, I would like to thank him profoundly. I would also like to express my gratitude to the Syrian Ministry of Higher Education for funding this work. Many thanks go to the staff members of the following ministries and organization in Syria: Ministry of Defence (the General Directorate of Meteorology); Ministry of Irrigation (Directorate of Water Resources Management); Ministry of Agriculture and Agrarian Reform (MAAR); General Organization of Remote Sensing (GORS); Arab Center for the Studies of Arid Zones and Dry Lands (ACSAD) for providing some of the data used in this study. I am particularly grateful to Prof. Dr. Ralf Ludwig for accepting to spend his precious time in reviewing my thesis and giving me valuable comments and suggestions. Special thanks go to my dear office-mates Dr. Markus Muerth and Dr. Daniel Waldmann, not only for introducing me to the model PROMET and helping me solve many technical computing problems that have arisen during the course of this work, but also for being good friends. I would also like to extend my thanks to all of my former and current colleagues (alphabetically arranged) Andrea Reiter, Dr. Carola Weiss, Dr. Christoph Heinzlerr, Florian Schlenz, Florian Zabel, Franziska Kock, Inga May, Johanna Dall' Amico, Lu Dong, Lu Gao, Matthias Locherer, Dr. Matthias Bernhard, Dr. Monika Prasch, Monika Tepfenhart, Ruth Weidinger, Dr. Sara Stober, Sascha Berger, Susan Niebergall, Tamara Avellan, Dr. Thomas Marke and Toni Frank for their unending support and encouragement. In addition, particular appreciations and thanks go to Dr. Florian Siebel, Dr. Heike Bach, Dr. Ingo Keding, Dr. Jochen Henkel, Prof. Dr. Karsten Schulz, Prof. Dr. Natascha Oppelt, Prof. Dr. Ralf Ludwig, Dr. Roswitha Stolz, Dr. Tobias Hank and Prof. Dr. Ulrich Strasser, who have always helped me with scientific advice.

Last, but not least, I'd like to thank my family, father, mother, lovely sisters and brothers for supporting me for such a long time and being so patient with me. My final, and most heartfelt, acknowledgment must go to my wife "*Ola*" for her unconditional love, constant encouragement and unwavering faith in me.

Abstract

The physically-based spatially-distributed model PROMET (Processes of Radiation, Mass and Energy Transfer) is applied to the Greater Damascus Basin, which is considered as one of the most important basins in Syria, to serve as a case study of using spatial data for Geo-environmental studies. Like most areas of the Middle East, the study area is characterized by large temporal and spatial variations in precipitation and by limited water resources. Due to the increasing water demand caused by the economic development and the rapid growth of population, the study area is expected to suffer from further water shortages in the future. This highlights the necessity of developing an integrated Decision Support System (DSS) to evaluate strategies for efficient and sustainable water resources management in the basin, taking into consideration global environmental changes and socio-economic conditions. The work presented here represents the first steps toward achieving this goal through applying a distributed hydrological model (an important component of any integrated DSS for water resources management) to the Greater Damascus Basin utilizing different types of spatial data used as time-dependent (e.g., meteorology) and time-independent (e.g., topography and soil) input parameters. The model PROMET, which was developed within the GLOWA-Danube project as part of the decision support system DANUBIA, is run on an hourly time step (for the period from 1991 to 2005) and a 180*180m spatial resolution to simulate the water and energy fluxes in this basin. The model is embedded within a raster-based GIS-structure which facilitates the integration of the diverse types of spatial data. The spatial information related to topography (such as elevation, slope, and exposition) as well as those related to runoff routing (such as upstream-area, channel width, and downstream proxel) are automatically extracted from Digital Elevation Model (Shuttle Radar Topography Mission, SRTM-90m DEM). The spatial patterns of the different land use/land cover classes are derived from remote sensing data (classification of a cloud-free LANDSAT 7 ETM+ image using the supervised classification algorithm). The spatial fields of meteorological input data are provided on an hourly basis through spatiotemporal interpolation of the measurements of the available weather stations. Spatial information about the soil texture is provided through generalization and aggregation of the soil type classes of the Soil Map of Syria (prepared by USAID) and transferring the soil types to texture classes. Several pedotransfer functions are then used to estimate the soil hydraulic properties for each soil texture class (and each soil layer) found in the study area. While plant physiological parameters (which are assumed to be static, such as minimum stomatal resistance) are estimated for each vegetation class using information taken from literature sources, the temporal evolution of Albedo and Leaf Area Index (LAI) are derived from five cloud-free LANDSAT-7 images acquired at different seasons of the year.

The goodness of the results obtained by the model PROMET are verified and/or validated by comparing them either with their corresponding data observed in the

filed or with remote sensing-derived information (e.g., snow cover). Two subcatchments are selected for the purpose of calculating the spatially-distributed annual water balances. The results indicate that the modelled mean annual runoff volume fits well with the measured discharge for both chosen subcatchment. In addition, the simulated discharge is compared to the observed one (at seven gauge stations) on a monthly basis, covering the whole simulation period (15 years). The results of the regression analysis for each of these gauge stations (with slope of regression line ranges from 0.79 to 1.04; coefficient of determination 0.69-0.90; and Nash-Sutcliffe Coefficient 0.73-0.95) indicate that there is a good correlation between simulated and observed monthly mean discharge volumes.

TABLE OF CONTENTS

Acknowledgements	I
Table of Contents	IV
List of FiguresVII
List of Tables	XII
List of Acronyms	XIII
List of Symbols	XV
1. Introduction	1
1.1. Definitions	1
1.1.1. Spatial Data	1
1.1.2. Geo-environmental Studies	2
1.2. The Role of Spatially-distributed hydrological modelling in Water Resources Management	3
1.3. Motivation, objectives and the structure of the thesis	4
2. The Study Area	6
2.1. General remarks	6
2.2. Physical Environment	7
2.2.1. Morphology / Topography	7
2.2.2. Geology	7
2.2.3. Hydrogeology	8
2.2.4. Soils	9
2.2.5. Climate	11
2.2.6. Vegetation and land use	12
3. The Model PROMET	14
3.1. Overview of the model PROMET	14
3.2. The architecture of the model PROMET	14
3.2.1. The meteorology component	17
3.2.1.1. Temporal interpolation and disaggregation	17
3.2.1.2. Spatial interpolation	18
3.2.1.3. Calculation of incoming radiation	18
3.2.2. The vegetation component	19
3.2.3. The land surface energy and mass balance component	21
3.2.4. The snow and ice component	22
3.2.5. The soil hydraulic and soil temperature component	23
3.2.6. The groundwater component	26
3.2.7. The channel flow component	27
3.2.8. The man-made hydraulic structures component	27
3.3. Data requirements (input data)	28

4. Land use / Land cover classification using Landsat-7-ETM image	30
4.1. Introduction	30
4.2. Image processing and Classification Methodology	31
4.2.1. Ground truth collection	31
4.2.2. Image acquisition	31
4.2.3. Image rectification (Geometric correction or georeferencing)	32
4.2.4. Specify Land use / Land cover Classification Scheme	33
4.2.5. Image Enhancement	35
4.2.6. Training Site Selection and Statistics Extraction	36
4.2.7. Supervised Classification	39
4.2.8. Classification Accuracy Assessment	41
4.3. Conclusion	44
5. Extraction of drainage network and watershed data from DEMs	46
5.1. Introduction	46
5.2. Data Acquirement and Preprocessing	46
5.2.1. Criteria for choosing suitable DEM data	46
5.2.2. Selecting an appropriate software package	47
5.2.3. Downloading, mosaicking and reprojecting SRTM- DEM data	47
5.2.4. Choosing an appropriate spatial resolution (level of aggregation)	48
5.3. DEM Processing	49
5.3.1. Creating a depressionless DEM	49
5.3.2. Determining flow direction.....	49
5.3.3. Generating flow accumulation raster	50
5.3.4. Extracting drainage network	51
5.3.5. Determination of watershed pour points (outlets)	52
5.3.6. Delineating watersheds	54
5.4. DEM visualization	55
5.5. Discussion of results	55
6. Preparation and analysis of the meteorological input data fields.....	57
6.1. Introduction	57
6.2. Weather observation network	57
6.3. Organizing the collected meteorological data in a single file " <i>Met-File</i> ".....	60
6.4. Spatial and temporal Interpolation of the meteorological variables	60
6.5. Reviewing and analyzing the collected meteorological datasets	61
6.5.1. Precipitation	61
6.5.2. Air temperature	64
6.5.3. Relative air humidity	66
6.5.4. Wind speed	67
6.5.5. Cloud cover and radiation budget	68

7. Parameterization of soil physical and hydraulic properties	69
7.1. Soil formation	69
7.2. Available Soil Maps	70
7.3. The classification and nomenclature of the soils of the study area	70
7.3.1. Order Aridisols (desert soils)	71
7.3.2. Order Entisols (new soils)	73
7.3.3. Order Inceptisols (young soils)	73
7.3.4. Order Vertisols (cracking clay soils)	74
7.4. Separating soil associations into their constituent subgroup soils	74
7.5. Inherent characteristics of soils of the study area	76
7.5.1. Soil Texture	77
7.5.2. Soil depth	79
7.5.3. Content of coarse fragments	80
7.6. Estimating soil hydraulic properties using Pedotransfer Functions	81
7.6.1. Bubbling pressure head	82
7.6.2. Pore size distribution index	82
7.6.3. Effective porosity	82
7.6.4. Saturated hydraulic conductivity	83
8. Estimation of vegetation parameters for hydrological modelling	84
8.1. Introduction	84
8.2. Basics of evapotranspiration	84
8.3. The plant parameters required to run the <i>vegetation-component</i> of PROMET	
8.3.1. Plant physiological parameters which are assumed to be static	86
8.3.1.1. The plant-specific minimum stomatal resistance	86
8.3.1.2. The slope parameter of the stomatal resistance with irradiance	
8.3.1.3. The threshold value of leaf water potential (soil suction)	88
8.3.1.4. Cardinal temperatures	89
8.3.2. The plant parameters required to describe the temporal evolution of	
vegetation	90
8.3.2.1. Albedo (daily) [%]	90
8.3.2.2. Leaf Area Index (daily) [m ² /m ²]	94
8.3.2.3. Plant height and root depth (daily) [m]	99
9. Model Results	100
9.1. The spatial distribution of the meteorological parameters in the study area	102
9.1.1. The spatial distribution of precipitation	102
9.1.2. The spatial distribution of air temperature	104
9.1.3. The spatial distribution of snow cover	105
9.1.4. The spatial distribution of solar radiation	107
9.2. Spatial distribution of evapotranspiration	110
9.3. Spatial distribution of groundwater recharge (percolation)	112

9.4. The annual water balance	115
9.5. Analysis of the simulated monthly streamflow (Discharge)	121
10. Summary and Outlook	126
10.1. Summary	126
10.2. Limitations of the study	129
10.3. Outlook and Recommendations	130
11. References	133
12. Appendix	150
13. Curriculum Vitae	177

List of Figures

Figure 1.1:	A schematic illustration of the environmental components and the interactions between them (based on the above mentioned definition).	2
Figure 2.1:	The location of the study area.	6
Figure 2.2:	A Digital Elevation Model (DEM, derived from 90m SRTM data) of the study area along with vector data (river channels and lakes) draped over it.	7
Figure 2.3:	The hydrogeological map of the study area (digitized from the hydrogeological hardcopy map using the ArcGIS software).	8
Figure 2.4:	Soil map of the study area (digitized from the hardcopy soil map of Syria which was prepared by FAO (1977) at a scale of 1:500,000).	10
Figure 2.5:	Land use / Land cover map of the central part of the study area (Al-Ghouta), which was prepared within the framework of cooperation between ACSAD and BGR. The location of this map in relation to the whole study area is shown in the top-left of this figure.	13
Figure 3.1:	A schematic structure of the model PROMET. Boxes represent components whereas arrows indicate the interfaces between them, through which data is exchanged (Mauser and Bach, 2009).	15
Figure 3.2:	The schematic representation of the proxel concept. The simulated area consists of 363768 proxel (659 proxel-columns and 552 proxel-rows). The number of proxels that belong to the catchment area is 161138.	16
Figure 3.3:	Soil water fluxes simulated by the soil moisture module (the modified 4-layer Eagleson model) of PROMET (Muerth, 2008).	25
Figure 3.4:	An overview of the different input data (parameters) that are needed to run the model PROMET for the Greater Damascus Basin.	29
Figure 4.1:	The colour composites for band combinations 1, 2, 3(left); 2, 3, 4 (middle) and 2, 4, 7 (right) from the same subset of the ETM+ imagery used in this study.	36
Figure 4.2:	A comparison between the vector-based land use map (prepared by G.O.R.S) and its corresponding subset of the Landsat ETM+ imagery.	37
Figure 4.3:	Training samples polygons (in yellow) delineated on top of both the Landsat ETM+ Imagery and the previously conducted vector land use map.	38
Figure 4.4:	The Land use / land cover map of the study area as derived from	40

classification of a Landsat 7 ETM+ image acquired on May 21, 2000.

Figure 4.5:	The estimated proportion for each land use/ land cover class at level- (III) of the adopted classification scheme.	45
Figure 5.1:	The SRTM data used for automatically delineating watershed boundaries and drainage network in our study area.	48
Figure 5.2:	Flow direction raster of the study area generated by TOPAZ, (based on D8-method).	50
Figure 5.3:	Flow accumulation raster of the study area (produced by TOPAZ).	51
Figure 5.4:	The resulting drainage network of the study area (converted into vector-based format).	52
Figure 5.5:	Section of the study watershed-area in the vicinity of a user-specified watershed outlet.	53
Figure 5.6:	The locations of the pour points (streamflow gauges) which were used to subdivide the whole watershed into several smaller subwatersheds.	54
Figure 5.7:	The study area (the whole watershed) subdivided into subwatersheds. The inset (on the right) shows in more detail the delineated subwatersheds using some streamflow gauges located along Barada River.	54
Figure 5.8:	A comparison between the performance of TOPAZ and ArcGIS in delineating the drainage network over flat areas.	56
Figure 6.1:	The spatial distribution of the available synoptic, climatic and rain-gauge stations within the study area.	58
Figure 6.2:	A sample of the collected meteorological variables organized in the same manner as the standard DWD data file.	60
Figure 6.3:	The spatial distribution of some meteorological fields exemplarily for a model time step in the year of 1996 (February 10 at 13:00).	61
Figure 6.4:	The annual precipitation at Damascus City Center for the time period from 1918 to 2007.	62
Figure 6.5:	The relationship between the annual precipitation observed at some selected rain-gauge stations for the very wet year (2002-2003) and their elevations, which in turn increase westward toward the Anti-Lebanon Mountains (toward the Mediterranean Sea).	63
Figure 6.6:	Average monthly precipitation obtained from four stations at different elevation for the time period (1959-2005).	64
Figure 6.7:	A climate graph for the Damascus plain (Al-Mazze station).	65

Figure 6.8:	The correlation between the long-term mean monthly temperature and the mean monthly relative humidity at “Al-Mazze” station.	66
Figure 6.9:	The long-term monthly mean wind speed as observed at three selected weather stations for the time period 1991-2005.	67
Figure 6.10:	The percentage of clear sky and the amount of diffuse and direct solar radiation, as estimated by the meteorological component of the model PROMET exemplarily for a model time step in the year of 1996 (February 3rd, 09:00 a.m.).	68
Figure 7.1:	The spatial distribution of soils of the study area (at order level) digitized from the soil map of Syria at a scale of 1:500,000 (USAID, 1982).	71
Figure 7.2:	The estimated spatial distribution of soils of the study area (classified at the level of Subgroup of the USDA Soil Taxonomy, based on the soil map of Syria that was produced by USAID, 1982).	76
Figure 7.3:	The estimated area (in km ²) covered by each soil type in the study basin.	76
Figure 7.4:	The USDA soil texture triangle showing grain-size distribution of each soil horizon (from the above presented soil profiles).	78
Figure 7.5:	The estimated spatial distribution of soil texture within the study area.	78
Figure 7.6:	The estimated spatial distribution of soil thickness; a) Thickness of surface soil, b) thickness of sub-surface soil, and c) the total soil depth.	79
Figure 7.7:	The estimated spatial distribution of the volumetric content of coarse fragments in a) surface soil horizon (or layer), and b) in sub-surface soil horizon.	80
Figure 8.1:	The albedo map resulted from the reflectance values of the spring Landsat image, together with the spatial distribution of the “Settlements” class draped over it to serve as an illustrative example for the calculation of the mean albedo value for each individual land use/land cover category.	93
Figure 8.2:	The spatial distribution of the Surface Albedo (%) and LAI (m ² /m ²) in the study area, as derived from the spring LANDSAT image (21.05.2000).	98
Figure 9.1:	An example of some of the long-term (1991-2005) spatially distributed results as simulated for a specific subcatchment within the study area using the model PROMET.	101
Figure 9.2:	The spatial distribution of long-term mean annual precipitation in the study area derived by interpolation of station data for the period from	102

1991 to 2005.

Figure 9.3:	The distribution of the climate-zones over the study area as derived from the map of the mean annual precipitation for a period of 15 years according to a simple system adopted in arid and semi-arid environments.	103
Figure 9.4:	The estimated area occupied by each climate zone derived from the map of climate zones, which in turn was derived from the map of the mean annual precipitation according to a simple scheme adopted in arid and semi-arid environments.	104
Figure 9.5:	The spatial distribution of long-term mean annual temperature in the study area derived by interpolation of point observations for the period 1991-2005.	105
Figure 9.6:	The spatial distribution of the percentage of long-term annual precipitation falling as snow, calculated using the model PROMET for a 15-year time period (1991-2005).	105
Figure 9.7:	Modelled long-term annual duration of snow cover (in days/year) derived from the simulated snow water equivalent for the period (1991-2005).	106
Figure 9.8:	A comparison between model- and satellite-observed snow-cover for the entire study area for the date 07 February 2003, 08:00 GMT (10:00 local time).	107
Figure 9.9:	A comparison between the long-term (15-years) observed and modelled value of the monthly mean daily global solar radiation on horizontal surface (Damascus station).	108
Figure 9.10:	Spatial distribution of the long-term mean daily global solar radiation for the month of January (left), the month of June (middle) and the annual (right), as calculated using the model PROMET for a 15-year time period (1991-2005).	108
Figure 9.11:	Spatial distribution of the long-term annual sum of incoming shortwave direct radiation (top left), diffuse radiation (top middle), incoming longwave radiation (top right), outgoing longwave radiation (bottom left), reflected shortwave radiation (bottom middle), and the radiation balance (bottom right) as simulated by the model PROMET in kW/m ² .	109
Figure 9.12:	The spatial distribution of the long-term mean annual evapotranspiration in the study region as simulated by the model PROMET for the period from 1991 to 2005.	110
Figure 9.13:	The long-term (catchment-average) monthly evapotranspiration as simulated using the model PROMET for a 15-year time period (1991-	110

2005).

- Figure 9.14: A comparison of the modelled actual evapotranspiration (PROMET) with temperature difference (T_{surface} (derived from LANDSAT image) - T_{air} (interpolated from station data)) on 21 May 2000, 10:00 local time. 112
- Figure 9.15: The spatial distribution of the long-term (15-years) mean annual groundwater recharge in the study area as simulated using the model PROMET, together with the river channel network draped over it. 113
- Figure 9.16: The long term monthly average groundwater recharge in the study area as simulated using the model PROMET for a 15-year time period (1991-2005). 114
- Figure 9.17: The annual variability of the simulated groundwater recharge for the hydrological years 1992-2005, along with the variability in the catchment-average annual precipitation. 114
- Figure 9.18: The locations of the two subcatchments used for the purpose of calculating the annual water balances in relation to the entire study area, together with the positions of the stream-flow gauge stations. 116
- Figure 9.19: The average modelled water balance in “Al-hama” subcatchment over the period from 1992 to 2005. The simulated mean annual runoff from this subcatchment (181 mm /y) compares well with the runoff (discharge) measured at its respective outlet gauge station (176 mm/y). 118
- Figure 9.20: A comparison between the modelled annual runoff volumes from “Al-hama” subcatchment (in mm/y and in m³/s) and those annual discharges measured at its outlet gauge station for the hydrological years from 1992-2005. 120
- Figure 9.21: The linear regression (forced through the origin) between the modelled and measured annual runoff volumes (in mm/y) at “Al-hama” outlet gauge station. 120
- Figure 9.22: The temporal course of modelled and measured monthly mean discharge at “Al-hama” gauge for the period (1991-2005). 122
- Figure 9.23: A comparison between simulated and observed mean monthly discharge at “Al-hama” gauge for the period (1991-2005). 122
- Figure 9.24: The linear regression line (forced through the origin) between the modelled and measured monthly mean discharge volumes (in m³/s) at “Al-hama” outlet gauge station for the period 1991-2005. 123

List of Tables

Table 1.1:	Different sources of spatial data used in this study.	1
Table 4.1:	Product specifications of the acquired Landsat 7 ETM+ image.	32
Table 4.2:	The Land use/ Land cover classification scheme used in this study.	34
Table 4.3:	The producer's accuracy, user's accuracy, and overall classification accuracy for the examined land cover classes.	42
Table 4.4:	The producer's accuracy, user's accuracy, and overall classification accuracy for the examined land cover classes.	43
Table 4.5:	Kappa coefficient for each of the 8 examined categories.	44
Table 6.1:	The names, geographical locations and elevations of the synoptic and climatic stations used in this study.	59
Table 7.1:	Taxonomic classification of soils of the study area taken from the soil map of Syria at a scale of 1:500,000 (USAID, 1982).	72
Table 7.2:	The quantitative values for some soil characteristics for two chosen soil profiles.	77
Table 8.1:	The acquisition dates of the LANDSAT-7 ETM+ images used for estimating the albedo value for each land use class, along with the solar altitude, azimuth angles, and the Sun-Earth distance.	91
Table 8.2:	The land cover dependent weighted functions proposed by Gratton et al., (1993) to derive the albedo values (α) from the calculated reflectance values of the LANDSAT ETM+ bands.	93
Table 8.3:	The mean albedo values (α %) estimated for each individual land use/land cover category of the study area, as derived from five LANDSAT images acquired during different seasons of the year.	94
Table 8.4:	The modelled annual means of the water balance components (in mm/y) for "Al-hama" subcatchment as simulated by PROMET for each of the 14 hydrological years (1992-2005).	97
Table 9.1:	Classification of various types of aridity according to UNEP's scheme.	104
Table 9.2:	The mean annual observed discharge (1991-2005) for each of the two subcatchments used for calculating the annual water balance, along with other information.	115
Table 9.3:	The mean annual water withdrawal from each subcatchment.	117
Table 9.4:	The modelled annual means of the water balance components (in mm/y) for "Al-hama" subcatchment as simulated by PROMET for each of the 14 hydrological years (1992-2005).	119
Table 9.5:	The slope of the regression line, the coefficient of determination, and the Nash-Sutcliffe coefficient for the regression relationship between the modelled and measured monthly discharge for each selected gauge for the period (1991-2005).	124

List of Acronyms

a.s.l.	above sea level
ACSAD	Arab Center for the Studies of Arid Zones and Dry Lands
AOI	Area of Interest
ASCII	American Standard Code for Information Interchange
BGR	Bundesanstalt für Geowissenschaften und Rohstoffe [the German Federal Institute for Geosciences and Natural Resources]
CSA	Critical Source Area
DAWSSA	Damascus Water Supply and Sewerage Authority
DEM	Digital Elevation Model
DN	Digital Numbers
DOY	Day of Year
DSS	Decision Support System
DTM	Digital Terrain Model
DWD	Deutscher Wetterdienst [German Weather Service]
E	Nash-Sutcliffe efficiency coefficient
ESRI	Environmental Systems Research Institute
ET	Evapotranspiration
ETa	Actual Evapotranspiration
ETM+	Enhanced Thematic Mapper Plus
ETp	Potential Evapotranspiration
FAO	Food and Agriculture Organization of the United Nations
FORTTRAN	Formula Translation
G.O.R.S.	General Organization of Remote Sensing
GCPs	Ground Control Points
GIS	Geographic Information System
GLCF	Global Land Cover Facility
GLOWA	Globaler Wandel des Wasserkreislaufs (Global Change and the Hydrological Cycle)
GPS	Global Positioning System
k	Kappa coefficient
LAI	Leaf Area Index
LAI-2000	Plant canopy Analyzer
LW	Long Wave
MAAR	Ministry of Agriculture and Agrarian Reform (Syria)
MM5	Mesoscale Model
MOI	Ministry of Irrigation (Syria)
MSCL	Minimum Source Channel Length
NDVI	Normalized Difference Vegetation Index
NIR	Near Infra Red
PAR	Photosynthetically Active Radiation
PID	Pixel Identification Number
PIXEL	Picture Element
PROMET	Processes of Radiation, Mass and Energy Transfer.
PROXEL	Process Pixel
PTFs	Pedotransfer Functions
R ²	Coefficient of Determination

RCMs	Regional Climate Models
REMO	RegionalMOdel
RMSE	Root Mean Square Error
SCALMET	Scaling Meteorological Variables
SHTM	Soil Heat Transfer Module
SRTM	Shuttle Radar Topography Mission
Std.	Standard Deviation
SVAT	Soil Vegetation Atmosphere Transfer
SVIs	Spectral Vegetation Indices
SW	Shortwave
TIN	Triangulated Irregular Network
TOPAZ	Topographic Parameterization
TRAC	Tracing Radiation and Architecture of Canopies
UNEP	United Nations Environment Programme
USAID	United States Agency for International Development
USDA	United States Department of Agriculture
USGS	United States Geological Survey
UTM	Universal Transverse Mercator Projection
VCF	Volumetric Coarse Fragments in the soil
WGS 84	World Geodetic System 1984

List of Symbols

Symbol	Description	
Δ	The slope of the water vapour pressure curve vs. temperature	
Q	The radiation balance	
B	The soil heat flux	
ρ	The density of air	
C_P	The specific heat of the air	
γ	The psychrometric constant	
e_s	The saturated water vapour pressure at gauging level	
e_a	The current water vapour pressure at gauging level	
r_a	The aerodynamical resistance	
r_s	The surface resistance (canopy stomatal resistance).	[sec/m]
$r_s(min)$	The plant specific minimum stomatal resistance	[sec/m]
b_{rs}	Slope parameter for stomatal resistance with solar irradiance	[W/m ²]
T_{MIN}	The minimum temperature at which stomatal closure occurs	[°C]
T_{MAX}	The maximum temperature at which stomatal closure occurs	[°C]
T_0	The optimum temperature (at which stomatal resistance is a minimum)	[°C]
S_{max}	Maximum storage Capacity	(mm)
$u(Z)$	Wind speed at height (Z)	[m.s ⁻¹]
d	Zero plane displacement height	[m]
Z_0	Roughness length	[m]
$k(\theta)$	The effective hydraulic conductivity	[cm/s]
$D(\theta)$	Hydraulic diffusivity	[m ² /s]
$\Psi(\theta)$	The soil matrix potential (as a function of moisture content)	[cm]
s	The degree of saturation (the ratio of moisture content to the porosity)	[%]
h_b	The bubbling pressure head	[cm]
λ	The pore size distribution index	-
k_s	The saturated hydraulic conductivity	[m/s]
n	Effective porosity	[%]
$D(\theta)$	Hydraulic diffusivity	[m ² /s]
$G(z)$	The heat flux at depth z	[W/m ²]
C_s	The heat capacity	[J/kgK]
k	The heat conductivity	[W/mK]
θ_s	Porosity	[%]
D	Bulk density	[g/cm ³],
OM	Organic Material	[%]
α	Albedo (daily)	[%]
LAI	Leaf Area Index (daily)	[m ² /m ²]
Ψ_0	The threshold value of leaf water potential (soil suction)	[MPa]
ρ_i	The at-satellite reflectance for band i	-
E_i	The solar constant for band i	
Θ	The Sun elevation angle in degrees	degrees
d	The Sun-Earth distance in astronomical units	

L_i	The spectral radiance for band i	
R_{SW-DIR}	Incoming shortwave radiation (direct).	W/m^2
R_{SW-DIF}	Incoming shortwave radiation (diffuse).	W/m^2
R_{LW-IN}	Incoming longwave radiation (emission from the atmosphere).	W/m^2
R_{SW-OUT}	Outgoing shortwave radiation (reflected).	W/m^2
R_{LW-OUT}	Outgoing longwave radiation (emission from the Earth's surface).	W/m^2
ΔS	The change in water storage (in groundwater, soil moisture and snow)	[mm/y].
WW	The estimated annual amount of water withdrawal (Water use)	[mm/y].
Q_{obs}	The observed monthly discharge at time t	
Q_{sim}	The simulated monthly discharge at time t	
Q_{obs}	The average observed monthly discharge over the total number of observations (T).	

1. Introduction

1.1. Definitions

1.1.1. Spatial Data

According to several authors (e.g., DeBarry and Quimpo, 1999; Easa and Chan, 2000; Goodchild et al., 1993), **spatial data** describes both the geographical location (e.g., coordinates in longitude and latitude) of a feature (or a natural phenomenon) on the earth's surface and its descriptive information that is used to classify and/or describe this feature, usually referred to as *attributes* (e.g., soil-type, land use-class). Spatial data are generally represented by two types of data structures: *vector data* (that are mostly created from digitized maps) and *raster data* (that are frequently derived from satellite images).

In vector representation, geographic features are represented by distinct points (e.g., rain gauges, streamflow gauges), lines (e.g., rivers, roads), and polygons or areas (e.g., boundaries of watersheds, lakes, fields, etc.).

In raster representation, features are represented in grid cells called pixels, with a certain value assigned to each pixel (e.g., satellite images, digital elevation models, digital orthophotographs, and other digital maps derived from remotely-sensed data such as land use classification). Raster data have become more popular in recent years owing to the increasing availability of remote sensing data and the improvements in their spectral and spatial resolution.

Geographic information System (**GIS**) provides a powerful framework for the integration of different types of spatial data obtained from diverse sources. It also gives users the ability to handle and analyze the spatial data more efficiently and accurately as well as to generate new spatial information by integrating the existing ones. Table 1.1 presents different sources of spatial data that are used in this study.

Table 1.1 Different sources of spatial data used in this study

Raster Spatial Data		
Derived from Landsat-7 images	Derived from DEM (SRTM-90m)	Provided by interpolation of station data
Land use / landcover, LAI, Albedo, Snow cover Surface-temperature	Elevation, Slope, Exposition, Upstream-area, channel width, Downstream-proxel, etc.	Precipitation, Air-temperature, Relative-humidity, Wind-speed, cloudiness, Incoming radiation
Vector Spatial Data		
Measured using GPS		Derived from digitizing paper maps
Points	Lines	Polygons
Locations of weather-stations Locations of streamflow-gauges Locations of soil-profiles sites	Stream-network (digitized blue-line)	Soil-texture Geological-units Land use classification

1.1.2. Geo-environmental Studies

According to several authors (e.g., Peng et al., 2002; Singh, 2006), the term **Environment** may be described as surroundings or control conditions affecting development or growth of human beings, animals, plants and other living organisms. Environment consists of four segments- atmosphere (the air enveloping the earth), hydrosphere (all types of water resources like oceans, seas, rivers, reservoirs, lakes and groundwater), lithosphere (soil, rocks) and the biosphere (life forms). This definition is schematically illustrated in Figure 1.1.

On the other hand, the term **Geo-environment**, as stated by Verma (2003), “has a reference to environment with a re-emphasis on the geo-sciences of geology and geography. It is an interface emerging out of human interference with atmosphere, hydrosphere, biosphere and lithosphere and their mutual interactions”.

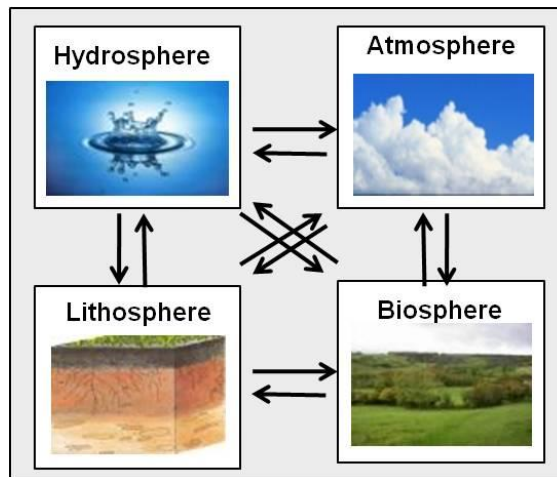


Figure 1.1 shows a schematic illustration of the environmental components and the interactions between them (based on the above mentioned definition).

Furthermore, according to some researchers (e.g., Aswathanarayana,1995; Peng et al.,2002; Bobrowsky and Fakudiny, 2002; Verma, 2003; Pandey, 2002; Martin-Duque et al.,2004) **Geo-environmental Science** can be understood as an interdisciplinary field that utilizes the different branches of geoscience such as geology, geomorphology, hydrology, geohydrology, geography, climatology, meteorology, soil science, natural resources, ecology, remote sensing and GIS for assessing, monitoring, and predicting environmental issues and phenomena that result from both natural and human-induced environmental changes. Geo-environmental specialists apply their knowledge and expertise to a wide range of **Geo-environmental Studies**, including, for example:

- Preparing thematic maps covering the above mentioned aspects of geoscience, which in turn form a fundamental database for conducting hazard and risk assessments (vulnerability of natural resources to specific hazards such as floods, droughts, soil erosion and contamination, desertification, pollution and depletion of water resources, landslides, etc.).

- Identifying, quantifying and predicting effects of climate change on the natural resources (such as land, soil, vegetation and water) at a regional scale.
- Developing integrated strategies for sustainable use and management of natural resources, taking into account potential future change in climate and socio-economic conditions.

However, regarding the Greater Damascus Basin (the “study area” of this work), water shortage and pollution together with the loss, degradation and contamination of land resources can be considered as major (geo-) environmental challenges facing the public health and socio-economic development in this region (Ministry of State for Environmental Affairs-Syria, 2003).

1.2. The Role of Spatially-distributed hydrological modelling in Water Resources Management

Many authors (e.g., Refsgaard and Abbott, 1996; Singh and Frevert, 2002) emphasized the importance of using spatially distributed hydrological models as basic (but far from sufficient) tools for improving water resources management. A distributed model is an essential component of any integrated decision support system for sustainable water management, which, in turn, integrate approaches from a wide range of natural and social science disciplines (e.g., hydrology, ecology, agriculture, public health, socio-economics, etc.). According to Kite and Droogers (2000), utilizing these distributed models in environmental studies in general and in hydrology in particular offers two significant advantages over relying only on collected spatial data. The first advantage is that these models have the ability to simulate processes that are difficult to measure owing to complexity or temporal and/or spatial scale. The second advantage is the ability of these models to study the effects of environmental change (land use, land cover and climate change) on natural resources, especially regional water resources (the impacts of alternative scenarios). Such models are usually embedded within a GIS structure allowing the integration of different spatial input data (e.g., elevation, slope, exposition, upstream-area, land use, soil texture, interpolated meteorological fields, etc.). Thereby, remote sensing data offer a good tool to characterize the heterogeneity of the landscape at different spatial (1m-5km) and temporal (30min-35days) scales. In addition to the derivation of land use/land cover classifications, remote sensing data can also be used to determine the temporal change of plant parameters (such as LAI and Albedo), which are required as input data for hydrological modelling.

According to Dooge (1992), distributed models are developed to accurately predict the partitioning of water between the different pathways of the hydrological cycle; in other words, to simulate the transfer of precipitation to runoff taking into account all of the natural processes involved (e.g., evaporation, transpiration, infiltration, percolation, surface flow, interflow, groundwater flow, etc.). Furthermore, distributed hydrological models can be applied at different scales, ranging from a single field to

mesoscale watershed, and provides substantially greater insight into the processes involved in the hydrological cycle. In contrast to those empirical-statistical (black-box) models and lumped conceptual models, which focus more on the input-output relationship, physically based distributed models (also called “white box models”) are based on the fundamental laws of physics. The values of their input parameters are therefore not calibrated against field observations (e.g., measured discharge) but are rather derived from remote sensing data or obtained from literature. According to Singh (1989), distributed models employ the concept of subdividing the watershed, a natural defined area that does not necessarily follow administrative boundaries and forms a natural landscape unit, into a number of smaller independent elements (pixels). These elements are supposed to be adequately small so that hydrologically important parameters can be considered homogeneous inside the element borders. One of the advantages of using the watershed concept in hydrological modelling is that the boundaries of a watershed allow the validation of the model results (especially the simulated water balance) through a comparison between the simulated runoff volumes with those measured at the watershed outlet.

The model PROMET, which is described in more detail in Chapter 3, belongs to those distributed models described above. It allows for the examination of the potential impacts of different climate change scenarios (which can be provided either by a regional climate models like REMO or MM5 or based on a stochastic weather generator) on the regional water resources. Proper quantification of these impacts is essential for determining optimal water management strategies to adapt to the changing environmental conditions.

1.3. Motivation, objectives and the structure of the thesis

Water is an important natural resource everywhere in the world, especially in the countries of the Middle East (including Syria) where water is becoming increasingly scarce due to frequent droughts and growing water demands caused mainly by fast population growth and inefficient water use (Shuval and Dwiek, 2007; Barrio, 2004). Scarcity and inefficient use of water resources (especially in irrigation sector) pose a significant and increasing threat to sustainable development and environmental quality of these countries (Zereini and Hötzl, 2008). The Greater Damascus Basin, a mesoscale catchment in the Middle East region (Chapter 2), is also subject to water stress and expected to suffer from further water shortages in the future due to the above mentioned causes (Bazza and Najib, 2003). In addition to water shortage, there are several other environmental challenges facing the public health and socio-economic development in this basin (e.g., water pollution, land degradation, droughts, soil erosion and contamination, etc.). It would be an almost impossible task to cover all these environmental challenges in a single study (PhD thesis). Therefore, this study will generally focus more on the comprehensive assessment of water resources, and at the same time it will provide a broad and comprehensive basis for further (geo-) environmental studies in this basin. Of course, accurate and reliable

assessments of water availability and its distribution and variability in space and time are essential to the development and management of water resources. These assessments are indispensable for developing an integrated decision support system (DSS) in order to evaluate strategies for efficient and sustainable water resources management in the basin, taking into consideration global environmental changes and socio-economic conditions. This study represents the first steps towards the realization of a DSS for water resources management through applying a distributed hydrological model (an essential component of any integrated DSS) to this basin using different types of spatial data. The model PROMET (Chapter 3), which was developed within the GLOWA-Danube project as part of the decision support system DANUBIA (GLOWA-Danube, 2009), is applied to this basin to simulate the water and energy fluxes as well as to serve as a case study of using spatial data for (geo-)environmental studies. According to the data requirements and the results that I am trying to obtain using the model PROMET, the general objective of this study can be broken down in the following **specific objectives**:

- 1) To generate land use/land cover map for the study area using remote sensing data (Landsat ETM+ image). The classification process is described in Chapter 4.
- 2) To derive topographic spatial information (e.g., slope, exposition, etc.) and to delineate watershed boundary and stream network from Digital Elevation Model (DEM), as described in Chapter 5.
- 3) To provide the spatial fields of meteorological input data on an hourly basis through spatiotemporal interpolation of station data (Chapter 6).
- 4) To parameterize the soil hydraulic properties for each soil texture class using Pedotransfer functions (Chapter 7).
- 5) To estimate plant physiological parameters (which are assumed to be static) using information taken from literature sources, and to derive the temporal evolution of Albedo and LAI from remote sensing data (a time series of Landsat images), as described in Chapter 8.
- 6) To present, discuss and validate some of the results obtained by modelling of land surface processes (the water and energy fluxes) using the model PROMET (Chapter 9). Hourly modelled outcomes will be aggregated in time to daily, monthly, and annual values using different types of aggregation functions (e.g., average, sum, etc.). Special emphasis will be given to the assessment of the long-term spatial distribution of the natural processes involved in the hydrological cycle (e.g., precipitation, evapotranspiration, groundwater recharge “percolation”, runoff, etc).

The thesis closes with a short summary and an outlook on future perspectives (Chapter 10).

2. The Study Area

2.1. General remarks

As mentioned previously in Chapter 1, the Greater Damascus Basin (sometimes referred to as “*Barada and Awaj Basin*” or wrongly as “*Damascus Basin*”) was selected to be the study area (Pilot Region) of this work. As can be seen in Figure 2.1, this basin is located in the southwest part of Syria (a country in southwest Asia bordered by Turkey, Iraq, Jordan, Lebanon and the Mediterranean Sea) and includes the capital of the country, the city of Damascus and its suburbs. It covers an area of approximately 8596 km² and constitutes a hydrologically closed basin (there is no excess water flowing out of the basin). It has a far higher population density than any of the Syrian regions. The estimated population living within the borders of this region is more than 4 millions (Census 2004). This basin is a rewarding subject for investigation, as it is a very heterogeneous landscape containing many different types of climates, topography, soil, vegetation and land uses. It can therefore be considered as a representative mesoscale test site of the different environmental conditions prevailing over the whole of Syria. The drainage system of this basin is represented mainly by two rivers (*Barada River* and *Awaj River*) and a few valleys that have dry river beds filled with water only during the rainy season. There are also two dry lakes (*Al-Outaibe* and *Al-Hajjaneh*) which are usually salty and drainless and only during the rainy season are covered by a thin layer of water. The eastern part of the basin (the eastern sub-basin) is characterized by: 1) very dry conditions (annual rainfall less than 90 mm), 2) its being hydrologically isolated from other water bodies (no inflow or outflow of water) and 3) lack of available information (especially meteorological data). Therefore it was excluded from this study. As a result, the study area constitutes the western part of the basin (5220 km²), which includes Damascus plain and the surrounding mountainous regions that feed this plain with surface and groundwater.

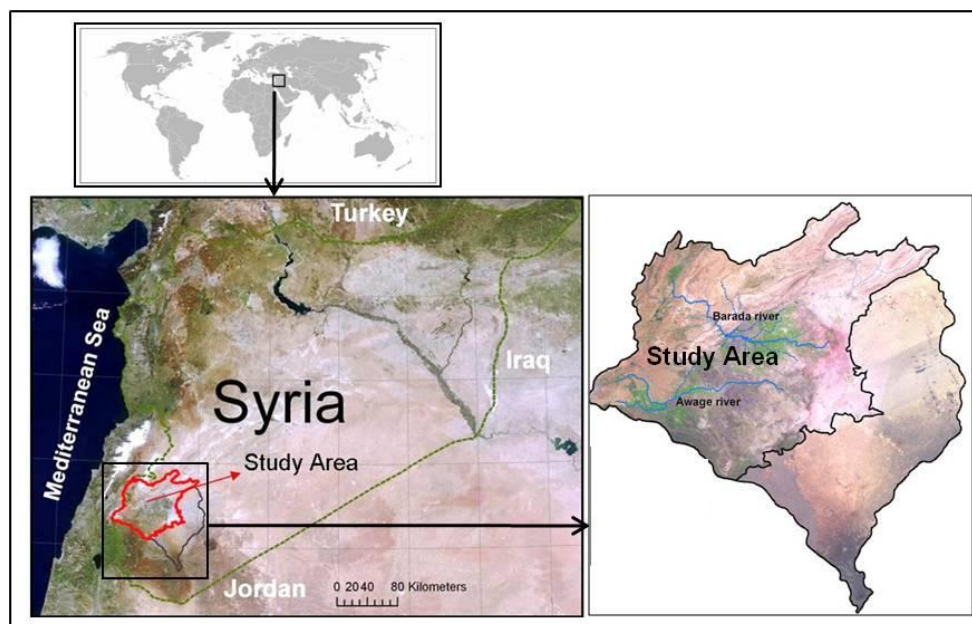


Figure 2.1 the location of the study area.

2.2. Physical Environment

2.2.1. Morphology / Topography

The morphology of the study area includes two main units: the mountains that extend in the northern and western regions of the basin (the *Anti-Lebanon mountains* including *Mount Hermon* “2814m” and *El-Kalamoun* mountains) and the plain (Damascus plain) that lies in the central and eastern regions. As can be seen from Figure 2.2, Damascus plain is characterised by a slightly levelled topography, with small variance in elevations (the average height of this plain is 650m). In the south part of Damascus plain lie the basaltic regions that are characterized by rough topography. The salty and mostly dry lakes represent the lowest regions of the study area. While the *Al-Outaibe Lake* forms the closed outlet of the *Barada River*, the *Al-Hajjaneh Lake* is considered as the closed outlet of the *Awaj River*.

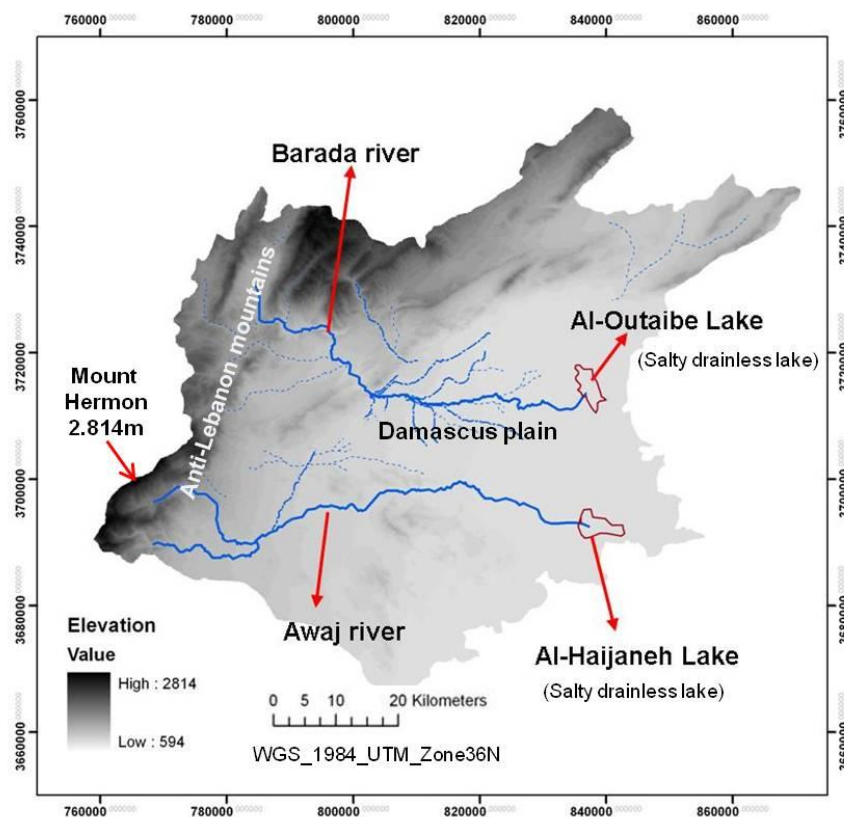


Figure 2.2 shows a Digital Elevation Model (DEM, derived from 90m SRTM data) of the study area along with vector data (river channels and lakes) draped over it.

2.2.2. Geology

According to the explanatory notes to the Geological Map of Syria, Scale: 1:200,000, Sheets I-37-VII Dimashq (Razvalyaev and Ponikarov, 1966), rocks of the Jurassic, Cretaceous, Paleogene, Neogene and Quaternary Systems are exposed in the study area. The oldest geologic deposits are Jurassic. These are composed of limestone and dolomitic limestone and mainly comprise the central part of the *Anti-Lebanon* mountains. They are characterized by karstic and fissured features. The Cretaceous then begins with sand-stones followed by fractured and fissured limestone. Then

overlie deposits represented by relatively softer rocks composed of Marl and marly dolomite. The Paleogene rocks are exposed on the south-eastern slope of Anti-Lebanon and are represented by clayey carbonaceous rocks, chalky limestone, Marl and flints. Neogene deposits, on the other hand, are represented by continental sedimentary and volcanic formations. The sedimentary deposits are exposed along the northern side of the Greater Damascus basin, and composed of a thick formation of conglomerates, sandstones, clays and limestones. The volcanic formations are represented mainly by basalts and extended widely southwards of the town of Damascus. Finally, The Quaternary deposits are also represented by sedimentary and volcanic formations. The sedimentary deposits cover predominantly Damascus plain and fill up the intermountain areas. They are divided into Lacustrine, Proluvial and Alluvial formations. Alluvial deposits are known in the valleys of *Barada River* and *Awaj River* and cover the central part of Damascus plain. They are composed of Flint, pebbles, sand and sandy clay. Proluvial deposits are formed of compact conglomerates which are mostly made up of angular limestone pebbles and clay with little sand. They are extended at the north western part of Damascus plain, especially at the foot of the mountain slopes. Lacustrine deposits are white compact lumpy marl alternating with sandy loam. They cover the eastern part of the plain including the *Al-Outaibe* and *Al-Hajjaneh* lakes.

2.2.3. Hydrogeology

Since the study area extends mainly over arid and semi-arid zones, groundwater constitutes the major source of the water supply. As shown in Figure 2.3, groundwater is connected with several aquiferous formations. Short description of these formations is presented below in stratigraphical sequence from younger to older ones (Razvalyaev and Ponikarov, 1966; Rofail and Al-Koudmani, 1986).

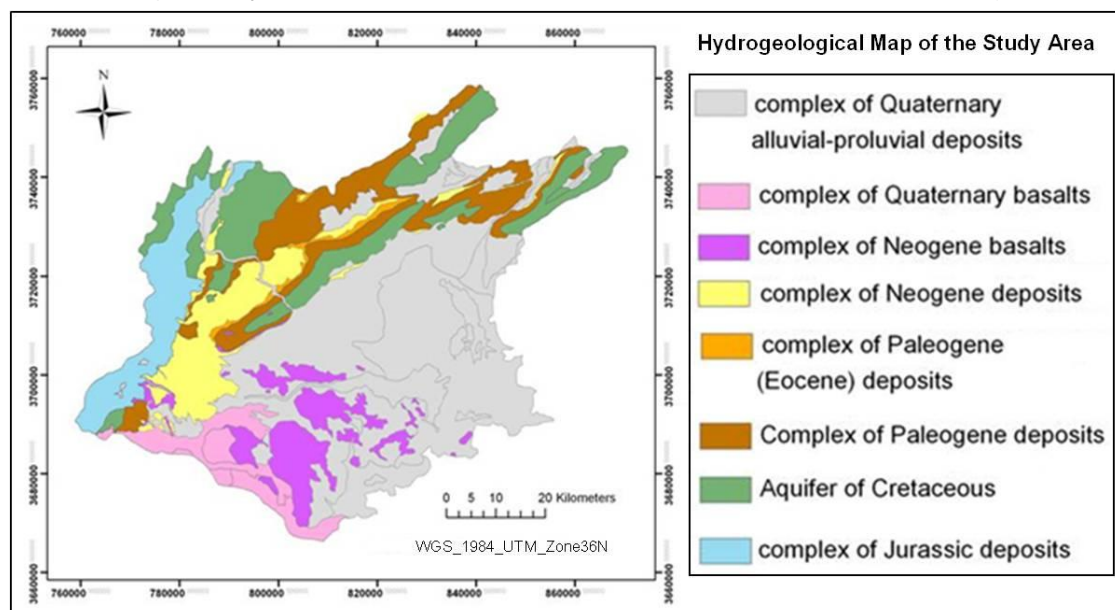


Figure 2.3 the hydrogeological map of the study area (digitized from the hydrogeological hardcopy map using the ArcGIS software).

- *Aquiferous complex of the Quaternary alluvial, proluvial and lacustrine deposits*: this complex is composed of loams, sandy loams, pebbles, conglomerates and lacustrine marls filling up the intermountain areas and essentially the plain of Damascus. All these deposits are permeable and contain groundwater which depth varies from 5 to 18 m and increases towards the central part of the depressions. The type of water depends fundamentally upon the lithological composition of the enclosing rocks. Thus, the water is fresh and slightly mineralized (0.3-0.5 g/L) in the proluvial deposits (loams, sands), whereas the water salinity increases (from 3.1 to 6.1 g/L) in the lacustrine deposits.
- *Aquiferous complex of Quaternary basalts*: it is represented by fissured basalts. Water is fresh having the salinity of (0.2 to 0.7 g/L).
- *Aquiferous complex of Neogene sedimentary deposits*: this complex is represented by pebbled conglomerates, sandstone, clay, marl and limestone. Springs connected with this aquifer have little discharge. Water is fresh having the salinity of 0.2-0.3g/L.
- *Complex of Paleogene deposits*: Deposits of the Upper Eocene are water-bearing and contain fresh water (salinity 0.1-0.3 g/L). The fissured deposits of Middle Eocene, especially flints, also compose an aquiferous horizon that feeds some small-discharge springs.
- *Aquiferous complex of Cretaceous deposits*: the deposits of lower Cretaceous are composed of fissured quartz sandstones and contain freshwater with salinity of 0.2 to 0.4 g/L. the deposits of Upper Cretaceous compose an important aquifer represented by a thick formation of fissured karsted limestones and dolomites. Water is fresh (salinity 0.2 g/L).
- *Jurassic aquiferous complex*: two aquiferous horizons are known in the Jurassic deposits. The first one is confined to the contact between a band of limestones and marl, the second is restricted between basalts and overlying limestones. Water of this aquifer is fresh (salinity 0.2-0.3 g/L).

From the viewpoint of water-supply and water content of the deposits, the Anti-Lebanon Mountains, where the amount of precipitation is high and the geological conditions are favourable for the formation of aquiferous horizons, represent good water collectors (water accumulation areas). Numerous springs here, especially those confined to large faults, are rich in water during the whole year (even during the dry summer months).

2.2.4. Soils

The study area is characterized by a large diversity of soil types, which is to be expected as a consequence of the broad differences in the natural factors of soil formation prevailing in the region including climate, parent material, relief, organisms, and time (see Chapter 7). According to USDA Soil Survey Staff (1999), the inherent properties of a soil at any one location are the product of the integrated influence of

climate and organisms, acting on soil parent material, as conditioned by topography, over a period of time. Soils may be classified in several ways. For example, they can be grouped according to dissimilarities in one soil characteristic (such as texture, permeability or colour), or they can be grouped as natural units of the landscape based on certain combinations of soil characteristics, as has been done to soils of the study area. During the second half of the 20th century, several soil survey projects have been conducted by different organizations and agencies in order to classify the soil of the Syrian Arab Republic (including the area under investigation). For example, according to the soil survey that was prepared by Food and Agriculture Organization of the United Nations (FAO) in 1977, soils of the study area can be classified into 5 different groups. The spatial distribution of these groups is shown in Figure 2.4, and a brief description of the soils is given below. The legend of the FAO soil map of Syria as well as the paper written by Shahaideh et al. (2001), constitute the main information sources of this description.

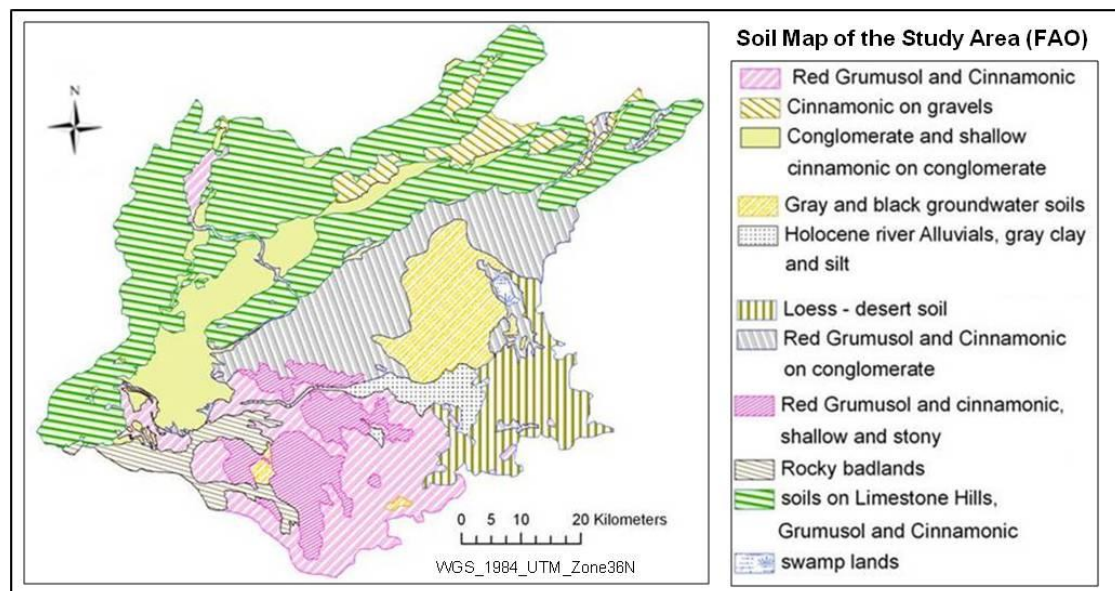


Figure 2.4 soil map of the study area (digitized from the hardcopy soil map of Syria which was prepared by FAO (1977) at a scale of 1:500,000).

- *Grumusol*: this type of soil is found in regions where annual precipitation ranges from 350 to 600mm. It is characterized by its dark red to brown colour (often referred to as brown soil), and is composed mainly of clay and silt. The organic matter content varies between 1.5 and 2.5%. Grumusol is regarded as productive soil, especially for wheat and some kinds of fruit trees.
- *Cinnamonic*: this soil occurs in areas where precipitation ranges from 150 to 300 mm for 5 months a year. It is characterized by the yellowish-brown colour, as well as the loam and clay loam texture. The properties of this soil are good (regarding the plant productivity), but shortage of water limits the opportunity to make use of it.

Leaching operations cause high level of calcium carbonate, comprising over 25% of the total soil volume (it could go up to 50%).

- *Desert soil*: this soil is characterized by the dominant brown-gray and gray colour. It is found in high temperature regions where precipitation is less than 150 mm for three months a year. It is poor in nutritive elements, and the quantity of organic matter is too small (less than 1%). The prevailing texture of this soil is loam.
- *Alluvial soil*: it is commonly considered the most fertile soil in the study area, as the quantity of organic matter can reach up to 5%. The high level of humus in this soil is considered to be responsible for its dark brown to black colour. Alluvial soils are generally connected with river floodplains, but they may also be developed on alluvial fans and lacustrine. The texture of this soil varies from clay loam to sandy loam.
- *Groundwater soil*: this type of soil originates under the influence of groundwater, capillary rise and evaporation.

Furthermore, other soil survey projects were conducted to classify the soils of Syria according to the USDA Soil Taxonomy. Soils were classified on the basis of diagnostic horizons that reflect the environments under which they form. Description of these classifications as well as the prepared soil maps is covered in detail in Chapter 7.

2.2.5. Climate

According to several authors (e.g., Akkad, 2001; Kattan, 1997; Wolfart, 1964), climate in the Greater Damascus Basin is generally characterized by a Mediterranean type with hot, dry summers and cold, rather humid winters. It is influenced mainly by the distance from the Mediterranean Sea and the local morphology. While the western part of the basin (the Anti-Lebanon Mountains) is characterized by a rainy and humid climate, the central and eastern parts are largely under the influence of a semi-arid and arid climate (see Chapter 9).

- **Precipitation**: the precipitation is unequally distributed over the basin due to the influence of the Anti-Lebanon Mountains, which form a barrier preventing humid sea-winds to penetrate deep into the eastern part of the basin. The rainy season usually starts in October and ends in April. Precipitation is concentrated for the most part during the period from December to February. It falls as snow on mountains (at altitude of over 1500m). The mean annual precipitation ranges from more than 800mm in the western part of the basin (the Anti-Lebanon) to less than 100 mm in the eastern part (the desert region).
- **Air Temperature**: the basin is characterized by high variability in daily temperatures. Differences between daily maximum and minimum temperatures can be as high as 30°C in the desert region. July and August are the hottest months of the year while December and January are the coldest. In winter the temperature often falls below the freezing point, while in summer it may rise up to 45°C.

- **Humidity:** as mentioned above, the Mediterranean Sea acts as a main source of humidity in the basin. Therefore, the relative humidity is influenced by the distance from the sea and decreases from west to east. Seasonal humidity variations are characterized by high values in winter and low values in summer.
- **Wind:** the basin is mainly subjected to westerly to north-westerly winds which bring rains from the sea. In spring and autumn winds from the Arabian Desert (dry winds called Hamsin or Khamsin) penetrate into Syria including the area under investigation.

2.2.6. Vegetation and land use

It is well known that the spatial distribution of vegetation (plant biodiversity) is influenced by many factors, including climate, elevation, soil types, etc. (Huston, 1994). Climate is generally recognized as a key determinant of species presence or absence (Perera et al., 2001). However, regarding the Greater Damascus Basin, four natural vegetation zones could be recognized according to the interactions between climate and elevation (Chikhali, 2008):

- *The high mountainous zone:* the climate conditions in this zone are generally characterized by low temperature, the presence of snow and long period of frost. This area comprises the central part of Anti-Lebanon mountains where the most precipitation falls as snow at elevations above 2000m. The vegetation of this zone consists of grass species such as *Astragalus* and shrub species such as *juniperus excelsa*.
- *The mountainous zone:* this zone comprises the mountainous region at elevation ranging from 1400m to 2000m. This area is locally covered by rare grass and forests species of *Cedrus*, *Juniperus* and *pinus*. In the western part of the mountainous region the slopes are rather densely covered by *juniper*.
- *The Syrian climate zone:* this zone is confined to the area between the Anti-Lebanon in the west and the arid steppe in the east. Vegetation of this zone consists of sparse shrubs such as *Anabasis*, *Salsola* and *Artemisia* and some tree species such as *Cretaegus* and *azarolus*.
- *The dry zone (Al-Badiyah):* this zone comprises the eastern part of the study area, where the annual rainfall is less than 200mm. Vegetation of this region consists of grass species such as *Vicia* and shrubs of *Atriplex* and *Artemisia*.

In respect to land use, as will be seen in Chapter 4, the prevalence of a wide range of agro-ecological conditions in the basin allows the production of many types of agricultural crops including cereals, legumes, vegetables and fruits. The cultivated land in the basin can be divided, according to the water source, into irrigated and rainfed land (agriculture). Rainfed agriculture is distributed mainly in the comparatively fertile depressions and valleys between the mountains. It is influenced by the heterogeneity of climate, relief and soil properties. Irrigated agriculture, on the other hand, is confined mainly to the *Damascus Ghouta (Oasis of Damascus)* and to

the river valleys. The *Damascus Ghouta*, through which the Barada River and its channels flow and irrigated the agriculture, is considered as the densest agricultural belt in the basin. Historically, it has supplied the inhabitants of Damascus with a variety of fruits, cereals, legumes and vegetables for thousands of years (Burns, 2005). Its agriculture is characterized by a mosaic-like of fruit trees (olives, apricots, plums and grapes) and field crops (wheat and barely dominated). Figure 2.5 shows the land use/land cover map of this oasis (the central part of the study area), which was prepared within the framework of cooperation between the Arab Center for the Studies of Arid Zones and Dry Lands (ACSAD) and the German Federal Institute for Geosciences and Natural Resources (BGR). The classification scheme of this map depends on the degree of irrigation, plant density and Geology (Lithology) of the bare exposed deposits. This map was acquired in hardcopy format and registered as image to image to the geo-referenced Landsat image (which was previously rectified) using ERDAS Imagine 9.1. It was then digitized into vector-based file using the ArcGIS software.

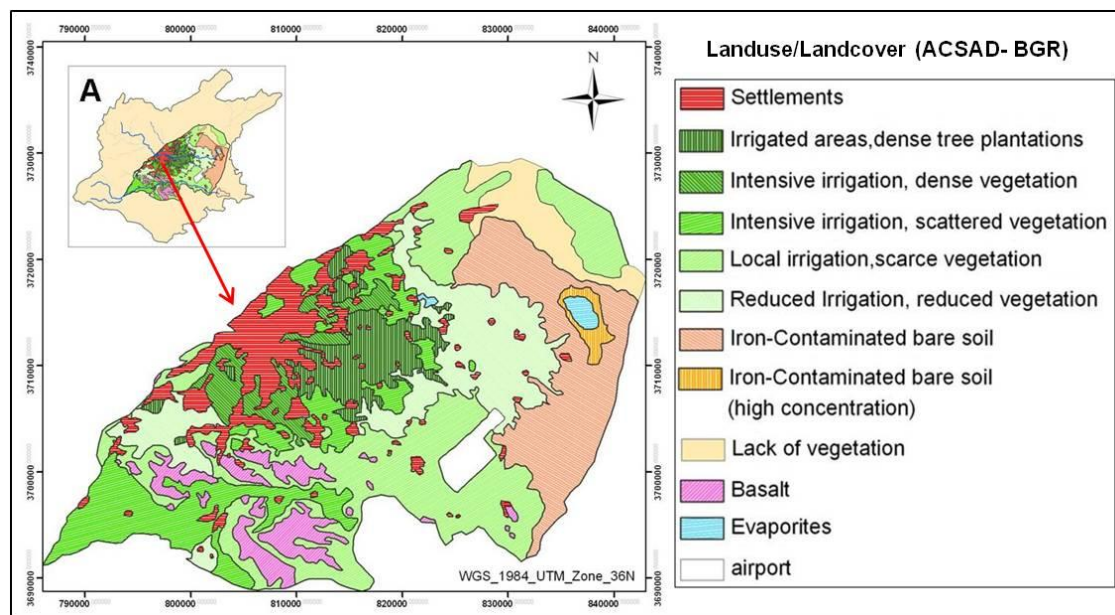


Figure 2.5 Land use/Land cover map of the central part of the study area (Al-Ghouta), which was prepared within the framework of cooperation between ACSAD and BGR. The location of this map in relation to the whole study area is shown in the top-left of this figure.

In addition, The General Organization of Remote Sensing in Syria (G.O.R.S) has also produced a land use/land cover map covering nearly the same part of the basin, as shown in Appendix 1. This map was extracted by visual interpretation of high resolution remote sensing data in combination with traditional land survey techniques. Its classification scheme was identified in such a way as to allow the discrimination between different agricultural species. This map was also registered and digitized in the same manner as described above.

3. The Model PROMET

3.1. Overview of the model PROMET

PROMET (Processes of Radiation, Mass and Energy Transfer) is a physically-based spatially-distributed model developed and enhanced by Mauser and Bach (2009) to simulate the fluxes of energy and matter (water, carbon, nitrogen) on the land surface. It evolved from a Soil-Vegetation-Atmosphere Transfer (SVAT)-scheme, which was originally designed by Mauser and Schädlich (1998) to simulate evapotranspiration using remote sensing data. It is designed for worldwide application and can be applied at different scales, ranging from single fields to a mesoscale catchment (100,000km²). PROMET has proven its reliability and applicability in a variety of research studies (e.g., Ludwig and Mauser, 2000; Strasser and Mauser, 2001; Bach et al., 2003) and has been adopted and integrated in the modelling framework of GLOWA-Danube (as part of the decision support system DANUBIA) to investigate the impact of climate change on the water cycle (GLOWA-Danube, 2009). According to Mauser and Bach (2009), PROMET takes full advantage of the use of physical and physiological descriptions of the processes related to water and energy fluxes so as to be able to cover the different feedbacks induced by climate change. For that reason, the values of the model input parameters are not calibrated using site-specific measurements but are rather taken from literature sources or derived from remote sensing data. It should also be mentioned that PROMET runs on an hourly time step and strictly conserves mass and energy as a whole and throughout all its components and interfaces. It is embedded within a raster-based GIS-structure which enables integration of spatial data from various sources (e.g., remote sensing data). Regarding the technical aspects, PROMET is implemented in FORTRAN with a graphical user interface for the use in the Windows environment on ordinary desktop PCs.

3.2. The architecture of the model PROMET

The architecture of the model PROMET, as depicted in Figure 3.1, is composed of the following eight components:

- The meteorology component
- The vegetation component
- The land surface energy and mass balance component
- The snow and ice component
- The soil hydraulic and soil temperature component
- The groundwater component
- The channel flow component
- The man-made hydraulic structures component

However, before I begin discussing these different interacting components, it may be useful to first illustrate the concept of the so-called “*Proxel*” (**process-pixel**). PROMET uses the proxel concept, which is composed of a pixel (picture element) in

the form of a cube, in which all processes and interactions with its environment (neighbour proxels) take place (Ludwig et al., 2003; Barthel et al., 2005). In view of that, proxel concept can be understood as a highly specialized pixel concept. Figure 3.2 shows the schematic representation of the proxel concept used by the model PROMET to simulate the different environmental processes occurring within the study area. As can be seen from this figure, the modelled area is composed of 363768 proxels, containing 659 proxel-columns and 552 proxel-rows. Each proxel represents an area of 180m*180m on the ground (choosing this spatial resolution will be discussed in Chapter 5). However, not every proxel is part of the catchment area. The number of proxels that belong to the boundary of the catchment area is equal to 161138 (comprising an area of about 5220 km²). Proxels of the raster-GIS that are situated beyond the boundary of the catchment are masked from the computation.

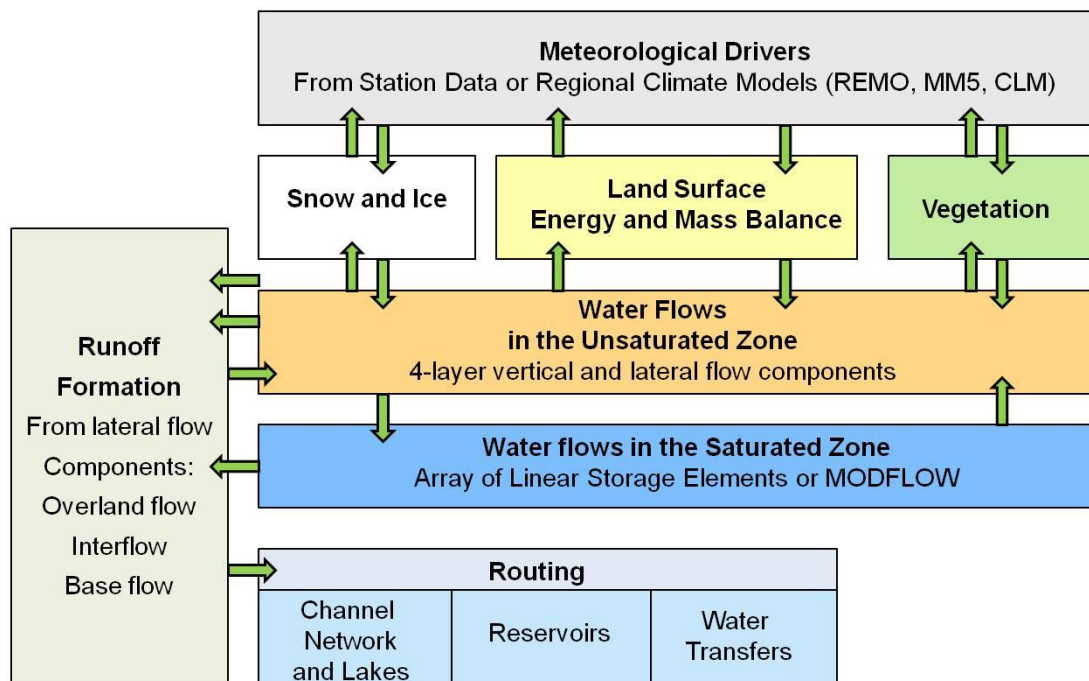


Figure 3.1 shows a schematic structure of the model PROMET. Boxes represent components whereas arrows indicate the interfaces between them, through which data is exchanged (Mauser and Bach, 2009).

After this overview of the architecture of the model PROMET and the concept of Proxel (the basic building block in a raster model), the following sections are intended to give a more comprehensive insight into its eight interacting components and the approaches used for each of them. For more information on the model and its different components, readers are referred to Mauser and Bach (2009), Mauser (2002), Mauser and Schädlich (1998), Strasser and Mauser (2001), Strasser et al., (2007), Marke (2008), Strasser (1998), and Muerth (2008).

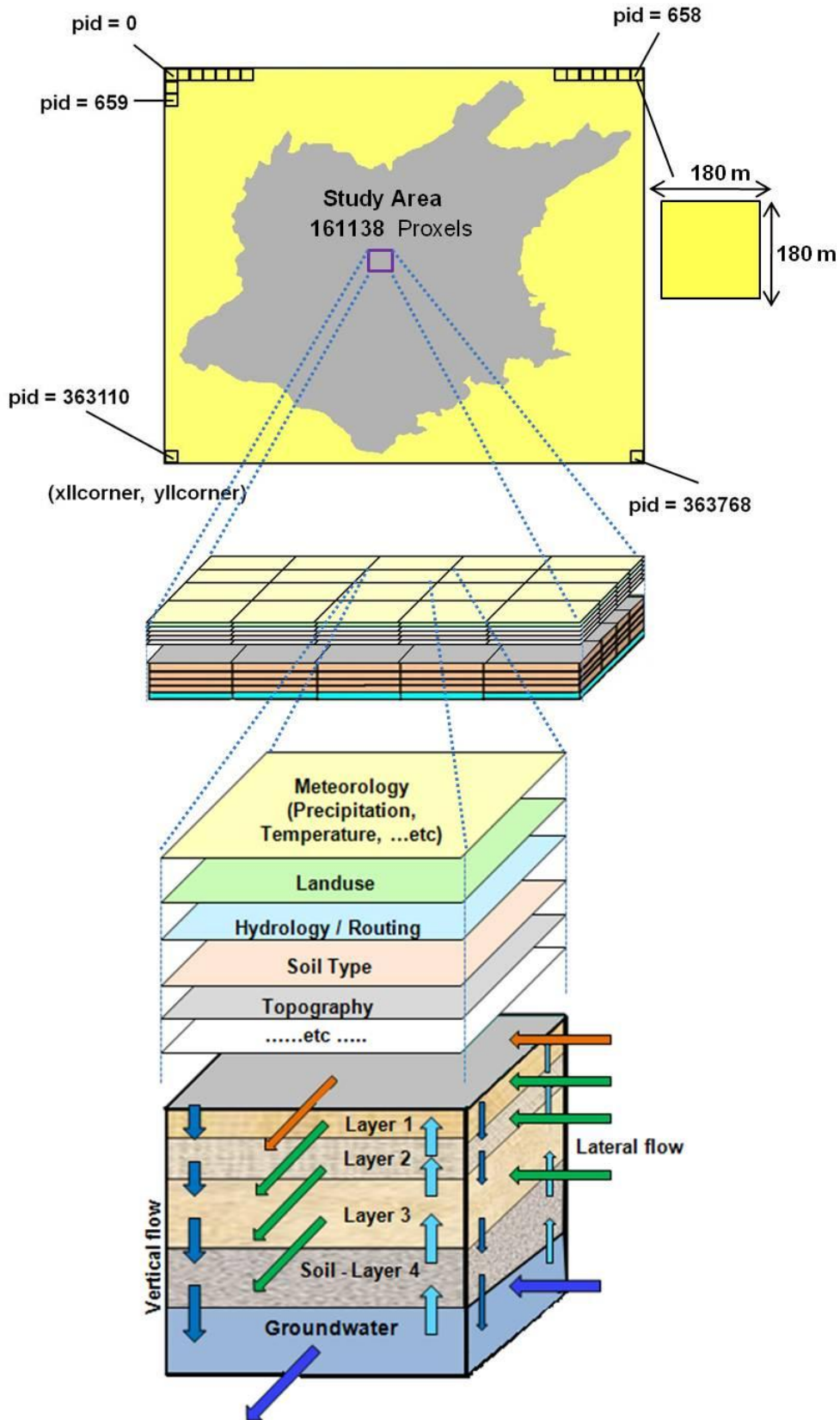


Figure 3.2 gives the schematic representation of the proxel concept. The simulated area consists of 363768 proxel (659 proxel-columns and 552 proxel-rows). The number of proxels that belong to the catchment area is 161138.

3.2.1. The meteorology component

The aim of this component, which consists of two sub-components, is to deliver the meteorological variables for the subsequent land surface components. Each of these two sub-components provides the following parameters on an hourly basis for each pixel in the study area:

- Precipitation [mm]
- Air temperature [°C]
- Relative air humidity [%]
- Wind speed [m/s]
- Incoming direct shortwave radiation (via cloudiness) [W/m²]
- Incoming diffuse shortwave radiation (via cloudiness) [W/m²]
- Incoming longwave radiation (via cloudiness) [W/m²]

The first sub-component, which is used in this study, provides the required meteorological fields by means of the interpolation and disaggregation of the measurements of the available weather stations. These measurements in turn represent discrete, punctual values, since they are only presented at the *Mannheimer Stunden* (at 7:00, 14:00 and 21:00 in case of climate stations) at individual proxels throughout the study area. Thus, in order to provide the required meteorological input parameter on an hourly basis for each proxel existing within the area under investigation, the measured station data have to be temporally and spatially interpolated. The fundamental approach of this sub-component (also referred to as “*AtmoStations*”) consists of three successive phases (Mauser, 2002): 1) temporal interpolation and disaggregation, 2) spatial interpolation, and 3) calculation of incoming radiation.

3.2.1.1. Temporal interpolation and disaggregation

The aim of the temporal interpolation and disaggregation of measurements is to assign a value to the measured meteorological parameters for each simulation time step. The meteorological parameters of temperature, relative humidity, and wind speed are presumed to be continuous; therefore, a cubic spline function is applied to interpolate them to hourly values. In contrast to these meteorological parameters, precipitation can be highly variable over time and occurs in discrete events. Therefore, the measured values of precipitation cannot be interpolated temporally; instead they have to be disaggregated temporally to retrieve values on an hourly basis. In addition to that, two different types of precipitation can be discerned using this meteorological sub-component: short events (one singular recording), for which a Gaussian distribution is presumed, and long-term events (two or more successive recordings), for which the recorded precipitation sum is equally distributed in time. In this study, however, the total amount of daily precipitation was distributed into equal hourly intensities. This is due to the fact that there was no hourly precipitation data available.

3.2.1.2. Spatial interpolation

Once the meteorological measurements have been temporally interpolated/disaggregated, the resulting hourly values, which are available only for those proxels that have a weather station, have to be spatially interpolated to gain meteorological input variables for all other proxels of the study area. The spatial interpolation takes into account the altitudinal gradient (the parameter-elevation dependencies) for many meteorological parameters. According to Mauser (2002), the process of spatial interpolation of the meteorological parameters is performed for each model time step (1 hour) in a 4-stage approach.

- In a first stage, a linear regression function between the measured meteorological parameters and the station altitudes is calculated. It represents the average behavior of the parameter with altitude (the prevailing parameter-elevation dependency) for the current model time step.
- This regression function is used along with the digital elevation model (DEM) to calculate a value for the considered meteorological parameter for each proxel in the study area (normal field). The same meteorological measurements used to derive the regression function are once again employed to account for local deviations from the normal field. This is done by subtracting the measurements from the normal field and creating a residual for each station.
- The resulting residuals are then interpolated using an inverse cubic distance approach, which, in this study, showed better results than those interpolated with the two other approaches tested (namely, the inverse distance and the inverse squared distance). Six surrounding stations were taken into account for each point of interest during this process.
- Finally, the resulting spatially interpolated residuals are added to the normal field. This process guarantees the reproduction of the station measurements and simultaneously takes into account the influence of relief in the spatial distribution of the meteorological variables.

In view of the fact that relative humidity has a nonlinear dependence on temperature and therewith the elevation, it is first converted to absolute humidity (water vapour pressure), then interpolated and converted back into relative humidity.

3.2.1.3. Calculation of incoming radiation

As incoming short and longwave radiation fluxes are not measured by the climate stations, they have to be derived indirectly. Incoming shortwave radiation at the earth's surface under clear-sky conditions is generally estimated as a function of terrain characteristics (elevation, slope, aspect) and astronomical factors (sunrise and sunset, local time, azimuth and zenith angle, distance sun-earth and the solar constant)(Liston and Elder, 2006). Taking into account the above mentioned topographic and astronomical factors, PROMET ("*AtmoStations*") simulates incoming short and longwave radiation fluxes based on the interpolated cloud cover measurements in two steps. In the first step, the cloud free irradiance is simulated as direct and diffuse fluxes using the approach of McClatchey et al. (1972). In the

second step, the resulting values are then corrected for cloud cover according to Möser and Raschke (1983). Incoming longwave radiation is computed using the interpolated air temperature and cloud cover.

On the other hand, the second sub-component of the meteorology-component offers the possibility of coupling the model with regional climate models (RCMs), such as REMO, MM5 and CLM, by using the downscaling interface SCALMET (Marke and Mauser, 2008). This interface downscales fluxes of energy and mass from climate models, which are generally provided in a coarser spatial resolution (10-45km), and makes them compatible with PROMET. A detailed description of this interface is found in Marke (2008).

3.2.2. The vegetation component

PROMET in its current version offers the user the possibility to choose between two different approaches (vegetation sub-components) for the simulation of the evapotranspiration processes. One of those two sub-components employs a completely dynamic physiological method for simulating the plant CO₂ exchange and plant growth as proposed by Farquhar et al. (1980). Using this sub-component, the temporal courses of LAI, plant height, albedo and root growth are modelled based on the net CO₂-assimilation rates. A detailed description of this approach is given in Hank (2008). In this study, however, PROMET was run using the other sub-component which calculates the actual evapotranspiration based on the scale-independent Penman-Monteith equation (Monteith, 1965) as a function of water availability, energy balance, physical soil characteristics and the physiological regulation mechanisms of heterogeneous plant stands (Mauser and Schädlich, 1998; Strasser and Mauser, 2001; Mauser and Bach, 2009). The Penman-Monteith equation can be expressed in a number of alternative forms (Jones, 1992). In its general form, however, it is usually written as follows (Eq. 3.1):

$$ETa = \frac{\Delta \cdot (Q - B) + \rho \cdot c_p \cdot \frac{(e_s - e_a)}{r_a}}{\Delta + \gamma \cdot \frac{1 + r_s}{r_a}} \quad (\text{Eq. 3.1})$$

With:

ETa = the actual evapotranspiration

Δ = the slope of the water vapour pressure curve vs. temperature

Q = the radiation balance

B = the soil heat flux

ρ = the density of air

C_p = the specific heat of the air

γ = the psychrometric constant

e_s = the saturated water vapour pressure at gauging level

e_a = the current water vapour pressure at gauging level

$(e_s - e_a)$: vapour pressure deficit

r_a = the aerodynamical resistance

r_s = the surface resistance (canopy stomatal resistance).

According to Raupach (1995), the Penman-Monteith equation is a physically based description of the evapotranspiration process, which combines the energy budget of the land surface with the concept of a species-dependent surface resistance to the water vapour transfer. Consequently, it does not necessitate specific calibration and it can be assumed that its application is valid at different scales from single field to a region. Allen et al. (1998) stated that this equation can be used for the direct estimation of any crop evapotranspiration since the surface and aerodynamic resistances are crop specific. Additionally, as mentioned earlier in this chapter, the Penman-Monteith-PROMET has demonstrated its validity, reliability and efficiency in a number of publications for various catchments of different sizes, and therefore can legitimately be proposed for modelling actual evapotranspiration in the study area.

Using the Penman-Monteith equation, PROMET calculates the water transport as a function of the specific canopy resistance, determined by its leaf area index, stomatal resistance, absorbed photosynthetic active radiation (PAR), temperature, humidity and soil moisture (Baldocchi et al. 1987; Mauser and Bach, 2009). The three last mentioned variables are introduced as limiting factors for the stomatal resistance in form of an environmental influence function (g), which ranges from 0 (total inhibition, stomatal resistance approaches infinity) to 1 (no inhibition). Thus, stomatal resistance is determined after Baldocchi et al. (1987) as follows (Eq. 3.2):

$$r_s(PAR) = \left[r_s(min) + b_{rs} \cdot \frac{r_s(min)}{PAR} \right] \cdot \frac{1}{g} \quad (\text{Eq. 3.2})$$

With:

$r_s(min)$ = the plant specific minimum stomatal resistance [sec/m]

b_{rs} = slope parameter for stomatal resistance with solar irradiance (a plant specific parameter equal to the PAR flux at twice the minimum stomatal resistance) [W/m^2]

The environmental influence function (g) can be written in a general form as follows (Eq.3.3):

$$g = g(T) \cdot g(\Psi) \cdot g(D) \quad (\text{Eq. 3.3})$$

With:

$g(T)$ = influence function for air temperature

$g(\Psi)$ = influence function for leaf water potential (depends on soil moisture)

$g(D)$ = influence function for humidity (or vapour pressure deficit)

Stomatal conductance (inverse of stomatal resistance) increases with increasing temperature until a threshold temperature, after which it decreases. The reaction of stomatal conductance to temperature (T) is calculated using the function proposed by Jarvis (1976) as follows (Eq. 3.4):

$$g(T) = \frac{T - T_{min}}{T_0 - T_{min}} \cdot \frac{(T_{max} - T)^b}{(T_{max} - T_0)^b} \quad (\text{Eq. 3.4})$$

With:

T_{MIN} = the minimum temperature at which stomatal closure occurs

T_{MAX} = the maximum temperature at which stomatal closure occurs

T_0 = the optimum temperature (at which stomatal resistance is a minimum)

b = is defined as $b = (T_{max} - T_0)/(T_{max} - T_{min})$

The relationship between stomatal conductance ($1/r_s$) and vapour pressure deficit (D) can be described by a linear function as follows (Eq. 3.5):

$$g(D) = 1 - b_v D \quad (\text{Eq. 3.5})$$

With b_v is a constant.

Water stress, which is caused by insufficient soil moisture, can be quantified in terms of leaf water potential (Ψ). According to Baldocchi et al. (1987), stomatal conductance is to some extent independent of leaf water potential until it falls below a plant-specific threshold value (Ψ_0), after which the stomata close rapidly. Thus, the dependence of stomatal conductance ($1/r_s$) on leaf water potential (Ψ) is modelled based on the following weight functions (Eq.3.6a and Eq. 3.6b):

$$g(\Psi) = 1, \quad \text{if } \Psi > \Psi_0 \quad (\text{Eq. 3.6a})$$

$$g(\Psi) = a \Psi + b_w, \quad \text{if } \Psi < \Psi_0 \quad (\text{Eq. 3.6b})$$

Where the parameter a and b_w are assumed constant for each plant species.

Finally, interception of rainfall by plant canopy is simulated by calculating a maximum storage capacity (the maximum thickness of the intercepted water layer), which is filled during rainfall. It depends mainly on the leaf area index (LAI) and is calculated as proposed by Von Hoyningen-Huene (1981) as follows (Eq. 3.7):

$$S_{max} = 0.935 + 0.498 * LAI - 0.00575 * LAI^2 \quad (\text{Eq. 3.7})$$

Where: S_{max} = Maximum storage Capacity (mm)

It should be mentioned here that the evaporation from the interception storage is assumed to occur at the potential rate (Ludwig and Mauser, 2000; Rosenberg et al., 1983).

3.2.3. The land surface energy and mass balance component

This component is used to close the energy balance on the land surface taking into consideration all energy fluxes including latent, sensible and ground heat fluxes

together with the reflected shortwave and emitted longwave radiation. In addition, depending on the aerodynamic resistance of the land surface (r_a), this component uses a radiative transfer model to describe the transportation of water vapour through the boundary layer into the atmosphere above the canopy (Monteith, 1973; Campbell and Norman, 1998). Assuming a spherical angle distribution of the leaves, the model calculates the fraction of shaded and sunlit leaves in the canopy depending on the sun elevation angle and leaf area index (LAI). Assuming a neutral boundary layer and logarithmic wind profile, r_a is modelled after Monteith (1965) as follows (Eq. 3.8):

$$r_a = \frac{1}{k^2 \cdot u(Z)} \cdot \ln^2 \left(\frac{Z-d}{Z_0} \right) \quad (\text{Eq. 3.8})$$

With:

$u(Z)$	= wind speed at height (Z)	[m.s ⁻¹]
d	= zero plane displacement height	[m]
k	= von Karman's constant, 0.41	[-]
Z_0	= roughness length	[m]

3.2.4. The snow and ice component

This component is designed for the purpose of modelling the energy balance, the water equivalent and the melt rate of the snow and ice cover. The spatiotemporally interpolated air temperature values are firstly used to determine whether precipitation falls as rain or as snow. Simultaneously, a distinction is made between potential melting conditions (air temperature ≥ 273.16 K) and no melt conditions (air temperature < 273.16 K) for each Proxel and model time step. In the first case, it is assumed that the snow surface temperature is equal to 273.16 K, and melt can take place. In the second case (air temperature < 273.16 K), snow surface temperature is assumed to equal air temperature, and no melt takes place. Commonly, the energy balance of the snowpack can be expressed as:

$$Q + H + E + A + B + M = 0 \quad (\text{Eq. 3.9})$$

where

Q: is the radiation balance (net radiation)

H: the sensible or convective heat gained from the air

E: the latent heat of evaporation, condensation or sublimation

A: the advective energy supplied by solid or liquid precipitation

B: the soil heat flux

M: the energy potentially available for melting of the snowpack

For a more detailed description of the model algorithms the reader is referred to Strasser et al. (2007), Strasser (1998), and Prasch et al. (2007).

3.2.5. The soil hydraulic and soil temperature component

The goal of this component is to simulate the volumetric soil water content (also called soil moisture content) and soil temperature as well as the vertical and lateral water movements in and on the unsaturated soil as a function of infiltration, exfiltration, percolation and capillary rise. The soil moisture module implemented in this component is based on an approach proposed by Eagleson (1978) to simulate soil moisture movement in a homogenous soil column, which was modified and enhanced by Mauser and Bach (2009) for simulating up to four soil layers. Figure 3.3 illustrates the basic processes simulated in this approach. Generally water fluxes are simulated for each soil layer characterized by its own static properties and dynamic conditions. A soil layer receives its water supply either by infiltration from above (effective precipitation or percolation from upper layer) or by capillary rise from below (from groundwater table or from lower soil layer). On the other hand, loss of water occurs from the soil mainly through evaporation (from the top soil layer), transpiration (root water uptake from each rooted layer) or gravitational drain (each layer). If the net percolation from a soil layer (excluding the deepest one) exceeds the infiltration capacity of the lower layer, the amount of excess water is discharged laterally to its hydraulic neighbour proxel as fast or slow interflow. Percolation from the deepest soil layer contributes to the groundwater recharge. Capillary rise may take place under dry conditions.

For a homogeneous soil column, the variability of the volumetric soil water content (θ) can be described by the one-dimensional Philip equation (Philip, 1957) as follows:

$$\frac{\partial \theta}{\partial t} = \frac{\partial}{\partial z} \left[D(\theta) \frac{\partial \theta}{\partial z} \right] - \frac{\partial k(\theta)}{\partial z} \quad (\text{Eq. 3.10})$$

where

t is the time in [s]

z is the depth in [cm]

$k(\theta)$ is the effective hydraulic conductivity in [cm/s]

$D(\theta)$ is the hydraulic diffusivity in [m^2/s], which can be defined as follows:

$$D(\theta) = k(\theta) \frac{\partial \Psi(\theta)}{\partial (\theta)} \quad (\text{Eq. 3.11})$$

with $\Psi(\theta)$ being the soil matrix potential (as a function of moisture content) [cm].

However, in order to obtain an analytic solution of the Philip equation, an approximation of $\Psi(\theta)$ and $k(\theta)$ on the basis of measurable, time-independent ("static") soil parameters should be found. Eagleson (1978) employed the equation derived by Brooks and Corey (1964) to determine the relationship between soil water content and soil matrix potential (also referred to as bubbling pressure head, tension, or suction).

$$\Psi(s) = h_b \cdot s^{\frac{-1}{\lambda}} \quad (\text{Eq. 3.12})$$

where

s is the degree of saturation (the ratio of moisture content to the porosity)

h_b is the bubbling pressure head [cm]

λ is the pore size distribution index.

According to Brooks and Corey (1964) the hydraulic conductivity of unsaturated soil $k(\theta)$ can be calculated as following equation:

$$k(\theta) = k_s \cdot s^c = k_s \cdot s^{(2+3\lambda)/\lambda} \quad (\text{Eq. 3.13})$$

where

k_s is the saturated hydraulic conductivity

$$c = (2+3\lambda) / \lambda$$

Since effective porosity (n) is constant for a modelling time step, the approximate equation of the hydraulic diffusivity $D(\theta)$ can be written as:

$$D(\theta) = k_s \cdot s^c \cdot \frac{\partial}{\partial \theta} \left(h_b \cdot s^{-1/\lambda} \right) = \frac{|h_b| \cdot k_s}{n \cdot \lambda} s^{c - (1/\lambda) - 1} \quad (\text{Eq.3.14})$$

$$\rightarrow D(\theta) = \frac{|h_b| \cdot k_s}{n \cdot \lambda} s^d \quad \text{with } d = c - (1/\lambda) - 1 \quad (\text{Eq. 3.15})$$

For solving this equation, the flowing static parameters must be known:

- Bubbling pressure head (h_b)
- Saturated hydraulic conductivity (k_s)
- Effective porosity (n)
- Pore size distribution index (λ)

However, in order to assure the reliability of the analytical solution of the Philip equation, Eagleson (1978) provided the following assumptions and simplifying boundary conditions:

- The groundwater table lies much deeper than the bottom of the simulated soil layer (the medium is assumed to be semi-infinite).
- The soil moisture is assumed to be uniformly distributed throughout the soil column. Each soil layer simulated within PROMET is considered homogeneous; exchange occurs only at the boundaries between soil layers.
- Distribution of roots for each plant is assumed to be uniform within the soil column in the single layer model. This is considered by the 4-layer module by accepting different root distributions only between layers, but not within a single soil layer.

Under these fundamental assumptions, Eagleson (1978) defined the following cases for in- and exfiltration:

- If precipitation intensity is less than the infiltration capacity of the soil, the soil is unsaturated and the infiltration rate equals the precipitation intensity (no surface runoff takes place).
- If precipitation intensity exceeds the infiltration capacity, the soil gets saturated and the infiltration rate equals the infiltration capacity (the excess water forms surface runoff).
- If the evaporation demand (potential evapotranspiration) is less than the exfiltration capacity, actual evaporation is not constrained by water scarcity and the soil surface does not dry out, as the soil supplies an adequate amount of water for surface evaporation.
- If the evaporation demand exceeds the exfiltration capacity, the soil runs dry and the actual evaporation rate is equal to the exfiltration capacity of the soil.

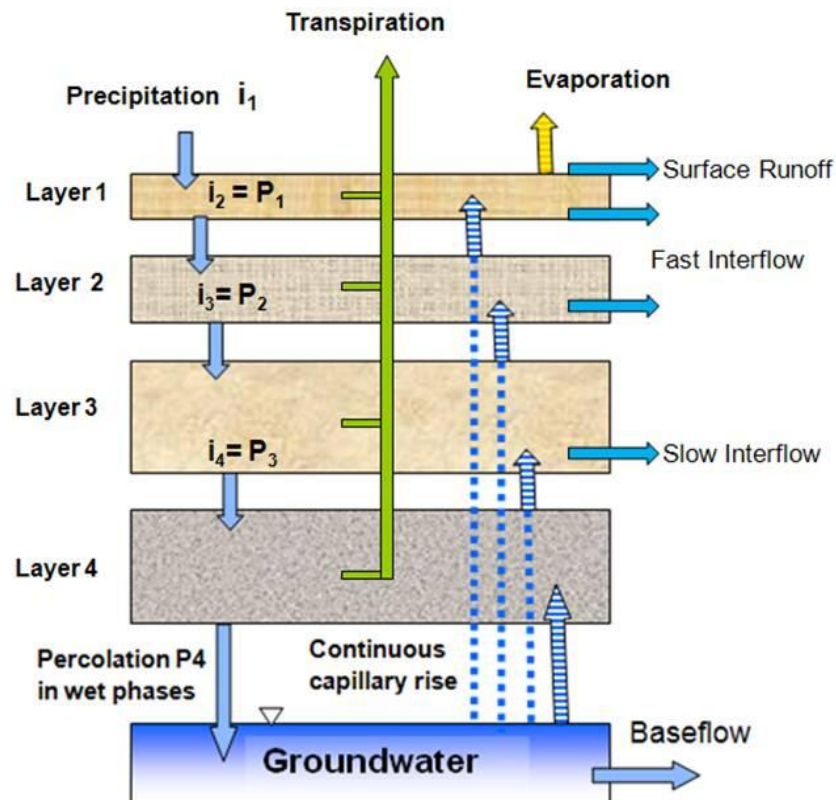


Figure 3.3 Soil water fluxes simulated by the soil moisture module (the modified 4-layer Eagleson model) of PROMET (Muerth, 2008).

On the other hand, the Soil Heat Transfer Module (SHTM) developed by Muerth (2008) and implemented within this model-component is used to compute heat fluxes between the four soil layers and the atmospheric boundary layer. The computation of

the soil temperatures is determined using the following one-dimensional heat conduction equations, which are solved for each soil layer:

$$G(z) = -k \frac{\partial T}{\partial z} \quad (\text{Eq. 3.16})$$

$$C_s \frac{\partial T}{\partial t} = \frac{\partial}{\partial z} \left(k \frac{\partial T}{\partial z} \right) \quad \rightarrow \quad \frac{\partial T}{\partial t} = \frac{k}{c_s} \left(\frac{\partial^2 T}{\partial z^2} \right) \quad (\text{Eq. 3.17})$$

where

$G(z)$ is the heat flux [W/m²] at depth z

C_s is the heat capacity [J/kgK]

k is the heat conductivity [W/mK]

While the soil surface temperature taken from the land surface energy and mass balance component represents the upper boundary condition, the lower boundary condition is given by an analytical solution of a fifth virtual layer, which is supposed to be located beneath the lowermost soil layer (in a depth of 2.5m), depending on annual air temperature. For further information on this component the reader is directed to Muerth (2008).

3.2.6. The groundwater component

This component is responsible for simulating water flow in the saturated zone of the catchment and exchanges water with the unsaturated zone and the channel network. It is composed of two sub-components, both of which depend on empirical estimation of aquifer parameters using measured recession curves.

The first sub-component, which represents the one used in the present work, employs a simplified groundwater storage model, in which each proxel in the catchment is equipped with a simple linear storage element that filled by the percolation from the bottom soil layer (groundwater recharge) and drains into a stream channel. A time constant is allocated to each linear storage element depending on the distance between the respective proxel and the next main channel. Under the assumption that all water that percolates to the groundwater body will discharge to the surface within one year, the time constant has a value ranging from one hour (proxels located on a main channel) to one year (proxels situated at the largest distances to the next main channel). The distance of each proxel to the main channel was derived by analyzing the DEM (*Digital Elevation Model*) using the topographical parameterization software TOPAZ (Garbrecht and Martz, 1999).

The second sub-component, on the other hand, provides an interface for coupling the model PROMET with the groundwater model MODFLOW (USGS, 2010). Through this interface, PROMET supplies the grid cells in MODFLOW with groundwater recharge (percolation from the bottom soil layer) and receives water that is discharged into the channel network. A more detailed description of this interface can be found in Barthel et al. (2007) and Harbaugh et al. (2000).

3.2.7. The channel flow component

The channel flow component is responsible for simulating the concentration of lateral water flows into river runoff and for routing the river runoff through the channel network according to the topographic conditions. It assumes that each proxel in the catchment is part of the channel network (each proxel has a channel) and that all proxels are hydraulically interconnected. The model makes a distinction between overland-flow (surface runoff), interflow and groundwater-flow (baseflow) components, and deals with each component in a different way. While surface runoff is directly transported to the proxel's channel, interflow of each soil layer enters the river channel when a major tributary is encountered. The network of major tributaries, as will be described in Chapter 5, is derived by applying a threshold value (critical source area) to the flow accumulation grid (upstream area) using the TOPAZ software package. Below this user-defined threshold interflow is delivered to the soil layers of the hydraulic neighbour proxels, and adds to their water content.

Once water has entered the channel network, it is routed in a self-organising process by transferring the channel-flow from each proxel to its hydraulic neighbour. Flow velocities and changes of water storage in the channel are simulated using the mass-conservative Muskingum-Cunge-Tonini approach (Cunge, 1969; Todini 2007). In order to avoid instabilities in the calculation of runoff routing, the time interval of the routing scheme should be smaller than the standard one-hour time step of the computation. Hence, it was set to be equal to 2 minutes. The parameterization of the routing coefficients for each proxel necessitates the knowledge of channel width, length and slope. While channel slopes and lengths can be derived by analyzing the *DEM* using TOPAZ, channel width is estimated using a two-step procedure. In the first step, channel width is determined at selected sites along the channel network using high resolution remote sensing data (e.g., images taken from Google Earth). In the second step, the obtained values of channel width are regionalized through a correlation with the flow accumulation grid determined using TOPAZ.

3.2.8. The man-made hydraulic structures component

The aim of this component is to simulate the hydraulic behaviour of reservoirs and the anthropogenic water transfers in the catchment. Reservoirs receive inflow and provide outflow to the channel network and therefore are handled in the same manner as lakes. Outflow from a reservoir is calculated based on its actual stored amount of water and a particular monthly lookup-table providing a translation of storage volume into discharge. Another set of lookup-tables (determining the amount of transferred water at each time step together with the coordinates of the respective withdrawal / receiving proxels) is also used to simulate the artificial water transfers between proxels that are not naturally connected. For more details on this component it is referred to Mauser and Bach (2009).

3.3. Data requirements (input data)

This section is intended to give only a brief overview of the input datasets that are required to run the model PROMET for the whole Greater Damascus Region. Each of these datasets will be discussed in detail throughout this thesis. However, as can be seen in Figure 3.4, the required datasets can be classified into two main categories:

(1) spatially-distributed input data (raster-based maps) provided in form of GIS digital layers (projected to UTM zone-36 and a 180m spatial resolution) and include the following spatial parameter fields:

- Meteorological input data fields: for this study, as mentioned earlier in this chapter, the meteorological fields of precipitation, air temperature, wind speed, relative humidity and cloudiness are provided on an hourly basis through spatiotemporal interpolation of station data. Incoming short- and longwave radiation are calculated based on the interpolated cloudiness. The collected meteorological data covers a period of 15 years (from 1991 to 2005).
- Topographic (spatial) information: elevation, slope, and exposition maps are derived from a 90m resolution digital elevation model (based on SRTM satellite mission digital elevation data).
- Land use/ land cover (spatial) information: the spatial patterns of the different land use/ land cover categories, which are assumed to be time-invariant during the whole simulation period, are derived from remote sensing data (classification of a LANDSAT ETM+ image using the supervised classification algorithm).
- Soil (spatial) information: soil texture spatial distribution is provided through generalization and aggregation of the soil type classes of the Soil Map of Syria (prepared by USAID at a scale of 1:500,000) and transferring the soil types to texture classes.
- Hydrological routing (spatial) information: spatially distributed hydrological/ routing characteristics (e.g., upstream-area, channel slope, downstream proxel, etc...) are derived by analyzing the DEM using TOPAZ.

(2) associated tabular input data (ASCII input files) provides the attributes of each of the different mapped soil-texture classes and plant types. While some plant specific parameters (e.g., minimum stomatal resistance) are taken from literature, others such as Albedo and Leaf Area Index (LAI) are derived from remote sensing data (a time series of LANDSAT images). Soil physical parameters (saturated hydraulic conductivity, effective porosity, pore size distribution index, and bubbling pressure head) are estimated for each soil texture category using Pedotransfer functions.

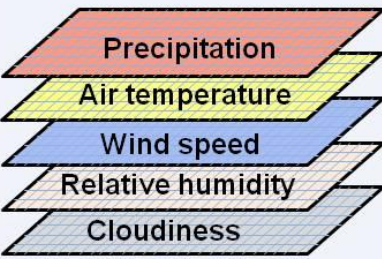
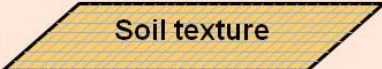
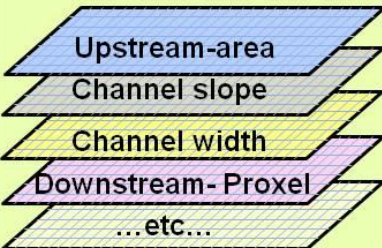
Model Input Data	GIS-INPUT DATA	
	Meteorology	
	Topography	
	Land Use / Land Cover	
	Soil	
		TABLE-INPUT DATA
		For each vegetation type
		Static parameters <ul style="list-style-type: none"> • Min stomatal resistance • Slope of stomatal resistance with irradiance • The threshold value of leaf water potential • Cardinal temperature Dynamic parameters <ul style="list-style-type: none"> • Albedo (daily) [%] • Leaf Area Index (daily) [m²/m²] • Plant height (daily) [m] • Root depth (daily) [m]
		For each soil texture type
		<ul style="list-style-type: none"> • Number of soil layers • Thickness per layer • Bubbling pressure head • Saturated hydraulic conductivity • Effective porosity • Pore size distribution index • Depth of groundwater table
Hydrology / Routing		
		The coordinates of the stream-flow gauge stations Lookup-tables for artificial water transfer etc...

Figure 3.4 gives an overview of the different input data (parameters) that are needed to run the model PROMET for the Greater Damascus Basin.

4. Land use / Land cover classification using Landsat-7-ETM image

4.1. Introduction

Information on land use and land cover is needed in various aspects of land use planning and policy development. It is considered as an essential requirement for monitoring and modelling environmental changes (Latham, 1998; Gregorio and Jansen, 1998). It is particularly required as spatial input data for physically-based distributed hydrological models such as the model used in this study (PROMET). While the present chapter will focus on the derivation of the spatial patterns of the different land use/land cover classes found within the study area, the estimation of plant static and dynamic parameters for each class will be discussed in Chapter 8.

In recent years the term “land cover” has come to be commonly used in association with the term “land use”. The two terms are not synonymous. According to Gregorio and Jansen (1998), land use refers to human activities on and in relation to the land, whereas land cover denotes the vegetation and artificial constructions covering the land surface. Furthermore, while land cover information can be inferred from remote sensing data, information on land use activities cannot always be deduced directly from land cover (additional information sources, such as aerial photographs and detailed topographic maps, are needed). Ideally, land use and land cover information should be presented on separate maps and not intermixed. From a practical point of view, however, it is most efficient to mix the two systems when the remote sensing data form the main data source for such mapping activities (Lindgren, 1985).

The generation of land use/land cover maps from satellite imageries can be considered as one of the most common and useful application of remote sensing (Wulder and Franklin, 2003). In comparison to the traditional mapping methods such as aerial-photo-interpretation and field survey, land use/land cover mapping using satellite imagery has the following advantages:

- Land use/land cover maps can be generated from satellite imageries faster and at considerably less cost than by other methods.
- Satellite images cover large geographic areas (the whole study area can be covered by one single image, as in our case).
- The possibility of inexpensively updating these maps. This is because satellite images are captured for the same geographic area at a high revisit rate. LANDSAT can revisit an area every 16 day (Lillesand and Kiefer, 1994).
- Satellite imagery data are captured in digital forms. They can therefore easily be analysed using computers, and the classified data can be used in geographic information system (GIS).

The derivation of land use/land cover map (in form of a thematic map) from satellite imagery requires a basic understanding of the image processing techniques, sound

knowledge of the spectral characteristics of each land use/land cover class, and a specific classification system (Chuchip, 1997; Mather, 2004).

4.2. Image processing and Classification Methodology

The land use/land cover map of the study area was produced using the following steps:

- Ground truth collection
- Image acquisition
- Image rectification (geometric correction)
- Specify Land use / Land cover classification scheme
- Image enhancement
- Training sites selection and statistics extraction
- Supervised classification
- Classification accuracy assessment

4.2.1. Ground truth collection

Ground truth is generally defined as the measurement, observation and collection of information about the real conditions on the ground in order to clarify the relation between remote sensing data and the object, area, or phenomenon under investigation (Steiner et al., 2007; Barrett and Curtis, 1999). Principally, ground truth should be gathered contemporaneously with the acquisition date of the remote sensing image, or at least within a period of time during which the environmental conditions remain invariant (Gupta, 2003; Buchroithner, 2001; Buiten and Clevers, 1994). However, the previously mentioned land use map (Appendix 1), which was prepared by G.O.R.S using traditional land survey techniques contemporaneously with the acquisition date of the acquired Landsat image (during spring 2000) , represents the principal source of ground truth information for this study. In addition, ancillary datasets including DEM, topographic maps, soil information and the spatial distribution of mean annual precipitation (climatic zones) were also collected and imported into the GIS. Using these different datasets, in combination with the personal knowledge of the study area, is helpful for land use/land cover discrimination, especially in the case of spectral similarity among distinct classes (Campbell, 2002; Navulur, 2006).

4.2.2. Image acquisition

Enhanced Thematic Mapper Plus (ETM+) image acquired on May 21, 2000 (path 174/Row 37) was selected as the basis for land cover analysis and classification. It was downloaded free of cost from the Global Land Cover Facility (GLCF) at the University of Maryland, USA. The study area (5220 km²) is contained well within this clear, cloud-free image. According to Tucker et al., (2004), the ETM+ spectral bands are ideal for studying and monitoring vegetation cover; thus, imageries that are acquired during the growing season are expected to be more useful than those

acquired during periods of senescence. To take advantage of this, Landsat 7 acquisition time should be selected during times when the historical normalized difference vegetation index (NDVI) shows the peak values. Accordingly, the acquisition date of the image used in this study (during the late spring when the vegetation is normally fully leafed out) can be considered as a very suitable for the classification of various types of agriculture.

However, it may be useful to mention here that ETM sensor has the same seven spectral bands as the TM. The ETM's main enhancement over the TM was the addition of an eighth, "panchromatic" band operating in the range from 0.50 to 0.90 μm and spatial resolution of 15m (Lillesand and Kiefer, 1994). The thermal-IR band in ETM+ has an improved ground resolution of 60m (in comparison to the 120m of TM and ETM). Information about the spectral range, ground resolution and the proposed applications of each ETM band is provided in Appendix 2.

Image processing, classification and spatial analysis were conducted using ERDAS IMAGINE-9.1. First the *GeoTIFF* Bands 1, 2, 3, 4, 5, and 7 of the ETM+ imagery were imported into ERDAS and converted into IMAGINE (.img) data files. These bands were then merged (using the "*layer stack*" command) to generate a combined image file contains 6 channels.

4.2.3. Image rectification (Geometric correction or georeferencing)

Geometric correction is concerned with the compensation for the distortions produced by changes in the attitude, altitude, velocity of the sensor platform, relief displacement and other factors in order to create a more faithful representation of the original scene (Lillesand and Kiefer, 1994 Eastman, 2006). However, most elements of systematic geometric restoration associated with image-capture are corrected by the distributors of the imagery (Eastman, 2006). The ETM+ image used in this study was already orthorectified (georeferenced) and registered to the Universal Transverse Mercator (UTM) map projection and the world geodetic system 1984 (WGS 84) datum. Product specifications of this image are provided in Table 4.1.

Table 4.1 Product specifications of the acquired Landsat 7 ETM+ image.

Number of spectral bands	All eight Enhanced Thematic Mapper bands
Cloud cover	Null (Cloud-free)
Image format	GeoTIFF
Resampling interpolation method	Nearest- neighbour (no interpolation)
Pixel size	28.5 m for six reflective bands, 14.25 m for the panchromatic band, and 57 m for the thermal band
Projection	UTM , Zone +36
Datum / Spheroid	WGS 84
Positional accuracy	< 50 meters, root-mean-square error

However, in spite of the fact that the acquired satellite imagery was already-georeferenced by the distributor, verification of the rectification accuracy was

performed in order to ensure that high accuracies were attained. One way to verify that the acquired image has been correctly rectified is to display it together with the reference image (e.g., topographic map) within a single viewer and then visually check that they conform to each other (ERDAS, 2006). The “*Blend*”, “*Swipe*” and “*Flicker*” utilities in the ERDAS IMAGINE viewer provide users with various display methods to exchange between two images displayed on one area of the computer screen as shown in Appendix 3.

Visually, it was found that the geometric rectification of the acquired imagery was not quite satisfactory (RMS greater than 2 pixels). Therefore, additional geometric correction was applied using 1: 50,000 topographical maps to increase the positional accuracy. Normally, the user specifies a certain amount (a threshold) of acceptable total RMS error. For the purpose of change detection, for instance, the average error should be less than half a pixel (Jensen, 1986). However, a low positional error was highly desirable in our case since the acquired image was chosen as the reference image for all other datasets to be registered to.

A total of 33 well distributed *ground control points (GCPs)* were identified on both the Landsat image and the topographic maps. Intersections of roads and rivers, airport runways and prominent buildings were the easiest points to identify. The image was then rectified (georeferenced) using *nearest neighbour* resampling algorithm with RMS (Root Mean Square Error) of less than 0.5 pixel. It may be useful to mention here that there are three main resampling techniques used in rectification: *nearest neighbour*, *bilinear interpolation* and *cubic convolution*. It should be obvious that if a *nearest neighbour* resampling procedure is used then the spectral characteristics of the pixel input to the process are conserved. If one of the other two is used the spectral characteristics are changed by interpolation between contiguous pixels (Thomas et al., 1987).

4.2.4. Specify Land use / Land cover Classification Scheme

One of the most decisive factors in determining the success of derivation of land use/land cover information from satellite images lies in the choice of an appropriate classification scheme (Lo, 1986). However, due to the fact that there is still no universal agreement on the definition and classification of both land use and land cover, a lot of classification schemes (systems) and a large number of map legends exist. Consequently, it can be expected that land use/land cover information (mainly in form of maps and statistics) from different countries, and in many cases even from the same country (e.g., the study area), are incompatible with each other (Gregorio and Jansen, 1998).

A lot of agencies and institutes, such as the Arab Center for the Studies of Arid Zones and Dry Lands (ACSAD), the German Federal Institute for Geosciences and Natural Resources (BGR) and the General Organization of Remote Sensing in Syria (GORS), have produced land use/land cover maps covering the central part of the area under investigation. The classification schemes of these maps were designed to meet

special needs and purposes. Accordingly, each map has its specific legend which differs from the legends of the others. This makes them difficult to combine into a single map.

According to Jensen (1986), the main differences between the different land use/land cover classification schemes lie in their emphasis and ability to integrate satellite-derived information. To be able to interpret the classification outcomes in light of other studies, it is recommended to adopt or modify one of the available nationally acknowledged classification schemes. According to Thomas et al., (1987), land cover classes may simply be aggregated into groups of similar classes: urban, rock, water, agricultural crops, etc. These main divisions may be further subdivided (e.g., the agricultural crop class may be divided into the subclasses of pasture and cereal crops). Finer and finer levels of differentiation may appear with enhanced spectral and spatial resolution of the detection system. According to the purposes of the study and the sufficiency of the available data, the analyst should identify the most appropriate level of class subdivision taking into account the possibility of confusion between sub-classes at the more detailed levels.

However, for the classification of land use/land cover classes of the study area, the U.S.G.S classification scheme was selected and modified taking into consideration the other classifications and inventory efforts established by other agencies that have worked in the Greater Damascus Basin. It should be mentioned here that the original USGS classification scheme consists of four levels of categorization (Lindgren, 1985). It is designed to be driven mainly by the interpretation of remote sensing data (Jensen, 1986). This hierarchical scheme was modified and developed to suit the prevailing conditions in the study area. The resulting scheme (after modification) consists of three levels of classification, as provided in Table 4.2.

Table 4.2 the Land use/ Land cover classification scheme used in this study.

Level (I)	Level (II)	Level (III)
Urban or Built-up Land	Residential areas	
	Industrial, commercial and services areas	
Agricultural Land	Mixed fruit orchards	Orchards (apricot & plum dominated)
		Orchards (olive dominated)
	Mixed farms (forage dominated)	
	Cropland and pasture	Cropland (cereals & legumes)
		Natural pasture
Rangeland / Steppe	Rangeland (mixed grass-shrub areas)	
	Steppe (sparse vegetation)	
Barren Land	Bare exposed rocks	Igneous rocks (Basalt)
		Sedimentary rocks
	Bare soil	
Water	Lakes and streams	

It should be noted that all agriculture subclasses within the level (III) such as olive, apricot, plum, natural pasture, etc, do not represent a unique land use, but they correspond to the dominant agricultural species spread in the region.

4.2.5. Image Enhancement

The aim of image enhancement is to enhance the visual analysis of an image by increasing the discrimination between the objects in the scene (Lillesand and Kiefer, 1994). Image Enhancement is an extremely broad subject, and it often involves a wide range of procedures which make various features of the image clearer. Within these procedures, only the *spectral rationing* and the *colour composites* were used.

- **Spectral rationing**

According to several authors (e.g., Lillesand and Kiefer, 1994; Jensen, 1986; Thomas et al., 1987), the differences in brightness values from identical objects on the earth's surface can sometimes be attributed to topographic conditions (slope and aspect), shadows or seasonal variations in sunlight illumination angle. One of the main benefits of ratio images is that they make it possible to extract and emphasize spectral characteristics of surface materials, regardless of changes in the illumination conditions under which the image was captured. Moreover, ratio images may provide us with matchless information not available in any single band that is helpful for distinction between different land use/land cover classes. For example, multispectral rations of near-infrared to red band can enhance radiance differences between soils and vegetation (Schowengerdt, 2007; Navulur, 2006). Several approaches for describing vegetation cover (in terms of LAI, biomass and vigour) using the characteristics of its spectral reflectance curve have been developed, for instance *vegetation indices* (Mather, 2004). Those indices were primarily developed to account for varying atmospheric conditions and eliminate soil background contribution in estimating vegetation responses (Navulur, 2006). In this study, however, reflectance values from the visible (RED) and near-infrared (NIR) bands of the Landsat ETM+ image were used to compute one of the most successful vegetation indices (the *Normalized Difference Vegetation Index NDVI*) based on the following ratio (Eq. 4.1).

$$NDVI = \frac{NIR - RED}{NIR + RED} \quad (\text{Jensen, 1986}) \quad (\text{Eq. 4.1})$$

NDVI was considered as another channel (band) of information for extracting land use/land cover patterns from the Landsat ETM+ imagery. In addition, it was used to estimate the LAI for each vegetation type recognized within the study area (see Chapter 8).

- **Colour Composites.**

For visual analysis, colour composite images give us the possibility to see the reflectance information from three individual bands in a single imagery at the same time (Eastman, 2006). Figure 4.1 demonstrates some composites made with various band combinations from the same subset of the ETM+ imagery used in this study.

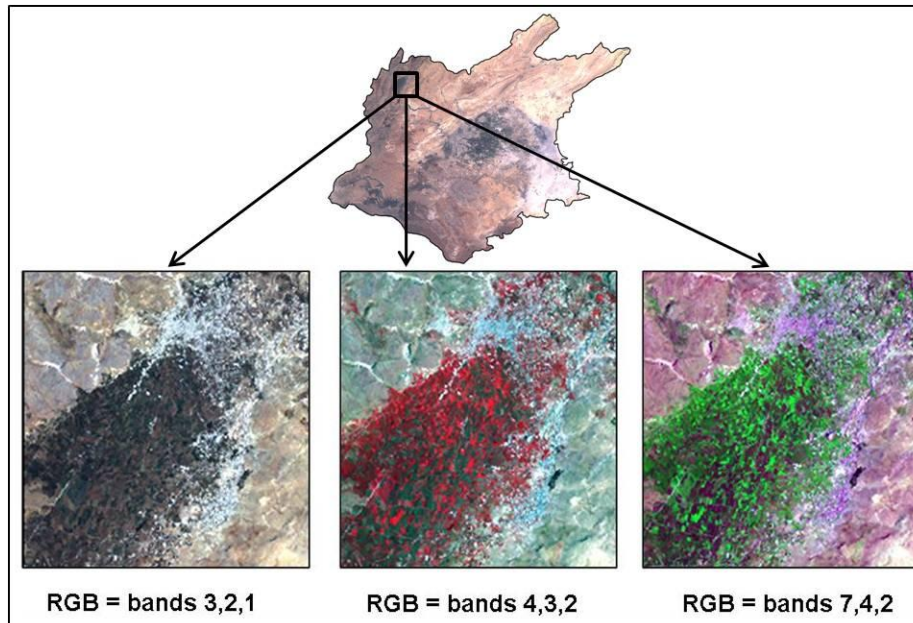


Figure 4.1 shows the colour composites for band combinations 1, 2, 3(left); 2, 3, 4 (middle) and 2, 4, 7 (right) from the same subset of the ETM+ imagery used in this study.

The subset on the left side of the figure 4.1 is a natural colour composite in which blue reflectance information (ETM1) is displayed with blue light in the computer display, green information (ETM2) with green light and red information (ETM3) with red light. The vegetation cover in this subset is shown as dark blue-green since the reflectance values are fairly low in the three visible bands. The residential areas appear bright grey to grey due to their high reflectance in the visible spectral range (Eastman, 2006). On the other hand, a standard false-colour composite (the middle of the figure 4.1) was also created by assigning bands 2, 3, and 4 to the blue, green, and red respectively. Vegetation in this subset is shown as bright red as the near infrared band (4), in which vegetation reflects very brightly, was assigned to the red component of the composite (Hoffman and Markman, 2001). It is also popular to involve other bands that are more particularly targeted to the discrimination of surface materials. For instance, the location of the Landsat ETM band 5 between two water absorption bands makes it useful for estimating soil and leaf moisture differences. Likewise, Landsat ETM band 7 is used primarily for discrimination of mineral and rock types (Drury, 2001).

4.2.6. Training Sites Selection and Statistics Extraction

The selection of training areas, which should adequately represent the spectral characteristics of each class, is very important for supervised classification since the quality of the training set has a severe effect on the validity of the result (Canty, 2006). It is very essential to distinguish between information classes and spectral classes. According to several authors (e.g., Hoffmann et al., 2005; Gao, 2009), information classes are those land use/land cover categories that we are trying to recognize in the image such as urban, crops, pasture, etc. whereas, spectral classes

are those groups of pixels that have similar spectral characteristics (brightness values) in the different spectral channels of the image. The main goal here is to match the spectral classes to the information classes (Borengasser et al., 2007). However, there is hardly ever a pure one-to-one correspondence between these two kinds of classes. For example, forest as information class may comprise a lot of spectral classes. This may be due to differences in age, species and density, or maybe as a consequence of changes in scene illumination (Hoffmann et al., 2005). The general goal of the training procedure is to gather a collection of statistics that determine the spectral response pattern for each land cover/land use type to be classified in the image (Lillesand and Kiefer, 1994). The spectral properties of these identified training areas are then used to “train” the classification algorithm (classifier) for final land use / land cover mapping of the whole image (Karimi and Hammad, 2004).

However, the process of choosing training areas is a simpler and more accurate when the *ERDAS IMAGINE Vector-Module* is implemented (Kappas et al., 2007). This module enables us to directly import vector data files for integration and manipulation within the image to be classified. This permits direct comparison of features (objects) between the imagery and any vector maps (e.g., land use maps prepared by traditional land survey techniques) during the selection of training and validation samples for the purposes of classification and accuracy assessment. Therefore, the land use map prepared by G.O.R.S was registered as image to image to the previously geo-referenced Landsat image to help in choosing the training and validation sites. It was then digitized and converted into vector-based file (vector map) and overlaid on the top of the ETM imagery as shown in the Figure 4.2.

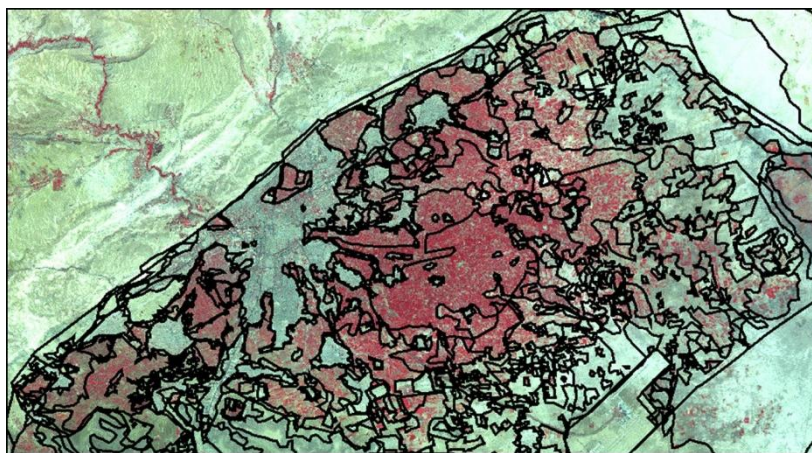


Figure 4.2 shows a comparison between the vector-based land use map (prepared by G.O.R.S) and its corresponding subset of the Landsat ETM+ imagery.

Furthermore, the process of selecting training areas require a thorough knowledge of the geographical area, the spectral characteristics of the features being analysed, the classes desired, and the algorithm to be used (Lillesand and Kiefer, 1994; Eastman, 2006). Ancillary data sets such as DEM, topographic and soil maps, spatial

distribution of annual precipitation, etc. were considered during this process (selection of appropriate training areas) so as to achieve high classification accuracy.

Several authors (e.g., Schowengerdt, 2007) emphasized that the training area should be homogenous sample of the respective class, but simultaneously involves the range of variability for that class. Therefore, more than fifteen training samples were selected for each land use/land cover category in the study area. A total number of 400 samples (half of them were preserved for the purpose of accuracy assessment at a later stage) were selected to represent 12 land use/land cover classes. Each class (set of training samples) was identified by a unique integer number, a meaningful name and a colour. The number of those samples, however, was reduced after statistical analysis. Training samples were treated to locate well within the boundaries of their corresponding (vector) categories. Figure 4.3 shows a subset of the image seen earlier with the addition of several training samples delineated on top of it.

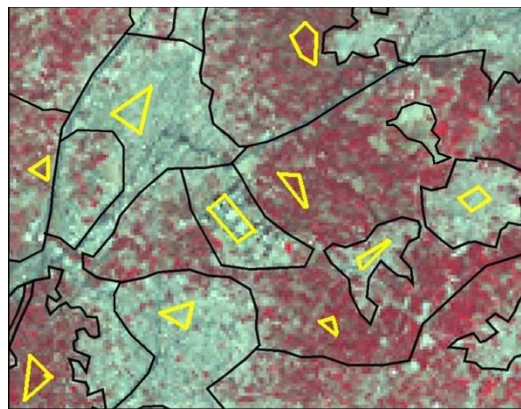


Figure 4.3 training samples polygons (in yellow) delineated on top of both the Landsat ETM+ Imagery and the previously conducted vector land use map.

After all the training areas were defined, the next step was to create and evaluate the signature for each class. This was executed using the *signature editor* included in *ERDAS IMAGINE-9.1*. Multivariate statistical parameters (means, standard deviations, covariance matrices, correlation matrices) were computed for each training area. The *Histogram Plot Control Panel* was used to analyze the histogram and the spectral curve for each training area. According to Jensen (1994), the histograms for training areas must be unimodal and follow a normal distribution. Additionally, in order to avoid overlap between classes (which often leads to misclassification of pixels), the training areas must be as separate and distinctively representative as possible (Gibson and Power, 2000). With the help of *Histogram dialogue* in *ERDAS IMAGINE*, a histogram can be produced with one or more signatures (ERDAS, 2006). Appendix 4 shows six histograms for multiple signatures in each of the six non-thermal bands of the Landsat ETM imagery.

Furthermore, statistical analyses were performed using ellipse diagrams and scatterplots between various spectral bands to graphically show the reciprocal relations of responses in various spectral bands for all of the classes (Gupta, 2003). The mean and the standard deviation of each signature were employed to delineate the ellipses in 2-dimensional feature space image (scatterplot). Appendix 5 shows ellipses for several land use/land cover types in a scatterplot, where the data file values of band-1 have been plotted versus the data file values of band-4.

Finally, a signature separability analysis, which measures the divergence and the statistical distance between signatures, was also computed for each spectral band. The classes that have inadequate statistical separability in all the bands were merged into each other. Accordingly, the adopted classification system was once again modified. Industrial/Commercial areas and residential areas were combined into one class (Urban or built-up land).

4.2.7. Supervised Classification

According to Lillesand and Kiefer (1994), classification is the procedure of grouping pixels into a limited number of distinct classes based on their data attributes. If a pixel fulfils a certain set of criteria, the pixel is categorized into the land use/land cover class that corresponds to those criteria. There are two approaches to classify pixels into different categories, one is the supervised classification and the other is the unsupervised classification. Supervised classification necessitates a prior knowledge about the image data, such as which types of land use exist in the study area together with their spatial distribution or reliable samples for each land use type (Jensen, 1986; ERDAS, 2006). In contrast to supervised classification, unsupervised classification necessitates only a minimum amount of information. By using this kind of classification, pixels are grouped into different spectral classes (clusters) based on some statistically specified criteria. It is then the task of the analyst to assign a class names to those clusters (Nag and Kudrat, 1998; Sahu, 2007). However, the supervised classification was used in this study, since the ground truth data were available and the author has a prior knowledge of the land cover types existing on the ground.

After a satisfactory signature had been achieved for each information class, the imagery was then classified based on those signatures. Each pixel in the imagery has a value in each of the six nonthermal ETM bands plus NDVI. These values create a unique signature which can be compared to each of the previously created signatures. The pixel can then be assigned to the information class that has the most similar signature (Richards and Jia, 2006; Gibson and Power, 2000). However, for assessing how similar signatures are to each other, several statistical techniques (also referred to as classifiers or decision rules) can be applied. The most frequently used classifiers are *Parallelepiped*, *minimum distance*, *Mahalanobis Distance*, and *Maximum Likelihood*. Choosing one of these classifiers relies on the characteristics of

the input data and the desired outcome (Jensen, 1986). However, several authors (e.g., Eastman, 2006; Pouncey et al., 1999) indicated that *Maximum Likelihood* tends to be the most accurate classifier if the training sites are good (if the input samples/ clusters have a normal distribution). Therefore, it was adopted for the classification of land use / land cover over the entire study area. This classifier evaluates the probability that a given pixel will belong to a particular class, and assigns it to the class with the highest probability of membership (De Jong and Van der Meer, 2004). Thus, the acquired ETM imagery was classified (using the *Maximum Likelihood* classifier) into 12 land use / land cover classes. The resulting classified image, as shown in Figure 4.4, is a thematic map in which every pixel in the acquired ETM imagery has been classified into one of those 12 land use / land cover classes.

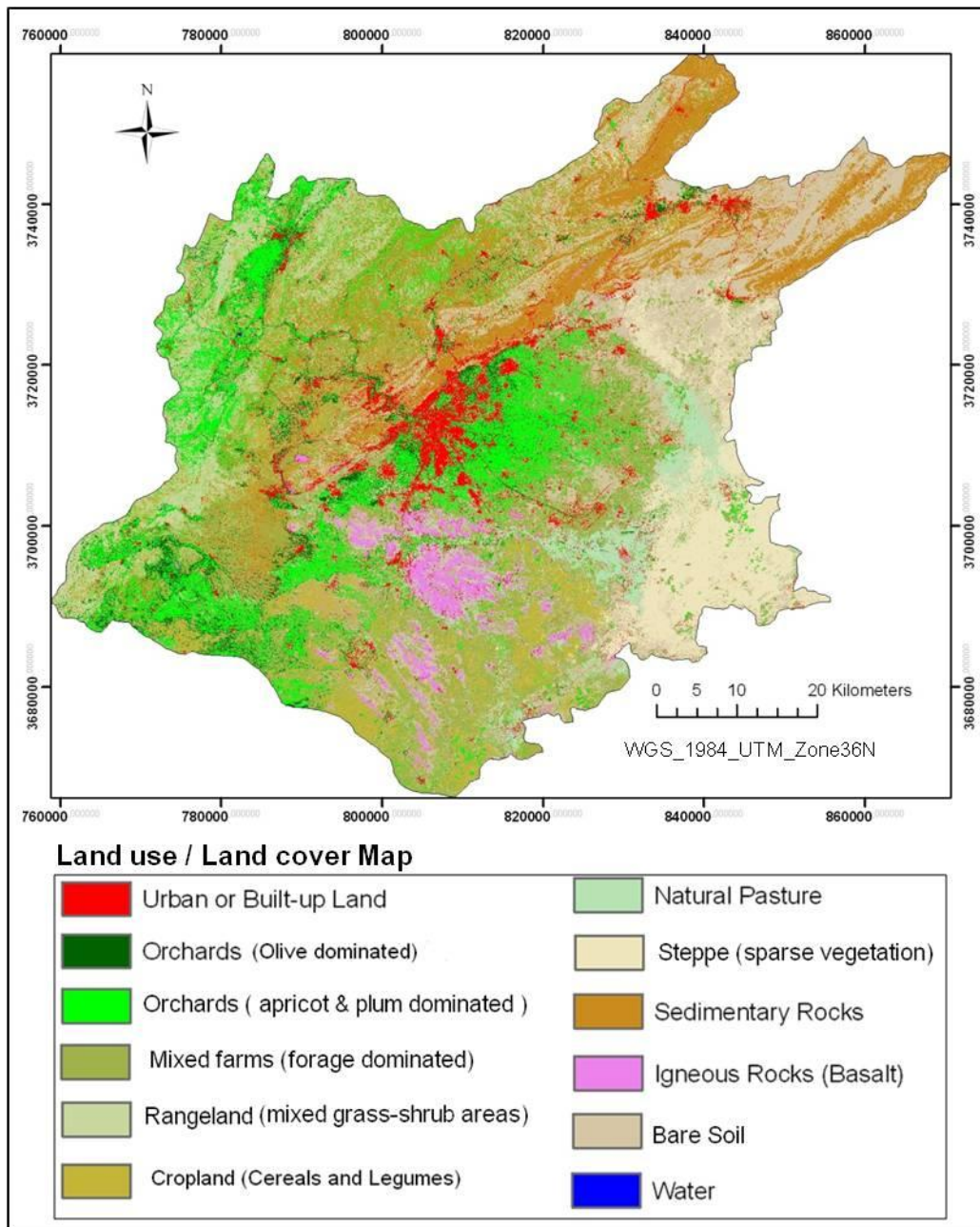


Figure 4.4 shows the Land use / land cover map of the study area as derived from classification of a Landsat 7 ETM+ image acquired on May 21, 2000.

4.2.8. Classification Accuracy Assessment

Accuracy assessment is an essential final step of an image classification. Lillesand and Kiefer (1994) stated that “A classification is not complete until its accuracy is assessed”. However, to properly execute classification accuracy assessment, it is required to compare two source of information: (1) classified information derived from remote sensing imagery (i.e. certain pixels in the thematic raster) and (2) reference information (ground truth data), known as *testing samples* (Jensen, 1986; Varshney and Arora, 2004; Congalton and Green, 1999). According to Gupta (2003), a classification is rarely perfect. Misclassification may occur due to unsatisfactory training or a poor approach of classification. Hence, there is a need for a quantitative assessment of how reliable the classification actually is. According to several authors (e.g., Congalton and Green, 1999; Chen, 2007), accuracy assessment can be quantitative (in terms of overall accuracy, producer’s and user’s accuracy, etc.) or qualitative (according to a visual comparison of the produced map with reference data).

A typical accuracy assessment of a classification starts with the choosing of testing samples in the classified image, and then testing their class assignment from the reference data (Varshney and Arora, 2004). This technique assumes that the reference data (which may be aerial photos, ground truth data, or previously tested maps derived from in situ investigation or from remotely sensed data obtained at higher resolution) are true. Furthermore, reference data should be collected as close as possible to the date of the remotely sensed data, and be kept absolutely independent (separate) from any training data (Congalton and Green, 1999; Jensen, 1986; Tso and Mather, 2001).

However, for the purpose of assessing the classification accuracy of the derived land use /land cover map for the study area, a set of 200 *testing samples* were employed. These samples were gathered from the same “assumed true” land use map which was used for selecting training samples (see Section 4.2.6). It should be mentioned here that these samples were not used in training the *Maximum Likelihood* classifier, but rather preserved and held back for the target of accuracy assessment.

However, due to the fact that the existing ground truth data (test data) cover only the central part of the study area, the quantitative accuracy assessment was applied only over that part (covering only 8 land use/land cover classes). For the rest areas, which were not supported by testing samples, a qualitative evaluation was conducted through a visual comparison of the produced map with other less accurate data sets such as small-scale land use / land cover maps, topographic maps, and agriculture statistics.

After all the testing samples (polygons) were selected, the next step was to convert these polygons from “AOI” format (*Area of Interest*) to vector format (shapefile). Each polygon was then identified by an integer number representing its corresponding information class. The shapefile was then converted to raster format and imported into the ERDAS IMAGINE software which allows the accuracy assessment to be

reported as an *error matrix* (one of the most common methods of reporting the classification accuracy). According to several authors (e.g., Gupta, 2003; Lillesand and Kiefer, 1994), *error matrix* (sometimes referred to as a confusion matrix or a contingency table) typically takes the structure of an $m \times m$ matrix, where m is the number of classes under examination. While the rows in the matrix stand for the “assumed true” classes, the columns are connected with the remote sensing-derived land use / land cover classes.

An Accuracy Assessment *CellArray* was produced to compare the classified image with reference data. A total of 3000 points were randomly selected throughout the reference image. To ensure that these points will be distributed only within the testing samples (polygons), the class *unclassified* was excluded from this process (using the “*select classes*” function). Appendix 6-a shows a section of the resulting *CellArray* which lists the exact geographic locations of the testing points (x, y), the class values for the pixels to be checked (*Class column*), and the class values for the ground truth pixels (*Reference column*). In addition, the function “*show all*” in the Accuracy Assessment dialog was used to display all of the random points in both the classified image and the testing samples image as shown in Appendix 6-b.

After the Accuracy Assessment *CellArray* was achieved, the utility “*Report*” was utilized to report error matrix, accuracy totals, and kappa statistics. Table 4.3 shows the resulting *error matrix* upon which we can determine how well pixels have been grouped into the correct land use/ land cover classes.

Table 4.3 the error matrix (Contingency table) used to assess the accuracy of the resulting Land use / Land cover map.

		Reference Data								Row Total
		U	OO	C	MF	BS	S	NP	OA	
Classified Data	U	331	1	0	1	12	0	0	0	345
	OO	1	174	4	42	0	0	0	9	230
	C	2	2	325	129	3	3	18	7	489
	MF	0	6	32	632	3	12	2	23	710
	BS	9	0	6	10	476	8	4	0	513
	S	0	0	23	7	11	300	10	0	351
	NP	0	0	4	0	1	36	144	2	187
	OA	0	7	1	39	0	0	0	128	175
Column Total		343	190	395	860	506	359	178	169	3000
U: Urban or Built- up land					BS: Bare Soil					
OO: Orchards (Olive dominated)					S: Steppe (sparse vegetation)					
C: Cropland (Cereals & Legumes)					NP: Natural pasture					
MF: Mixed Farms					OA: Orchards (Apricot & plum dominated)					

For an optimal classification, it is anticipated that all the testing samples would be located along the major diagonal of the error matrix (running from upper left to lower

right) pointing out the perfect agreement. The off-diagonal elements denote the differences (disagreements). They are frequently called the errors of omission and commission. According to several authors (e.g., Varshney and Arora, 2004; Congalton and Green, 1999; Mather, 2004), errors of omission occur when pixels that are actually class (*j*) become categorized as members of some other class, whereas errors of commission arise when pixels that are actually members of some other class are classified as members of class (*i*).

Several indices of classification accuracy can be obtained from the error matrix. The *overall accuracy* is obtained by dividing the total number of correctly categorized pixels by the whole number of reference pixels. Accordingly, the overall accuracy of the classified imagery in this study was calculated as:

$$(331 + 174 + 325 + 632 + 476 + 300 + 144 + 128) / 3000 = 2510 / 3000 = \mathbf{83, 67\%}$$

This overall accuracy handles the classes as a whole and does not give particular information about the accuracy of each distinct class. Therefore, in order to estimate the accuracy of each information class individually, the conceptions of *producer's accuracy* and *user's accuracy* can be applied (Tso and Mather, 2001). Producer's accuracies are calculated by dividing the number of correctly categorized pixels in each class (on the major diagonal) by the number of testing pixels used for that class (the column total). While the user's accuracies are obtained by dividing the number of correctly categorized pixels in each class by the whole number of pixels that were categorized in that class (the row total). Accordingly, the producer's and user's accuracy for each checked class were calculated based on the *error matrix* and the results are listed in Table 4.4.

Table 4.4 gives the producer's accuracy, user's accuracy, and overall classification accuracy for the examined land cover classes.

ACCURACY TOTALS					
Class Name	Reference Totals	Classified Totals	Number Correct	Producer's Accuracy	User's Accuracy
Urban or Built-up land	343	345	331	96.50%	95.94%
Orchards (Olive dominated)	190	230	174	91.58%	75.65%
Cropland (Cereals & Legumes)	395	489	325	82.28%	66.46%
Mixed farms	860	710	632	73.49%	89.01%
Bare soil	506	513	476	94.07%	92.79%
Steppe (sparse vegetation)	359	351	300	83.57%	85.47%
Natural pasture	178	187	144	80.90%	77.01%
Orchards (Apricot dominated)	169	175	128	75.74%	73.14%
Totals	3000	3000	2510		
Overall Classification Accuracy =		83.67%			

However, due to the fact that a certain number of pixels might be correctly identified by chance, even in the most uncertain situations, the *Kappa coefficient (k)* was formulated to take this phenomenon into account and thus to decrease the accuracy allocated to the map tested (Lillesand and Kiefer, 1994; Tso and Mather, 2001). The proportion of agreement by chance is the product of the misclassification represented by the off-diagonal entries of the confusion matrix. Thus, *k* employs all the entries of

the confusion matrix and not only the diagonal entries (as is the case with overall accuracy). Kappa is computed as follows (Congalton and Green, 1999):

$$\hat{k} = \frac{P_{correct} - P_{chance}}{1 - P_{chance}} \quad (Eq. 4.2)$$

Where $P_{correct}$ is the proportion of correctly classified elements and P_{chance} is the proportion of elements that could be predicted to be classified correctly by chance.

K usually ranges between 0 and 1. A value of 0 indicates no agreement, while a value of 1 demonstrates ideal agreement between the remotely sensed classification and the reference data (Mather, 2004). Table 4.5 lists the Kappa value for each examined Land use / Land cover class.

Table 4.5 shows Kappa coefficient for each of the 8 examined categories.

Class Name	Kappa
Urban or Built-up land	0.95
Orchards (Olive dominated)	0.74
Cropland (Cereals and Legumes)	0.61
Mixed farms	0.84
Bare soil	0.91
Steppe (sparse vegetation)	0.83
Natural pasture	0.75
Orchards (Apricot dominated)	0.71
Overall Kappa Statistics = 0.80	

4.3. Conclusion

The spatial patterns of the different land use/land cover classes in the Greater Damascus Basin were successfully derived from a Landsat ETM+ imagery using the supervised classification algorithm. In the course of evaluating the signature for each class, it turned out that the adopted classification scheme had to be again modified. It was not possible to distinguish cereals from legumes, and likewise Industrial/Commercial areas from residential areas due to the spectral similarity between these classes. Therefore, these spectrally similar classes were merged into each other. The resulting classification was quantitatively assessed using an “assumed true” land use map covering the central part of the study area. An overall accuracy of 83.67% with Kappa coefficient of 0.80 was achieved. In addition, the comparison of the whole classified image with other less accurate data set (such as small-scale land use/ land cover maps, topographic maps, and agriculture statistics) has also yielded relatively good results.

It was also found that some land use /land cover classes showed better results than others. While the highest producer’s and user’s accuracy was achieved in classification of “Urban or Built-up areas” (95.9%), the lowest value was found in

classification of “Cropland” (66.46%). The inability to differentiate between some classes is because of the spectral similarity among those classes.

The final resulting land use / land cover map of the study area consists of 12 classes (ranging from level-I to level-III). The agriculture classes within the level (III), however, do not represent a unique species, but rather they correspond to the prevailing species distributed in the study area. Due to the fact that the classification scheme is hierarchical in structure, the resulting 12 classes could be aggregated into 9 categories (level-II) or even 5 categories (level-I). According to first level (Level-I) classification results (as shown in Appendix 7), there are five classes with the following percentages: “Urban or Built-up” 4.9%, “Agricultural” 46.8%, “Rangeland / Steppe” 14.8, “Barren land” 33.6, and “Water” 0.003%.

The level-I Agricultural-Land category could be subdivided into three level-II classes with the following percentages: “Mixed fruit orchards” 16%, “Mixed Farms” 19.4, and “Cropland and Pasture” 11.4%. Likewise, the level-I “Rangeland / Steppe” and “Barren Land” could be further broken down into finer level-II classes. Classes of level-II and their percentages are shown in Appendix 8.

Furthermore, an even finer level of discrimination was recognized within the level-(II) agricultural classes. The class “Mixed fruit orchards” was subdivided into two subclasses, namely, “Apricot and Plum dominated” and “Olive dominated”. Classes of level-III and their percentages are shown in Figure 4.5.

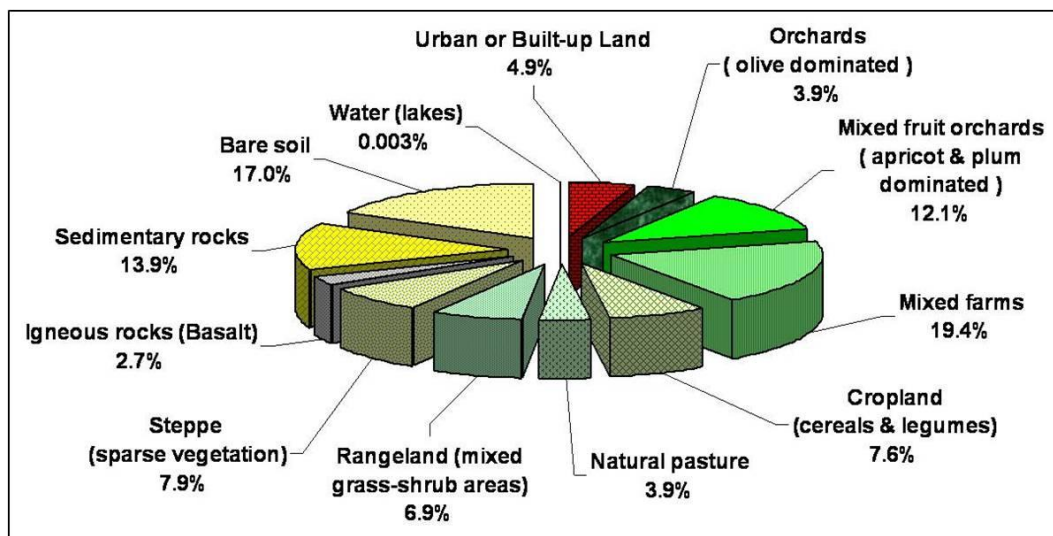


Figure 4.5 shows the estimated proportion for each land use/ land cover class at level-(III) of the adopted classification scheme.

Finally, it is anticipated that reducing the number of classes by aggregating the 12 level-(III) classes into 9 level-(II) classes, or even into 5 level-(I) classes, would lead to higher level of accuracy.

5. Extraction of drainage network and watershed data from DEMs

5.1. Introduction

According to several authors (e.g., Garbrecht and Martz, 2000; Beven, 1989), topography has an important influence on the distribution and flux of water and energy within the natural landscape. It is essential to the description, quantification and interpretation of many land surface processes. In particular, it is important for determining the runoff generation and flow accumulation in a watershed. In addition, topography is one of the most important input requirements for many hydrologic, hydraulic, ecologic and natural resource models, mostly referred to as environmental models (DeBarry and Quimpo, 1999).

Several authors (e.g., Garbrecht and Martz, 1999; Wilson and Gallant, 2000) have stated that the process of extracting topographic information by traditional, manual techniques can be a cumbersome, time consuming, and error-prone task. However, with the advent of computerized mapping and analysis techniques, approaches of digitally representing the landscape surface have been developed. The automated extraction of topographic parameters from Digital Elevation Models (DEMs) is acknowledged as a feasible substitute for traditional surveys and manual analysis of topographic maps, especially as the quality and coverage of DEM data increase (Maidment and Djokic, 2000). Moreover, compared to the traditional manual techniques, the automated extraction of topographic parameters from DEMs is faster, less subjective and provides reproducible digital information that can be easily imported and analyzed by geographic information system (Garbrecht and Martz, 2000).

According to Moore et al. (1991), terrain parameters (attributes) can be classified based on their complexity into primary and secondary (or compound) parameters. Primary parameters are directly computed from a DEM such as slope, aspect and upslope-contributing area. Secondary parameters (generally referred to as indices) include combinations of the primary parameters (functions of two or more primary parameters). These indices are usually used to describe or characterize the spatial variability of certain processes taking place in the landscape, such as surface water saturation (wetness index) and potential for sheet erosion. In this chapter, however, I will focus on the primary attributes of the terrain that influence the matter and energy fluxes of the land surface.

This chapter has two main objectives. The first is to automatically delineate watershed boundaries and stream network from DEMs. The second is to compare the performance of two software packages (TOPAZ, Ver. 1.10 and ArcGIS 9.1) that will be used to achieve the first objective.

5.2. Data Acquisition and Preprocessing

5.2.1. Criteria for choosing suitable DEM data

The two significant criteria in the choice of a DEM for hydrologic modelling are the quality (accuracy) and resolution (both horizontal and vertical) of the DEM data

(DeBarry and Quimpo, 1999). Both quality and resolution must be consistent with the scale of the physical processes that are modelled, the extent of the landscape features that are to be characterized, the kind of used hydrologic model, and the study objectives (Maidment and Djokic, 2000). In practice, however, the choice of DEM resolution for a specific application is often driven by data coverage and availability (Garbrecht and Martz, 2000).

According to Jenson and Domingue (1988), the accuracy and detail of watershed boundaries and drainage networks derived from DEMs relies on the resolution and quality of the DEMs. Hence, the analyst should make sure that the relevant and important topographic features are adequately resolved by the chosen DEM. It has been suggested that a 1-m vertical DEM resolution may be adequate to derive the slope values, and consequently, the flow direction and drainage network in mountainous terrain, but for low-relief landscapes and flat areas, which are determined by adjacent cells with the same elevation, this vertical resolution (1m) may be insufficient (Maidment and Djokic, 2000). This problem, however, can be overcome by "*burning in*" the streams using known stream locations (digitized pathways layers). This procedure adjusts the DEM raster elevation so that the flow of water is forced into the identified stream locations. This is performed by artificially lowering the elevation of the DEM cells along the previously digitized flow lines or increasing the whole DEM excluding along these lines. This approach, however, must be applied with caution since it may generate flow channels that are not consistent with the topography surrounding the flat surface (Wilson and Gallant, 2000).

DEMs are commonly saved in one of three data structures (formats): rasters (grids), Triangulated Irregular Network (TIN), and contour-based formats. Due to the fact that PROMET is a raster (grid)-based model, a decision was made to look for DEM data provided in raster format, and at the same time have adequate vertical and horizontal resolutions.

5.2.2. Selecting an appropriate software package

Two software packages (ESRI's ArcGIS 9.1 with spatial analyst extension, and TOPAZ ver.1.10) were used to automatically delineate watershed boundaries and drainage network from DEMs. The outcomes from those software packages were compared with each other and with the manually digitized data to evaluate the accuracy with which each program performs the calculation. It should be mentioned here that TOPAZ does not contain raster display facilities. Therefore, the raster outcomes of TOPAZ were imported into ArcGIS for the purposes of display, manipulation and interpretation.

5.2.3. Downloading, mosaicking and reprojecting SRTM- DEM data

The first step in the process of automated extraction of drainage network and watershed data was to obtain DEM data covering the whole catchment. In this study, the Shuttle Radar Topography Mission (SRTM) (approx. 90m resolution) DEM data

were used. These data are assumed to be the most accurate digital elevation model available for this study. Two SRTM tiles (files) covering the study area (*N33E035.hgt* and *N33E036.hgt*) were chosen (according to their names) and downloaded free of charge from the USGS ftp site. They were then converted from “*hgt*” format (BIL data without a file header) to *ArcInfo* raster format. Each tile covers an area of 1*1degrees, with 1201*1201 pixels. The two files were then mosaicked into a single raster file and reprojected to UTM (zone 36) projection system. Figure 5.1 shows the SRTM data used for this study.

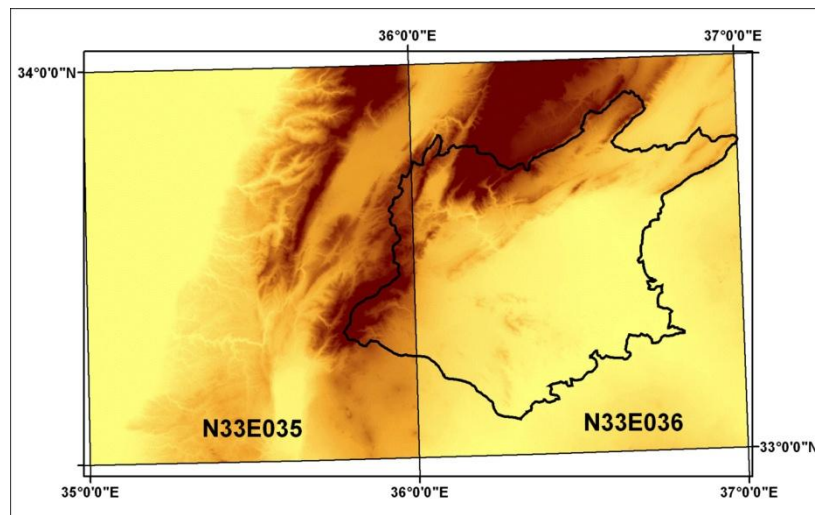


Figure 5.1 shows the SRTM data used for automatically delineating watershed boundaries and drainage network in the study area.

For working with TOPAZ software, however, DEMs data have to be converted into ASCII-format (without header information) to make them readable and compatible with its (TOPAZ) requirements. In addition, some important user-specified parameters have to be identified before starting DEM analysis. These parameters include, among others, number of rows and columns, maximum and minimum elevation values, and the grid size (resolution).

5.2.4. Choosing an appropriate spatial resolution (level of aggregation)

As mentioned previously in this chapter, the derivation of drainage network and watershed data is highly affected by the resolution (vertical increment and horizontal spacing) of the DEM used. DEM vertical resolution (elevation increment) was already discussed in Section 5.2.1. On the other hand, the choice of an appropriate DEM horizontal resolution for distributed hydrological modelling necessitates taking into account not only the characteristics of the landscape and the scale of the physical processes, but also the needed memory and computational resources (Shamsi, 2005; Vieux, 2004; Maidment and Djokic, 2000). For instance, physically-based distributed hydrologic models that rely on high-resolution DEMs may necessitate large computational and memory resources that may not be currently attainable. This may

be a limiting factor for using DEMs with high-resolution and promotes the choice of lower resolution. In view of that, a decision was made to aggregate the relatively high-resolution DEM (small cell size) to low resolution DEM (large cell size).

As mentioned earlier in this chapter, the acquired DEM has an original horizontal grid spacing of 90m and a vertical resolution of 1m. This DEM was aggregated to create additional DEMs of 180, 500, and 1000m for the whole study area. The loss of information due to aggregation (increasing the grid cell size) was examined by considering variations in the spatial distribution of the watershed boundary and drainage network produced at each DEM resolution (see Section 5.5). As a result of this examination, the grid cell size of 180m (two times less linear resolution of the 90m-SRTM data and six times less linear resolution of the 30m-Landsat data) was assumed to be appropriate resolution to extract the topographic parameters, and at the same time to simulate the hydrological processes within the study area.

5.3. DEM Processing

5.3.1. Creating a depressionless DEM

According to several authors (e.g., Garbrecht and Martz, 1999), DEMs usually include localized depressions (pixels which do not have neighbors at lower elevation) and flat areas (characterized by neighbouring pixels with the same altitude). It is common practice to rectify these depressions and flat areas prior to drainage identification, since these features form an obstacle to the application of the flow routing concept (the backbone of many DEM processing models). Several approaches have been developed for dealing with depressions (sinks) and flat areas in DEMs for automated extraction of drainage network and other topographic parameters. Some approaches presume that depressions are consequences of only underestimation of elevation values of individual or groups of DEM pixels (Jenson and Domingue ,1988), whereas other approaches presume that depressions can be the result of both under and overestimation of elevation (Martz and Garbrecht, 1999). Both software packages used in this study (ArcGIS and TOPAZ) incorporate the last mentioned approach. They rectify the depressions using the breaching/ filling concept. However, TOPAZ has an advantage over the ArcGIS because it rectifies the flat surfaces by using an additional relief imposition approach (landscape configuration gradients) which takes into account the increasing and decreasing topography around the flat surfaces to ensure explicit downslope drainage at every location in the DEM (Martz and Garbrecht, 1999).

5.3.2. Determining flow direction

Flow direction is very important in hydrologic modeling, since it determines in which direction water will flow out (drain) of the pixel. The single flow path algorithm (referred to as D8 method or eight-direction pour point model) calculates flow direction depending on the direction of steepest downslope path from each raster pixel to one of its 8 adjacent pixels (Jenson and Domingue, 1988; O'Callaghan and

Mark, 1984). The resulting flow direction raster can be encoded in different ways depending on which software may be used. Appendix 9 shows a comparison between two different flow-direction encoding schemes that have been adopted by the software packages used in this study (ArcGIS and TOPAZ). A raster of flow direction was created by each of these two programs. The differences between the resulting rasters lie not only in the encoding scheme but also in the method these two programs adopt in dealing with flat surfaces. ArcGIS 9.1 expands the search width in flat areas until a direction of steepest descent is found (Maidment, 2002). Large extents of flat surfaces, however, may generate unnatural drainage networks (parallel flow paths), as will be shown in Section 5.5. On the other hand, TOPAZ, as indicated above, defines the flow direction in flat surfaces by imposing two independent gradients: one away from higher terrain into the flat surface, and the other out of the flat surface towards lower terrain. According to Garbrecht and Martz (1997), the linear association between these two gradients is adequate to produce realistic and topographically consistent drainage patterns over flat areas. Figure 5.2 shows the flow direction raster of the study area which was produced using TOPAZ (based on D8 method).

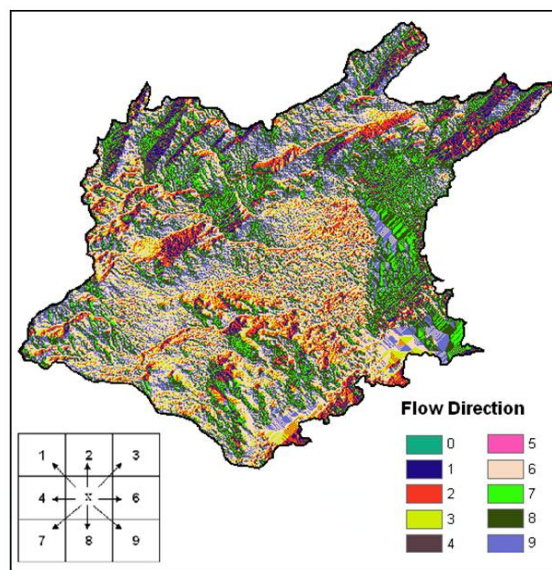


Figure 5.2 flow direction raster of the study area generated by TOPAZ, (based on D8-method).

5.3.3. Generating flow accumulation raster

After the terrain-sinks have been filled and the flow directions have been determined, the flow accumulation for every cell of the DEM raster has been calculated. The output raster represents the catchment area of each cell in the used DEM measured in number of upstream cells. In other words, each cell in the resulting flow-accumulation raster is assigned a value equal to the number of cells that flow to it (O’Callaghan and Mark, 1984; Jenson and Domingue, 1988). Accordingly, cells at the drainage divide which have no upstream drainage area (to which no other cells flow),

are assigned a value of 0, whereas high values in the accumulation raster represent areas of concentrated flow. These high values are commonly used to extract the drainage network, as will be discussed in the next section. Figure 5.3 shows the flow accumulation raster of the study area which was produced using the software package TOPAZ.

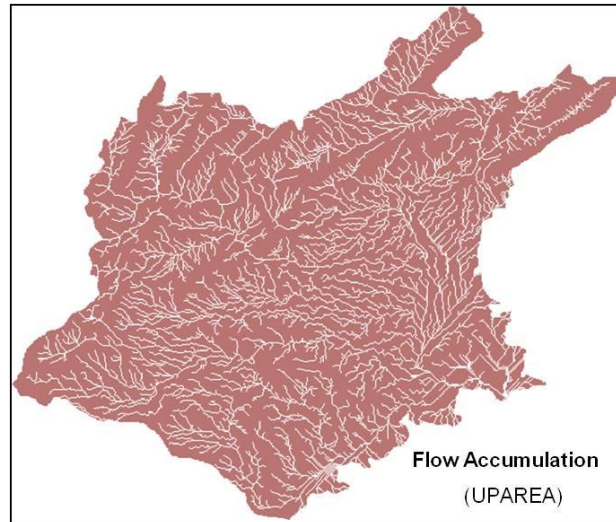


Figure 5.3 flow accumulation raster of the study area (produced by TOPAZ).

5.3.4. Extracting drainage network

As mentioned above, the resulting flow accumulation layer can be used to produce a drainage (stream) network by applying threshold values to choose pixels with high accumulated flow values. This can be easily done in ArcGIS using a map query or by changing the classification of the legend of the flow accumulation raster (Maidment, 2002). Thus, all cells whose flow accumulation is larger than the chosen threshold value can be classified as stream (flow path) cells, while the residual cells are regarded as the areas draining to those streams.

On the other hand, TOPAZ requires two important user-specified network parameters to be identified before starting DEM analysis: the Critical Source Area (CSA), and the Minimum Source Channel Length (MSCL). The CSA value identifies a minimum drainage area above which a permanent channel is maintained (Martz and Garbrecht, 1992). It relies on, among other things, surface slope, land use, soil type and climatic conditions (Lyon, 2003). The MSCL allows to clip channel links that are shorter than the selected MSCL value (Armstrong and Martz, 2003; Shaw et al., 2005). However, the selection of an appropriate CSA and MSCL values requires some thought and consideration due to the fact that the degree of watershed segmentation and the drainage network density are functions of the values assigned to these two parameters. If a small CSA value is chosen a high degree of segmentation, many subwatersheds, and a dense drainage network are obtained. Whereas, only the main streams (channels) and few subwatersheds can be obtained if a large CSA is selected. Normally, the analyst starts with an estimated value (low value) and adjusts (increase) the initial value by comparing the extracted drainage network with existing

topographic maps or digitized blue line network (Shamsi, 2005; Lyon, 2003). Figure 5.4 shows the resulting drainage network of the study area which was derived from the upslope contributing area (flow accumulation raster), and converted to a vector-based format (polyline) for further analysis and comparison.

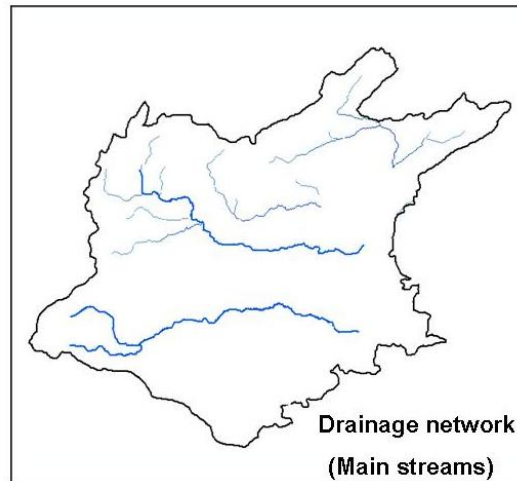


Figure 5.4 the resulting drainage network of the study area (converted into vector-based format).

The drainage network extracted from DEM was compared with the manually digitized blue line stream. Based on the results of this comparison, it can be said that the automated extraction of drainage network from DEM gives good results in the mountainous areas of the study basin, but it fails to derive the stream network over the plain of Damascus, where each of the two main rivers divides into several separate branches and artificial canals. Only the main channel of each river (over the Damascus plain) was successfully extracted from the DEM.

5.3.5. Determination of watershed pour points (outlets)

According to several authors (e.g., Kennedy, 2006; Huggett and Cheesman, 2002), watershed pour points (also referred to as outlets) are usually cells of high-accumulated flow at the border of the raster or, just downstream of main confluences. Each of these points has the lowest elevation value within its correspondent (sub-) watershed at which water flows out of the area. In this study, the geographical locations of the stream-flow gauges were used as pour points (outlets). Based on these points, the entire watershed can be subdivided into several smaller subwatersheds, as will be discussed in the next section. However, it should be mentioned that pour points should be located directly over raster cells from the drainage network. This task can be achieved in different ways, depending on which software package may be used. TOPAZ, for example, displays a section of the watershed-area values (measured in number of upstream cells) around the initial outlet point to the monitor as shown in the Figure 5.5.

	494	495	496	497	498	499	500	501	502	503
394	0	0	0	0	0	0	0	0	0	0
395	0	0	0	0	0	0	0	0	0	0
396	610	0	0	0	0	0	0	0	0	0
397	0	612	0	0	0	0	0	0	0	0
398	162964	0	615	0	0	0	0	0	0	0
399	0	163022	0	618	0	0	0	0	0	0
400	0	0	163418	0	620	621	624	0	0	0
401	0	0	0	163435	163436	163450	163451	164077	164078	164244
402	0	0	0	0	0	0	0	0	0	0
403	0	0	0	0	0	0	0	0	0	0
404	0	0	0	0	0	0	0	0	0	0
405	0	0	0	0	0	0	0	0	0	0
406	0	0	0	0	0	0	0	0	0	0
407	0	0	0	0	0	0	0	0	0	0
408	0	0	0	0	0	0	0	0	0	0

THE DRAINAGE AREA OUTLET IS DEFINED BY ROW 401 AND COLUMN 499.
 ENTER 0 IF YOU WANT TO CHANGE THESE VALUES;
 ENTER 1 IF YOU WANT TO PROCEED WITH THESE VALUES:

Figure 5.5 Section of the study watershed-area in the vicinity of a user-specified watershed outlet.

On this display, large upslope contributing area values define the channels of the drainage network, whereas values of 0 identify overland (non-channel) areas (Garbrecht and Martz, 1999). Thus, the information on this display helps us in the final choosing of the watershed outlet position (identifying its row-column coordinates).

ESRI's ArcGIS, on the other hand, provides us with the ability to define pour points either by adding pre-chosen points such as the locations of gauging stations, or interactively by adding and editing a new point shapefile (ESRI, 2005). In the first case, tabular data that contains the geographic locations of the streamflow gauges (in form of x, y coordinates) can be added to the previously calculated flow accumulation raster. Each pour point must assign a unique integer ID value, since the sub-watersheds resulting in the next step will have the same values as the cells of pour points.

The next step in determining the watershed pour points was to snap these points to the locations of higher accumulated flow (snapping distance was set to 50 m). This process was achieved using the "Snap Pour Point" tool in ArcGIS 9.1 which also transforms the point-shapefile of the pour points into a raster file. Figure 5.6 shows the locations of the streamflow gauges which act as pour points to delineate the watershed-area of each gauge existing within the study area.

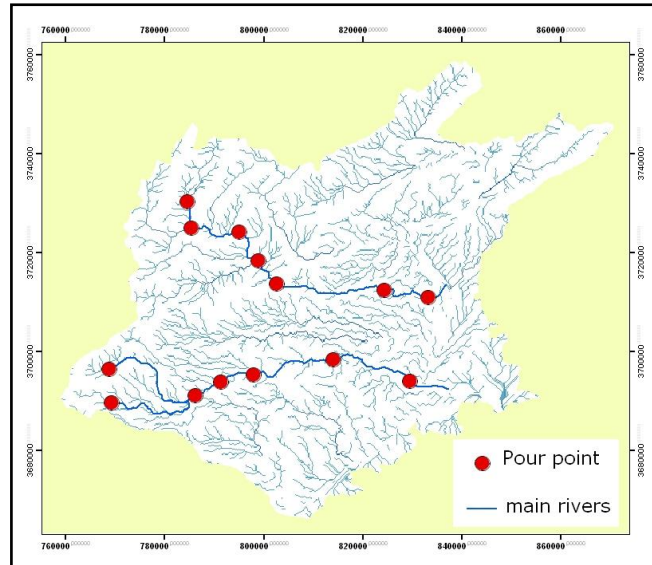


Figure 5.6 the locations of the pour points (streamflow gauges) which were used to subdivide the whole watershed into several smaller subwatersheds.

5.3.6. Delineating watersheds

A watershed (also referred to as river basin or catchment area) is normally described as the entire area that drains water and other substances to a specific pour point (Maidment, 2002; ESRI, 2005). After the pour points were snapped to cells with high flow accumulation values, the subwatersheds were delineated for each pour point. Figure 5.7 shows the study area (the entire watershed) subdivided into several smaller subwatersheds. Each sub-watershed was assigned the same identification number as its corresponding outlet. Watershed subdivision makes it possible to compare measured and simulated discharges at the selected streamflow gauges.

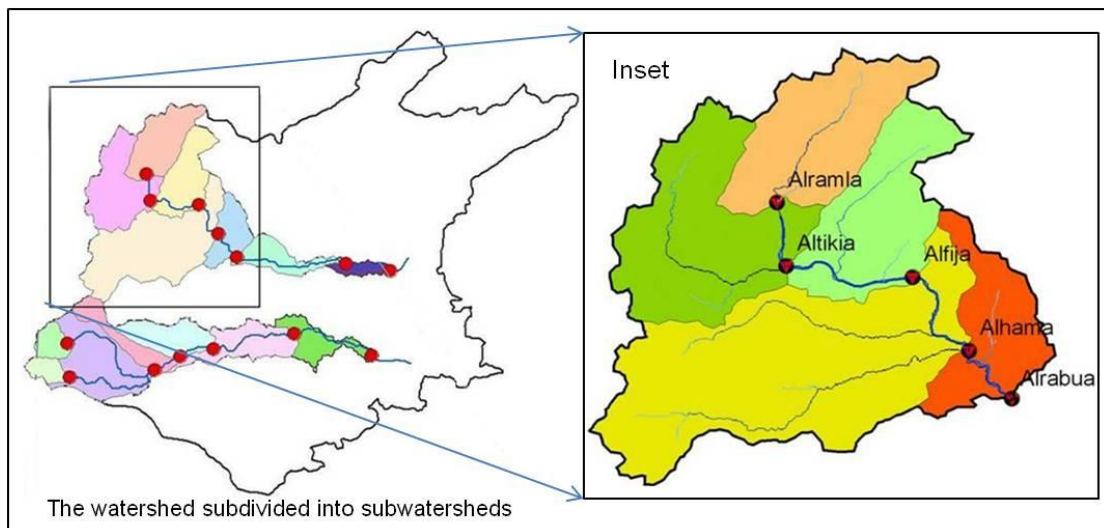


Figure 5.7 the study area (the whole watershed) subdivided into subwatersheds. The inset (on the right) shows in more detail the delineated subwatersheds using some streamflow gauges located along Barada River.

Finally, for further analysis and comparison, the resulting subwatersheds and drainage channels were then vectorized (converted) to polygon and polyline features respectively.

5.4. DEM visualization

With the development of computer graphics technology, 3D visualization has become one of the most popular techniques used for DEM visualization. This technique is considered as a good approach to get more understanding of the shape of the land surface by providing a degree of realism inaccessible from 2D image structure. It gives us the ability to view the land surface from any angle, elevation or distance (Kraak and Ormeling, 2003). In addition, 3D DEM can also be used as a base map for draping other images such as satellite images (as shown in Appendix 10), aerial photographs, land use, and other vector-based data (e.g., rivers, roads, etc.). Draping the resulting drainage network over the 3D terrain model allows us to see the close relationship between its spatial configuration (distribution) and the general shape of its surrounding landscape. Likewise, draping the resulting land use/ land cover map over the 3D terrain model, as shown in Appendix 11, can create perspective views reflecting the relationship between the land use/land cover patterns and the landscape they occupy. It should be mentioned here, however, that the overlaid image and the DEM must be perfectly registered to each other so that the same position in each image has the same map coordinates. In addition, for the sake of visualization the hillshade raster was also created from the DEM by calculating the brightness and shadows (illumination) for each cell in the raster from a hypothetical light source. Hillshade, aspect, slope, and curvature rasters calculated for a mountainous subwatershed within the study area are depicted in Appendix 12.

5.5. Discussion of results

Generally speaking, it can be said that the drainage network and the watershed data of the study area were successfully extracted from DEM (SRTM) using two software packages (ArcGIS 9.1 and TOPAZ, ver.1.10). To investigate the influence of decreasing the horizontal resolution of DEM on the delineation of the watershed boundary and drainage network, the same automated delineation process was applied to the original (90m resolution) and aggregated DEMs (180, 500, and 1000m resolution). Watersheds and drainage networks derived from these DEMs (with various resolutions) were then compared with the blue line streams (drainage paths) which were manually digitized from 1:50000 topographic maps and assumed to be the most accurate data (reference data). Appendix 13 shows a comparison between the manually digitized and automatically delineated drainage network (within a selected subwatershed of the study area) at different DEM resolutions. As can be seen from this figure (Appendix 13), variations in the extent of the DEM-derived drainage networks for grid size up to 180m tend to be relatively small compared with the manually-delineated blue line stream. A similar result was also obtained by

comparing the watershed boundaries delineated at different DEM resolutions as shown in Appendix 14. However, based on these comparison results, and taking into account the required memory and computational resources, the grid cell size of 180m was assumed to be appropriate resolution to extract the drainage network and watershed parameters, as well as to simulate the various land surface processes in the study area using the model PROMET.

On the other hand, comparing the outcomes of the two used software packages with each other and with the manually digitized data reveals that TOPAZ performs better than ArcGIS in creating a realistic drainage pattern over the flat surfaces as shown in Figure 5.8. Excluding the differences appeared over those flat surfaces, there is no difference between the outcomes of these software packages.

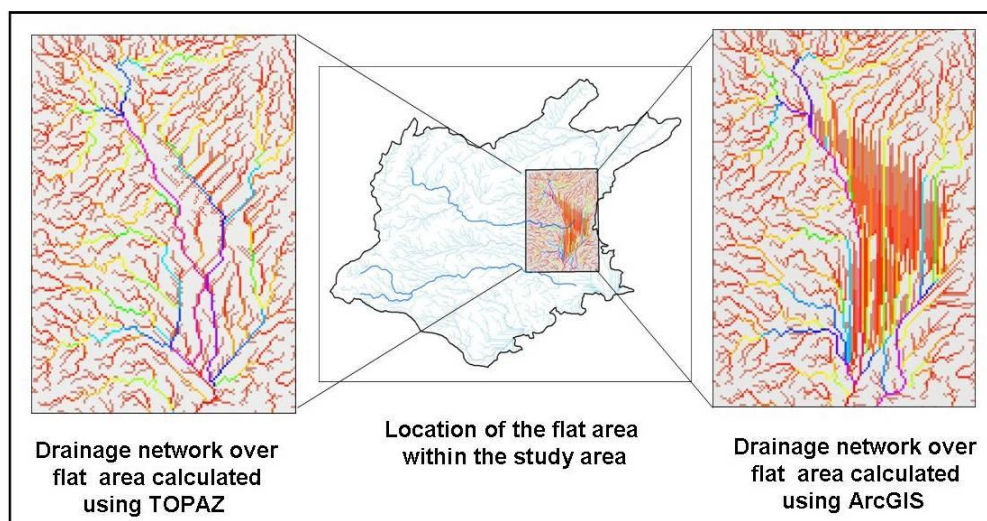


Figure 5.8 shows a comparison between the performance of TOPAZ and ArcGIS in delineating the drainage network over flat areas.

Finally, although the main objective of this chapter was to extract the spatially distributed topographic parameters that are required to run the model PROMET, the results of this chapter (including, among others, raster maps of depressionless DEM, slope, flow direction, flow accumulation, drainage network and watershed boundary) have a wide range of applications in many other (geo-) environmental studies. For example, they form important input to the development of soil erosion models and landslide prediction (Zhou and Liu, 2002).

6. Preparation and analysis of the meteorological input data fields

6.1. Introduction

The meteorological data are usually considered the most important input data for modelling hydrological processes within a catchment area. They are required to drive the evapotranspiration process and to determine the water and the energy budgets at the land surface. For example, a proper calculation of transpiration, interception, evaporation, soil water storage, snow storage, snowmelt, and radiation balance depends for the most part upon a correct determination of the meteorological input data fields (Singh and Frevert, 2002).

As mentioned previously in Chapter 3, the model PROMET requires the main driving meteorological variables, including precipitation, air temperature, relative humidity, wind speed and the radiation balance, which is derived from the interpolated cloud cover observations. However, due to the fact that each of these parameters has its own characteristics and its own level of availability, it was necessary to apply a variety of procedures to generate spatial fields of each one. For example, air temperature, relative humidity and wind speed show relatively small fluctuations in both spatially and temporally scales, therefore, they were treated as continuum variables. Precipitation, on the other hand, can be highly variable over space and time, so it was handled as discrete variable. The meteorological component of the model PROMET was used for interpolating the driving meteorological fields from measurements of the available weather stations (located within and around the study area) in order to provide the required meteorological input data with a temporal resolution of one hour. In this chapter, I will give an overview of the process of collection and preparation of the meteorological measurements, and how they will be organized in the so-called "*Met-File*". In addition, the spatiotemporal variability of each required meteorological parameter will also be discussed.

6.2. Weather observation network

Collection and preparation of meteorological data in arid and semi-arid regions is usually considered one of the greatest challenges facing the modelling of hydrological processes. The task becomes more difficult, as in our case, when developing decades of hourly distributed meteorological data is required. Therefore, a considerable effort has been made by the author in order to obtain the required input data that are limited to the governmental institutions and are not published for the public.

The meteorological observation network in the study region is administrated by three ministries: the Ministry of Defence (the General Directorate of Meteorology), the Ministry of Irrigation (Directorate of Water Resources Management) and the Ministry of Agriculture and Agrarian Reform. Each ministry has installed its own observation network in order to meet its own policy objectives. As a matter of fact, this distribution of the meteorological data in different institutions has hampered the process of data collection. However, to ensure a high level of quality, continuity and consistency,

meteorological measurements from all available synoptic, climatic and rain-gauge stations were used for the generation of the meteorological fields required for the simulation of land surface processes with PROMET. In total, data from 66 stations distributed in and around the study catchment were collected. The data cover the period from 1991 to 2005 (15 years). Five of these stations (the synoptic stations) have the ability to provide hourly measurements of the most meteorological variables (except rainfall every 24 hour). Whereas, two of these stations (climate stations) provide weather observations three times a day (but daily rainfall). The remainder of the stations (59 rain-gauge stations) record only daily precipitation. It should be mentioned here that the precipitation measurements that were taken from these rain-gauge stations suffer from intermittency. The locations of the available synoptic, climatic and rain-gauge stations within the study area are illustrated in figure 6.1. While the names of the synoptic and climate stations (along with their elevations and geographical locations) are presented in Table 6.1, the names, geographical locations and elevations of all rain-gauge stations used in this study are found in Appendix 15.

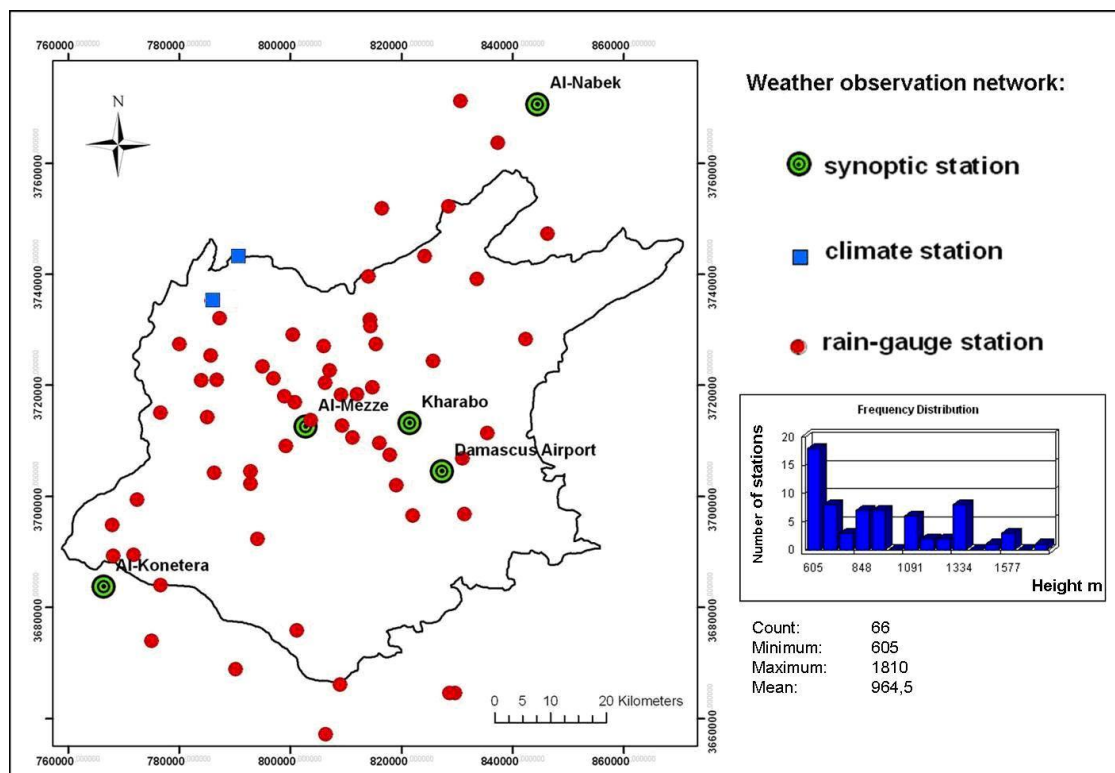


Figure 6.1 the spatial distribution of the available synoptic, climatic and rain-gauge stations within the study area.

Table 6.1 lists the names, geographical locations and elevations of the synoptic and climatic stations used in this study.

Station name	Type	Longitude	Latitude	Elevation (m)
Al-Mezze	Synoptic	36.26	33.51	750
Damascus Airport	Synoptic	36.52	33.43	610
Kharabo	Synoptic	36.46	33.51	620
Al-Konetera	Synoptic	35.86	33.26	941
Al-Nabek	Synoptic	36.73	34.02	1329
Sorghaya	Climate	36.14	33.79	1409
Al-Zabadani	Climate	36.09	33.72	1145

With regard to the spatial distribution of the weather observation network (figure 6.1), the horizontal distribution of the rain-gauge stations shows an acceptable degree of homogeneity, whereas, synoptic and climate stations are distributed unequally over the study area. This may lead to a considerable degree of uncertainty associated with the results of the spatial interpolation of the meteorological parameters. The vertical distribution of the stations, on the other hand, exhibits a clear trend towards a lesser number of stations at higher elevations. This is mainly due to the fact that it is more difficult to install and operate permanent meteorological stations in high mountainous terrain. Accordingly, only 7 stations or approximately 10 % of the whole observation network are measuring the meteorological variables at height above 1400m. The limited number of weather stations from 1400 m on leads to the necessity for extrapolation of meteorological data from low-elevation stations (stations located in lowlands) to regions located above the highest existing station. It should be mentioned here, however, that the decrease of the density of the observation network with altitude stands in contrast with the requirements of the spatial interpolation and extrapolation. According to Barry (1992), the observation network in mountainous terrain must be denser than in lowlands to estimate the correct trend of the different meteorological variables. This can be attributed to the fact that the topographic heterogeneity found in mountainous regions causes a wide variety of local weather conditions.

However, the average density of the rain-gauge stations (one station per 80 km²) may perhaps be considered as adequate to represent the rainfall patterns across the study area. But, presence of interruption in the series of rainfall measurements at some stations, as well as the coarse temporal resolution (only daily measurements are available), render it less adequate. On the other hand, the average density of the weather stations (one station per 750 km²) may be considered as fairly low for the purpose of spatial interpolation of meteorological data.

6.3. Organizing the collected meteorological data in a single file “Met-File”

As previously mentioned in Chapter 3, PROMET uses meteorological data provided either by regional climate models or by standard weather station networks. In its standard mode PROMET is driven by spatiotemporally interpolated meteorological measurements which are taken from the climatic stations of the German weather service (DWD) as standard ASCII-file. For the purpose of allowing more flexibility in access to data, the DWD standard ASCII datasets are merged in common binary file containing the entire available meteorological information for the entire simulation period. This user-defined (binary) file is denoted by the extension *.MET*. The meteorological data within this file are organized in records. Each record has a length of 80 bytes (Mauser, 2002).

However, due to the fact that the collected meteorological data for this study are stored in many files in different formats, it was necessary to organize them in a single ASCII-file in the same way that the measurements of DWD were organized. This was done by using a number of useful Java and FORTRAN routines. Figure 6.2 shows a sample of the resulting ASCII-file organized in rows and columns in the exact same manner as the standard DWD data file. Each column should contain the same type of data. For example, the value of air temperature measured at seven o'clock in the morning would be expected in column 16 with a length of 4 bytes. The corresponding parameter for each column (or range of columns) is listed in Appendix 16. It should be noted here, however, that the meteorological data have been “integerized”, i.e., the values are converted into integer. To maintain significant digits for some of these meteorological parameters, the values are multiplied by 10 before writing the value to the output file.

```
KL0000119960102 58 109 70 87 75 88 1 2 2 12 5 5 4-99 6 7 7 21 101 101 301
KL0000119960103 54 97 61 88 76 88 2 3 2 22 4 5 3-99 6 7 6 101 1121 1121 3351
KL0000119960104 42 99 60 91 73 85 1 3 2 19 5 5 5-99 5 6 5 1121 601 601 1801
KL0000119960105 47 83 53 88 80 87 2 2 1 15 6 6 4-99 5 6 6 601 881 881 2651
KL0000119960106 40 90 58 90 69 90 1 1 1 10 5 5 4-99 5 5 6 881 381 381 1151
KL0000119960107 33 81 43 92 74 87 1 2 1 13 4 5 4-99 6 6 6 381 371 371 1101
KL0000119960108 27 98 40 91 63 86 2 2 1 16 3 3 4-99 8 8 7 371 71 71 201
KL0000119960109 33 90 42 86 69 89 1 2 1 12 4 4 4-99 7 6 6 71 11 11 31
KL0000119960110 33 94 54 88 67 80 1 2 2 15 5 4 3-99 5 7 6 11 81 81 251
KL0000119960111 39 108 48 78 60 78 2 2 2 16 3 3 3-99 7 7 7 81 11 11 21
KL0000119960112 27 102 39 82 63 82 1 1 0 8 3 2 1-99 6 8 7 11 00 00 00
```

Figure 6.2 depicts a sample of the collected meteorological variables organized in the same manner as the standard DWD data file.

6.4. Spatial and temporal Interpolation of the meteorological variables

The data obtained from the meteorological stations are point data. While synoptic stations provide hourly measurements, observations from climatic stations are available at 7-hour interval (at 7:00, 14:00 and 21:00). In order to generate the meteorological input data fields for spatially distributed hourly modelling, these measurements have to be temporally and spatially interpolated. This is achieved within the *meteorological component* of the model PROMET as I have mentioned

earlier in Chapter 3. An example of the spatially interpolated meteorological fields for a model time step in the year of 1996 (February 10 at 13:00) is given in Figure 6.3.

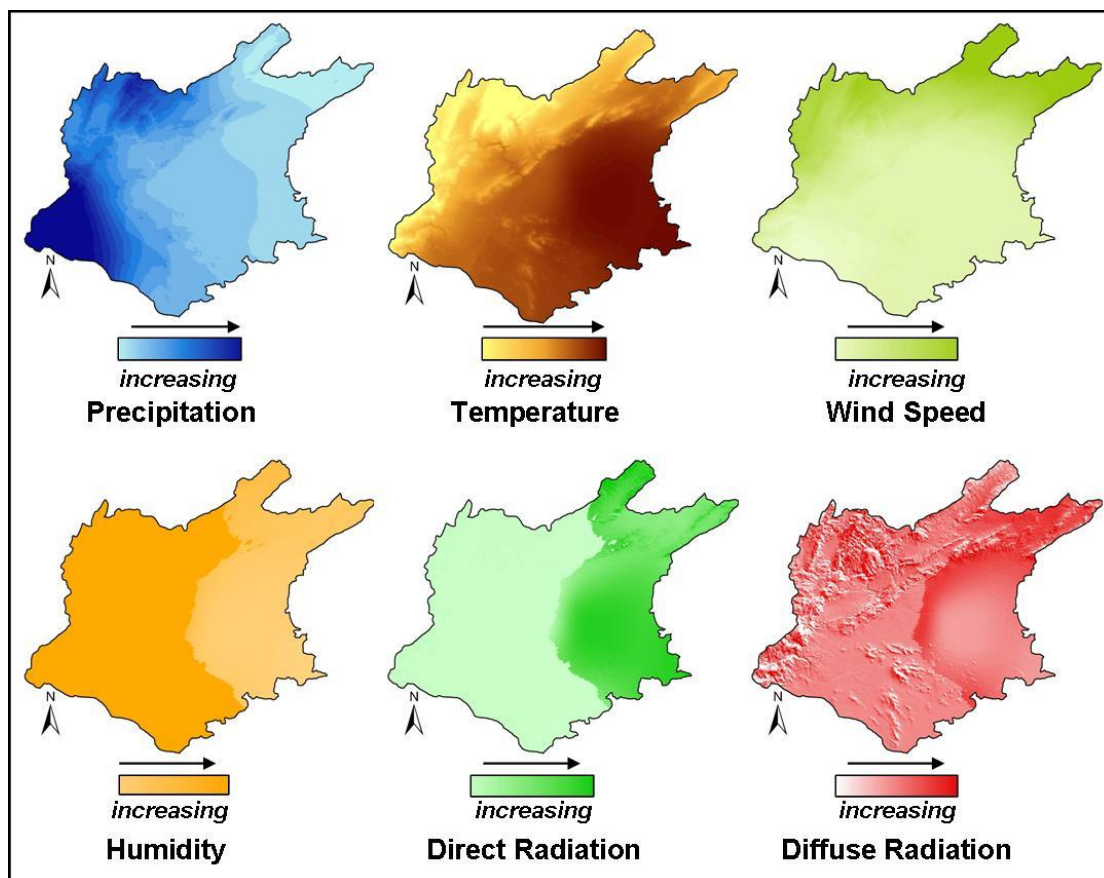


Figure 6.3 illustrates the spatial distribution of some meteorological fields exemplarily for a model time step in the year of 1996 (February 10 at 13:00).

In the following sections I will discuss the general characteristics of each meteorological variable required by the model PROMET, together with its spatial and temporal distribution within the study area as well as the availability of its measured data. In particular, I will focus on the relationship between each meteorological variable and elevation.

6.5. Reviewing and analyzing the collected meteorological datasets

6.5.1. Precipitation

Precipitation is considered as one of the most important meteorological elements for any hydrological simulation. Model results are generally highly sensitive to the distribution of precipitation and its variability over space and time (Beniston, 2002). However, taking into consideration the obstacles attached to the obtaining of adequate long-term continuous data records, the developing of 15-years gridded precipitation dataset at hourly resolution for whole study area can be regarded as a challenging endeavor. Therefore, long-term precipitation time series from all available stations were collected, reviewed and in some cases statistically corrected to prevent

erroneous values. It should be noted here, however, that the individual time series of the existing stations do not always cover the whole simulation period (15 years). Accordingly, the number of concurrently available station records is variable throughout this period. In the case of missing data, a special code (-999) is entered into the precipitation data array.

Precipitation measurements from the Damascus station, which was established in 1918, are considered to be the oldest data record within the study area. Figure 6.4 depicts the annual precipitation at Damascus station from 1918 to 2007. The mean annual precipitation observed at this station is approximately 206mm.

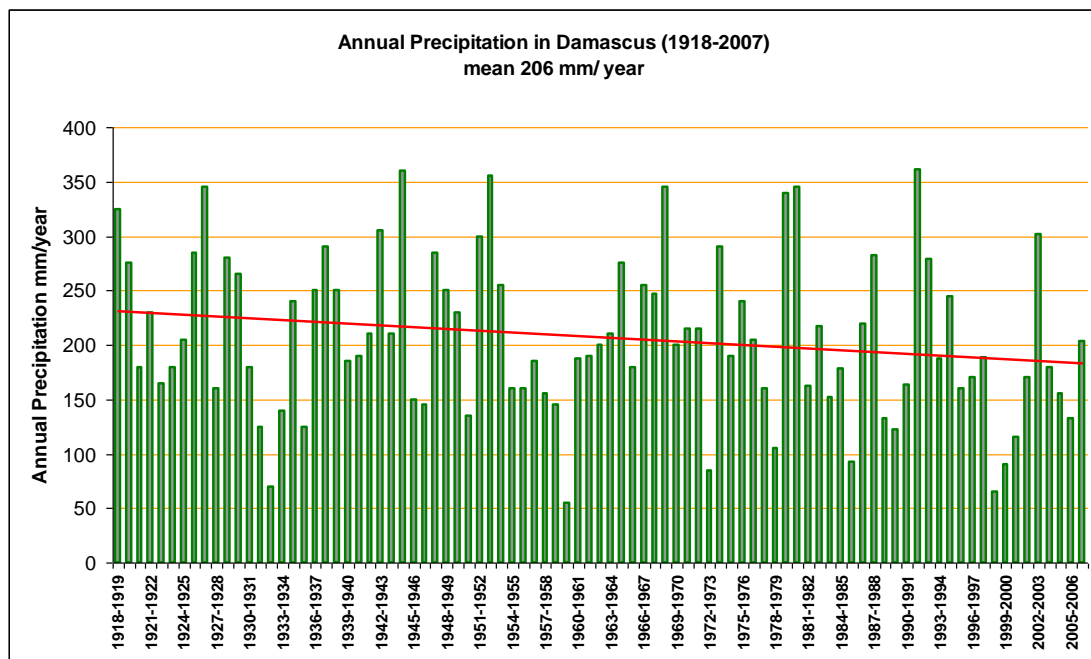


Figure 6.4 shows the annual precipitation at Damascus City Center for the time period from 1918 to 2007.

Regarding the spatial distribution of precipitation, as indicated previously in Chapter 2, the mean annual precipitation is unevenly distributed over the study area and subject to the influence of two main factors. The first is the distance from the Mediterranean Sea, and the second is the blocking effect of the Anti-Lebanon mountain range, which acts as a barrier hindering the penetration of precipitation and moisture into the interior parts of the study area. In other words, the annual precipitation amounts can be characterized as a function of elevation and longitude. As shown in Figure 6.5, the annual precipitation amount decreases with distance from the principal source of moisture, the Mediterranean Sea, so that the longitude can be assumed as the prevailing descriptive factor determining the spatial distribution of precipitation. This is also consistent with the decreasing of elevation eastwards.

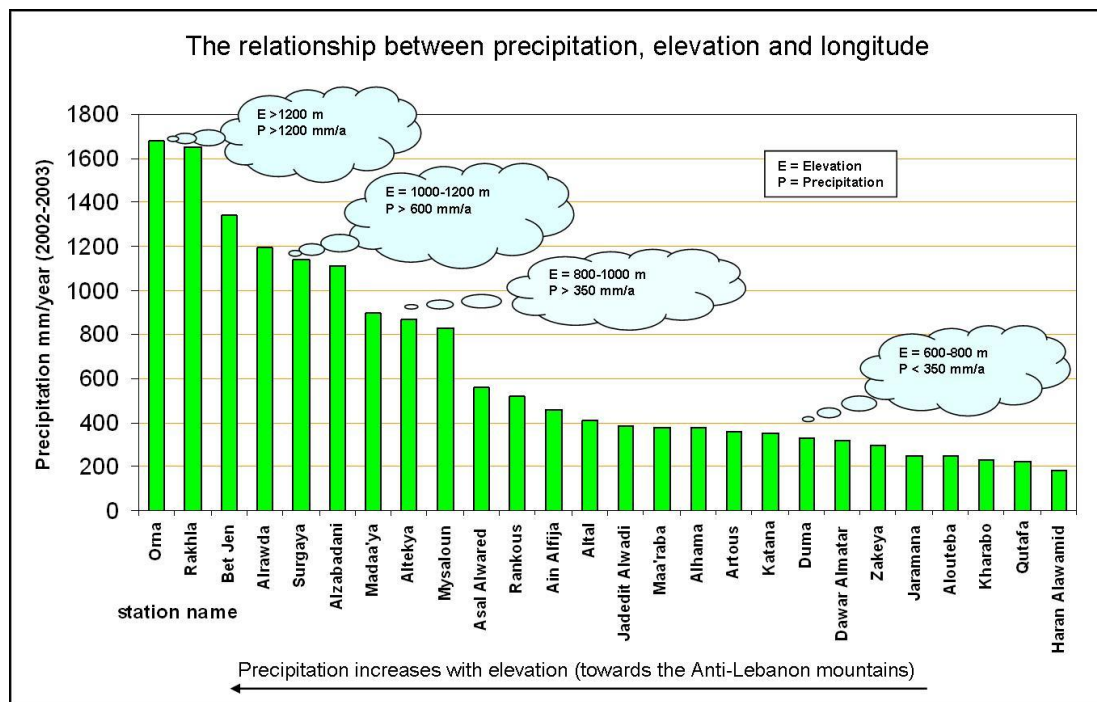


Figure 6.5 shows the relationship between the annual precipitation observed at some selected rain-gauge stations for the very wet year (2002-2003) and their elevations, which in turn increase westward toward the Anti-Lebanon Mountains (toward the Mediterranean Sea).

On the other hand, with regard to the temporal distribution of precipitation (the annual variability), analysis of long-term time series of precipitation in the study area reveals the following results: 1) There is a substantial year-to-year variation in the annual accumulated precipitation which can reach over 150% of the annual mean precipitation in wet years, and less than 50% in dry years; 2) There are also some short-term (4-years) climatic cycles characterized by a wet year after three dry ones; and 3) There is a very wet year that occurs in a medium-term climatic cycle of 10-years and can reach over 170% of the annual mean precipitation.

However, by focusing on the precipitation measurements that were recorded during the simulation period (1991-2005), it could be seen that some extreme years have occurred. For example, from 1999 to 2001 there had been three consecutive years of drought (with less than 50% of the mean precipitation), whereas the hydrological years of 1991-1992 and 2002-2003 have been very wet years (with more than 150% of the mean precipitation).

Furthermore, analysis of monthly precipitation in the study area reveals that precipitation is generally restricted to the cold and wet winter months (early November to late April). It reaches its peak in January, the coldest month of the year. In the mountainous region, however, the rainy season begins as early as October and lasts till the end of May. While the period from December to February accounts for 50 to 65% of the annual precipitation, there is generally no precipitation observed during

the hot and dry summer months (early June to middle September). Figure 6.6 shows the temporal distribution of the average monthly precipitation measured at four selected stations for the period 1959-2005.

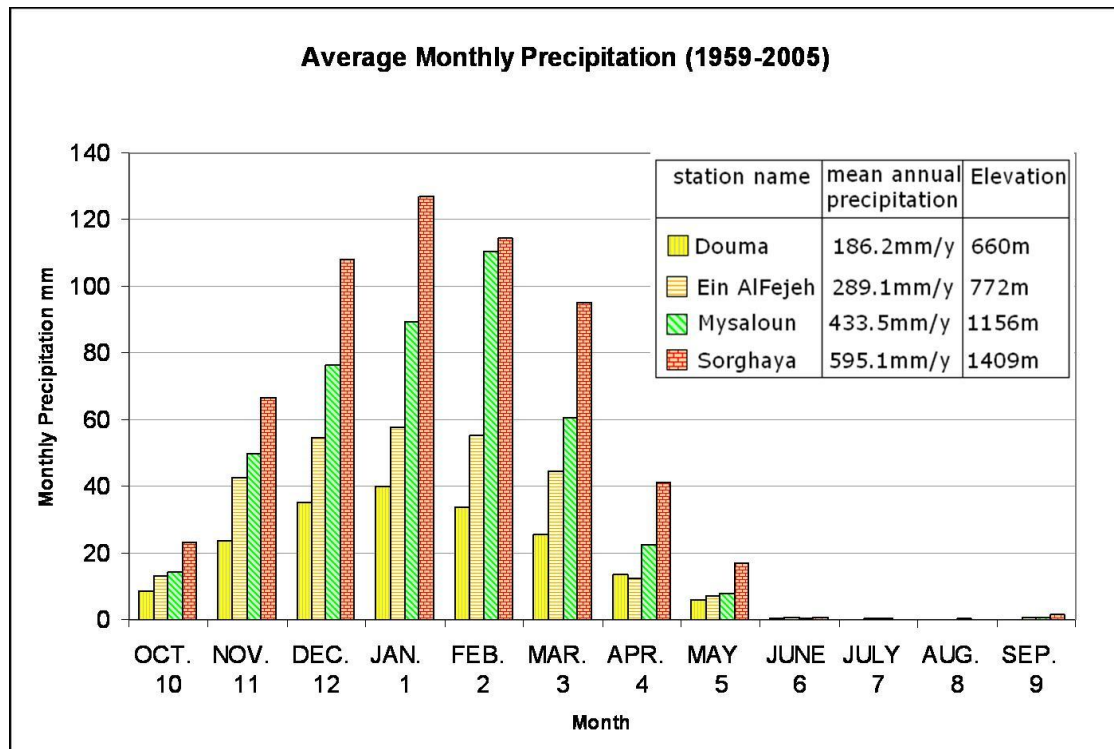


Figure 6.6 Average monthly precipitation obtained from four stations at different elevation for the time period (1959-2005).

6.5.2. Air temperature

Temperature is another factor of great importance as input data for hydrological models. It influences the amount of evapotranspiration and snowmelt (Jain et al., 2007). Accurate assessment of its spatial and temporal distribution within the study area is, therefore, a decisive step in the simulation of land surface processes. However, as in the case of precipitation, distributed air temperature measurements were generated using a set of point measurements taken from the available weather stations and application of an appropriate interpolation method. The interpolation mechanism has been previously discussed in Chapter 3. Long-term air temperature measurements, measured 2m above the surface, were collected from 7 weather stations (5 synoptic and 2 climatic). These temperature time series cover the time period from January 1991 through December 2005. A particular code (-999) was also inserted into these series to represent missing values.

Based on the long-term mean monthly air temperature and precipitation, a climate chart (climate graph) was drawn to describe the climate of the Damascus plain (the *Oasis of Damascus*). As shown in Figure 6.7, the climate of this region is generally characterized by a dry, hot summer and a mild, wet winter. Spring and autumn are

transition periods between these two major seasons. It can also be seen that December (8 °C) and January (7 °C) are the coldest months of the year while July (27 °C) and August (26 °C) are the hottest. Besides, an inverse correlation between the mean monthly air temperature and precipitation can be easily recognized.

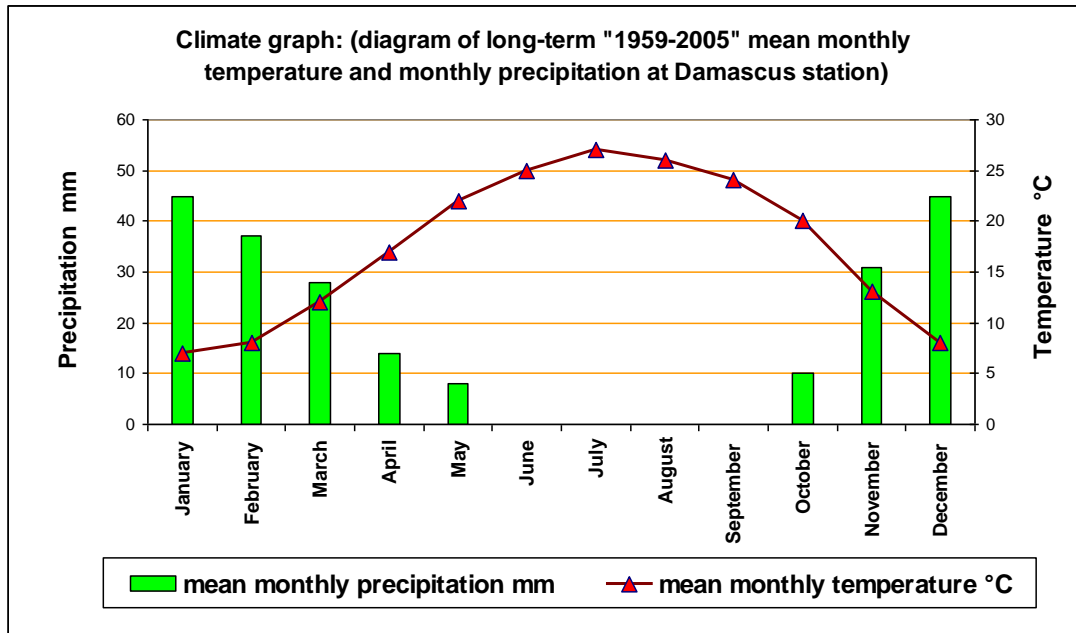


Figure 6.7 shows a climate graph for the Damascus plain (Al-Mazze station).

Furthermore, based on the analysis of the long-term hourly observations of air temperature, it can be said that the study area is subjected to high daily differences between the maximum and minimum temperatures. This difference can sometime exceed 30°C in the desert zone (the eastern part of the catchment). On the other hand, differences in temperature between summer and winter (seasonal differences) are also highly evident. The temperature value could drop down during winter months to less than -17°C in mountainous regions (above 1400 m elevation), while in summer it can rise repeatedly up to 44°C in low-altitude regions (at elevation that are less than 650m).

Moreover, a comparison of the long-term monthly mean, maximum, minimum, absolute maximum, and absolute minimum temperature between two stations located at different elevations (“Al-Mazze” station with an elevation of 750m and “Sorghaya” station 1409m) was also illustrated to provide an overview of its variations from month to month, as shown in Appendices 17,18,19,20, and 21 respectively.

Temperature usually decreases with increasing altitude above sea level. The rate of temperature change with elevation is commonly defined as the temperature lapse rate, or the vertical temperature gradient (Lazaridis, 2010). Its value varies with elevation from place to place and from time to time. To investigate this rate in the study area, long-term mean monthly temperature measurements taken from the two

last mentioned weather stations were used as shown in Appendix 22. While the highest mean monthly lapse rate value recorded between these two stations was found to be 1.07°C per 100m (in August), the lowest value was found to be 0.82 (in January), which may be attributed to the frequent presence of temperature inversions in the winter months. The mean annual value, obtained by averaging the mean monthly lapse rates, is estimated to be 0.95°C per 100m. By comparing this value with the standard temperature lapse rate value (0.65°C per 100m) defined by the International Civil Aviation Organization (ICAO), it can be said that the Greater Damascus Basin is subjected to high temperature lapse rate.

6.5.3. Relative air humidity

The term “*Relative humidity*”, usually expressed in percent, is used to refer to the ratio of the actual moisture content to the maximum moisture that a volume of air can hold at a given temperature (Shipman et al., 2007; Lydolph, 1985). As mentioned previously, the Mediterranean Sea is considered the main source of humidity in the catchment. Accordingly, the relative humidity is expected to decrease from west to east with distance from the moisture source.

As in the case of air temperature measurements, long-term observations of relative humidity were also collected from the available weather stations for the same period of time (1991-2005). However, the interpolation of relative humidity is not straightforward as it relies on air temperature in a non-linear way. Therefore it was converted into water vapor pressure, which can be interpolated in a similar manner as air temperature.

On the other hand, based on the analysis of the long-term observations, it was found that the values of relative humidity are to a large extent connected with the fluctuations of air temperature. Illustrating the mean monthly temperature along with relative humidity, as shown in Figure 6.8, reveals that there is a negative correlation between these two factors in the study area.

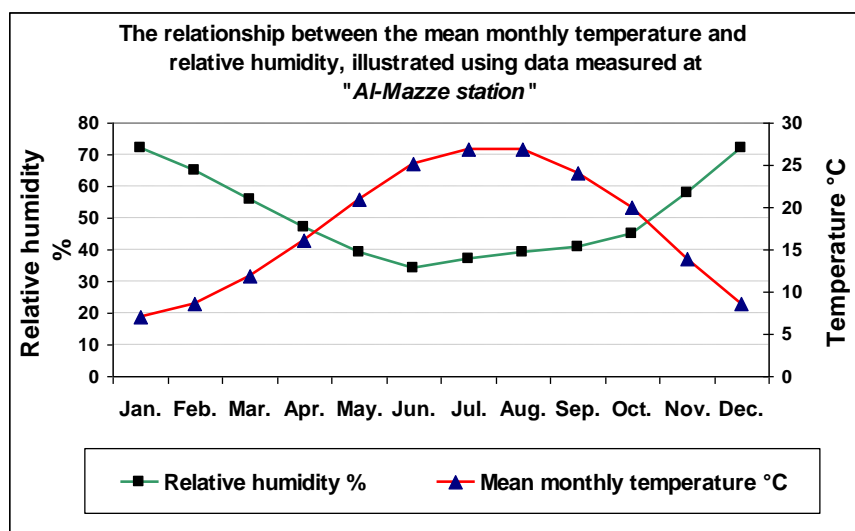


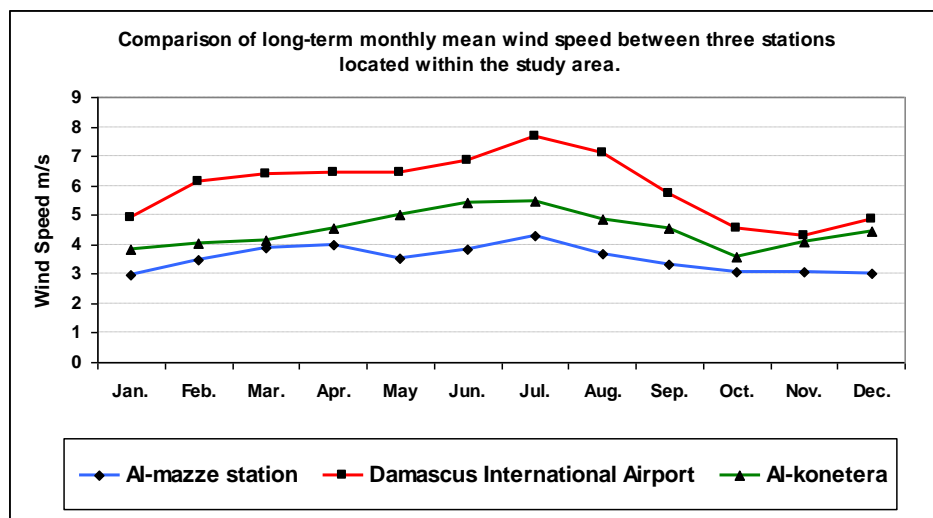
Figure 6.8 the correlation between the long-term mean monthly temperature and the mean monthly relative humidity at “Al-Mazze” station.

It can be seen from the above figure (Figure 6.8) that the highest mean monthly relative humidity values (up to 70 %) were recorded during the cold months (December and January), while the lowest values (34–39%) were registered during the summer months (May to August). Furthermore, in addition to the above mentioned seasonal fluctuations in relative humidity, daily oscillations in its value were also noticed, especially in the summer months, when its minimum daily value can be as low as 7% (especially in the central and eastern parts of the catchment).

6.5.4. Wind speed

Wind speed is another meteorological factor required by the hydrological model PROMET. It plays an important role in the melting process of the snow cover and influences the rates of evapotranspiration over a given area (De Jong et al., 2005). Long-term spatially distributed wind speed fields were also generated by interpolation of point observations (station data) covering the whole simulation period.

Analysis of the long-term monthly mean wind speed measurements reveals that its value in summer months is more than that in winter months. Figure 6.9 illustrates a comparison of the long-term monthly mean wind speed between three stations located within the study area. The names of these selected stations, together with their geographical locations and elevations are also given.



Station name	Longitude	Latitude	Elevation(m)
Damascus International Airport	36.52	33.43	610
Al-mazze station	36.26	33.51	750
Al-konetera	35.86	33.26	941

Figure 6.9 the long-term monthly mean wind speed as observed at three selected weather stations for the time period 1991-2005.

Finally, it should be mentioned that the measured wind speed data were converted into Beaufort numbers in order to make them compatible with the requirements of the meteorological component of the model PROMET.

6.5.5. Cloud cover and radiation budget

Cloudiness constitutes one of the most significant factors in the earth radiation balance, since it greatly affect the radiation exchanges between space and the earth's surface. It plays a significant role in reflecting incoming solar shortwave radiation and in absorbing and emitting longwave radiation (Stensrud, 2007; Lydolph, 1985). Therefore, cloud cover data (estimated in 8th of cloud cover "oktas") covering the entire simulated period were collected to calculate solar radiation at the earth's surface. However, for further use within the model PROMET, these data were converted into percent clear sky.

As mentioned previously in Chapter 3, incoming short- and longwave radiation fluxes are simulated using the interpolated cloud cover observations. Figure 6.10 illustrates the simulated direct and diffuse radiation exemplarily for a model time step in the year 1996 (3rd February). It is obvious from this figure that the amount of direct and diffuse shortwave solar radiation falling on the surface is mainly controlled by the interpolated cloud cover.

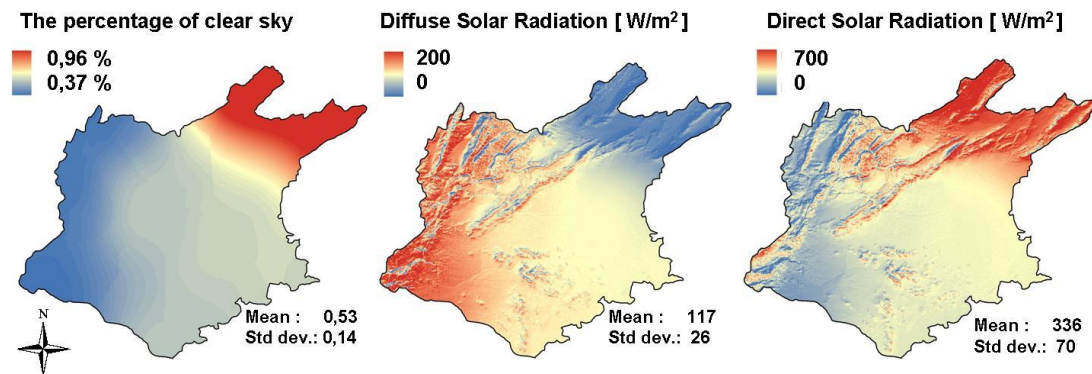


Figure 6.10 shows the percentage of clear sky and the amount of diffuse and direct solar radiation, as estimated by the meteorological component of the model PROMET exemplarily for a model time step in the year of 1996 (February 3rd, 09:00 a.m.).

In addition to the incoming shortwave (direct and diffuse) radiation fluxes, PROMET requires the incoming longwave radiation to calculate the radiation balance for each grid cell and each modelling time step. According to Arya (2001), longwave radiation mainly includes two components: emission from the atmosphere (R_{LW-IN}) and emission from the Earth's surface (R_{LW-OUT}). The longwave radiation balance (R_{LW-BAL}) can thereby be expressed as:

$$R_{LW-BAL} = R_{LW-IN} - R_{LW-OUT}$$

The amount of longwave radiation emitted by the atmosphere depends primarily on the atmospheric variables such as air temperature, cloud cover, and air moisture content (Liston and Elder, 2006). The meteorological component of the model PROMET estimates incoming longwave radiation based particularly on the interpolated air temperature and cloud cover (Mauser and Bach, 2009). As air temperature normally decreases with increasing altitude, incoming longwave radiation can be expected to decrease with height above the level of the sea.

7. Parameterization of soil physical and hydraulic properties

7.1. Soil formation

According to several authors (e.g., Jenny, 1994; Certini et al., 2006), differences in soil properties are generally caused by differences in one or more of the following soil-forming factors:

- I. *Climate*: climate is one of the most significant factors of soil formation which influences the rate of chemical and physical weathering (Lavelle and Spain, 2002). It also affects both vegetation cover and the activity of organisms. Accordingly, due to the fact that the study area, as will be shown in a later chapter (see Chapter 9, Section 9.1.1), can be divided into four climatic zones ranging from sub-humid to arid, soil moisture and temperature regimes are expected to vary according to the climatic zone under which the soil was formed. As an example, the taxonomic term used to describe the moisture regime of soils developed under arid environment is aridic (Han and Singer, 2007).
- II. *Parent material*: the two soil properties that are attached most tightly to parent material are texture and mineralogy (Troeh and Thompson, 2005). According to the geological map of the Greater Damascus Basin, which shows the age and lithology of the sediments, Limestones, marls, conglomerates and basalts comprise the principal parent materials of the soils of the study area. According to Razvalyaev and Ponikarov (1966), some of the existing Limestones are extremely resistant to weathering and thus form outcrops and cliffs. Other Limestones and marls that include iron and silicate minerals weather more easily producing deep to moderately shallow and fine textured soils. On the other hand, the volcanic formations (basalts) represent the main parent material in the southern part of the basin.
- III. *Topography (Relief)*: According to Goudie (2001), relief affects the process of soil formation through its influence on drainage, erosion, vegetation cover and soil temperature. Runoff of precipitation is high when slopes are steep so that less water infiltrates the soil to cause weathering and support vegetation. Consequently, the resulting soils in such areas are shallow. If topography is nearly level, runoff is less, more water infiltrates the soil, weathering is more effective, vegetation is more vigorous and the resulting soil is deep.
- IV. *Organisms*: living organisms, including plants, animals, bacteria, actively affect the soil forming process (Whalen and Sampedro, 2010). Plants in particular have a great influence on the amount of organic matter build-up in the soil. In view of that, the soils of the study area are anticipated to be poor in organic matter due to the absence of thick vegetation cover, especially in the arid zone.
- V. *Time*: according to several authors (e.g., Schaetzl and Anderson, 2005; White, 2006), the process of breaking down rocks into smaller particles, often referred to as weathering, and the extent of it, is fully dependent on the intensity and the length of time that the four above mentioned soil-forming factors have been operative. Thus, a younger soil reflects characteristics of the parent material better

than an older soil, as inadequate time has elapsed to allow important development. For example, in many Entisols in the study area (which usually occur on slopes where the rate of erosion is high), the time has been too short for the development of pedogenic horizons (Berger, 1982).

7.2. Available Soil Maps

Three major soil survey projects were conducted to describe and map the soils of Syria including the study area (Ilaiwi, 2001; Berger, 1982). However, despite the fact that the scale of these surveys is not as detailed as required for the purposes of the parameterization of soil hydraulic properties, these surveys provide very good information on the general characteristics and the distribution of the existing soils. All available soil observations and maps were collected in hardcopy formats (paper) from different sources (the maps were then digitized and geo-referenced). The collected soil maps include:

- I. Soil map of Syria at a scale of 1:500,000 prepared by FAO in 1977. According to this map, as discussed previously in chapter 2, soils were divided into seven major groups (only five of them are found within the study area).
- II. Soil map of Syria and Lebanon at a scale of 1:1.000.000 prepared by ACSAD. According to this map, soils were divided into 55 groups of soil associations (USDA Soil Survey Staff, 1975). Only eight of these soil groups are found within the boundary of the study area.
- III. Soil map of Syria at a scale of 1:500,000 prepared as a technical assistance project of the United States Agency for International Development (USAID) to the government of Syrian Arab Republic. The main objective of this project was to classify, map, and describe soil characteristics of the country, with a specific focus on the interpretations of soils according to their physical and chemical properties (Ilaiwi, 2001; Berger, 1982). The legend of this map, which was produced in 1982, was made up of association of subgroups of the USDA Soil Taxonomy (1975). The soils of the country were grouped in 99 associations (only 13 of them were found within the study area). This map along with its report represents the main source of soil information for this study.

7.3. The classification and nomenclature of the soils of the study area

According to the above last-mentioned soil map, soils of the Greater Damascus Basin were classified using the comprehensive soil classification system of the United States Department of Agriculture (USDA Soil Survey Staff, 1975). An essential attribute of this system is the nomenclature employed to classify different soil groups. The names of the mapping units are combinations of syllables, most of which are derived from Latin or Greek. Each syllable of a soil name carries a conception of soil character or origin, thus the name directly indicates the general kind of soil being classified (USDA Soil Survey Staff, 1999; Brady and Weil, 1996). This soil classification system has six categories. Beginning with the broadest, these

categories are the order, suborder, great group, subgroup, family, and series. Soils of the study area, however, are classified at the subgroup level.

Aridisols, Entisols, Inceptisols, and Vertisols are the principal soil-orders found within the boundary of the Greater Damascus Basin. The spatial distribution of these soil-orders is illustrated in Figure 7.1, and brief description of them is given below.

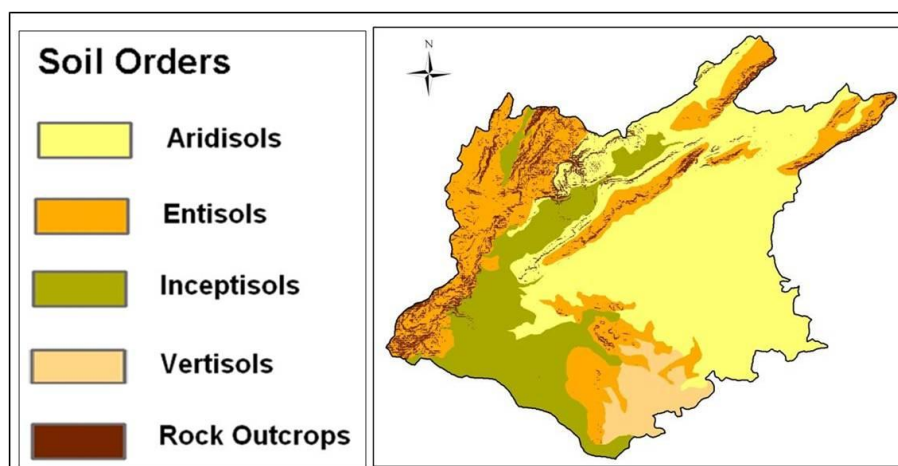


Figure 7.1 the spatial distribution of soils of the study area (at order level) digitized from the soil map of Syria at a scale of 1:500,000 (USAID, 1982).

7.3.1. Order **Aridisol** (desert soils)

According to several authors (e.g., Edwards-Jones, 2001; Ilaiwi, 2001; Berger, 1982), Aridisols (from the Latin *aridus*, for “dry”, and *solum*, for “soil”) are soils that are developed in areas where the potential evapotranspiration significantly exceeds the amount of precipitation during most of the year, and very little or no water percolates through the soil. Owing to the limited amount of water available in the soil profile, the soil development processes are less intense than in the humid areas. Thus, these soils inherit a lot of their morphological features from the underlying bedrocks.

Aridisols occupy a relatively large area (2000 km² or 39% of the total study area). They cover almost all of the central and eastern part of the basin where the annual precipitation drops below 250mm. In addition, Aridisols are characterized by an aridic (hot and dry) soil moisture regime, and they have light colour as there is not enough vegetation to add organic matter to the soil profile. Furthermore, they often accumulate calcium carbonate, gypsum, and other materials that are readily leached from soils in more humid environments (Edwards-Jones, 2001).

To reduce the heterogeneity in this order category, classification is done at the next lower categories (Suborder, Great Group, and Subgroup). A complete list of the soil taxonomic categories identified in the study basin is given in Table 7.1.

Table 7.1 Taxonomic classification of soils of the study area taken from the soil map of Syria at a scale of 1:500,000 (USAID, 1982).

Order	Suborder	Great Group	Subgroup
Aridisol	Orthid	Calciorthid	Typic
			Lithic
			Xerollic
		Camborthid	Typic
			Lithic
			Xerollic
Entisol	Orthent	Torriorthent	Typic
			Lithic
		Xerorthent	Lithic
Inceptisol	Ochrept	Xerochrept	Typic
			Lithic
			Petrocalcic
			Vertic
Vertisol	Xerert	Chromoxerert	Typic
			Entic

The suborder **Orthid** is the only Aridisols suborder found in the region. Its subdivisions (great groups) are *Calciorthids* and *Camborthids*. The spatial distribution of soils of the study area at the level of Suborder and Great Group is shown in Appendix 23.

- **Great Group Calciorthids:** these are Aridisols that have an ochric epipedon (surface horizon with little organic matter) and a calcic horizon (a subsoil horizon with a secondary accumulation of carbonates, usually of Ca). These soils cover about 12% of the total study area. They are split into three subgroups based on the depth of the soil and the amount of organic matter in the epipedon (Berger, 1982):
 - **Subgroup Typic Calciorthids** are deep soils (deeper than 100 cm).
 - **Subgroup Lithic Calciorthids** are similar to Typic but they have bedrock within 50cm of the surface.
 - **Subgroup Xerollic Calciorthids** have more moisture and more organic matter than Typic Calciorthids. They are encountered in areas where the moisture regime is a transition between the xeric (moist in winter and dry in summer) and the aridic.
- **Great Group Camborthids:** these are Aridisols with an ochric epipedon and a cambic horizon (a subsoil horizon with some alteration of the parent material and a weak indication of development). These soils occupy nearly 27% of the total study area. They are characterized by the absence of a horizon of carbonate accumulation, and they have relatively homogeneous texture from the surface downward. Three subgroups are distinguished in the area under investigation, separated according to drainage characteristics, depth and the amount of organic matter in the epipedon (Edwards-Jones, 2001; Berger, 1982):
 - **Subgroup Typic Camborthids** are deep, well drained soils.

- *Subgroup Lithic Camborthids* are similar to Typic but the bedrock is found within 50cm of the surface and they generally have more organic matter than the Typic Camborthids.
- *Subgroup Xerollic Camborthids* are like Typic but they have more organic matter and are moist for longer periods than Typic Subgroup.

7.3.2. Order **Entisols (new soils)**

Entisols (from the root *ent*, for “recent”, and *solum*, for “soil”) are soils that have little or no indication of development of pedogenic horizons (USDA Soil Survey Staff, 1999). Entisols in the study area are generally found as shallow soils in mountainous regions (especially in the Anti-Lebanon Mountain range) where the rate of erosion exceeds the rate of soil development, and they occupy an area of about 1500 km² (31% of the total study area). Some of these soils have an ochric epipedon, especially when they are to some extent protected from erosion. According to several authors (e.g., Edwards-Jones, 2001; Berger, 1982), Entisols may have any moisture or temperature regime, vegetation, or parent material. They are generally characterized by the absence of distinct horizons and by their mineral nature.

The Suborder **Orthent** is the only Entisols suborder encountered in the study basin, whereas two Great Groups are recognized based on their moisture and temperature regimes: *Torriorthents* and *Xerorthents*.

- Great Group **Torriorthents**: these are the dry Entisols of arid regions (occupying about 16% of the study basin). They are mostly calcareous and have a torric (aridic) moisture regime. Some are very gravelly and have coarse texture. They are separated into two Subgroups:
 - Subgroup **Typic Torriorthents** are relatively deep and gravelly.
 - Subgroup **Lithic Torriorthents** are shallow to moderately deep soils.
- Great Group **Xerorthents**: these are soils of sub-humid climate that have a xeric moisture regime (Kolay, 2007). They cover about 15% of the total study area. They are mostly steep and lose water via runoff. Only one Subgroup is distinguished: namely Lithic Xerorthents.
 - Subgroup **Lithic Xerorthents** are shallow to very shallow soils.

7.3.3. Order **Inceptisols (young soils)**

Inceptisols (from the Latin *inceptum*, for “beginning”, and *solum*, for “soil”) are soils of semiarid to sub-humid environments that generally show only moderate degrees of soil weathering and development (USDA Soil Survey Staff, 1999). Even though they are better developed than Entisols, they are still young soils and resemble very closely the parent material (Harpstead et al., 2001). They cover an area of about 1100 km² (23% of the total study area).

The Suborder **Ochrept** is the only Inceptisols suborder recognized in the study basin. Its soils are found in the regions with xeric moisture regime, and accordingly, only great group is recognized, namely Xerochrept.

- Great Group **Xerochrepts**: these soils are moist in winter and spring but are completely dry in summer (Edwards-Jones, 2001; Berger, 1982). Soils of this great group in the study basin are mostly deep and developed on Neogene deposits. They are usually characterized by an ochric epipedon and a cambic horizon. Four subgroups are recognized in the study area:
- Subgroup **Typic Xerochrepts** are deep to moderately deep, nearly level to undulating, well drained soils.
 - Subgroup **Lithic Xerochrepts** are shallow and the bedrock is found within 50 cm of the surface.
 - Subgroup **Petrocalcic Xerochrepts** are deep, well drained soils.
 - Subgroup **Vertic Xerochrepts** are clayey soils that have deep, wide cracks in the summer if they are not irrigated.

7.3.4. Order Vertisols (cracking clay soils)

Vertisols (from the Latin *verto*, for “vertical cracking“, and *solum*, for “soil”) are soils with a high clay content that mainly developed under a xeric moisture regime (Al-Qudah, 2001). The most significant feature of these soils is the presence of deep and wide cracks which may extend to a depth of 1 m or more (Ahmad, 1996; Brady and Weil, 1996). These soil occupy an area of about 330 km² (6% of the total study area) and have a fine texture. All Vertisols in the study basin belong to the **Xerert** suborder in which only the Great Group **Chromoxerert** is recognized. Soils of this great group, however, are separated into two subgroups, namely Typic Chromoxerert and Entic Chromoxerert. The Typic subgroup is better drained and lighter colour than the Entic one (Berger, 1982).

7.4. Separating soil associations into their constituent subgroup soils

Although soils of Syria have been classified at the level of subgroup of the USDA Soil taxonomy (1975), the legend of the final map is not built up from the individual recognized subgroup soils rather with soil mapping units, referred to as soil associations. Each map unit (soil association) on the 1:500,000-scale soil map represents an area on the landscape made up of several subgroup soils (hereafter referred to as soil types) for which the unit is named. Most soil mapping units are usually composed of two to four dominant soil types that are geographically associated.

The soil survey report (which was also produced by USAID in 1982) provides a quantitative analysis of the physical and chemical properties of each soil type along with a detailed description of its representative profile. In addition, this report includes general characteristics of each soil unit (without going into the details of its constituents) along with interpretation of its agricultural potentials and limitations. The spatial distribution of the soil associations found within the study area together with the dominant soil types in each unit is illustrated in Appendix 24.

However, due to the fact that a single soil association can contain two or more (in this study up to 5) soil types with different attributes, the use of simple averaging methods for calculating average representative attributes for each soil association may produce results that are misleading. For instance, if a soil association consists of two soil types with different soil texture, e.g. one soil with sandy texture and the other with clayey texture, the averaged soil texture will be described as loam. It is obvious, that this description does not indicate the correct soil properties. According to several authors (e.g., Lagacherie et al., 2007; Legros, 2006), the averaging procedure is suitable only if the soil components (the constituent soil types) of each soil mapping unit have fairly uniform characteristics. Unfortunately this is not the case for soils of the study basin. Therefore, in order to parameterize the properties of the soil mapping units with an acceptable accuracy, a decision was made to separate these units (the soil associations) into their constituent soils (at the level of subgroup of the USDA Soil Taxonomy). It is expected that the separation of the soil associations by isolating their principal components will create a new soil map which is more useful for the purpose of parameterization. A better separation should make use of all available information and that information should properly be merged. For this study, however, the general description of each soil type together with the detailed information obtained from its representative profile formed the most important source of information. I especially benefited from the comprehensive description of slope (%), elevation (m), and parent material (Lithology) provided for each soil type. The Digital Elevation Model (DEM) was used to provide the elevation of the landscape, as well as to derive the slope. The geological map of the study area (scale of 1:100,000) was also digitized, geo-referenced, and stored as vector format. The geological units on this map were then classified according to their lithology to match well with the descriptions of soil parent materials. ArcGIS 9.1 software was used to achieve the process of soil separation. It should be mentioned here, however, that the priority given to each of the separating factors (i.e. slope, elevation, and lithology) differs from soil mapping unit to another. Therefore, each mapping unit on the map of soil associations was processed separately from the other units, taking into account all available auxiliary information. Figure 7.2 shows the estimated spatial distribution of soils of the study area classified at the level of Subgroup of the USDA Soil Taxonomy. The estimated area covered by each soil type is illustrated in Figure 7.3.

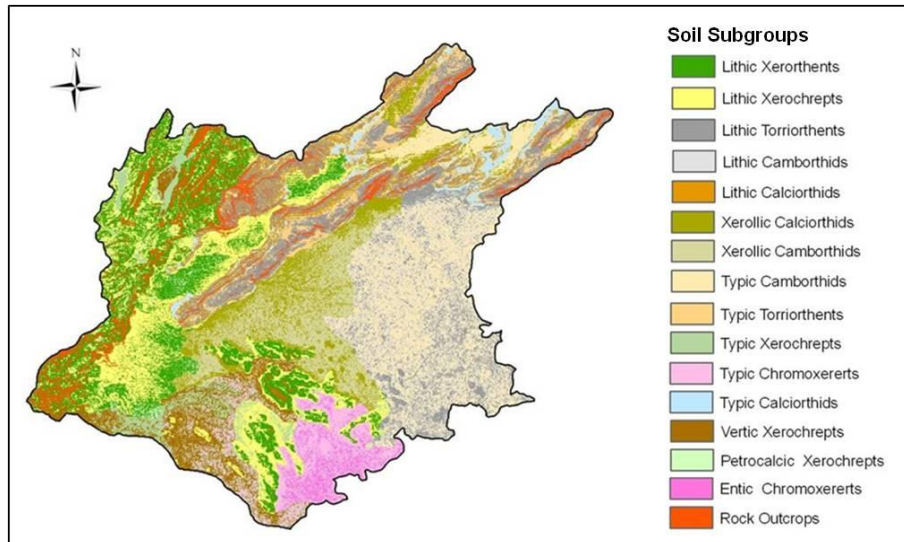


Figure 7.2 shows the estimated spatial distribution of soils of the study area (classified at the level of Subgroup of the USDA Soil Taxonomy, based on the soil map of Syria that was produced by USAID, 1982).

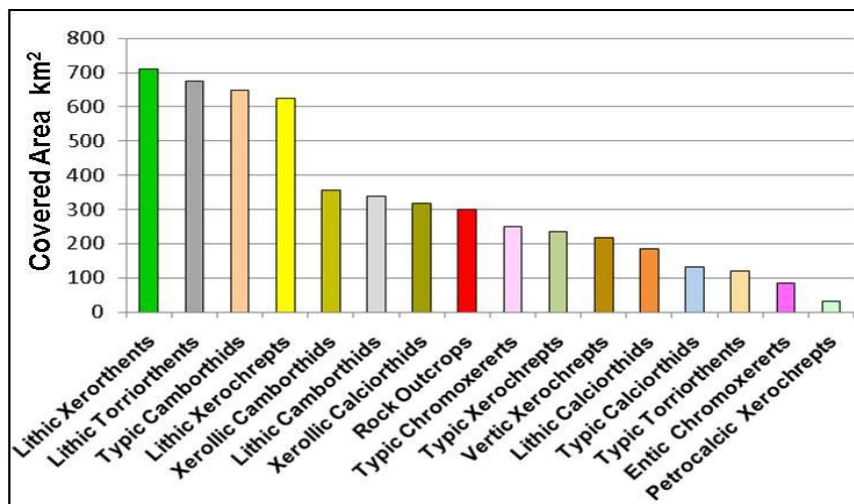


Figure 7.3 shows the estimated area (in km²) covered by each soil type in the study basin.

7.5. Inherent characteristics of soils of the study area

In the following sections I will discuss some of the inherent characteristics of the soils of the study area, including, among others, soil texture, depth for both surface and subsurface horizons, and percent of coarse fragments per horizon. The soil observations carried out by USAID staff (1982) during the course of soil survey as well as the laboratory analysis of the collected soil samples (from representative profiles) represent the main sources of information about these characteristics.

7.5.1. Soil Texture

Soil texture is an important soil property which refers to the relative proportion of different grain sizes of mineral particles (excluding the organic matter) in a given volume of soil (Troeh and Thompson, 2005; Chapin et al., 2002). These particles are classified by the USDA into clay (having diameters of less than <0.002 mm), silt (0.002-0.05mm), and sand (0.05-2mm). Soil texture is largely determined by the mineral rock material (parent material) from which the soil is developed and the rate at which it is weathered. It controls the quantity of water a soil can retain and make available to plants. For example, fine-textured soils such as clay have good water-holding characteristics, whereas coarse textured soils such as sandy soils have low water-holding capacity but good drainage (Brown, 2008; De Pauw, 2001; Holden, 2005).

Each soil of the 15 estimated (separated) soil types is described by a typical soil profile with quantitative values of the main soil characteristics (soil texture, depth of each soil horizon[cm], water holding capacity[%], organic material content[%], clay[%], silt[%], sand[%], coarse material content[%] and others). For the purpose of illustrating the interrelationships between some of those soil characteristics, two soil profiles were chosen and listed in Table 7.2. The USDA textural triangle was used to determine the soil textural for each horizon of each typical soil profile according to its percentages of clay, silt, and sand. According to this classification system, there are 12 textural classes into which soils may be classified. For example, if a soil horizon contains about 39% sand and 42% silt, it would be classified as loam. However, for the purpose of explanation, each soil horizon (from the two chosen soil profiles) was plotted on the USDA textural triangle as shown in Figure 7.4.

Table 7.2 shows the quantitative values for some soil characteristics for two chosen soil profiles.

Profile number	Soil name	Depth cm	Horizon	Sand %	Silt %	Clay %	Texture	Organic Carbon %	Water content %	
									1/3 bar	15 bar
40	Lithic Torriorthents	0 - 3	A11	39	42	19	Loam ^{[1]*}	2.0	18.9	8.0
		3-12	A12	36	28	36	Clay Loam _[2]	1.4	25.0	11.0
		12-33	C1	39	30	31	Clay Loam _[3]	1.5	22.9	10.1
		33-42	C2	27	33	40	Clay Loam _[4]	1.6	27.6	12.5
62	Typic Camborthids	0-6	A11	54	24	22	Sand Clay Loam _[5]	0.2	17.7	7.4
		6-17	A12	40	26	34	Clay Loam _[6]	0.3	23.7	10.5
		17-49	B21c	36	32	32	Clay Loam _[7]	0.2	23.6	10.5
		49-82	B22	20	28	52	Clay _[8]	0.2	32.6	15.2
		82-115	Bc	18	36	46	Clay _[9]	0.1	30.9	14.3

^{[1]*} Number was given to plot the texture of its corresponding soil horizon on the USDA Texture Triangle.

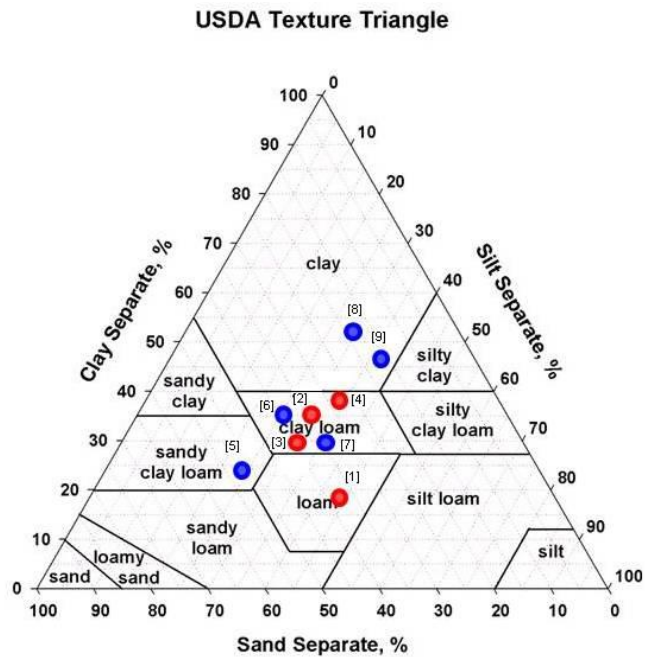


Figure 7.4 the USDA soil texture triangle showing grain-size distribution of each soil horizon (from the above presented soil profiles).

Soil texture map was also provided through generalization and aggregation of the previously separated soil type classes (each represented by its representative soil profile) and transferring the soil types to texture classes, as shown in Figure 7.5. It can be seen from this map that texture of the existing soils is very heterogeneous ranging from clay to sandy loam.

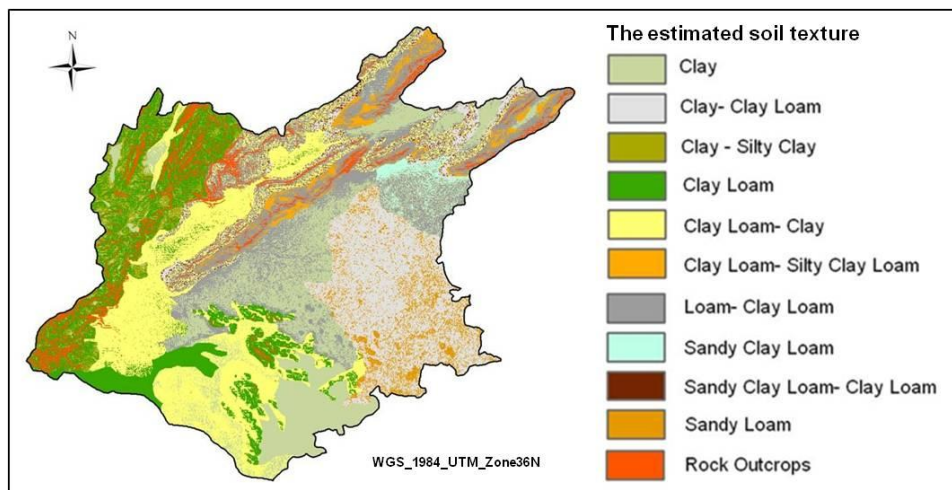


Figure 7.5 the estimated spatial distribution of soil texture within the study area.

For each soil profile, however, the soil texture was determined for each horizon (or layer of soil) and not averaged vertically. Soil types with similar vertical soil texture sequences were then merged to produce a texture map consisting of 10 different texture classes. The legend of the resulting map was created so that the first part of the texture class name refers to the texture of the surface horizon, whereas the

second part refers to the texture of the subsurface horizon. If a soil has a uniform texture throughout the profile, its texture will be represented by a single name.

7.5.2. Soil depth

Soil depth (thickness) is an essential soil characteristic affecting, among other things, water movement and water storage capacity of the soil profile (Mohamed and Antia, 1998; Park, 2001). For example, deep soils can hold more water than shallow soils with similar properties. This, in turn, can exert a strong influence on plant growth and suitability for agriculture. According to Berger (1982), slope angle is thought to be the most important predictor of the soil depth in the study area. This is because it is closely related to erosion and deposition of soil material. Consequently, shallow soils are encountered in mountainous areas associated with steep slopes, whereas deep soils are mainly found on depressions and lowlands.

Maps of soil depth were created in a similar way as the soil texture map, by generalizing and aggregating the separated soil type classes and converting them into thickness classes. Figure 7.6 shows the estimated spatial distribution of surface-soil thickness (left), subsurface-soil thickness (middle) and the total soil thickness (right) in the study area.

However, as mentioned previously in Chapter 3, for the purpose of modelling the soil water content as well as the vertical and lateral flows of water in the unsaturated zone, soil types were divided into up to 4-layers with different thicknesses.

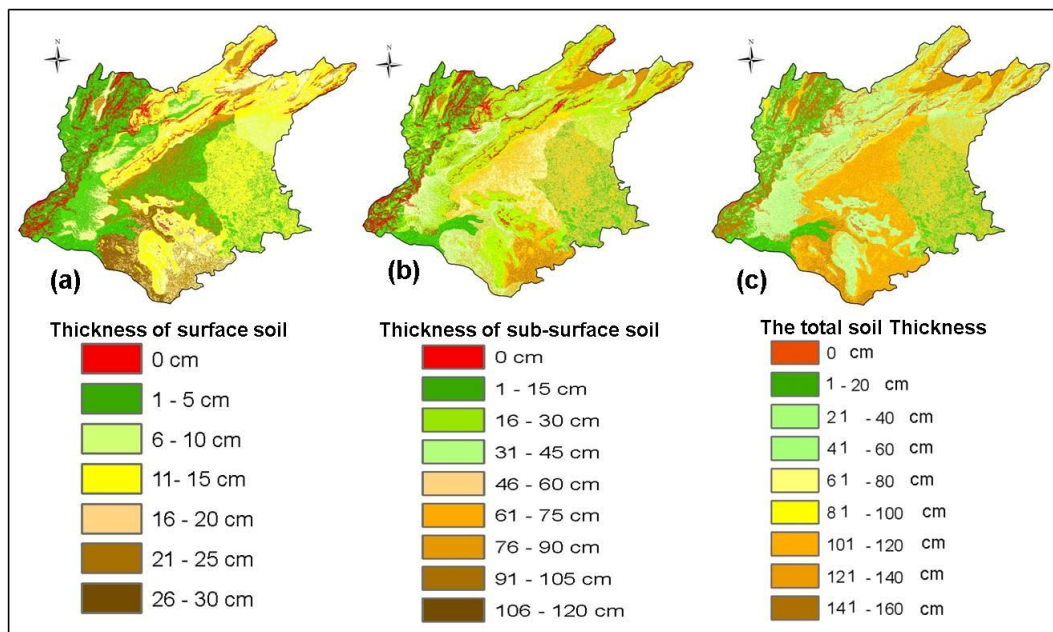


Figure 7.6 the estimated spatial distribution of soil thickness; a) Thickness of surface soil, b) thickness of sub-surface soil, and c) the total soil depth.

7.5.3. Content of coarse fragments

According to several authors (e.g., Al-Qinna et al., 2010; Miller and White, 1998), the presence of coarse fragments (i.e. stones and gravel with a diameter > 2mm) in a soil has a significant effect on its physical and hydraulic properties, including saturated hydraulic conductivity, water-holding capacity, bulk density, and porosity. Based on a study conducted by Brakensiek and Rawls (1994), coarse fragments in the soil matrix directly influence (reduce) the soil porosity, which in turn reduces the rate of infiltration and the rate of soil water storage and movement. In addition, coarse fragments are regarded as a fundamental factor for determining erosion rates, especially in arid and semiarid regions where vegetation cover is very sparse. Several studies (e.g., Zavala et al., 2010; Nichols, 1984) have shown that large content of rock fragments in and on the surface of soils reduce erosion rates. Therefore, it is very important that we know the volumetric space in the soil occupied by coarse fragments and identify how these fragments are spatially distributed.

Maps representing the content of coarse fragments (expressed as a percentage of the total soil volume) were created in the same manner as the soil texture and soil depth maps. The volumetric fraction of coarse material for each soil type was taken from its comprehensive description provided by the USAID staff, 1982. The estimated spatial distribution of the volumetric content of coarse fragments in both surface and subsurface horizons (or layer of soil) is illustrated in Figure 7.7.

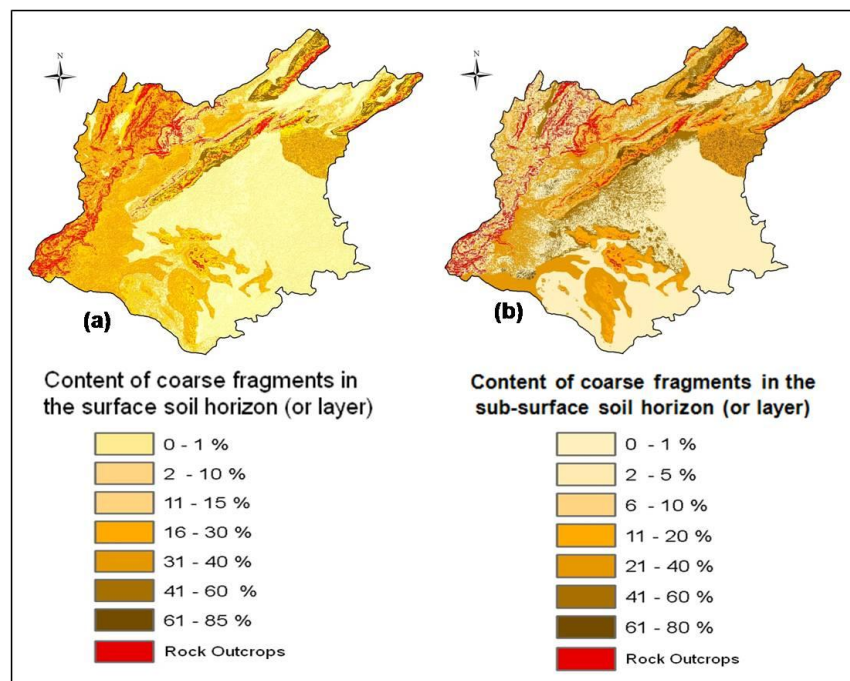


Figure 7.7 the estimated spatial distribution of the volumetric content of coarse fragments in a) surface soil horizon (or layer), and b) in sub-surface soil horizon.

7.6. Estimating soil hydraulic properties using Pedotransfer Functions

The use of distributed hydrologic modelling has created a pressing need for detailed information on spatial distribution of soil properties. There is also a general acknowledgment that reliable results from distributed hydrologic models depend to a large extent on high-quality estimation of the parameters that describe the hydraulic behaviour of each soil type existing within the simulated region (Nützmann et al., 2005). This may be due to the fact that soil hydraulic properties and their inherent spatial variability greatly influence the exchange of water fluxes between the different components of the soil-plant-atmosphere system. However, it is well known that the conventional determination (direct measurement) of soil hydraulic parameters, especially for regional simulations, is time-consuming and very expensive. Alternatively, to achieve this task (parameterization of soil hydraulic properties) in a short time and in a cost-effective manner, pedotransfer functions (*PTFs*) can be used (McBratney et al., 2002; Wösten et al., 1999). PTFs are usually regarded as useful tools to estimate difficult-to-measure soil hydraulic parameters from easily measurable or already available soil properties. Several studies (e.g., Brakensiek and Rawls 1994; Pachepsky et al. 2003) have used such functions to generate the required input parameters for soil hydrological models from basic soil properties, which are usually collected during the course of the soil survey such as particle-size distribution, organic matter contents, and bulk density. However, pedotransfer functions should be used with caution, since they often exhibit high prediction errors due to their simplifying nature. Therefore, they have to be carefully chosen with respect to the existing data, the required accuracy, the wanted hydraulic parameters and the geographical area (Pachepsky and Rawls, 2004).

In this study, however, the pedotransfer functions of Rawls and Brakensiek (1989) were chosen to predict the water retention parameters *bubbling pressure head* and *pore-size distribution index* of the Brooks and Corey model (Brooks and Corey 1964). In contrast to other PTFs that mostly have been developed using datasets that are representative of a specific region or a small area, Rawls and Brakensiek (1989) PTFs have been developed from a very wide variety of soil samples (Rawls and Brakensiek, 1989). Consequently, they are expected to provide a relatively good accuracy in estimating the soil water retention parameters of the study area. Estimating the saturated hydraulic conductivity, on the other hand, was done by using the regression equation of Wösten et al. (1999). This equation is highly recommended by Wagner et al., (2001), as one of the best PTFs to estimate this hydraulic parameter. Finally, regarding the soil parameterization accuracy, it should be mentioned that the validation of soil parameterization at a point scale does not make sense when the soil model is applied at a catchment scale. Indirectly, however, a good agreement between simulated and observed runoff, as well as a realistic simulation of the regional scale plant available water content, could to some extent be considered as an indication of acceptable soil parameterization accuracy.

In the following sections I will present the pedotransfer functions used to achieve the hydraulic parameterization of the soil types existing within the study basin.

7.6.1. Bubbling pressure head (h_b)

Bubbling pressure head (also called *air entry tension*) denotes the value of the suction head at which gas is first drawn through the soil sample during the dewatering process (Eagleson, 1978). However, *Bubbling pressure head (cm)*, as mentioned above, was estimated by using the pedotransfer function proposed by Rawls and Brakensiek (1989), which is fully based on the basic soil properties, namely *clay content* [%], *sand content* [%], and *porosity* θ_s [volumetric fraction].

$$h_b = \exp (5.3396738 + 0.1845038 * clay - 2.48394546 * \theta_s - 0.00213853 * clay^2 - 0.04356349 * sand * \theta_s - 0.61745089 * clay * \theta_s + 0.00143598 * sand^2 * \theta^2 - 0.00855375 * clay^2 * \theta^2 - 0.00001282 * sand^2 * clay + 0.00895359 * clay^2 * \theta_s - 0.00072472 * sand^2 * \theta_s + 0.0000054 * clay^2 * sand + 0.5002806 * \theta_s^2 * clay)$$

7.6.2. Pore size distribution index (λ)

The other hydraulic input parameter, which also needs to be identified, is the *pore size distribution index*. This parameter is usually defined as a dimensionless number characterizing the width of the pore-size distribution (or the steepness of the retention function) in porous medium (Wakeman et al., 1999). An empirical equation developed by Rawls and Brakensiek (1989) was used to compute this index for soils of the study region as following:

$$\lambda = \exp (-0.7842831 + 0.0177544 * sand - 1.062498 * \theta_s - 0.00005304 * sand^2 - 0.00273493 * clay^2 + 1.11134946 * \theta_s^2 - 0.03088295 * sand * \theta_s - 0.00026587 * sand^2 * \theta_s^2 - 0.00610522 * clay^2 * \theta_s^2 - 0.00000235 * sand^2 * clay + 0.00798746 * clay^2 * \theta_s - 0.00674491 * \theta_s^2 * clay)$$

7.6.3. Effective porosity (n)

Effective porosity is defined as the ratio of the volume of interconnected pore spaces to the total volume of material (soil), expressed as a percentage (Bear, 1988). It accounts for the fact that pore spaces that are not connected, or are very tiny for water to overcome the force of capillary attraction, do not participate in water flow through the soil. The difference between total porosity and effective porosity is largely manifest in clay, where total porosity is very high, and effective porosity is very low (Jacobs et al., 2001; Weiner, 2000). The value of effective porosity was estimated for each soil type (and each soil layer) as the difference between the saturated (θ_s) and residual volumetric water content (θ_r). The pedotransfer function of Rawls and Brakensiek (1989) was employed to calculate θ_r as following:

$$\theta_r = - 0.0182482 + 0.00087269 * sand + 0.00513488 * clay + 0.02939286 * \theta_s - 0.00015395 * clay^2 - 0.0010827 * sand * \theta_s - 0.00018233 * clay^2 * \theta_s^2 + 0.00030703 * clay^2 * \theta_s - 0.0023584 * \theta_s^2 * clay$$

7.6.4. Saturated hydraulic conductivity (K_s)

Saturated hydraulic conductivity (also called *permeability*) is frequently defined as a key input parameter for many soil water and hydrological simulation models. It reflects how fast the water can flow through the soil (Pachepsky and Rawls, 2004). However, for the purpose of estimating this parameter for each soil type (and each soil layer) found within the study area, the regression equation of Wösten et al (1999) was used. This equation is founded on some fundamental soil characteristics, namely *silt content* [%], *clay content* [%], bulk density (D) in [g/cm^3], organic material (OM) in *weight percent*, and *topsoil*. Thus, K_s [m/s] can be expressed as following:

$$K_s = 0.000000115741 * \exp(x)$$

Where:

$$x = 7.755 + 0.0352 * \text{silt} + 0.93 * \text{topsoil} - 0.967 * D^2 - 0.000484 * \text{clay}^2 - 0.000322 * \text{silt}^2 - 0.001/\text{silt} - 0.0748 /OM - 0.643 * \text{LN}(\text{silt}) - 0.01398 * D * \text{clay} - 0.1673 * D * OM + 0.02986 * \text{topsoil} * \text{clay} - 0.03305 * \text{topsoil} * \text{silt}$$

Topsoil: is a parameter that is set to **1** for topsoils and to **0** for subsoils. Consequently, the hydraulic conductivity can be distinguished depending on the soil horizon (or layer depth).

Furthermore, the volumetric coarse fragments (>2mm in size) in the soil (VCF) were also taken into consideration for the final parameterisation of K_s . A correction factor developed by Brakensiek et al., (1986) was used to account for the presence of coarse material in each soil type. This correction factor is given by the following formula:

$$\text{Coarse Fragment Correction} = (100 - VCF) / 100$$

The saturated hydraulic conductivity of each soil was then multiplied by this correction factor to provide the final parameterized K_s value required by the hydrological model PROMET. It may be useful to mention here that a good agreement between the simulated and measured runoff was achieved in this study (see Chapter 9). This good agreement could to some extent be considered as evidence of a good parameterization of the soil's saturated hydraulic conductivity, which is believed to be the key parameter for the simulation of infiltration and lateral runoff generation (Bowles and O'Connel, 1991).

Finally, it should be mentioned that all soil input parameters required by the model PROMET are considered as time independent data (static data). Values of these parameters were stored in tabular format (ASCII input file) in such a way that soil properties of each soil type can be assigned to their corresponding spatially-distributed information (to the relevant soil category on the soil-types map). Appendix 25 lists the estimated values of the hydraulic parameters for each soil type found within the study area, as derived from basic soil characteristics using the above mentioned pedotransfer functions.

8. Estimation of vegetation parameters for hydrological modelling

8.1. Introduction

According to several authors (e.g., Caroline and Raffy, 1997; Nemani and Running, 1989), the vegetation cover acts as an interface between soil and atmosphere. Its existence, its spatial distribution and its architecture play an important role in energy and matter exchanges. It strongly affects the water balance by shading the earth surface and inhibiting the soil evaporation on one side, and by contributing greatly to the atmospheric water vapour content through plant transpiration on the other. However, for modelling the water balance of the study area with the model PROMET, a set of plant parameters is needed to describe the phenological development stages for each plant species, as well as to describe the reaction of plant species towards the affecting environmental factors such as air temperature, air humidity, photosynthetic active radiation, and soil moisture.

In this chapter, I will provide an overview of the estimation of the plant physical and physiological parameters for each vegetation category recognized in the study basin using information derived either from satellite images (e.g., LANDSAT ETM+7) or from literature (e.g., Körner, 1994; Kelliher et al., 1995; Baldocchi et al., 1987; Torrecillas et al., 1988; FAO ECOCROP database). I begin by briefly discussing the basics of landsurface evapotranspiration.

8.2. Basics of evapotranspiration

Evapotranspiration can be defined as a process by which water is returned to the atmosphere in its gaseous state (Gerard, 1998). It is composed of evaporation from open water surfaces, bare soil surfaces, water intercepted by vegetation canopy, in addition to transpiration of the plants through leaf stomata. It is an essential hydrological process that affects the water balance of the catchment. Especially in arid and semi-arid region, which are typically affected by water stress and water scarcity, evapotranspiration consumes about 80 -95% of the long term rainfall (Pilgrim et al., 1988). According to several authors (Allen, 2005; Monteith and Unsworth, 2008; Kirkham, 2005; Pilgrim et al., 1988), the process of evaporation is governed by several meteorological factors (net radiation, air temperature, humidity and wind speed), the nature of the evaporating surface, and water availability. On the other hand, the amount and rate of transpiration, the process by which plants lose water by evaporation into the atmosphere, relies on the type of vegetation and their stage of growth, season of the year, time of the day, the moisture availability in the root zone plus the same meteorological variables that influence evaporation. Because it is not always easy to separately quantify evaporation and transpiration, they are commonly combined into one term called evapotranspiration (*ET*) (Hudak, 2005).

Potential evapotranspiration (*ET_p*) is the *ET* that would take place from surfaces or vegetation canopies if there were no limitation on the supply of water. Actual evapotranspiration (*ET_a*) usually falls below this potential level as the soil dries out

under the predominant meteorological conditions and the availability of water (Weiss, 2009; Hoekstra and Shachak, 1999). Assessments of potential evapotranspiration in arid and semi-arid climates are far greater than the rainfall depth. Subsequently, the actual evapotranspiration rates are much smaller than the potential rates due to the limited quantity of water (moisture) stored in the soil (Stephenson et al., 2004).

A large number of measurements of ETa over various land-cover types and climatic conditions at the point scale have revealed the large complexity and variety of the evapotranspiration process. On the basis of these observations, several physically based SVAT models (Soil Vegetation Atmosphere Transfer) were developed to estimate evapotranspiration at different levels of complexity, and for homogeneous surfaces at the point scale (Shuttleworth and Wallace, 1985; Raupach, 1995; Meyers and Tha Paw, 1986). A review of the relevant literature shows that the various approaches available for estimating the evapotranspiration range from data-intensive physical methods such as the Penman-Monteith equation (Monteith, 1965), which can be considered the most widely used approach applied in hydrological modelling, to the less data-demanding empirical methods such as the HAUDE formula (Haude, 1955). Most of the empirical methods, however, are developed for particular climate zones and therefore should not be applied to conditions different from the ones they are developed for.

8.3. The plant parameters required to run the *vegetation-component* of PROMET

As mentioned earlier in Chapter 3, the vegetation sub-component of Penman-Monteith equation, which does not model the growth of vegetation, was used to simulate the evapotranspiration in the study area. Therefore, temporal course of vegetation properties is required during model initialization for each vegetation class distinguished on the related spatially distributed landuse map. In this model, the plant growth is represented through the temporal evolution of the following plant parameters:

- Albedo (daily) [%]
- Leaf Area Index (daily) [m^2/m^2]
- Plant height and root depth (daily) [m]

Values of these dynamic plant parameters (as will be described in section 6.4.3) are provided in tabular format (in separate files) as a function of DOY (Day-of-Year).

On the other hand, PROMET also requires a set of other plant physiological properties which are introduced as static (time-invariant) parameters, including:

- The plant-specific minimum stomatal resistance, r_s [$s.m^{-1}$]
- The slope parameter of the stomatal resistance with irradiance, b_{rs} [W/m^2]
- The threshold value of leaf water potential (soil suction), ψ_0 [MPa]
- Cardinal temperatures (T_{max} , T_{min} and T_{opt}) [$^{\circ}C$]

I begin with discussing the time-invariant plant physiological parameters.

8.3.1. Plant physiological parameters which are assumed to be static

8.3.1.1. The plant-specific minimum stomatal resistance, r_s [$\text{s}\cdot\text{m}^{-1}$]

Stomata control the flow of water vapour, carbon dioxide, oxygen and other gases across the surface of the leaf (Roberts, 1986). The degree of stomatal opening, expressed as the diffusive conductance of leaves for water vapour (g), is governed by physiological processes, which in turn react to environmental conditions such as photosynthetically active radiation, air temperature, leaf water potential, and vapour pressure deficit (Kelliher et al., 1995; Baldocchi et al., 1987). The maximum rate of water vapour loss of vegetation for any given meteorological condition is determined by the maximum stomatal conductance of leaves (the inverse of minimum stomatal resistance), and the total amount of leaf area per unit of land area (Leaf Area Index). Körner (1994) stated that at any given leaf stomatal resistance, the moisture deficit of the atmosphere and the aerodynamic resistance in and above the plant canopy significantly affect the transpiration rates. The latter factors are deeply influenced by the geometry and density of the plant canopy. Thus, in order to predict transpiration from canopies, not only the leaf minimum stomatal resistance, but also LAI, are required. Körner (1994) has published a very valuable and comprehensive survey of the plant physiological data in the form of average values of maximum stomatal conductance (g_{max}) for more than 20 principal vegetation types covering about 200 species and several hundreds of individual research studies. Thanks to a number of intensive surveys in South America, Africa, Australia and the Mediterranean region, a fairly good data set for vegetations from arid, semi-arid and dry sub-humid environments is available.

All values for stomatal conductance ($1/r_s$) are presented as molar flux values ($\text{mmol m}^{-2} \text{s}^{-1}$). However, in order to make these values compatible with the requirements of the used vegetation sub-component of the model PROMET, as well as for the sake of comparison with other related studies, they were converted in a first step into velocity values (m s^{-1}). In the second step, the average values of maximum stomatal conductance (m s^{-1}) were converted into average values of minimum stomatal resistance ($\text{s}\cdot\text{m}^{-1}$). The inter-conversion of conductance from [$\text{mmol m}^{-2} \text{s}^{-1}$] to [m s^{-1}] was set to 20°C and atmospheric pressure of 1000hPa. Under these circumstances, the conversion factor is equal to 41000 (Körner, 1994; Jones, 1992).

However, in the words of Körner (1994), there is little, if any, difference in maximum stomatal conductance for the major biomes of the world. The global average value of g_{max} for the most significant groups of woody vegetation is $218 \pm 24 \text{ mmol m}^{-2} \text{ s}^{-1}$ (corresponds to a minimum stomatal resistance of $188 \text{ s}\cdot\text{m}^{-1}$), for semi-arid shrubs an average value of $198 \text{ mmol m}^{-2} \text{ s}^{-1}$ ($\sim 207 \text{ s}\cdot\text{m}^{-1}$) was given. However, from all of the vegetation types covered by Körner (1994), only those types for which it may be possible to correlate with the vegetation categories of the study area were chosen and listed together with their respective stomatal conductance / resistance values (see Appendix 26).

In addition to that, Kelliher et al., (1995) compared individual data sets of the maximum stomatal conductance (g_{\max} , for single leaf) and bulk surface conductance (G_{\max} , for a vegetated surface encompassing the plant canopy and soil) for evapotranspiration. The data sets were carefully chosen to cover most major vegetation types and a broad range of leaf area index (LAI). However, while g_{\max} is commonly determined from the measurement of evaporation and vapour pressure deficit for a leaf put in a ventilated chamber (porometry), G_{\max} is calculated in fact by measuring evaporation and its driving meteorological variables above vegetation canopy, and then inverting the Penman-Monteith equation (Baird, 1999; Valentini, 2003). According to Kelliher et al., (1995), the major biomes of the globe can be further aggregated into three super-classes: (1) woody vegetation, (2) natural herbaceous and (3) agricultural crop plants. Average values of minimum stomatal resistance r_s (at leaf-scale) and R_s (at canopy-scale) derived by inversion of stomatal conductance (g_{\max} and G_{\max} , respectively) of the three above mentioned super-classes are listed in Appendix 27.

Furthermore, Kelliher et al., (1995) concluded that there is a remarkable consistency between the observed r_s and R_s . This consistency comes from the compensating effects of declining canopy conductance (increasing canopy resistance) and increasing soil evaporation as the leaf area index (LAI) declines. This conclusion could provide an acceptable basis for estimating the value of R_s from knowledge of r_s and LAI alone. At high leaf area indices (> 3), the ratio r_s / R_s is approximately 3.

Appendix 28 lists the minimum values of canopy resistance (R_s) for some types of agricultural crops (at different values of LAI in the case of wheat), as presented by Kelliher et al., (1995).

Finally, concerning the parameterization of the vegetation types existing within the study region, values of the plant-specific minimum stomatal resistance were estimated based on correlations with the outcomes of the above mentioned literature studies (see Appendix 29).

8.3.1.2. The slope parameter of the stomatal resistance with irradiance, b_{rs} [W/m^2]

For most types of vegetation, stomata openings increase with increasing amount of photosynthetically active radiation incident on a leaf; thus, this decreases the stomatal resistance (Teh, 2006). Values of the slope parameter of the stomatal resistance with irradiance (b_{rs}), which is defined as a plant specific constant equal to the amount of PAR at which stomatal resistance is twice its minimum, were roughly estimated for each vegetation type (see Appendix 29) based on the limited available literature (e.g., Baldocchi et al., 1987; Ojima and Svensson, 1992). However, based on a fairly extensive sensitivity analysis of the model PROMET for the plant physiological parameters, changing the value of slope parameter (b_{rs}) has shown a relatively small influence on the transpiration rate in comparison with the other

required vegetation parameters (Taschner, 1997). Appendix 30 lists the values of this plant specific parameter (in W/m^2) for some plant species, as reported in literature. Additionally, according to Ojima and Svensson (1992), a slope parameter value of $25W/m^2$ and $40W/m^2$ were assigned to the land cover type “forest” and “agricultural land”, respectively.

8.3.1.3. The threshold value of leaf water potential (soil suction), Ψ_0 [MPa]

According to several authors (e.g., Rajan, 2002; Solomon and Shugart, 1993), the status of water in soils, vegetations, and the atmosphere is usually expressed in terms of water potential (Ψ) [i.e., the potential energy of water in a particular element of the system, in relation to the potential energy of free water at the same temperature and atmospheric pressure; it is commonly measured in units of pressure (MPa)]. By definition, pure water at temperature of $20^\circ C$ and at atmospheric pressure (0.1 MPa) has a water potential of 0 MPa (Lambers et al., 2008). However, it's well known that the movement of water from the soil through the plant to the atmosphere behaves as a continuum and should be considered as a whole in the modelling of transpiration process. Furthermore, Chapin et al., (2002) stated that the low partial pressure of water vapour in air compared with that inside the leaves is the main driving force for water loss from leaves, which in turn drives water movement along a pressure gradient from the roots to the leaves, which consecutively drives water transport from the soil into the roots. In other words, in order for water to move from the soil into the plant, the suction in the plant (the diffusion pressure deficit) should be higher than the soil suction (Hillel, 1998).

However, as mentioned earlier in chapter 3 (see Eq.3.6), leaf water potential has no influence on stomatal resistance until a threshold value (Ψ_0) is reached at which stomatal closure takes place (Baldochi et al.,1987; Roy et al., 1995). Several studies (e.g.,Tyree and Sperry, 1989) have reported that this threshold value is a species-specific parameter. Nevertheless, field work conducted in the 1970's has revealed that there is no unique leaf water potential producing stomatal closure. Begg and Turner (1976) proved that this threshold value differs with location of the leaf in the canopy, age of the plant, and growth circumstances.

However, for modelling the evapotranspiration processes with the model PROMET, a threshold value of leaf water potential (measured in MPa) is required for each vegetation type presented in the study area. These values (see Appendix 29) were also coarsely estimated due to the limited literature available, especially for species of arid and semi-arid regions which are usually drought-adapted and have much lower leaf potential threshold value than the well-watered species (Sperry, 2000). Some of those (plant-specific) threshold values of leaf water potential reported in literature for some plant species are listed in Appendix 31.

8.3.1.4 Cardinal temperatures (T_{max} , T_{min} and T_{opt}) [°C]

It is well known that temperature is a crucial factor that influences most biological processes in plants, including transpiration, respiration, photosynthesis, and plant growth. In addition, temperature affects all stages of plant development, beginning with germination and ending with flowering and grain-filling (Reddy and Hodges, 2000). By definition, cardinal temperatures refer to the minimum cold (T_{min} , below which development ceases), maximum hot (T_{max} , above which development ceases), and optimum (T_{opt}) temperatures for the stages of development of each plant species (Somani, 1989; Chang, 2009). These cardinal temperatures vary among different species and among different stages of development of the same species (Hodges, 1991).

However, concerning the influence of temperature on stomatal opening, the stomatal resistance, as indicated previously in Chapter 3 (see Eq. 3.4), reaches its minimum value $r_{S(min)}$ at the optimum temperature (T_{opt}) and increases symmetrically with both increasing and decreasing temperature (Jarvis, 1976 ;Schädlich, 1998).

According to Chang (2009), the estimated values of cardinal temperatures for nearly all plant species are known. For example, for cool-season crops, such as oats, rye, wheat and barley, the cardinal temperatures are all relatively low ($MIN=0-5^{\circ}C$, $OPT=25-31^{\circ}C$, and $MAX=31-37^{\circ}C$). Whereas, for hot-season crops, such as sorghums, these temperatures are larger ($MIN=15-18^{\circ}C$, $OPT=31-37^{\circ}C$, and $MAX=44-50^{\circ}C$). However, for the most plant species of the study area, values of cardinal temperatures were taken from the FAO ECOCROP database which provides good information on arable crops, grasses, trees and other plant species with economic uses. Appendix 32 presents the cardinal temperatures for some plant species existing in the study region as reported in the above mentioned database. These temperatures, which vary among plant species, can be generalized for plant types as presented in Appendix 29.

Finally, regarding the approximate values of the physiological parameters which were estimated for each vegetation type existing with the study area, the following facts should be considered:

- The assignment of the plant physiological parameters (estimated from literature correlations) to their respective vegetation categories (land use/land cover map) represents a significant regionalization step. This is due to the fact that values of physiological parameters (usually measured in laboratory) for a given individual plant species were used to be representative for an association of similarly reacting plant species (vegetation type).
- A number of simplifying assumptions were made implicitly during the estimation of some plant physiological parameter values for some existing vegetation categories. This is because not all the required parameter values are fully documented in the available literature for all land use/land cover categories.

8.3.2. The plant parameters required to describe the temporal evolution of vegetation

While landuse information is supplied on a spatially distributed basis and is supposed to be invariant during the course of the simulation, the development of the different landuse types over the year (represented through the temporal evolution of the plant height, Albedo, LAI and root depth) is supplied in tabular format and daily increment.

8.3.2.1. Albedo (daily) [%]

Albedo of the land surface (defined as the ratio of the reflected to incident solar radiation) is an important factor affecting the net radiation of the surface, which in turn represents the main source of the energy exchange governing the evapotranspiration process (Peixoto and Oort, 1992). Albedo of a given surface varies diurnally and seasonally due to the variation in the angle at which the sun's rays strike the earth's surface (Ernst, 2000; Park, 2001). In addition to the sun angle, albedo is also largely influenced by many surface characteristics, including the type and condition of the vegetation cover, the snow cover and the soil moisture content (Berger et al., 1989). For example, concerning the effect of vegetation cover, forest vegetation with multilevel canopy (complex canopy) traps more radiation, and thus has a low albedo. Chapin et al., (2002) stated that albedo of dense vegetation is determined by the characteristics of the dominant plant types, with an albedo value decreasing from grasses (0.16-0.26) to deciduous shrubs and trees (0.15-0.20) to conifer (0.05-0.15). On the other hand, in regions with sparse vegetation, albedo is largely influenced by the variations in the soil moisture content that can cause a large change in the absorbance and reflectance properties of the soil. In general, the higher the soil moisture content, the darker the colour and lower the albedo of the soil (Lal, 2006). In the case of snow covered ground, albedo depends on the physical state, age, depth and contamination of the snow. Generally, the albedo of snow cover varies between 0.65 and 0.75 for old snow, and can reach as high as 0.75-0.90 for freshly fallen snow (Briggs and Smithson, 1986).

However, to estimate the mean albedo value (α) for each landuse/landcover class existing within the study area, satellite remote sensing data, that offer a convenient means for measuring and monitoring the surface albedo, were used. Five clear and cloud-free LANDSAT-7 ETM+ images, acquired in different seasons (autumn, winter, spring, early- and mid-summer), were used to estimate the mean albedo value for each landuse category. It should be mentioned here, however, that the spatial distribution of the land use categories is assumed to be time-invariant during the entire simulation period (15-years). Accordingly, satellite images acquired during different seasons and even during different years can legitimately be used to estimate the variations in the value of the albedo and LAI throughout the year.

In contrast to the images acquired during the spring and summer seasons, the LANDSAT images acquired during the winter and autumn seasons exhibit deep influence of illumination effects because of the relatively low incidence angle of the

sun (sun-elevation) at this time of the year. Further information on these satellite images, including the illumination geometries is listed in Table 8.1.

Table 8.1 lists the acquisition dates of the LANDSAT-7 ETM+ images used for estimating the albedo value for each land use class, along with the solar altitude, azimuth angles, and the Sun-Earth distance.

Season	Acquisition date	DOY	Sun-azimuth (degree)	Sun-elevation (degree)	Sun-Earth distance (Astronomical units)
Winter	08.03.2002	67	140.85	44.08	0.99260
Spring	21.05.2000	142	116.93	66.08	1.01230
Early summer	22.06.2000	174	108.50	66.72	1.01557
Mid summer	07.08.1999	219	120.69	62.15	1.01414
Autumn	06.11.2000	311	155.78	37.18	0.99102

The Landsat imagery acquired during the spring period (21st of May) was previously used for the purpose of Land use/Land cover classification. It was rectified (geo-referenced) to the Universal Transverse Mercator (UTM, zone-36) map projection and the world geodetic system 1984 (WGS 84), as described in a former chapter (see Chapter 4, Section 4.2.3). The four other images were registered as image to image to the above mentioned geo-referenced image (RMSE less than 0.5 pixel) in order to compare the albedo value estimated for each pixel of the five satellite images acquired at different seasons of the year.

Visual analysis of these images revealed that there is an absence of atmospheric haze and clouds, whose existence represents the primary impediment to the use of remote sensing data for the derivation of land surface parameters. The study region is generally known to have very little aerosol and atmospheric water vapour, especially during the summer months. This was also supported by meteorological observations recorded at the available climate stations at the same time of the acquisition date of each image. On the other hand, raw digital numbers (DN) for each spectral band of each LANDSAT image were converted into spectral reflectance using the software, ERDAS IMAGINE 9.3. This conversion process is essential to correct for (normalize) the illumination effects as a function of the variation in the incidence angle of the Sun's rays, guaranteeing that the measured value of the spectral reflectance is independent of the direction from which it approaches to sensor (Sahu, 2007; Wulder and Franklin, 2007).

In a first step, the digital numbers (DN) were converted to spectral calibrated radiance (L) using a conversion formula provided by Markham and Barker (1986), as follows (Eq.8.1):

$$L_i = G_i * DN + B_i \quad (\text{Eq.8.1}):$$

Where G_i and B_i are LANDSAT ETM+ sensor gain and bias for band i , respectively.

The gain and bias values for each spectral band (the coefficients of Eq.8.1) were computed from the lower (L_{min}) and upper (L_{max}) limits of the post-calibration spectral radiance range by using the following formula (Eq. 8.2):

$$G_i = (L_{i(max)} - L_{i(min)})/255 \quad \text{and} \quad B_i = L_{i(min)} \quad (\text{Eq. 8.2})$$

The values of the L_{min} and L_{max} for each spectral band were obtained from the metadata file (MTL-extension) provided with each LANDSAT image, as presented in Appendix 33.

In the second step, the spectral calibrated radiance values (L) for each individual band were converted to spectral reflectance values (ρ) using the following equation (Huang et al., 2002):

$$\rho_i = \frac{\pi \cdot L_i \cdot d^2}{E_i \cdot \sin(\theta)} \quad (\text{Eq. 8.3})$$

Where

ρ_i is the at-satellite reflectance for band i (unitless)

E_i is the solar constant for band i

θ is the Sun elevation angle in degrees

d is the Sun-Earth distance in astronomical units

L_i is the spectral radiance for band i computed as described above.

It should be mentioned here that this equation is sometimes given in literature with the “*cosine*” of the “*solar zenith angle*”. This is due to the fact that the cosine of solar zenith angle is equal to the sine of the solar elevation angle (Bonan, 2002).

After the conversion from digital numbers (DN) to reflectance values, the resulting new images were processed to provide albedo-maps for the study area at different seasons (autumn, winter, spring, early and mid-summer) using the approach proposed by Gratton et al., (1993). According to this approach, the albedo value can be calculated from the knowledge of the general reflectance pattern of the landcover, even the fact that the Landsat ETM+ bands cover only part of this spectrum. Weighted functions of the LANDSAT ETM+ bands 2, 4, and 7, presented in table 8.2, were utilized to compute the albedo values for the different types of land surface.

Table 8.2 the land cover dependent weighted functions proposed by Gratton et al., (1993) to derive the albedo values (α) from the calculated reflectance values of the LANDSAT ETM+ bands.

Land cover type	Function used to derive albedo from LANDSAT ETM+ bands
Bare ground	$\alpha = 0.493 \text{ (ETM2)} + 0.507 \text{ (ETM4)}$
Vegetated surfaces	$\alpha = 0.493 \text{ (ETM2)} + 0.353 \text{ (ETM4)} + 0.154 \text{ (ETM7)}$

The Land use/Land cover map, which was derived from classification of the LANDSAT image acquired on May 21st 2000, was used to determine the suitable function to be applied to each pixel, as well as to calculate the mean albedo value for each individual land use/land cover category. As an example of this calculation, Figure 8.1 shows the spatial distribution of the land use category “Settlements” draped over the Albedo map derived from the spring Landsat image (21.05.2000) in order to estimate the mean albedo value (α) for this category at this time of the year. This process was repeated five times for each individual land use/land cover type existing within the study area to calculate the variations in mean albedo value (α) throughout the different seasons of the year, as presented in Table 8.3.

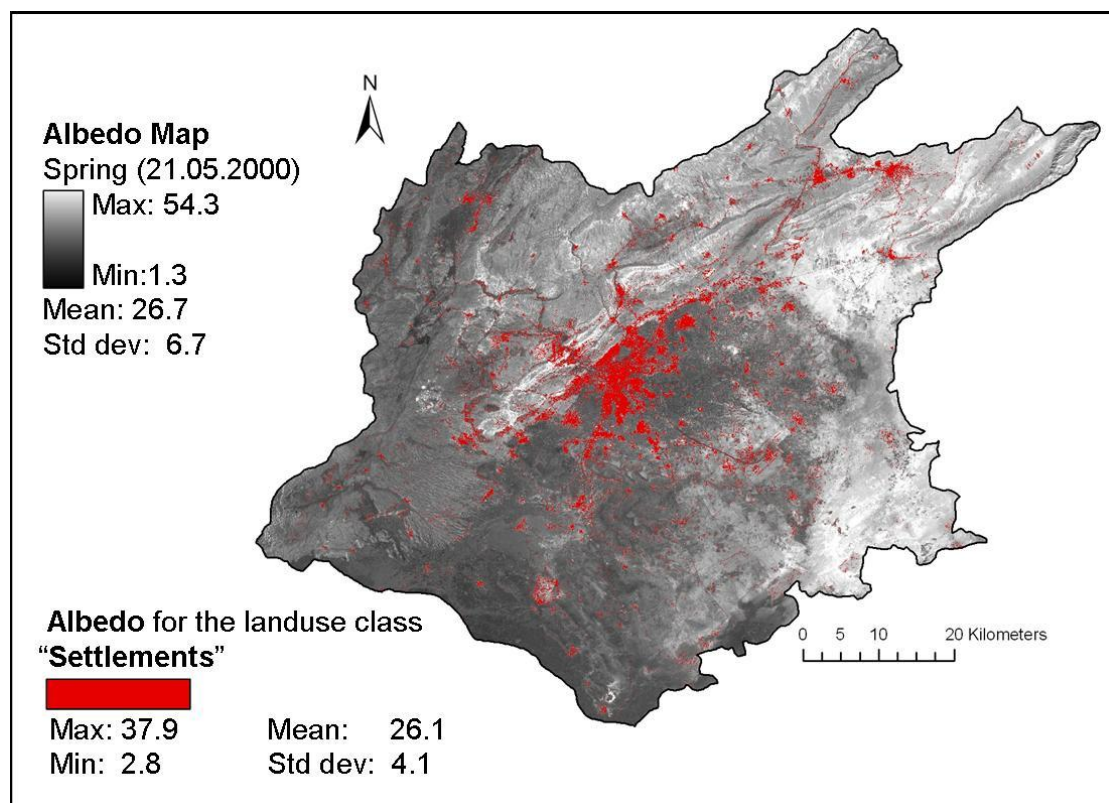


Figure 8.1 shows the albedo map resulted from the reflectance values of the spring Landsat image, together with the spatial distribution of the “Settlements” class draped over it to serve as an illustrative example for the calculation of the mean albedo value for each individual land use/land cover category.

Table 8.3 the mean albedo values (α %) estimated for each individual land use/land cover category of the study area, as derived from five LANDSAT images acquired during different seasons of the year.

Landuse/Landcover class	Winter 08.03.2002		Spring 21.05.2000		Early summer 22.06.2000		Mid summer 07.08.1999		Autumn 06.11.2000	
	α %	Std	α %	Std	α %	Std	α %	Std	α %	Std
Orchards (Olive dominated)	18.1	5.3	19.6	3.0	20.6	3.6	20.8	4.3	20.6	5.3
Mixed Fruit orchards (Apricot & plum dominated)	19.9	5.9	21.3	5.0	22.2	4.8	21.8	5.0	22.5	5.6
Mixed Farms (Vegetables & forage)	21.9	4.9	24.3	5.0	24.8	4.9	23.9	5.1	25.4	4.8
Cropland (Cereals and Legumes)	21.2	6.2	23.3	5.0	23.4	5.3	22.7	5.3	24.7	4.8
Natural Pasture	22.9	3.9	25.4	4.0	25.6	4.2	24.7	4.5	26.5	4.6
Rangeland (Mixed Grass-Shrub)	22.5	6.0	23.9	4.0	24.3	3.7	23.6	3.7	25.1	5.5
Steppe (Sparse vegetation)	32.8	5.3	36.7	4.0	36.6	6.1	35.4	4.6	37.3	4.9
Settlements	21.9	4.7	26.1	4.0	26.3	4.7	25.0	5.1	26.9	5.5
Sedimentary Rocks	25.3	7.8	29.9	5.0	28.2	8.7	28.3	6.2	30.8	6.6
Igneous Rocks (Basalt)	18.3	3.0	21.0	3.0	21.5	2.8	21.3	3.2	21.9	4.1
Bare soil	28.8	7.9	32.7	7.0	32.0	8.7	30.7	6.8	33.0	7.6
Water	7.2	2.8	7.4	2.5	7.9	3.1	---	---	----	----
Average for the whole study area	24.0	7.7	26.7	6.7	26.8	7.6	26.0	6.8	27.1	7.8

Std: Standard Deviation

From these results it can be concluded that the temporal variability of the albedo values, which is believed to be attributed to the seasonal evolution of the vegetation cover as well as to the variations in soil moisture content, is relatively small. The average albedo value for the whole study area has been estimated to range between 24.0 (during the winter season) and 27.1 (during the autumn season).

Finally, mean albedo values for each individual land use/land cover category were interpolated in time between the acquisition dates of the Landsat images, and were provided in tabular format and daily increment.

8.3.2.2. Leaf Area Index (daily) [m^2/m^2]

Leaf Area Index (LAI) is defined as the total one-sided area of all leaves in the canopy per unit area of the ground, and is thus a non-dimensional quantity, even though units of m^2/m^2 are frequently reported, as an indication of its meaning (Newton, 2007; Packham et al., 1992). LAI is the most important vegetation parameter that significantly influences evapotranspiration, carbon and nutrient cycle, rainfall

interception and photosynthesis (Sellers et al., 1997; Fageria et al., 2006). The LAI values vary broadly among the different vegetation types and plant species, but values of 3-5 are common for many full-grown plants. For a given plant species, green LAI varies throughout the seasons depending on its phenology (stage of development) and usually arrives at its maximum before or at flowering (Allen et al., 1998). The traditional way of assessing LAI is to harvest vegetation in a particular region and measure all the one-sided leaf areas directly. This direct method is accurate but extremely labour intensive, time-consuming and involves destructive sampling. However, in recent years, numerous indirect in-situ methods have been developed to measure LAI using optical instruments such as LAI-2000 (Plant canopy Analyzer) and TRAC (Tracing Radiation and Architecture of Canopies) sensor (Schröder et al., 2008). Although these in-situ techniques can provide relatively accurate results, it is not practical to utilize them to monitor the spatial and temporal changes in LAI over large geographic regions. However, many studies have shown that satellite remote sensing data offer the only feasible alternative for the estimation and monitoring of LAI at regional scales (Ramsey et al., 2004; Badhwar et al., 1986; Caroline and Raffy, 1997). During the last three decades, several models have been developed for application to remotely sensed data depending on regression-based relationships between ground measured LAI and canopy spectral reflectances, commonly expressed in the form of spectral vegetation indices (SVIs). The most widely used SVI is the Normalized Difference Vegetation Index (NDVI), which can be calculated as mentioned in Chapter 4 (see Section 4.2.5). Several studies have revealed that NDVI is a good estimator of LAI and has been used to indirectly estimate LAI across diverse vegetation types in heterogeneous landscapes (Spanner et al., 1990; Caroline and Raffy, 1997; Fan et al., 2009; Propastin and Kappas, 2009; Xavier and Vettorazzi, 2004; Gonzalez-Sanpedro et al., 2008; Nemani et al., 1993). In addition, NDVI values can be correlated to a wide variety of vegetation parameters, including biomass, photosynthetic activity, amount of green cover and productivity (Sellers, 1987; Baret and Guyot, 1991). One of the advantages of NDVI is that it has less effect from sun angle and illumination (i.e., it minimizes topographic effects) and offers fairly reliable information about vegetation cover dynamics (Holben and Justice, 1981; Kuligowski et al., 2006; Baret and Guyot, 1991). NDVI values range between -1.0 and +1.0, where increasing positive values indicate increasing green vegetation and negative values represent surfaces free of vegetation such as water and bare soil (Wang et al., 2003).

However, the use of NDVI for generating LAI-maps of the study area requires a comparison between NDVI values and in-situ measurements of LAI to develop statistical relationships LAI-NDVI (regression models) to be applied at a regional scale. Moreover, due to the fact that the used model PROMET requires the temporal LAI curve for each vegetation type, field measurements of the same location should be repeatedly conducted throughout the year to observe the seasonal variations in

LAI (phenological development). Unfortunately, no field measurements of LAI are available in the study area to be correlated with the values of NDVI images. Therefore, a literature search was conducted to find regression models which can represent the situation in the study region as much as possible. It should be mentioned here that the canopy reflectance is a function of many variables that differ across spatial and temporal scales. As a result, the transferability of an empirical LAI-NDVI relationship to other areas may possibly be influenced by exogenous factors such as the geometry of observation, atmospheric effects, and background reflectance (Baret and Guyot, 1991; Turner et al., 1999). Therefore, caution should be exercised while selecting the appropriate LAI-NDVI relationship, so as to confine our attention to those models that have been developed for use in environmental conditions similar to those found in the study area.

However, according to several authors (e.g., Sellers, 1985; Pontailier et al., 2003), the use of NDVI for estimating LAI has a limitation in its applicability at high LAI values (greater than 3). This is mainly attributed to the fact that NDVI saturates as the vegetation density increases (canopy tends to be closed), and in this case NDVI is no longer sensitive to variations in the LAI. Consequently, a linear relationship between NDVI and LAI may not be the ideal regression function for estimating the values of LAI in dense canopies. Therefore, many studies (e.g., Spanner et al., 1990; Lu et al., 2004; Gowda et al., 2007; Richardson and Wiegand, 1992; Wiegand et al., 1992; Blackburn and Pitman, 1999; Ma et al., 2007; Caroline and Raffy, 1997) have proposed non-linear regression models such as power and exponential functions to give the best fit for LAI-NDVI relationships.

In view of the above discussion, a non-linear power regression function of the general form $LAI = a * NDVI^b$ has been chosen to estimate LAI for the vegetation types found in the study area at different dates. The coefficients **a** and **b** are empirical and depend to some extent on vegetation type (Turner et al., 1999). However, due to the lack of ground-based measurements of LAI for each individual vegetation type in the study region, values of these coefficients were roughly considered to be constant for all vegetation categories. The values of these two coefficients, as reported in the above mentioned studies, range from 3 to 9 for the coefficient **a**, and from 1.7 to 4 for the coefficient **b**. However, for the study area, the values of these coefficients were taken from the power regression function proposed by Gowda et al., (2007) for estimating LAI for major agricultural crops grown in semi-arid environment, as the following:

$$LAI = 8.7 * NDVI^{3.6} \quad (\text{Eq. 8.4})$$

The same five LANDSAT-7 ETM+ images, which were previously utilized for estimating the mean albedo value for each landuse class existing within the study area, were also used to derive the NDVI images at different dates throughout the year (autumn, winter, spring, early- and mid-summer). The resulting NDVI images, in turn, were used together with the Land use/Land cover map to roughly estimate the mean

LAI value for each individual vegetation type, as presented in Table 8.4. The estimated LAI values, however, are supposed to be associated with a relatively high level of uncertainty due to the lack of in-situ observations of LAI.

Table 8.4 the mean LAI values estimated for each individual vegetation type within the study region, as derived from the NDVI images which in turn were calculated from five LADNSAT images acquired at different seasons of the year.

Landuse/Landcover class (vegetation classes)	Winter		Spring		Early summer		Mid summer		Autumn	
	08.03.2002		21.05.2000		22.06.2000		07.08.1999		06.11.2000	
	LAI	Std	LAI	Std	LAI	Std	LAI	Std	LAI	Std
Orchards (Olive dominated)	2.1	1.2	2.6	1.1	2.3	1.2	2.1	1.0	1.7	0.8
Mixed Fruit Orchards (Apricot & plum dominated)	0.8	0.5	2.9	1.3	2.4	1.3	2.2	1.1	0.8	0.4
Mixed Farms (Vegetables & forage dominated)	1.3	1.2	1.7	0.7	1.5	0.8	1.2	0.7	0.4	0.3
Cropland (Cereals and Legumes)	1.3	0.6	1.2	0.3	0.9	0.3	0.5	0.3	0.1	0.2
Natural Pasture	1.2	0.5	1.0	0.4	0.9	0.6	0.8	0.6	0.2	0.3
Rangeland (Mixed Grass-Shrub)	0.7	0.3	1.2	0.3	1.0	0.4	0.8	0.5	0.2	0.2
Steppe (Sparse vegetation)	0.3	0.2	0.6	0.2	0.4	0.3	0.3	0.3	0.1	0.1

These resulting mean LAI values for each individual vegetation type were temporally interpolated (on a daily increment basis) between the acquisition dates of the Landsat images, taking into consideration the information available in the literature on the phenological development stages for some vegetation categories (or dominant plant species). The knowledge of the phenological phases of plant development is helpful in predicting the temporal course of the LAI over the growing season. This is due to the fact that each plant species develops following specific phenological stages. However, according to several authors (e.g., Jones, 1992; Dharani, 2006), the beginning and end of each phenological stage is governed by weather conditions (particularly temperature), crop variety, water availability and length of daylight (photoperiod).

According to the *FAO Irrigation and drainage paper-56* (Allen et al., 1998), the growth period can be divided into the following four distinct phases (development stages):

- *Initial stage*: it starts from planting date (or green-up date, in the case of perennial plants) to nearly 10% ground cover. During this stage, the leaf area index is small, and the evapotranspiration process is mostly in the form of soil evaporation.
- *Crop development stage*: it extends from 10% ground cover to effective full cover, which, for many plants, occurs at the beginning of flowering. During this period, the transpiration increasingly becomes the main process at the expense of evaporation from the soil surface. The LAI continues to increase until it comes close to its maximum value at the end of this stage.

- *Mid-season stage*: it extends from effective full cover (70% ground cover and higher) through the time of the start of maturity. For many plant species, LAI reaches its maximum value at the beginning of this stage.
- *Late season stage*: it extends from the start of maturity to harvest, crop death, frost-kill, or full senescence. During this stage, LAI decreases until it reaches its minimum value (zero, in the case of deciduous plants) at the end of this development phase.

Allen et al., (1998) have provided a very helpful and comprehensive database containing information on the general length (in days) for each of the above mentioned growth stages for more than 75 plant species growing in different climates and locations (latitudes). Many of those species are grown in the study region, comprising in some cases the dominant species for some vegetation types. The general length for each growth stage as well as the planting date (or green-up date) for some of those plant species distributed within the study region are selected from the above mentioned database (Allen et al., 1998) and are presented in Appendix 34. But it should be mentioned here that these data serve only as indicative for general conditions, since they may differ significantly from place to place with climate, elevation, planting date and crop variety.

Finally, a visual comparison of the spatial distribution between LAI- and Albedo-maps, as shown in Figure 8.2, reveals that these two parameters behave quite differently from each other. For example, areas with high plant density such as the “*Mixed Fruit Orchards*” exhibit a relatively high value on the (*spring*) map of LAI (with a mean value of $2.9 \text{ m}^2/\text{m}^2$), and a relatively low value on the Albedo map (with a mean value of 21%). Whereas, non-vegetated areas such as the “*Bare Soil*” which have a very low value of LAI (zero) show a comparatively high value of Albedo (up to 33%).

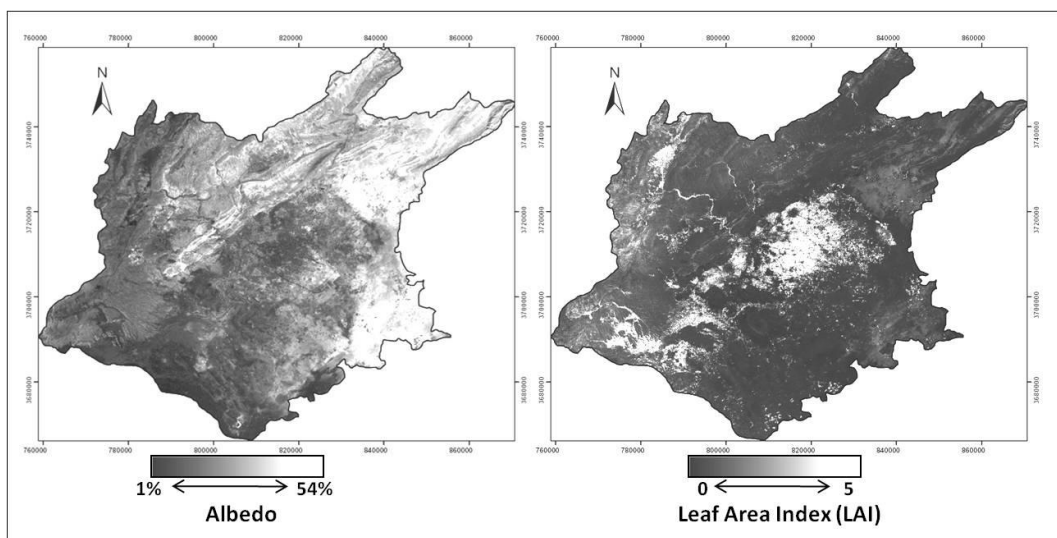


Figure 8.2 shows the spatial distribution of the Surface Albedo (%) and LAI (m^2/m^2) in the study area, as derived from the spring LANDSAT image (21.05.2000).

8.3.2.3. Plant height and root depth (daily) [m]

Plant height affects the aerodynamic resistance (r_a) of the Penman-Monteith equation (see Chapter 3, Eq.3.1) and the turbulent movement of water vapour and sensible heat from the vegetated land surfaces into the atmosphere (Baldocchi et al., 1987; Smith, 1980; Monteith and Unsworth, 2008). Several studies (e.g., Slabbers, 1977) emphasize the significance of taking plant roughness into consideration when calculating the evapotranspiration. In general, taller plants have a comparatively larger aerodynamic roughness, which in turn enhances their extraction of energy from the ambient air and increases the quantities of water evaporated by such plants (Rosenberg et al., 1983; El Nadi and Hudson, 1965). On the other hand, root depth is considered as an important vegetation parameter which determines the access of the plant to the soil water storage. In consequence, whether plant roots stretch to a particular soil horizon or not in the hydrological modelling may significantly modify the total water balance of the soil profile. It should also be mentioned that root depth is a highly uncertain factor since it is affected by a diversity of factors connected with plant-specific properties, soil texture and structure, and the conditions of the underlying bedrock.

Thus, for each vegetation type existing within the study area, daily courses of plant height and root depth were estimated based on the available information about the phenological development stages (Appendix 34) as well as the maximum plant height and the maximum root depth of its dominant plant species (see Appendix 35). The comprehensive database that was compiled by Allen et al., (1998) represents the main source of information.

9. Model Results

In this chapter, some of the results obtained by modelling the water and energy fluxes using the model PROMET will be presented, briefly discussed, and validated (in the case where validation data are available). Spatial model runs for the whole study area were carried out without calibration covering a simulation period of 15 years (from 01.01.1991 to 31.12.2005). All calculations were performed with a spatial resolution of 180 x180m and a time resolution of 1-hour. The reason of choosing this relatively short time interval (1-hour) is to meet the requirements of the nonlinearities in most land surface hydrological processes, especially the process of evapotranspiration. Hourly modelled results were then aggregated in time to daily, monthly, and annual values using different types of aggregation functions such as Average, Maximum, Minimum, and Sum. The use of GIS in the model PROMET allows the available data on land use, soil type, elevation and other factors to be used as spatially distributed input data. The driving meteorological fields were taken from measurements of the available weather stations and were temporally and spatially interpolated. Other input parameter required by the model such as the (static) soil and the (dynamic) plant parameters were provided in tabular format and assigned to their corresponding spatially distributed information.

The results of the model PROMET consist of both a particular collection of output parameters for some pixels that can be selected based on their respective coordinates during the model initialization, and of spatially distributed output maps for the entire study area or any given sub-basin, describing e.g., the runoff components, snow water equivalent, the spatially distributed meteorological variables, etc. Figure 9.1 serves as an example of some of the long-term spatially distributed results as calculated for a particular sub-basin within the study area using the model PROMET for the period from 1991 to 2005.

In order to validate the quality of the results obtained by the model PROMET, a comparison between modelled and measured data has to be accomplished. For example, in order to show the model's ability to simulate river discharge conditions in the study area, the modelled streamflow should be compared to the discharge records that were measured at the gauge stations of the respective river sub-basins. Unfortunately, not all parameters that are mapped by the model can be covered by a validation effort, especially when we are talking about the spatially distributed outcomes. Therefore, the validation process is carried out only for those model results that could be supported with measurement data. For other results that play an important role in simulating the various hydrological processes and are not supported by validation data, a relative analysis can be performed.

Remotely sensed data offer an opportunity to qualitatively validate some of the modelled spatially distributed results such as snow cover and evapotranspiration. These data, however, provide only snapshots –for LANDSAT images minimally at

repeat overpass period of 16 days if the sky is free of clouds- and thus they offer only an instantaneous assessment of the results at a given moment (the time of image acquisition).

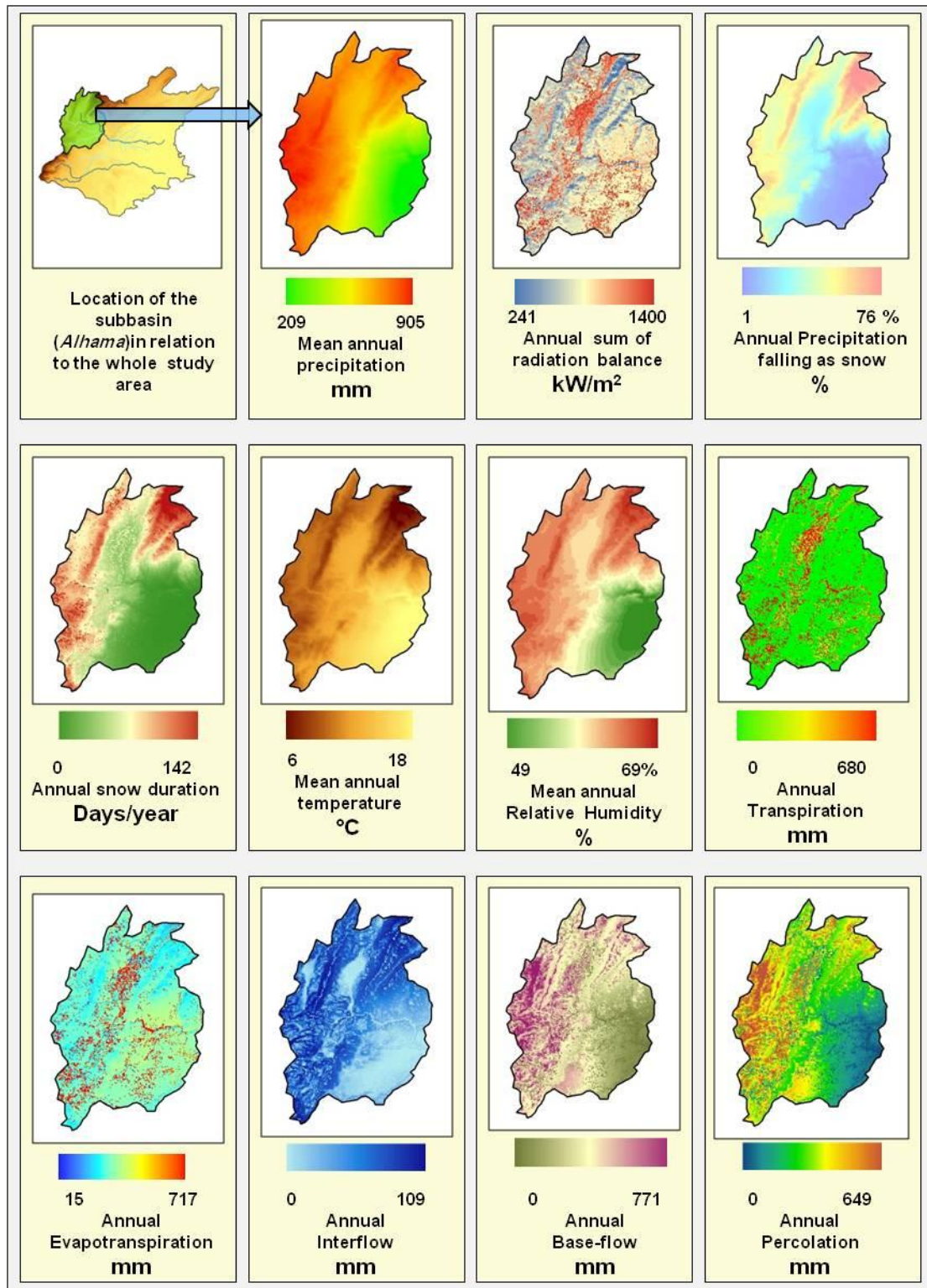


Figure 9.1 shows an example of some of the long-term (1991-2005) spatially distributed results as simulated for a specific subcatchment within the study area using the model PROMET.

In this chapter, however, I begin by presenting and discussing the spatially distributed meteorological parameters used to force the hydrological model PROMET. This is mainly due to the fact that a comprehensive knowledge of the quality related to the spatial distribution of the meteorological variables is very important for the later interpretation and analysis of the spatially distributed model results. The focus will be on the spatial distribution of precipitation, air temperature, snow cover and solar radiation, as these parameters are the most important factors determining most of the hydrological processes in the watersheds (Kotlarski et al., 2005).

9.1. The spatial distribution of the meteorological parameters in the study area

9.1.1. The spatial distribution of precipitation

According to the results of the spatial interpolation of precipitation for the period 1991-2005, the Anti-Lebanon mountain-range including Mount Hermon (2814 m.a.s.l) which is located in the western part of the basin is receiving the maximum value of mean annual precipitation with more than 800 mm/year. This value decreases dramatically eastward from the mountains into the plain of Damascus and reaches a value of about 200 mm/year at Damascus city center. The eastern part of the study area receives the lowest amount of annual precipitation (less than 100 mm / year). Figure 9.2 illustrates the spatial distribution of mean annual precipitation in the study area obtained by interpolation of point observations for the period 1991-2005. The mean annual precipitation over the entire study area was also estimated to be 277mm. As a result of this low value, it could be said that the catchment area is suffering from a shortage of renewable water resources.

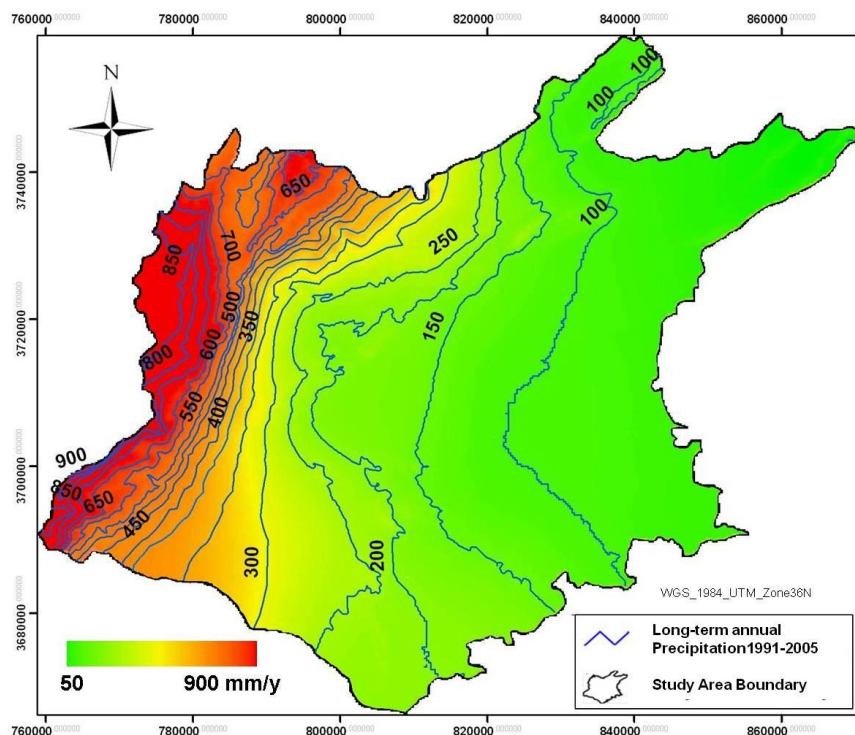


Figure 9.2 the spatial distribution of long-term mean annual precipitation in the study area derived by interpolation of station data for the period from 1991 to 2005.

Based on the above-presented map (the mean annual precipitation), the catchment can be classified according to a simple scheme adopted in arid and semi-arid environments into four climate types (FAO/ISRIC, 2001; McGinnies et al., 1968; Meigs, 1953). These four distinguished categories, as illustrated in Figure 9.3, are greatly influenced by elevation. The nomenclature for these four climate-zones, along with their respective range of mean annual precipitation as well as the predominant elevation, is expressed as the following:

- *The moderate-Precipitation (sub-humid) region:* this area is characterized by heavy rainfall in winter (more than 500 mm / year) and a moderate climate in summer. This region comprises the Anti-Lebanon Mountains at elevation above 1000m.
- *The semi-arid region:* the mean annual rainfall in this area varies between 250 and 500 mm. Its elevation ranges from 750 to 1000 m.
- *The arid region:* this region occupies the central part of the study area, including Damascus city, where the precipitation ranges from 100 to 250 mm. Elevations range from 650 to 750 m.
- *The desert region (hyper-arid):* this region receives very little precipitation (less than 100 mm/ year). It occupies the eastern part of the basin at elevation lower than 650m.

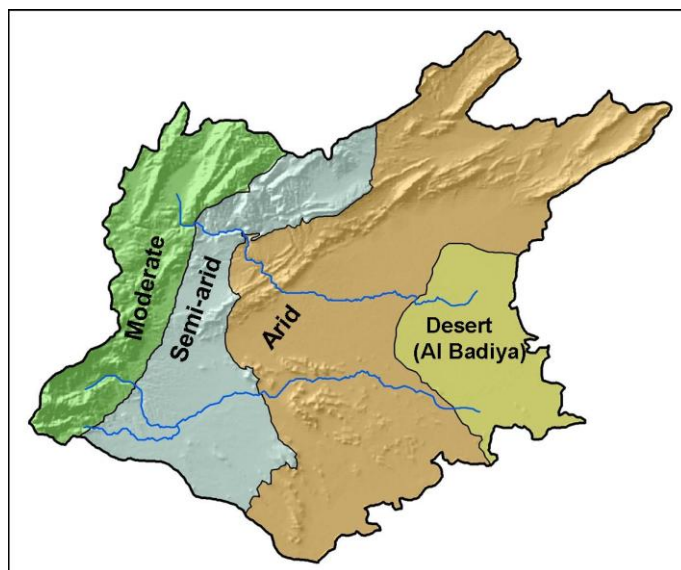


Figure 9.3 illustrates the distribution of the climate-zones over the study area as derived from the map of the mean annual precipitation for a period of 15 years according to a simple system adopted in arid and semi-arid environments.

The estimated area covered by each climate zone as percentage of total study area is shown in Figure 9.4. It can be seen from this figure that the land which receives less than 250 mm of annual precipitation occupies an area of approximately 3314 km² and constitutes the major part of the study area (51%+12%=63% of the total area). Whereas, region that receives an amount of about 250-500 mm precipitation per annum occupies an area of about 1037 km² (21%). Only 819 km² (16% of the total area) receives more than 500 mm of annual precipitation.

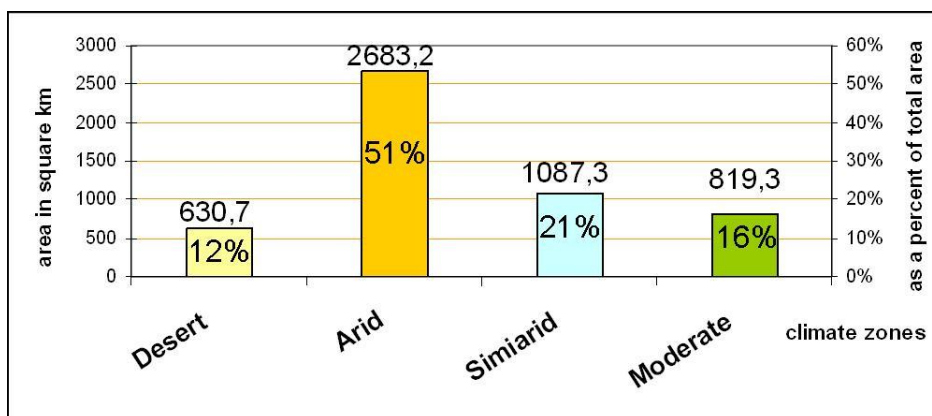


Figure 9.4 the estimated area occupied by each climate zone derived from the map of climate zones, which in turn was derived from the map of the mean annual precipitation according to a simple scheme adopted in arid and semi-arid environments.

It should be noted here, however, that the used categorization scheme may vary from area to area since it was based exclusively on annual precipitation. A better sorting of the climate zones in the study area may be achieved by using the aridity index (P/PET) used in the Atlas of desertification (UNEP, 1992). Where P stands for the average precipitation, and PET stands for potential evaporation. Table 9.1 lists the four categories of this scheme together with their corresponding aridity index and their annual rainfall variability in % of the average.

Table 9.1 Classification of various types of aridity according to UNEP's scheme (1992).

Climate zones	P/ PET ratio	Rainfall variability in % of the average
Hyper-arid	< 0.05	100
Arid	0.05 - 0.20	50-100
Semi-arid	0.20 - 0.50	25-50
sub-humid	0,50 - 0.65	< 25

9.1.2. The spatial distribution of air temperature

The spatially distributed mean annual air temperature derived by interpolation of data from weather stations for the period 1991-2005 is illustrated in Figure 9.5. As shown in this map, temperature decreases with increasing elevation in the study area. The mean annual temperature ranges from 18 °C in the central part of the study area (at an elevation of less than 800m) to less than 6 °C in the high mountainous regions (above 2400m elevation).

It should be mentioned again that the time step of the calculation was set to one hour. The model PROMET, however, has the capacity to aggregate the hourly results to daily, monthly or annual values. As another example of the temporal aggregation operation, the long-term mean annual maximum temperature was also calculated for the whole study area and illustrated in Appendix 36.

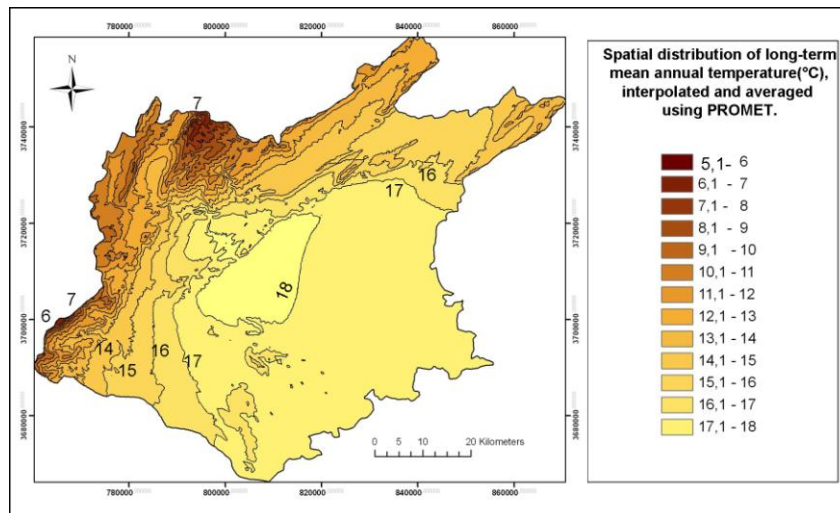


Figure 9.5 the spatial distribution of long-term mean annual temperature in the study area derived by interpolation of point observations for the period 1991-2005.

9.1.3. The spatial distribution of snow cover

Snow is an essential element of the hydrological cycle and it plays a very important role in the land surface energy, as well as in the water budgets. Therefore, realistic simulation of snow cover and snowpack over the mountainous regions of the study area is needed to understand the actual hydrological condition, and to estimate snow water equivalent which in our case represents the main source of surface water supply and groundwater recharge.

Whether precipitation falls as rain or snow depends on the air temperature, which in turn usually decreases with altitude (lapse rate) and results in snow at high altitudes and rain at low altitudes. Accordingly, the fraction of annual precipitation falling as snow increases dramatically westward from the plain of Damascus into the mountainous regions and reaches a value of more than 70 percent at an elevation of over 2000 m as shown in Figure 9.6.

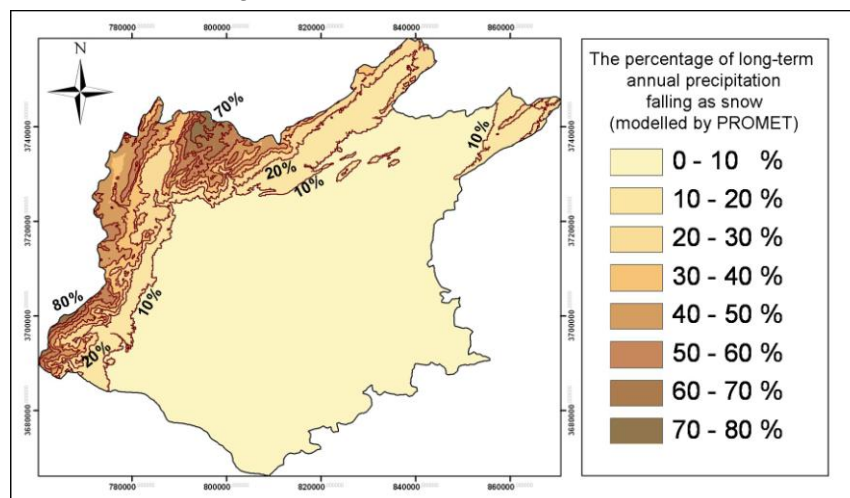


Figure 9.6 illustrates the spatial distribution of the percentage of long-term annual precipitation falling as snow, calculated using the model PROMET for a 15-year time period (1991-2005).

Additionally, the mean annual duration of snow cover was also calculated for the same period of time (1991-2005). A threshold of 1mm snow water equivalent was taken as the minimum value above which the regions can be considered to be covered with snow. As shown in Figure 9.7, the average number of days with snow-cover increases with altitude; it ranges from less than one day at low elevation (< 800 m) to more than 3 months at high elevation (> 2300 m) in the Anti-Lebanon Mountains.

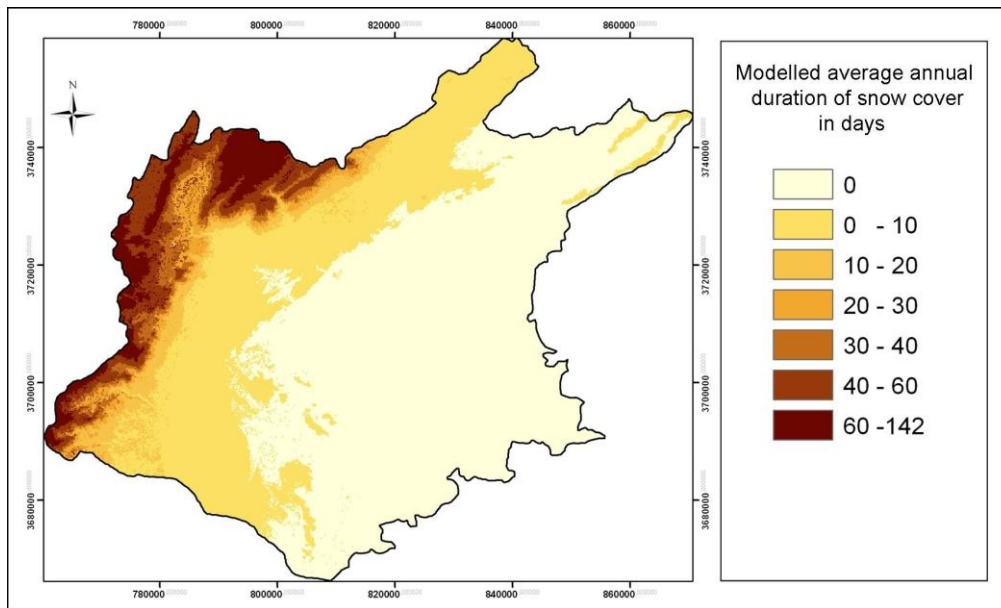


Figure 9.7 Modelled long-term annual duration of snow cover (in days/year) derived from the simulated snow water equivalent for the period (1991-2005).

However, the paucity of ground measurements on snow distribution renders satellite information a suitable alternative for validation the spatial distribution of snow cover simulated by the model PROMET. Hence, several LANDSAT images collected during the winter months (October -March) were used in this study in order to compare the snow cover maps modelled using the model PROMET with their corresponding snow-cover maps derived from these images. It may perhaps be useful to mention here that snow cover extent can easily be identified in the visible and near-infrared wavelength bands of the LANDSAT images due to its high reflectance. This fact enables us to simply classify the image into snow covered and snow free areas. For the purposes of visual (qualitative) comparison, however, the modelled snow cover can be compared with the Landsat image itself. Figure 9.8 shows an example of such qualitative comparisons, in which the output modelled snow cover for the whole study area is presented together with a LANDSAT sub-scene acquired at the same date/time (07 February 2003, 08:00 GMT). The turquoise colour on the LANDSAT sub-scene is snow.

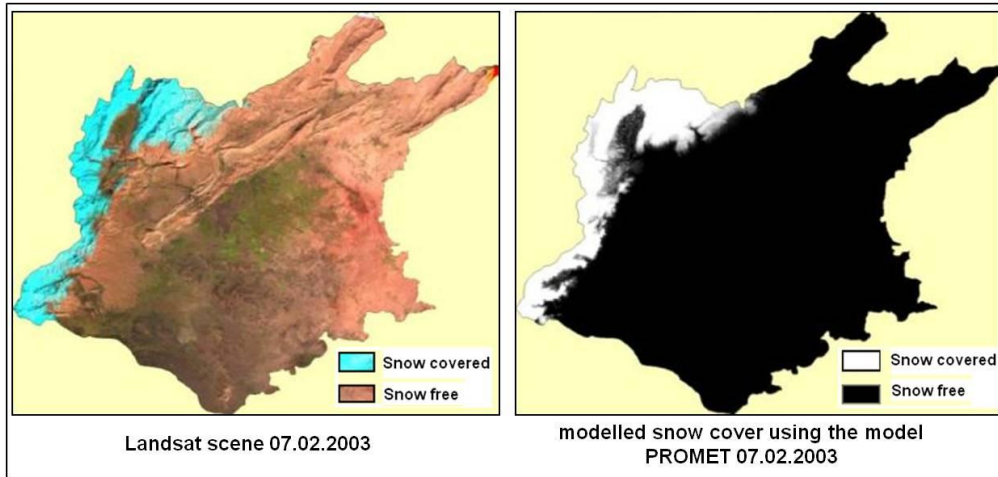


Figure 9.8 shows a comparison between model- and satellite-observed snow-cover for the entire study area for the date 07 February 2003, 08:00 GMT (10:00 local time).

The comparisons between these pairs of independently derived snow cover maps (on specific dates throughout the simulation period) show large similarities. Thus, it can be concluded that the spatial distribution and temporal dynamics of snow cover in the study area were simulated with a good accuracy using the Model PROMET.

9.1.4. The spatial distribution of solar radiation

A detailed knowledge of the spatial and temporal distribution of solar radiation is required for distributed energy and water balance modelling (Ranzi and Rosso, 1995). For example, the surface radiation balance (also known as surface net radiation) is considered as the main driving force for evapotranspiration processes and is a key input parameter to the Penman-Monteith equation. Methods of calculating the individual components of radiation balance were briefly discussed in Chapters 3 and 6.

The sum of all shortwave radiation arriving on a horizontal surface, both directly from the sun (direct solar radiation) and indirectly (diffuse radiation) from the sky and clouds, is known as total or global solar irradiance (Holden, 2005; Monteith, et al. 2007). Measured data on solar radiation are not available for most parts of the study region. In fact, there is only one station (Damascus station) where mean daily global solar irradiance measurements have been performed. These measurements can be utilized to verify the accuracy of the modelled radiative fluxes by comparing the measured values with those simulated for the same period of time. Figure 9.9 shows a comparison between long-term (15-years) measured and simulated monthly mean daily global radiation at Damascus station.

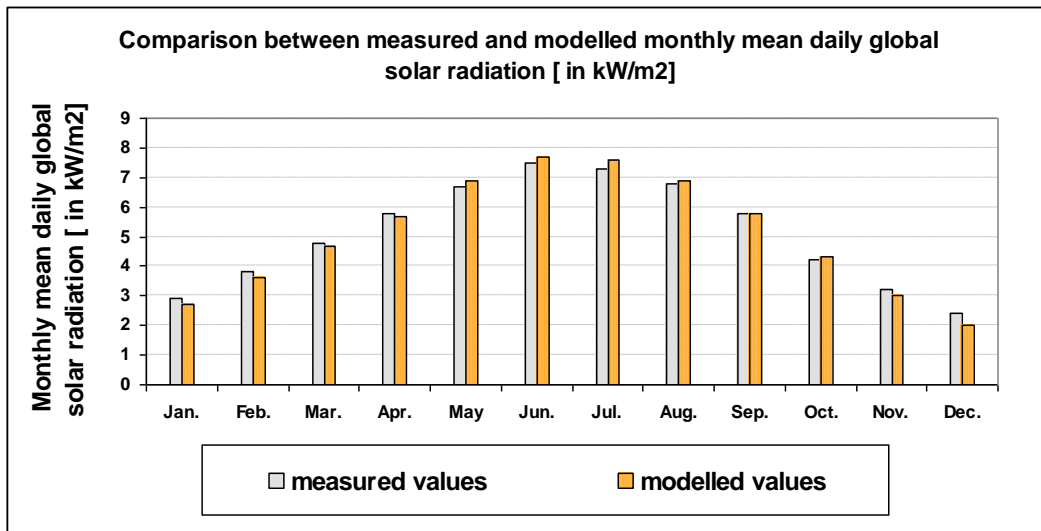


Figure 9.9 a comparison between the long-term (15-years) observed and modelled value of the monthly mean daily global solar radiation on horizontal surface (Damascus station).

Based on the monthly mean daily global solar radiation values, it can be said that the study area receives more radiation during the summer months (May to August) than during the winter months (November to February). For example, the long-term mean daily global radiation at Damascus station reaches its maximum value of about 7.5 kW/m² in June, whereas the lowest value of about 2 kW/m² was recorded in December. Figure 9.10 illustrates the spatial distribution of the long-term mean daily global solar radiation of the month of January (left), June (middle) as well as the annual distributed mean daily values (right), as simulated by PROMET in W/m².

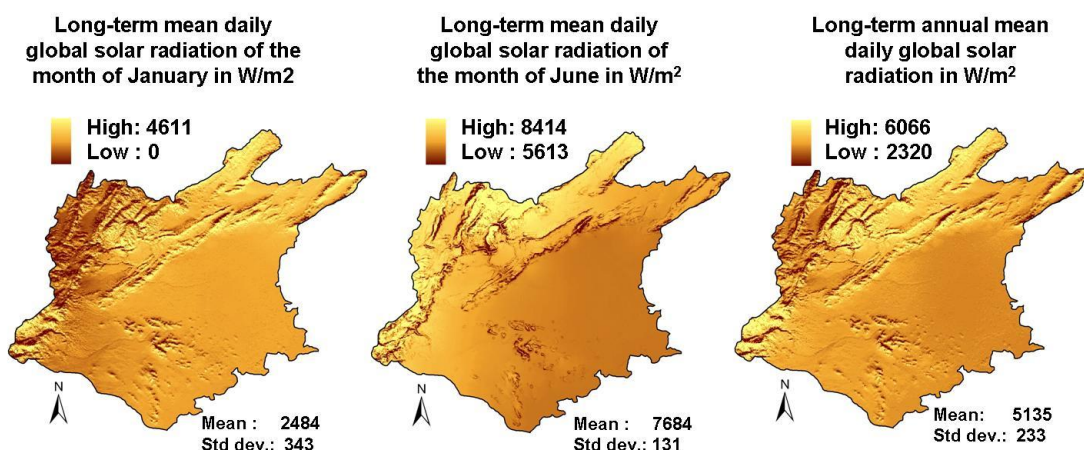


Figure 9.10 spatial distribution of the long-term mean daily global solar radiation for the month of January (left), the month of June (middle) and the annual (right), as calculated using the model PROMET for a 15-year time period (1991-2005).

According to Arya (2001), the radiation balance of the earth's surface can be written as follows:

$$R_{BAL} = (R_{SW-DIR} + R_{SW-DIF} + R_{LW-IN}) - (R_{SW-OUT} + R_{LW-OUT}) \quad (Eq.9.1)$$

Where:

R_{BAL} : is the radiation balance of the earth's surface.

R_{SW-DIR} : incoming shortwave radiation (direct).

R_{SW-DIF} : incoming shortwave radiation (diffuse).

R_{LW-IN} : incoming longwave radiation (emission from the atmosphere).

R_{SW-OUT} : outgoing shortwave radiation (reflected).

R_{LW-OUT} : outgoing longwave radiation (emission from the Earth's surface).

Spatial distribution of the long-term (1991-2005) annual sum of radiation balance, as well as its components, namely: 1) direct radiation, 2) diffuse radiation, 3) incoming longwave radiation, 4) outgoing longwave radiation, 5) reflected radiation, simulated by the model PROMET in kW/m² are illustrated in Figure 9.11. For more detail and clarity on these radiation maps see Appendices 37, 38, and 39.

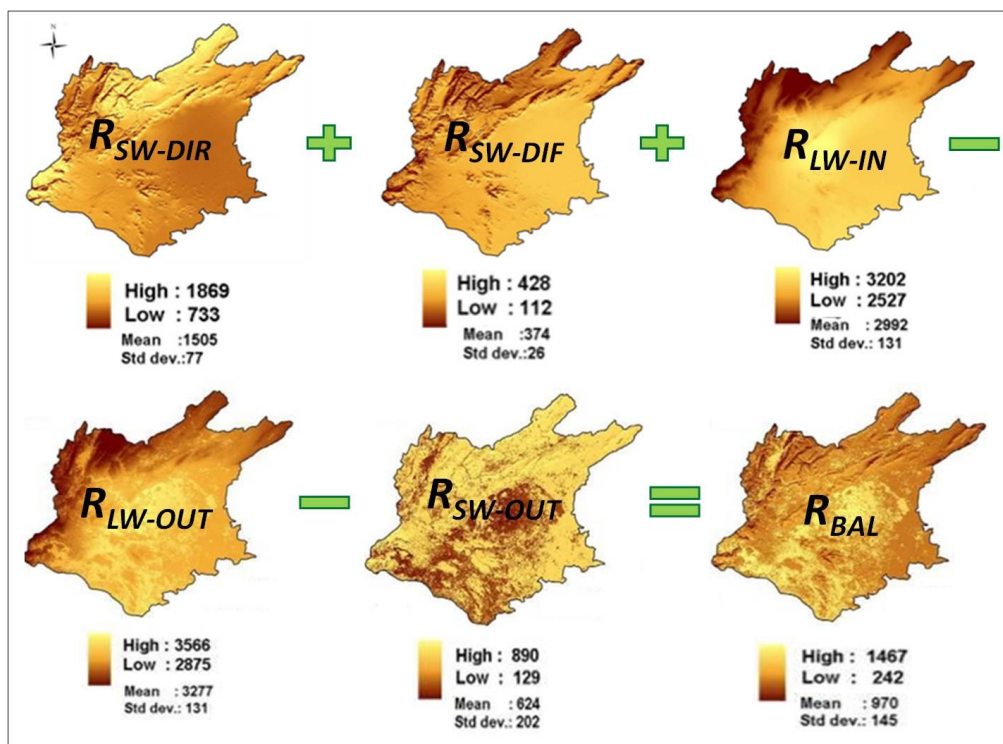


Figure 9.11 spatial distribution of the long-term annual sum of incoming shortwave direct radiation (top left), diffuse radiation (top middle), incoming longwave radiation (top right), outgoing longwave radiation (bottom left), reflected shortwave radiation (bottom middle), and the radiation balance (bottom right) as simulated by the model PROMET in kW/m².

9.2. Spatial distribution of evapotranspiration

Actual evapotranspiration (ET_a) was calculated for each pixel in the study area on an hourly basis for the entire simulation time period (15 years). The resulting spatially distributed hourly ET_a were then temporally accumulated and averaged to give the long-term mean annual evapotranspiration as shown in Figure 9.12. The average annual evapotranspiration rate for the whole study region for the given time period (15-year) was estimated to be 258mm/y (1347 Million Cubic Meters), ranging from 15 to 850mm/y. However, in addition to this spatial variation, actual evapotranspiration also undergoes temporal variation, mostly in response to water-availability (soil moisture), temperature (energy balance), and the presence of vegetation (vegetation type and its growth stage). Figure 9.13 shows the long-term (catchment-average) monthly variability of evapotranspiration as simulated using PROMET for the entire simulation period (1991-2005).

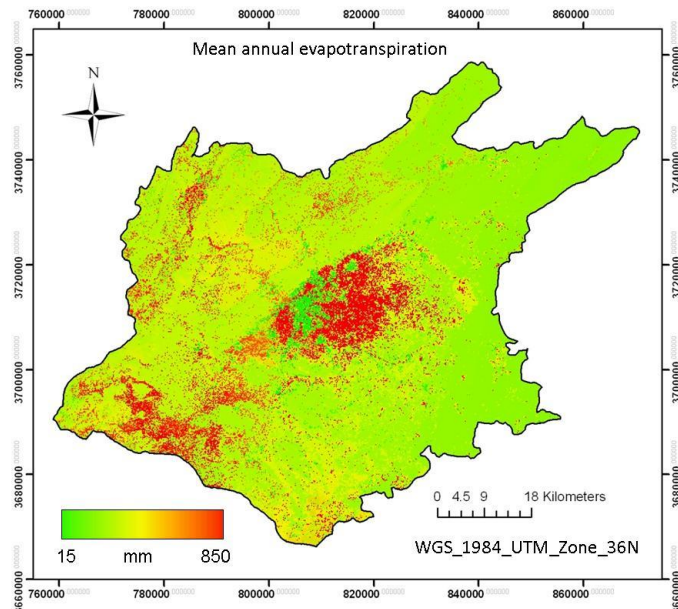


Figure 9.12 shows the spatial distribution of the long-term mean annual evapotranspiration in the study region as simulated by the model PROMET for the period from 1991 to 2005.



Figure 9.13 the long-term (catchment-average) monthly evapotranspiration as simulated using the model PROMET for a 15-year time period (1991-2005).

Based on the above figure (Figure 9.13), average monthly evapotranspiration reaches its maximum value (33-35 mm/month) during the spring period (April and May) which typically coincides with warm temperatures, high soil moisture levels, and a relatively high value of vegetation leaf area index (LAI).

As mentioned earlier in this chapter, not all results that can be outputted by the model are supported by measurement data. Evapotranspiration, for example, can be considered as one of these parameters that are very difficult to measure on a large spatial scale. However, if runoff data are available for a long period of time, evapotranspiration rate can be indirectly calculated (on the catchment scale) as the residual in the water balance equation (see Eq.9.3).

On the other hand, remotely sensed thermal data offer an opportunity to qualitatively validate the modelled actual evapotranspiration pattern, due to its correlation with surface temperature. The procedure relies on the fact that evapotranspiration directly influences the thermal regime of the land surface by its cooling effect on the surface temperature (Kirkham, 2005; Steffen and Sanderson, 2005). In view of the fact that surface temperature is not utilized in the model PROMET, this approach represents an independent means for the validation of ETa , but just for a single moment when the satellite image is captured. It is therefore essential to determine the difference between the radiative surface temperature and air temperature. Figure 9.14 serves as an example of such instantaneous qualitative assessments, in which the modelled spatially distributed ETa is compared to the image of the difference between the surface temperature and air temperature. In this example, the thermal band (band 6) of a cloud-free LANDSAT ETM+ image acquired on 21 May 2000 was used. In the first step, the digital numbers (DN) were converted to at-satellite radiance values (L_i) using the *Gain* and *Bias* settings provided in its associated header file as mentioned in a previous chapter (see Chapter 8, Section 8.3.2.2). In the second step, radiance values were converted to brightness temperature values by using the inverse of the Planck function as follows:

$$T = \frac{K_2}{\ln\left(\frac{K_1}{L_i} + 1\right)} \quad (\text{Eq.9.2})$$

where:

T = Effective at-sensor temperature in degrees Kelvin

L_i = the spectral radiance for band 6 in watts/ (m² * ster * μm)

K_2 = calibration constant 2(1282.71 for ETM+) (Irish, 2000)

K_1 = calibration constant 1(666.09 for ETM+) (Irish, 2000)

In the third step, the spatially interpolated air temperature image (produced by the model PROMET using station data at the same time of LANDSAT's overpass) was subtracted from the satellite-derived surface temperature. The resulting raster image, called as *temperature difference*, was then used for the purpose of qualitative validation of the modelled ETa as mentioned above. Cool surfaces on this image can be identified as areas of relatively high evapotranspiration rate (Price, 1989).

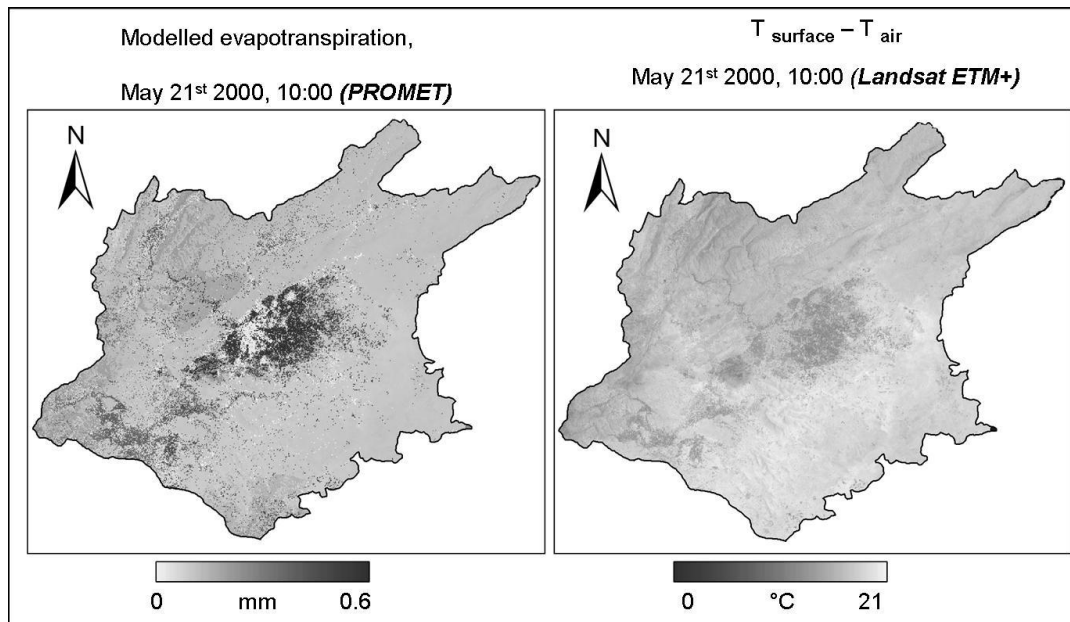


Figure 9.14 shows a comparison of the modelled actual evapotranspiration (PROMET) with temperature difference (T_{surface} (derived from LANDSAT image) - T_{air} (interpolated from station data)) on 21 May 2000, 10:00 local time.

As can be seen from the above presented figure, both images are very similar in their spatial distribution pattern. This match between the modelled ET_a pattern and the spatial pattern of the temperature difference (*surface brightness temperature – air temperature*) provides an indication of the model's capability to capture the spatial distribution of evapotranspiration.

The coldest areas in the image of *temperature difference* correspond well to those densely vegetated regions which in turn show the high values on the image of modelled evapotranspiration. On the other hand, urban areas and bare dark-colored soils (including the volcanic rock exposures) show the highest values on the image of *temperature difference* and the lowest ones on the modelled ET_a .

9.3. Spatial distribution of groundwater recharge (percolation)

Estimating the amount and the spatial distribution of groundwater recharge (percolation from the deepest soil layer into groundwater storage) is of great importance in water balance modelling. It is particularly important in semi-arid regions where there is usually a large demand for groundwater supplies. The spatial distribution of groundwater recharge is dependent on a multitude of factors that work together in a complex system including, but not limited to, the precipitation amount, evapotranspiration rate, land-use, soil types, snowmelt, frozen soil, depth to the groundwater table and the hydraulic conductivity of the unsaturated zone (Healy and Scanlon, 2010; Froukh, 2002; Seiler and Gat, 2007). Figure 9.15 gives the spatial distribution of the long-term mean annual groundwater recharge in the study region as simulated using the model PROMET for the entire simulation period (1991-2005). The average annual groundwater recharge rate for the entire study area was

estimated to be 128 mm/y (668 Million Cubic Meters / year), ranging from 0 to 649 mm/y. Obviously, regions that receive the largest amount of groundwater recharge are typically those that get the largest amount of precipitation, have appropriate surface conditions for infiltration, and are less subjected to high temperatures, and thus, evapotranspiration. These regions comprise the western parts of the study area (the Anti-Lebanon Mountains) and emerge as the primary water supplier of the study area. On the contrary, regions that receive less groundwater recharge are those with less rainfall and higher temperatures that promote high rates of evapotranspiration. These regions comprise the central- and the eastern parts of the study area.

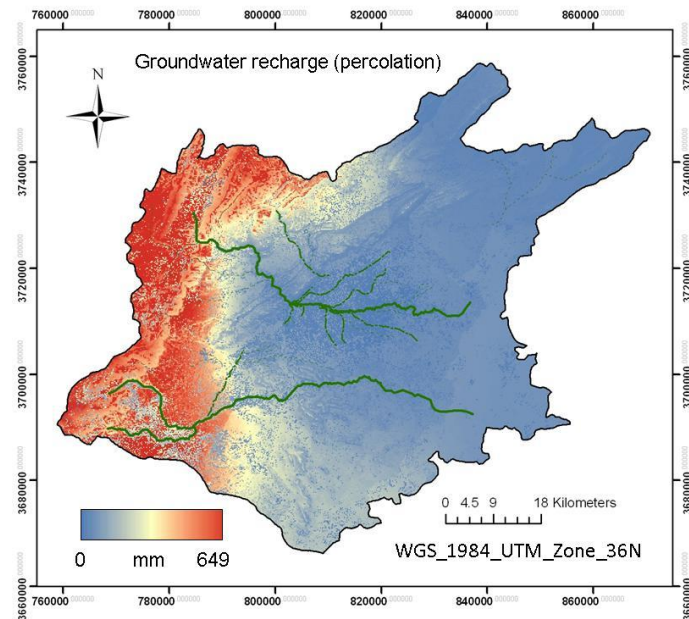
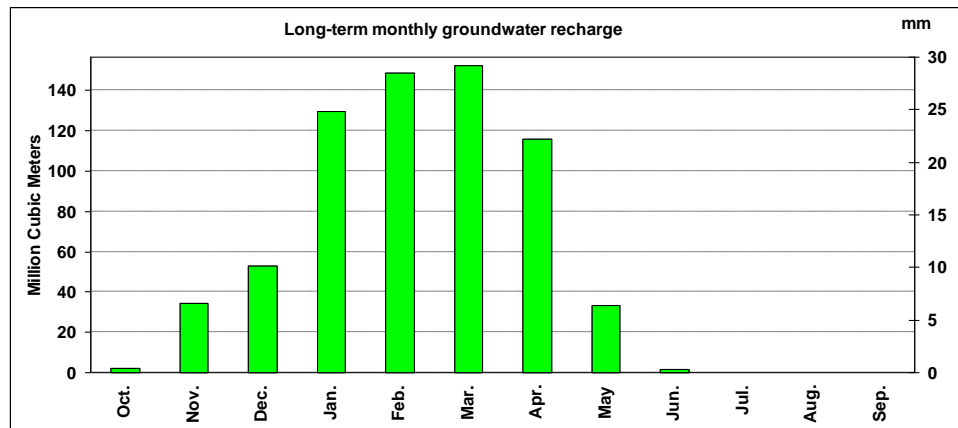


Figure 9.15 shows the spatial distribution of the long-term (15-years) mean annual groundwater recharge in the study area as simulated using the model PROMET, together with the river channel network draped over it.

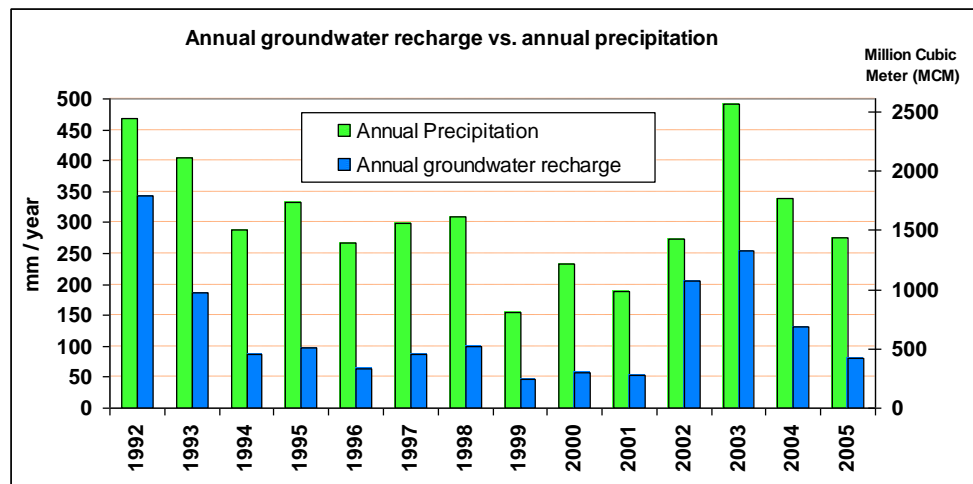
In addition to the fact that the amount of groundwater recharge can be unevenly distributed over space as in the case of the study area, it can also vary greatly over time. Generally, in humid regions where precipitation typically exceeds potential evapotranspiration throughout most seasons, there is a surplus of water which leads to nearly continuous groundwater recharge. In semi-arid areas, however, no such continuous surpluses exist for all seasons of the year. In the study area, groundwater recharge occurs only during two seasons, namely, the rainy winter, when precipitation exceeds the potential evapotranspiration, and spring, when the snow cover melts. Figure 9.16 shows the long term inter-seasonal (month-to-month) variability in groundwater recharge as calculated using the model PROMET for the entire study area for the time period (1991-2005). As can be seen from this figure, there is very little or no recharge occurring during summer and autumn months (from June to October) as there is no (or very little) precipitation or snowmelt. Furthermore, analyzing the simulated annual groundwater recharge reveals a substantial year-to-year variability in its magnitude which can be attributed mainly to variations in the

annual precipitation amount. Figure 9.17 presents the annual variability of groundwater recharge rate for the entire study area as simulated using PROMET for the hydrological years (1992-2005), together with the catchment-average annual precipitation. It can be seen from this figure that recharge during very wet years, such as 1992 and 2003, can be 3-5 times the quantity of recharge in very dry years, such as 1999 and 2001.



recharge	Oct.	Nov.	Dec.	Jan.	Feb.	Mar.	Apr.	May	Jun.	Jul.	Aug.	Sep.
mm	0.4	6.6	10.1	24.8	28.5	29.2	22.2	6.4	0.3	0	0	0
MCM	2.1	34.5	52.7	129.5	148.8	152.4	115.9	33.4	1.6	0	0	0

Figure 9.16 the long term monthly average groundwater recharge in the study area as simulated using the model PROMET for a 15-year time period (1991-2005).



Recharge	1992	1993	1994	1995	1996	1997	1998	1999	2000	2001	2002	2003	2004	2005
mm	344	186	86	97	64	87	101	46	58	54	206	254	131	80
MCM	1795	970	449	504	335	456	525	238	302	280	1077	1325	685	417

Figure 9.17 shows the annual variability of the simulated groundwater recharge for the hydrological years 1992-2005, along with the variability in the catchment-average annual precipitation.

9.4. The annual water balance

For the purpose of calculating the spatially distributed annual water balances, two main subcatchments, namely, “*Al-hama*” and “*Om Al-sharatit*”, were selected as representatives of those relatively water-rich regions in the study area from which the two main rivers (Barada and Awaj) emerge and flow down to the plain of Damascus. Choosing these two subcatchments, each represented by the location of its respective outlet gauge station, was done carefully in order to ensure the following:

- Each gauge station is located along its respective river valley before that place after which the river divides into several separate branches and artificial channels.
- Each gauge station is located at a place where a permanent flow of water is maintained throughout the year, which enables us to compare the modelled runoff volumes with those measured at the gauge stations.

The locations of these two sub-basins in relation to the whole study area are illustrated in Figure 9.18, which also depicts the locations of all available stream-flow gauge stations. The segmentation of the whole study area into several sub-basins, which is necessary for calculating the water balance components, was done with the help of the geographic coordinates of the gauge stations, the digital elevation model (DEM) and the topographic analysis tool TOPAZ (see Chapter 5). The mean annual discharge for each of these two subcatchments for the observation period 1992-2005, in addition to other information, is presented in Table 9.2. Discharge data are also given in Million Cubic Meters per year [Mm³/y] as well as in [mm/y], which facilitates a straight forward comparison between the values of the different water balance components without the influence of the respective area of each subcatchment.

Table 9.2 lists the mean annual observed discharge (1991-2005) for each of the two subcatchments used for calculating the annual water balance, along with other information.

Subcatchment Name	River Name	Number of Pixels	Upstream Area km ²	Mean annual discharge		
				m ³ /s	Mm ³ /y	mm/y
Al-hama	Barada	23494	761.2	4.3	134	176
Om Al-sharatit	Awaj	9232	299.1	2.06	65	217

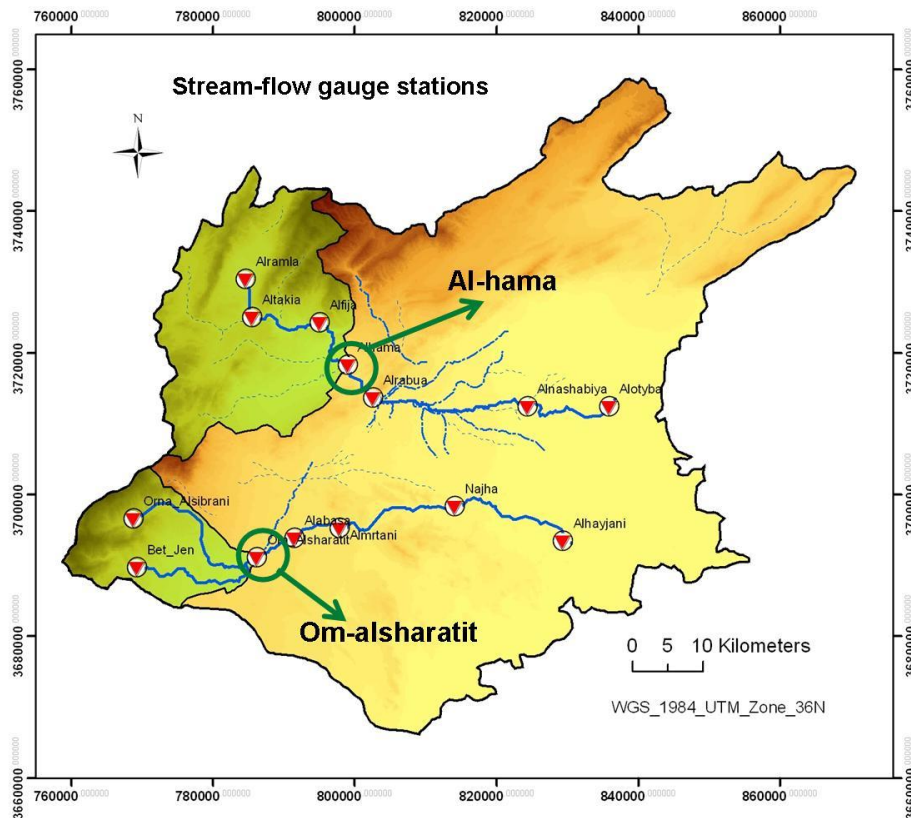


Figure 9.18 shows the locations of the two subcatchments used for the purpose of calculating the annual water balances in relation to the entire study area, together with the positions of the stream-flow gauge stations.

Taking into consideration the water withdrawal (water use) from each of the above mentioned subcatchments, spatially distributed annual water balances were established for each of the 14 hydrological years (1992-2005) using the interpolated precipitation and the modelled evapotranspiration as components in the simplified water balance equation which can be expressed as follows:

$$P = ETa + Q + \Delta S + WW \quad (\text{Eq. 9.3})$$

where

P : Interpolated Precipitation [mm/y]

ETa : Modelled actual Evapotranspiration [mm/y]

Q : The stream discharge (Runoff) [mm/y]

ΔS : The change in water storage (in groundwater, soil moisture and snow) [mm/y].

WW : The estimated annual amount of water withdrawal (Water use) [mm/y].

However, in order to simplify the calculation of water balances, the following assumptions are made:

- Ground water divides coincide with surface water divides (known as topographic divide or watershed boundary); and thus, there are no natural inflows/outflows of groundwater into/from the boundaries of the two selected subcatchments.

- All water that enters the aquifer (the groundwater recharge) will discharge to the surface within one year through several ways including, the artificial withdrawal by pumping and the natural discharge to the stream channel (river baseflow) and to springs, such as the “Fijah Spring” (7.7 m³/s) and the “Barada Spring” (3.1 m³/s) which are used as the main water resources for Damascus City.
- The amount of water withdrawal (*WW*) from each subcatchment is assumed to remain constant over time (from day-to-day and from year-to-year) during the whole simulation period. According to statistics provided by several authorities and institutions involved in water management in the study area, such as the “Damascus Water Supply and Sewerage Authority” (*DAWSSA*), the “Ministry of Agriculture and Agrarian Reform” (*MAAR*), and the “Ministry of Irrigation” (*MOI*), water withdrawal from each subcatchment can be approximately estimated as presented in the table below (Table 9.3). It should be mentioned here that the largest volume of water withdrawal takes place in the “*Al-hama*” subcatchment, particularly from the “*Fijah Spring*” which is used to provide the city of Damascus (which is located outside this subcatchment and inhabited by 4 million persons) with drinking water. According to Higano and Melhem (2002), the annual average amount of water withdrawal from this spring (for drinking purposes) is estimated at about 4.6m³/s (145 Mm³/y).

Table 9.3 lists the mean annual water withdrawal from each subcatchment.

Subcatchment	River	Mean annual water withdrawal (<i>WW</i>)	
		m ³ /s	Mm ³ /y
Al-hama	Barada	5.5	173
Om Al-sharatit	Awaj	1.3	42

- If we chose the hydrological year (1st November to 31st October of the following year) to be the observation period, then it can be assumed that the amount of water stored in each subcatchment (as groundwater, soil moisture and snow cover) will not change over that time period (i.e., $\Delta S=0$). In other words, water storage (*S*) will be the same as it was on the same date a year ago.

Taking these above-mentioned assumptions into account, the analysis of the annual water balance for each subcatchment was carried out in two steps. In the first step, the long term (spatially distributed) average annual water balance was determined for each subcatchment over the whole simulation period (from 1992 to 2005). The modelled annual sums of precipitation (*P*) and evapotranspiration (*ETa*) were averaged for these 14 hydrological years. The long-term spatially distributed mean annual runoff was then calculated by subtracting the evapotranspiration and water withdrawal (*ww*) from Precipitation ($Q = P - ETa - WW$). The resulting water volume from each subcatchment (the calculated runoff) can be compared to the measured discharge volume at its respective outlet gauge station. In view of that, the average simulated water balance for “*Al-hama*” subcatchment is made up of 662mm/y precipitation, 254mm/y evapotranspiration, 227mm/y (5.5m³/s) water withdrawal and

thus 181mm/y runoff. The comparison between this simulated runoff rate and discharge measured at its respective outlet gauge station (176 mm/y) demonstrates a good agreement. The deviation equals 3% (5 mm/y). This result shows that the used model reliably describes the long-term water balance of “Al-hama” subcatchment. Likewise, water balance for the “Om Al-sharati” subcatchment is composed of 703mm/y precipitation, 337mm/y evapotranspiration, 140mm/y (1.3m³/s) water withdrawal and as a consequence 226mm/y runoff. Comparing this modelled runoff value to the recorded discharge of 217mm/y at its respective gauge station reveals that the simulated runoff overestimates the real conditions by about 4% (9mm/y). Thus, in general, it can be said that the simulated mean annual runoff fits well with the observed runoff for both selected subcatchment. Figure 9.19 shows the spatial distribution of the mean annual components of the water balance in “Al-hama” subcatchment as simulated using the model PROMET over the simulation period (1992-2005). The spatially distributed water balance of the “Om Al-sharati” subcatchment is presented in Appendix 40.

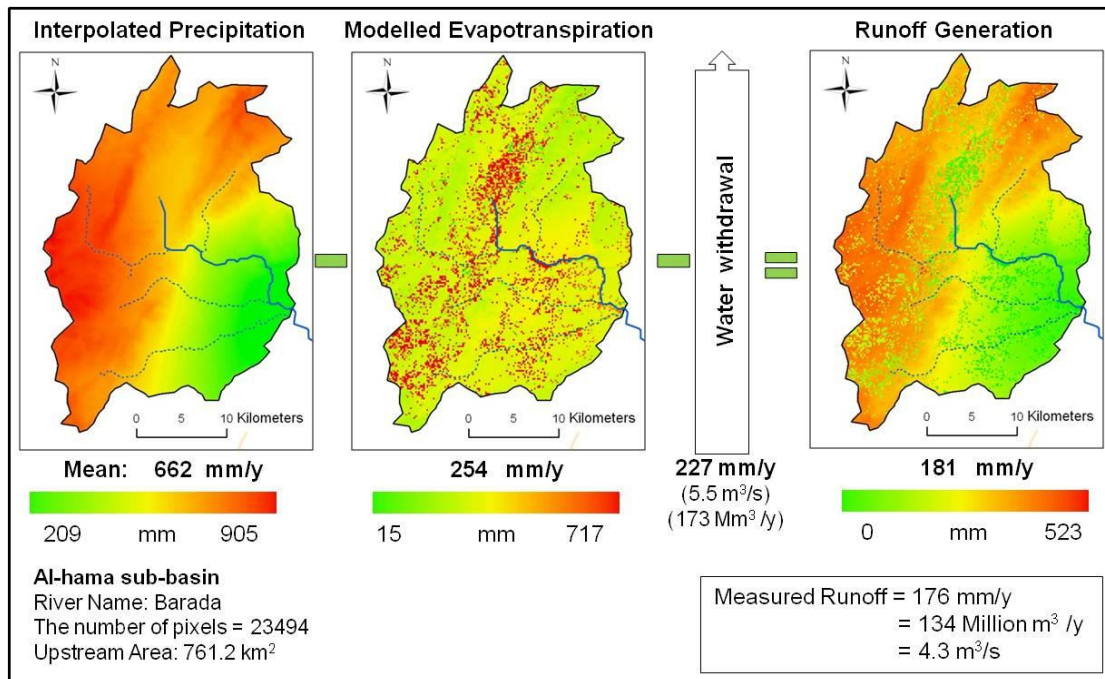


Figure 9.19 the average modelled water balance in “Al-hama” subcatchment over the period from 1992 to 2005. The simulated mean annual runoff from this subcatchment (181 mm /y) compares well with the runoff (discharge) measured at its respective outlet gauge station (176 mm/y).

As can be seen from this figure, the spatial distribution of the resulting annual runoff generally reflects the spatial distribution of the annual precipitation. It should be mentioned here, however, that the resulting runoff image is considered as a remainder or residual term of the water balance equation (the amount of annual precipitation at each pixel of the subcatchment which is not evaporated or

transported and is thus available for all runoff components, including overland flow, interflow and baseflow).

Finally, the analysis of the mean annual water balance for the “*Al-hama*” subcatchment for the period (1992-2005) indicates that around 38% of mean precipitation is evapotranspired, around 34% is abstracted (mainly for drinking and other domestic purposes), and about 27% is transformed to direct runoff. On the other hand, the percentage of each component of the water balance in the “*Om Al-sharati*” subcatchment is given as follows: 48% of the mean precipitation is lost through evapotranspiration, 20% through water withdrawal, and 32% through runoff.

In the second step of the annual water balance analysis, I try to investigate whether the interannual (from year-to-year) variability of the runoff volume in both selected subcatchments is well captured by the used model (PROMET). For this purpose, the annual simulated runoff volumes for each subcatchment (mm/y) were compared with those measured at its respective gauge station for the period of 14 hydrological years. Table 9.4 lists the annual means of the modelled water balance components (in mm/y) for “*Al-hama*” subcatchment as calculated by the model PROMET for each hydrological year from 1992 to 2005. The results of the water balance for “*Om Al-sharati*” subcatchment are presented in Appendix 41.

Table 9.4 presents the modelled annual means of the water balance components (in mm/y) for “*Al-hama*” subcatchment as simulated by PROMET for each of the 14 hydrological years (1992-2005).

<i>Al-hama</i> Sub-basin River Name: Barada Upstream Area: 761.2 km ² P: Interpolated Precipitation (mm/y) ETa: Modelled actual Evapotranspiration (mm/y)							
Hydrological Year 1.Nov.- 31.Oct	P mm/y	ETa mm/y	WW (withdrawal) mm/y	Q = P-ETa – WU (Calculated Runoff) mm/y	Measured Runoff mm/y	Deviation	
						mm/y	(%)
1992	975	285	227	463	412	51	12
1993	837	251		359	303	56	18
1994	654	288		139	158	-19	-12
1995	674	266		181	176	5	3
1996	616	256		132	109	23	21
1997	596	266		103	122	-19	-15
1998	656	239		190	161	29	18
1999	447	208		12	25	-13	-52
2000	487	240		20	46	-26	-57
2001	468	223		18	30	-12	-40
2002	602	270		105	63	42	67
2003	960	266		467	422	45	11
2004	661	247		187	265	-78	-29
2005	638	255		156	172	-16	-10
Mean	662	254	227	181	176	5	3 %

WW: water withdrawal (water use) from “*Al-hama*” subbasin is estimated to be 227 mm/y (173 Million Cubic Meters/year or mean annual withdrawal rate of **5.5m³/s**).

As can be seen from the above mentioned tables, the volumetric deviations between modelled and measured runoff vary from year to year, covering the range from -78mm/y (-29%) to +56 mm/y (+18%) for the case of “Al-hama” subcatchment, and from -64mm/y (-36%) to +89mm/y (+45%) for the case of “Om Al-sharati” subcatchment. These negative and positive signs of the deviations also indicate that there is no systematic over- or under-estimation of the simulated annual runoff.

The visual comparison between the simulated and measured annual runoff for “Al-hama” subcatchment (given in both mm/y and m³/s) is shown in Figure 9.20. For the case of “Om Al-sharati” subcatchment, the comparison is presented in Appendix 42.

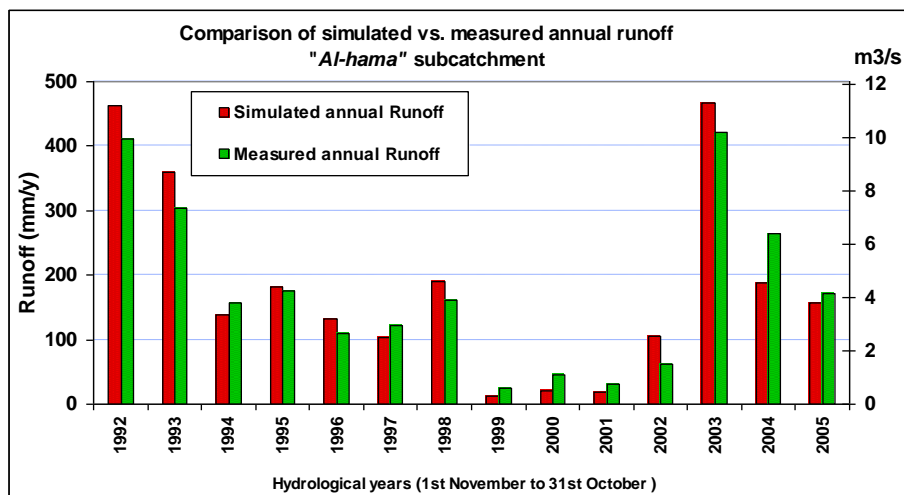


Figure 9.20 shows a comparison between the modelled annual runoff volumes from “Al-hama” subcatchment (in mm/y and in m³/s) and those annual discharges measured at its outlet gauge station for the hydrological years from 1992-2005.

Furthermore, in addition to this graphic comparison, a linear regression between the measured and the simulated annual runoff volumes was carried out to illustrate their relationship to each other, as shown in figure 9.21.

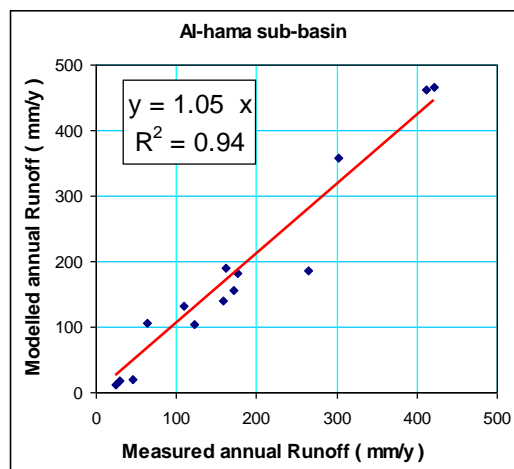


Figure 9.21 illustrates the linear regression (forced through the origin) between the modelled and measured annual runoff volumes (in mm/y) at “Al-hama” outlet gauge station.

The coefficient of determination (R^2) and the slope of the regression line (b), which was forced through the origin, were taken as a measure for the accuracy with which the interannual variability of the runoff volume is captured by the model PROMET. For “*Al-hama*” subcatchment, the slope of the regression line ($b=1.05$) as well as the coefficient of determination ($R^2= 0.94$) were found close to 1. Similarly, relatively good results were also found for the case of “*Om Al-sharati*” subcatchment, with $b= 1.07$ and $R^2 = 0.93$, as shown in Appendix 43. These values indicate that the interannual variability of runoff volume from each selected subcatchment can be well explained by the model.

9.5. Analysis of the simulated monthly streamflow (Discharge)

As mentioned earlier in this chapter, the analysis of water balance on an annual basis (hydrological year) does not take into account the variations in water storage components (snow, soil moisture, groundwater), which were assumed to be invariable from year to year ($\Delta S= 0$). However, in order to account for these variations, the simulated water balance (mainly in terms of discharge) should be further analyzed over shorter time scales. The objective of this section is, therefore, to reveal the extent to which the seasonal variations in river discharge can be explained by the model PROMET. In other words, I try to investigate how accurate does the model reproduce the observed discharge. For this purpose, the simulated discharges for the whole simulation period should be compared to the observed ones (at several gauge stations) over different time intervals, ranging from hourly to seasonally. However, regarding the availability of gauge stations and discharge data records, two points should be mentioned here. The first point is that some gauge stations do not have complete data records for the entire period (gauges with missing data), and therefore, they were excluded from this analysis. The second point is that the monthly mean values are the only discharge measurements available from all existing gauges. Consequently, a comparison between the modelled and measured discharge at shorter time scales (e.g., hourly, daily, or weekly) is not possible now due to limited available observed data. Therefore, the modelled hourly values of discharge were first aggregated (averaged) into daily values for each pixel in the study area (161138 pixels). The daily averages were then aggregated into monthly averages (means). Pixels that correspond to the locations of the streamflow gauge stations were selected. Each of these seven selected pixels, referred to as “*outlet*” or “*pour point*”, determines a particular subcatchment. As a consequence, seven sub-catchments of different sizes were chosen for this comparative analysis.

Two examples illustrating the comparison between the simulated and the observed discharge volumes on a monthly basis, covering the period from 1991 to 2005, will be presented in detail in this study.

- The first example, as shown in Figure 9.22 (in terms of temporal course of monthly mean discharge) and in Figure 9.23 (in terms of long-term mean monthly values), illustrates the results for “Al-hama” subcatchment.
- The second example, as shown in Appendix 44 (in terms of temporal course of monthly mean discharge) and in Appendix 45 (in terms of long-term mean monthly values), demonstrates the results for “Om Al-sharati” subcatchment.

Again, it should not be forgotten that water withdrawal, which was assumed to be constant throughout the simulation period, was also taken into account here. Hence, water withdrawal rate of $5.5\text{m}^3/\text{s}$ and $1.3\text{m}^3/\text{s}$, as pointed out earlier in this chapter, were subtracted from the simulated monthly mean discharge at “Al-hama” and “Om Al-sharati” gauge stations, respectively.

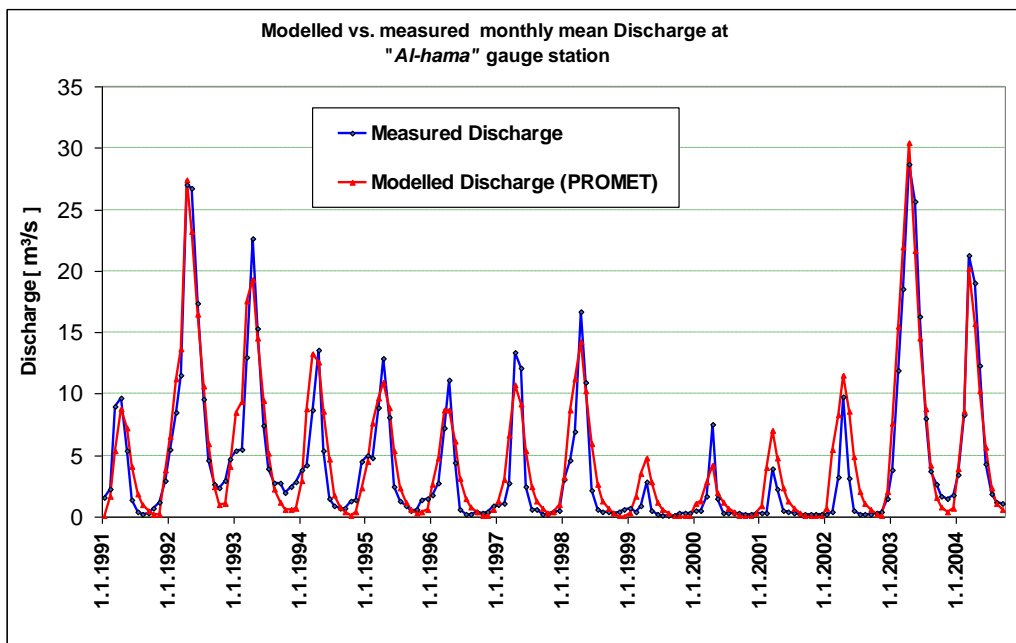


Figure 9.22 shows the temporal course of modelled and measured monthly mean discharge at “Al-hama” gauge for the period (1991-2005).

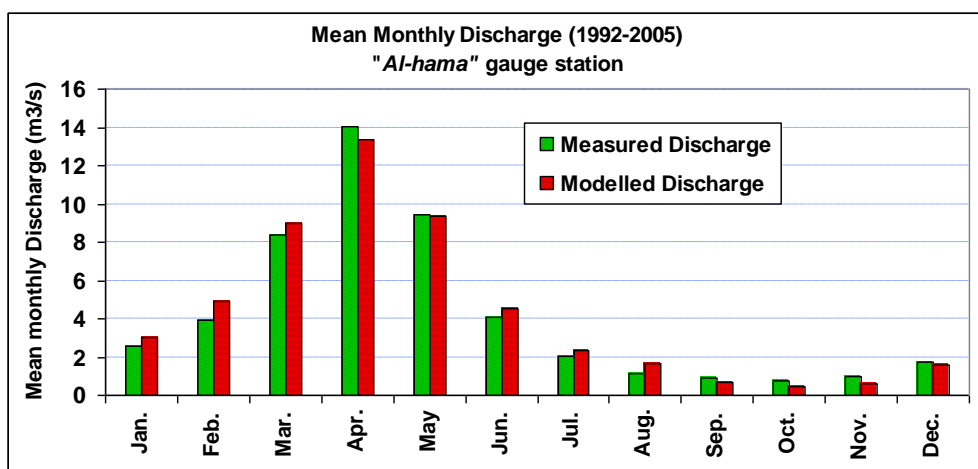


Figure 9.23 shows a comparison between simulated and observed mean monthly discharge at “Al-hama” gauge for the period (1991-2005).

In addition to the high interannual variability in river discharge between wet and dry years (Figure 9.20), analyzing the mean monthly discharge patterns for the seven selected subcatchments within the study area reveals that these patterns are very similar (in terms of their temporal courses) and subject to a high degree of variability (in respect of their magnitude) from month to month throughout the year. Taking the discharge observed at “Al-hama” gauge as a typical example (Figure 9.23), the highest streamflow values occur in spring (March through May); low flow values take place during the season from midsummer (August) until late autumn (November). Here again it must be mentioned that most precipitation in the study area occurs (mainly in the form of snow) during the cool winter season (December to March). As a consequence, the amount of water that is stored in temporary snow cover, together with the amount of water that has percolated down into groundwater storage represent the main source of water that flows down the rivers during the rest of the year. The peak discharge which usually occurs in spring (April) can be mainly attributed to the snowmelt from mountainous areas.

However, in a similar way as it was done for the annual discharge data, a linear regression line was fitted to the monthly data (simulated vs. measured monthly discharge volumes). Figure 9.24 shows the result of the regression analysis for “Al-hama” subcatchment. For the subcatchment of “Om Al-sharati”, the result is depicted in Appendix 46.

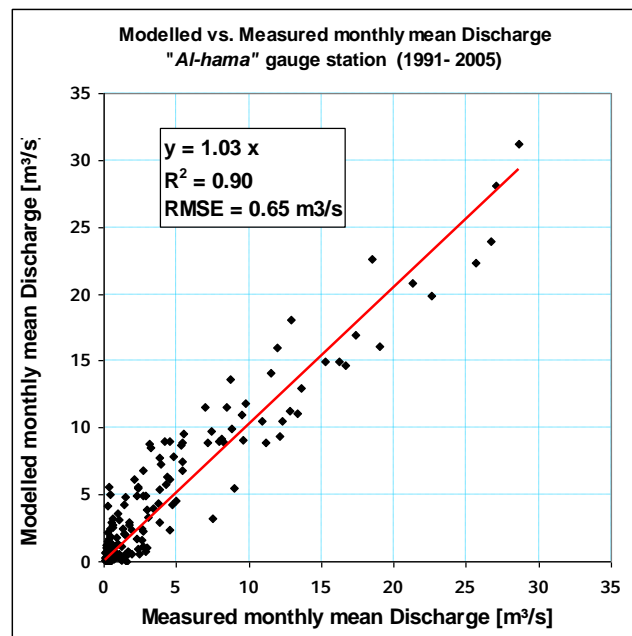


Figure 9.24 demonstrates the linear regression line (forced through the origin) between the modelled and measured monthly mean discharge volumes (in m^3/s) at “Al-hama” outlet gauge station for the period 1991-2005.

As can be seen from the above figures, each represented by a scatterplot and a regression line, there is a good correlation between simulated and observed monthly mean discharge volumes. However, an overall view of the model performance in terms of reproducing the monthly observed discharge can be obtained by looking at the results of the regression analysis for each of the seven selected gauge stations. Table 9.5 lists the slope of the regression line (forced through the origin) and the coefficient of determination (R^2) for the linear regression between the simulated and observed monthly mean discharge for each selected outlet gauge. In addition to that, the Nash-Sutcliffe coefficient (Nash and Sutcliffe, 1970) was also used to assess the goodness of fit between the simulated and measured monthly discharge. It is defined by the following equation:

$$E = 1 - \frac{\sum_{t=1}^T (Q_{obs}^t - Q_{sim}^t)^2}{\sum_{t=1}^T (Q_{obs}^t - \overline{Q_{obs}})^2} \quad (\text{Eq. 9.4})$$

where:

Q_{obs}^t : is the observed monthly discharge at time t

Q_{sim}^t : is the simulated monthly discharge at time t

$\overline{Q_{obs}}$: is the average observed monthly discharge over the total number of observations (T).

Table 9.5 presents the slope of the regression line (forced through the origin), the coefficient of determination, and the Nash-Sutcliffe coefficient for the regression relationship between the modelled and measured monthly discharge for each selected gauge for the period (1991-2005).

Gauge name	River	Upstream Area km ²	Slope of regression line (b)	R2	Nash-Sutcliffe coefficient (E)
Al-hama	Barada	761.2	1.03	0.90	0.93
Om Al-sharatit	Awaj	299.1	1.04	0.88	0.95
Al-Rabwa	Barada	837.8	0.96	0.87	0.88
Al- Fijah	Barada	431.1	1.03	0.80	0.86
Al-Tekeya	Barada	173.1	0.84	0.72	0.82
Orna	Awaj	42.2	0.79	0.69	0.79
Al-Ramla	Barada	101.6	0.82	0.70	0.76
Al-Nashabeya	Barada	905.3	0.92	0.78	0.75
Al-Abasa	Awaj	364.1	0.86	0.73	0.73

As presented in the table above, the slope of regression line (b) ranges from a minimum of 0.79 (“Orna” gauge) to a maximum of 1.04 (“Om Al-sharatit” gauge). Slope values greater than or less than one normally indicate that the used model over- or under-estimated the monthly mean discharge, respectively. A value of unity (close to 1.0) indicates that there is a perfect correlation between the two variables (simulated vs. observed discharge). On the other hand, the coefficient of

determination (R^2), which describes the percentage of variability explained by the simulated discharge in the linear regression model, varies from a low of 0.69 (“Orna” gauge) to a maximum of 0.90 (“Al-hama” gauge). An R^2 close to 1.0 indicates that simulated and observed discharges match closely. In addition to that, the value of the Nash-Sutcliffe coefficient (E) was found to vary from 0.73 (“Al-Abasa” gauge) to 0.95 (“Om Al-sharati” gauge). It is acknowledged here that the closer the value of E is to 1.0, the more accurate the model is.

In general, the values of the coefficients b , R^2 and E (listed in table 9.5) shows that the correlations between the measured and simulated monthly discharges at several gauges within the study area for the whole period of time (1991-2005) are generally high. This leads to the final conclusion that interannual and seasonal variations in river discharge were reproduced with good accuracy using the model PROMET without calibration against observed data.

10. Summary and Outlook

10.1. Summary

The aim of this study is to simulate land surface processes (the water and energy fluxes) in the Greater Damascus Basin using the model PROMET as an example of using spatial data for Geo-environmental studies. Some of the main reasons for choosing the spatially distributed model PROMET for this aim, as presented in more detail in Chapter 3, are: (1) it is a physically-based model and takes advantage of the physical properties of the land surface to simulate the fluxes of energy and matter, (2) embedded within a raster-based GIS-structure which facilitates the integration of spatial data like e.g., remotely sensed data, (3) designed for worldwide application, (4) can be applied at different scales, (5) able to study the impact of climate change on the water cycle of complex catchments, (6) its input parameters are derived from remote sensing data or taken from literature sources, but not calibrated to site specific data, and (7) strictly conserves mass and energy.

Due to the different environmental conditions in the Greater Damascus Basin, a mesoscale basin in southwest Syria, it was chosen as study area (Pilot Region). Many types of climates, topography, soil, vegetation, and land uses are found in this basin which can be divided into *Barada River Basin*, *Awaj River Basin*, and other small valley basins. The basin is characterized by large temporal and spatial variations in precipitation and by limited water resources. According to the results of this study, the mean annual precipitation over the whole study region for the period from 1991 to 2005 was estimated to be 277mm, ranging from more than 800mm in the western part of the basin (the anti-Lebanon mountain-range) to less than 100mm in the eastern part (the desert region).

In this study, PROMET was run using the scale-independent Penman-Monteith equation on an hourly time step and a 180m*180m spatial resolution. All required input datasets were provided either in form of spatially-distributed GIS digital layers (such as topography, soil type, landuse, etc...) or in form of associated tabular input files containing information about the properties of soil types and landuse categories.

The required land use/land cover map, which is assumed to be time-invariant during the whole simulation period, was successfully derived from classification of a cloud-free LANDSAT 7 ETM+ image acquired on May 21st 2000. The acquisition date of this image, during the spring season when the vegetation is typically fully leafed out, was considered very suitable for the classification of various types of agriculture. The land use map which was previously produced by the General Organization of Remote Sensing in Syria (GORS) using the traditional land survey techniques was used in this study as the main reference ground-truth during the map classification. The USGS land use/land cover hierarchical classification system was selected and modified to suite the conditions and the heterogeneity of the study area. The image was classified into 12 land use/land cover classes using the supervised classification

algorithm (the maximum likelihood classifier). The quantitative accuracy assessment of the derived land use map which was performed only over the central part of the study area (Damascus and its surrounding oasis) reveals a good agreement to the reference data (with an overall accuracy of 83.67% and Kappa coefficient of 0.80).

Terrain parameters such as elevation, slope, aspect, upslope area, drainage network, and watershed boundaries were automatically extracted from DEM (Digital Elevation Model) using two software packages (ESRI's ArcGIS 9.1 and TOPAZ ver.1.10). For this purpose, Shuttle Radar Topography Mission (SRTM) DEM with a horizontal grid spacing of 90m and a vertical resolution of 1m was used. However, in order to investigate the influence of increasing grid cell size on the delineation of the drainage network in the study area, this 90m-DEM was aggregated into additional DEMs (180, 500, and 1000m spatial resolution). The results show that the deviations in the extent of the DEM-derived drainage network for a grid size up to 180m tend to be relatively small compared with the manually-digitized blue line stream. Therefore, taking the memory and computational resources into consideration, the grid cell size of 180m was chosen as an appropriate spatial resolution for extracting the required topographic- and channel routing parameters as well as for simulating the various land surface processes in the study area using PROMET.

On the other hand, comparing the outcomes of the two above-mentioned software packages with each other and with the manually digitized data reveals that TOPAZ performs better than ArcGIS 9.1 in creating a realistic drainage pattern over flat areas.

The required meteorological fields were provided on an hourly basis by the meteorological component of the model PROMET through spatiotemporal interpolation of the measurements of the available weather stations. In order to ensure a high level of quality and consistency of the meteorological fields, data were collected from all existing synoptic, climatic, and rain-gauge stations, covering the period from 1991 to 2005 (15 years). Since incoming short and longwave radiation fluxes are not measured by the available weather stations, they were indirectly derived based on the interpolated cloud cover.

Parameterization of soil hydraulic properties was done based on the soil map of Syria which was prepared by USAID at a scale of 1:500,000. Despite the fact that the existing soils have been classified at the level of subgroup of the USDA Soil taxonomy (1975), the legend of the map is not constituted by the individual discerned subgroup soils rather with soil associations. Therefore, in order to parameterize the required soil hydraulic properties with good accuracy, the soil associations were separated into their major components (soil types) by making use of all available information provided with each soil type. The USDA textural triangle was used to determine the soil texture for each separated soil type represented by its typical soil

profile. Bubbling pressure head and pore size distribution index were estimated by using the pedotransfer functions of Rawls and Brakensiek (1989). The saturated hydraulic conductivity was calculated by using the regression equation of Wösten et al. (1999). Values of all soil parameters needed by the model PROMET are regarded as time-invariant data and provided in tabular format, ensuring that soil properties of each soil type are assigned to their related spatially-distributed information.

Plant physiological parameters (which are assumed to be static) such as the minimum stomatal resistance, the slope parameter of the stomatal resistance with irradiance, the threshold value of leaf water potential, and cardinal temperature were estimated for each vegetation class using information taken from literature sources. While the landuse information is provided on a spatially distributed basis, the development of the different landuse categories over the year is provided in tabular format and daily increment. The plant growth is represented through the temporal evolution of the Albedo, LAI, plant height, and root depth. The temporal evolution of albedo for each individual land use class was derived from five cloud-free LANDSAT-7 images (acquired in different seasons) using the approach proposed by Gratton et al., (1993). Whereas, LAI values were derived from these images using a regression function proposed by Gowda et al., (2007) for estimating LAI for agricultural crops grown in semi-arid environment. The evolutions of plant height and root depth for each vegetation type were estimated based on the comprehensive database compiled by Allen et al., (1998).

The quality of the results obtained by the model PROMET were validated by comparing them either with their corresponding data measured in the field or with remote sensing-derived information. However, not all results that are simulated by the model can be covered by validation attempts. Validation processes were applied only to those results that are supported by measurement data. Remotely sensed data (time series of LANDSAT images) were also used to qualitatively validate some of the simulated spatially distributed results (e.g., snow cover and evapotranspiration). These data, however, offer only an instantaneous evaluation of the modelled results at a specific moment at which the satellite passes over the study region. Comparing the snow cover maps modelled by PROMET with their corresponding snow-cover maps derived from several LANDSAT images exhibits large similarities, and indicates that the spatial distribution of snow cover as well as its temporal dynamics were simulated with a good accuracy. In addition to that, remotely sensed thermal data (band 6 of LANDSAT images) were also used to qualitatively validate the modelled actual evapotranspiration patterns. The used approach is based on the fact that evapotranspiration directly affects the thermal regime of the land surface by its cooling effect on the surface temperature. The agreement between the simulated actual evapotranspiration pattern and the spatial pattern of the satellite-derived temperature difference (*surface temperature minus air temperature*) indicates that

the spatial distribution of evapotranspiration is well captured by the used model. Quantitative validation of the simulated rate of evapotranspiration can also be carried out by comparing it with the rate (the residual term) that can be indirectly calculated from the water balance equation. While the mean annual evapotranspiration rate for the entire study area for the period 1991-2005 was simulated to be 258 mm/y, the mean annual groundwater recharge rate was modelled to be 128mm/y. On the other hand, two subcatchments ("*Al-hama*" and "*Om al-sharait*") were chosen for the purpose of calculating the spatially-distributed annual water balances. The results indicate that the modelled mean annual runoff volume fits well with the measured discharge for both chosen subcatchment. In addition, the interannual (from year-to-year) variability of the runoff volume is well captured by the model. The negative and positive signs of the volumetric deviations between the simulated and measured runoff volumes indicate that there is no systematic over- or under-estimation of the simulated annual runoff. Furthermore, the simulated discharge was compared to the observed one (at seven gauge stations) on a monthly basis, covering the whole simulation period (15 years). The results of the regression analysis for each of these seven gauge stations (with slope of regression line ranges from 0.79 to 1.04; coefficient of determination 0.69-0.90; and Nash-Sutcliffe Coefficient 0.73-0.95) indicate that there is a good correlation between simulated and observed monthly mean discharge volumes.

10.2. Limitations of the study

Some of the problems, difficulties, and limitations that are encountered during the course of this study can be briefly summarized as follows:

- The lack of temporal high-resolution precipitation data (e.g., hourly or even 7-hourly time step) may be considered as one of the major limiting factors to hydrological modelling in the study area (only total daily precipitation measurements are available). The provision of the required hourly precipitation intensities, which was achieved by temporal disaggregation of these daily values, is expected to be subjected to high levels of uncertainty.
- Lack of comprehensive ground truth data required both to derive the land use map from satellite data, and to assess the accuracy of this map. The land use map which was used as a reference ground truth during the image classification process (using the LANDSAT7 ETM+ image) covers only the central part of the study area. Thus, the resulting overall classification accuracy (83.7%) does not represent the entire study area, but rather only its central part. Extrapolation of these ground truth data to areas with no ground truth may lead to inaccurate results (misclassification).
- Although the required land use map was derived from a LANDSAT image acquired at a single moment of time, the spatial distribution of the different land use types is assumed to be static (time-invariant) during the entire simulation

period (15years). This assumption is made for simplicity, but it may not be realistic for all land use classes.

- While the automated extraction of drainage network from digital elevation model (DEM) has given good results in the mountainous regions of the study area, it has failed to derive the stream network over the flat areas (in the plain of Damascus, where each river divides into several separate branches and artificial canals). Only the major channel of each river (over those flat areas) was successfully extracted from the DEM.
- Lack of a detailed soil-texture map, which is necessary for estimating the soil hydraulic properties for each soil-texture type existing within the simulated region. The soil-texture map used in this study, which was derived by the author through the separation of soil associations (on the soil map of Syria) into their constituent soil types and transfer the soil types into soil-texture classes, may be not accurate enough for purposes of soil parameterization.
- Due to the fact that not all plant-parameter values are fully documented in the available literature for all vegetation types existing within the study area, a number of simplifying assumptions were made during the estimation of some parameter values for some vegetation types.
- Lack of ground-based measurements of LAI for each individual vegetation type, which are required to develop regression models (LAI-NDVI) for estimating LAI at regional scale. Although caution was exercised in choosing an empirical LAI-NDVI relationship developed for use in environmental conditions similar to those found in the study area, the transferability of this relationship may possibly be influenced by exogenous factors and leads to inaccurate estimates of the LAI.
- Lack of river discharge data measured at short intervals (e.g., hourly, daily or even weekly), which are required to investigate how accurate does the model reproduce the measured discharge at those time-scales. The monthly average values are the only river discharge observations available from all existing gauge stations.
- Although the simplified groundwater storage model (array of linear storage elements) used in this study has given a satisfactory results, the study is still lacking the coupling of the model PROMET with a detailed physically based groundwater model (e.g., MODFLOW) for more accurate modelling of groundwater flow.
- PROMET in its current configuration is still lacking an irrigation model to provide the plants (especially those grown in the oasis of Damascus "*Ghouta*") with an adequate water supply, particularly in dry seasons.

10.3. Outlook and Recommendations

Outlook for future work would include the investigation of the impact of climate change on the hydrological regime and water resources of the Greater Damascus Basin. Due to the fact that PROMET is a physically-based model and does not

depend on calibrations carried out under present-day climate conditions, it is expected to be valid for simulating landsurface processes under future climate conditions. The meteorological input data required for the modelling of the different future scenarios will be generated through a proper stochastic rearrangement of historically measured weather data using a Stochastic Weather Generator (Mauser et al., 2007). On the other hand, while the required meteorological fields in this work were provided through interpolation and disaggregation of weather station data using the first sub-component of the meteorological component of PROMET, future work will be done using the second sub-component (the downscaling interface SCALMET), which enables the coupling of PROMET to the regional climate models, such as REMO, MM5 and CLM. Apart from these, PROMET will further be coupled with the groundwater model MODFLOW to simulate the groundwater-flow which represents a significant contribution to the water balance of the Greater Damascus Basin, especially in low flow periods. Furthermore, the achievements of this study provide a broad and comprehensive basis for further (geo-) environmental studies within this basin. For example, in order to delineate the groundwater protection against pollution zones (or to prepare the groundwater vulnerability maps), input information related to soils, climatology, hydrology, hydrogeology, and geology will be required. Most of this required information is now available in digital format and integrated into a GIS.

However, although the present study has answered a lot of questions concerning the modelling of landsurface processes within the study area, there are still many questions that need to be answered in future studies. For example, will a higher spatial resolution of model input data necessarily lead to a better model performance and what effect does the rain-gauge network density have on the simulated results?

A key recommendation of this study is to take full advantage of the results obtained by using the model PROMET in the study area together with all input information (parameters) in order to develop strategies for sustainable use and management of natural resources (especially fresh water), taking into consideration potential future change in climate and socio-economic conditions. However, even in the case of a neutral climate change scenario, which assumes no precipitation decrease (and no further temperature increase) in the future, the Greater Damascus basin is expected to suffer from further water shortages. This can mainly be attributed to the increasing water demand caused by the economic development and the rapid growth of population. Therefore, to cope with this situation, several strategies and mitigation measures can initially be recommended, including:

- Utilizing the available water resources more effectively and more efficiently. Here it should be mentioned that the agricultural sector consumes most of the available water resources in the study area. Substituting traditional irrigation methods with modern water-saving techniques (such as the use of sprinkler or drip systems) can be considered an appropriate local solution to water shortage problems in the region.

- If possible, replace the intensively irrigated agriculture with rainfed (non-irrigated) agriculture.
- Reallocating the available water from agriculture sector to meet the needs of other sectors (e.g., domestic and industrial uses), especially during periods of drought.
- Due to the fact that groundwater constitutes the major source of the water supply in the study area, it should be protected against pollution and over-exploitation.
- Finally, alternative solutions (but very expensive) which can also be recommended to cope with the increasing demand of water resources are: 1) desalinating seawater on the eastern shore of the Mediterranean Sea, 2) inter-basin water transfer from another “water-surplus” basins (such as Euphrates River and Coastal Region). However, it should be taken into account that the transfer of water from one basin to another, which seems to be a reasonable solution to water shortage at the present day, may not be possible in the future. This is because it is not certain that the basins that are still in “water-surplus” today will be always in surplus in the future.

11. References

- Ahmad, N. (1996): Vertisols and technologies for their management. Elsevier Science.
- Akkad, B. (2001): Driving forces of land use change in Syria 2001. Euro-Mediterranean Information System on know-how in the Water sector, SEMIDE/ EMWIS.
- Allen, R.G. (2005), The ASCE standardized reference evapotranspiration equation. American Society of Civil Engineers.
- Allen, R.G. and Pereira, L.S. and Raes, D. and Smith, M. and others, (1998): Crop evapotranspiration-Guidelines for computing crop water requirements-FAO Irrigation and drainage paper 56. FAO, Rome, Volume 300.
- Al-Qinna, M.I. and Salahat, M.A. and Shatnawi, Z.N. (2010): Effect of Carbonates and Gravel Contents on Hydraulic properties in Gravely-Calcareous Soils. Dirasat: Agricultural Sciences, Volume 35, Issue 2.
- Al-Qudah, B. (2001): Soils of Jordan. Soil resources of southern and eastern Mediterranean countries. CIHEAM-IAMB, Bari, pp.127-141.
- Armstrong, R.N., Martz, L.W. (2003): Topographic parameterization in continental hydrology: a study in scale. *Hydrological Processes*, volume 17, Issue 18, pp. 3763-3781.
- Arya, S.P. (2001): Introduction to the micrometeorology. Academic Press.
- Aswathanarayana, U. (1995): Geoenvironment: an introduction. AA Balkema.
- Bach, H., Braun, M., Lampart, G., Mauser, W. (2003): Use of remote sensing for hydrological parameterisation of Alpine catchments. *Hydrology and Earth System Sciences*, Volume 7, Issue 6, pp. 862-876, CiteSeer.
- Badhwar, G.D. and MacDonald, R.B. (1986): Satellite-derived leaf-area-index and vegetation maps as input to global carbon cycle models- a hierarchical approach. *International Journal of Remote Sensing*, Volume 7, Issue 2, pp. 265-281, Taylor & Francis.
- Baird, A.J. and Wilby, R.L. (1999): Eco-hydrology: plants and water in terrestrial and aquatic environments. Routledge.
- Baldocchi, D.D. and Hicks, B.B. and Camara, P. (1987): A canopy stomatal resistance model for gaseous deposition to vegetated surfaces. *Atmospheric Environment*, Volume 21, Issue 1, pp. 91-101, Elsevier.
- Baret, F. and Guyot, G. (1991): Potentials and limits of vegetation indices for LAI and APAR assessment. *Remote Sensing of Environment*, Volume 35, Issue 2-3, pp. 161-173, Elsevier.
- Barrett, E.C. and Curtis, L.F. (1999): Introduction to environmental remote sensing. Routledge.
- Barrio, A.M. (2004): Environmental challenges in the Mediterranean 2000-2050. Volume 37, Springer Netherlands.
- Barry, R.G. (1992): Mountain Weather and climate. Routledge, London.
- Barthel, R. and Rojanschi, V. and Wolf, J. and Braun, J. (2005): Large-scale water resources management within the framework of GLOWA-Danube. Part A: The

- groundwater model. *Physics and Chemistry of the Earth, Parts A/B/C*, Volume 30, Issue 6-7, pp. 372-382, Elsevier.
- Barthel, R., Mauser, W., Braun, J. (2007): Integrated modelling of global change effects on the water cycle in the upper Danube catchment (Germany) - the groundwater management perspective. *Groundwater flow understanding: from local to regional scale*, Volume 12, pp. 47 -72.
- Bazza, M. and Najib, R. (2003): Towards improved water demand management in agriculture in the Syrian Arab Republic. The First National Symposium on Management and Rationalization of water Resources Use in Agriculture organized by the University of Damascus, Arab Republic of Syria. FAO, Rome.
- Bear, J. (1988): *Dynamics of fluids in porous media*. Dover Publications.
- Begg, J.E. and Turner, N.C. (1976): Crop water deficits. *Advances in Agronomy*, Volume 28, Issue 16, Elsevier BV, Radarweg 29, Amsterdam, 1043 NX, United States.
- Beniston, M. (2002): *Climatic change: implications for the hydrological cycle and for water management*. Springer Netherlands.
- Berger, A. and Schneider, S.H. and Duplessy, J.C. (1989): *Climate and Geo-sciences: A Challenge for Science and Society in the 21st Century*, Springer.
- Berger, L. (1982): *Land Classification/ Soil Survey Project of the Syrian Arab Republic*, Volume 3, International, Inc. East Orange, New Jersey, U.S.A.
- Beven, K. (1989): Changing ideas in hydrology- The case of physically-based models. *Journal of hydrology*, Volume 105, Issue 1-2, pp. 157-172, Elsevier.
- Blackburn, G.A. and Pitman, J.I. (1999): Biophysical controls on the directional spectral reflectance properties of bracken (*Pteridium aquilinum*) canopies: results of a field experiment. *International Journal of Remote Sensing*, Volume 20, Issue 11, pp. 2265-2282, Taylor & Francis.
- Bobrowsky, P.T. and Fakundiny, R.H. (2002): *Geoenvironmental mapping: methods, theory and practice*. *Environmental and Engineering Geoscience*, Volume 8, Issue 4, pp. 335, Association of Engineering Geologists.
- Bonan, G.B. (2002): *Ecological climatology: concepts and applications*. Cambridge University Press.
- Borengasser, M. Hungate, W.S. and Watkins, R. (2007): *Hyperspectral Remote Sensing: Principles and Applications*. CRC Press.
- Bowles, D.S. and O'Connell, P.E. (1991): *Recent advances in the modelling of hydrologic systems*. Springer.
- Brady, N.C. and Weil, R.R. (1996): *The nature and properties of soils*. Issue Ed.11, Prentice-Hall Inc.
- Brakensiek, D.L. and Rawls, W.J. (1994): Soil containing rock fragments: effects on infiltration. *Catena*, Volume 23, Issue 1-2, pp. 99-110, Elsevier.
- Brakensiek, D.L. and Rawls, W.J. and Stephenson, G.R. (1986): A note on determining soil properties for soils containing rock fragments. *Journal of Range Management*, Volume 39, Issue 5, pp. 408-409.

- Briggs, D.J. and Smithson, P. (1986): Fundamentals of physical geography. Rowman & Littlefield Publishers, Inc.
- Brooks, R.H. and Corey, A.T. (1964): Hydraulic properties of porous media. Hydrology Paper 3, Colorado State University, Fort Collins, CO.
- Brown, R.B. (2008): Soil Texture. Fact Sheet SL-29. Soil and Water Science Department, University of Florida, Institute of Food and Agricultural Sciences.
- Buchroithner, M.F. (2001): A Decade of Trans-European Remote Sensing Cooperation: Proceedings of the 20th EARSeL Symposium, Dresden, Germany, Taylor & Francis.
- Buiten, H.J. and Clevers, J.G.P.W. (1994): Land observation by remote sensing: theory and applications. Volume 3, CRC Press.
- Burns, R. (2005): Damascus: a history. Routledge, Psychology Press.
- Campbell, G.S. and Norman, J.M. (1998): An Introduction to Environmental Biophysics. Springer, New York.
- Campbell, J.B. (2002): Introduction to remote sensing. Taylor & Francis, 621 pages.
- Canty, M.J. (2006): Image analysis, classification and change detection in remote sensing: with algorithm for ENVI/IDL. CRC Press, 348 pages.
- Caroline, G.H. and Raffy, M. (1997): Elaboration of multispectral models for heterogeneous media: Application to the LAI. Remote sensing Reviews, Volume 15, Issue 1, pp. 223-234, Taylor and Francis.
- Certini, G. and Scalenghe, R. and Ugolini, F.C. (2006): Soils: basic concepts and future challenges, Cambridge University Press.
- Chang, J.H. (2009): Climate and agriculture: an ecological survey, Aldine De Gruyter.
- Chapin, F.S. and Matson, P.A. and Mooney, H.A. (2002): Principles of terrestrial ecosystem ecology. Springer.
- Chen, C. (2007): Signal and image processing for remote sensing. Volume 978, CRC Press, 648 pages.
- Chikhali, M. (2008): Flora Syria On Line, Natural Environment Consultant. <http://florasyria.com/>
- Chuchip, K. (1997): Satellite Data Analysis and Surface Modelling for Land Use and Land Cover Classification in Thailand. Technical University Berlin, Institute for Geography.
- Congalton, R.G. and Green, K. (1999): Assessing the Accuracy of Remotely sensed Data: Principles and Practices (Boca Raton, FL: Lewis).
- Cunge, J.A. (1969): On the subject of a flood propagation computation method (Muskingum method). Journal of Hydraulic Research, Volume 7, Issue 2, pp. 205-230, Taylor and Francis.
- De Jong, C. and Collins, D.N. and Ranzi, R. (2005): Climate and hydrology in mountain areas. Wiley Online Library.
- De Jong, S.M. and Van der Meer, F. (2004): Remote sensing image analysis: including the spatial domain. Kluwer Academic Publishers.
- De Pauw, E. (2001): An agroecological exploration of the Arabian Peninsula. Icarda.

- DeBarr, P.A. and Quimpo, R.G. (1999): GIS Modules and Distributed Models of the Watershed: report, American Society of Civil Engineers.
- Dharani, N. (2006): Field Guide to Acacias of East Africa, Struik Publishers.
- Dooge, J.C.I. (1992): Hydrologic models and climate change. Journal of Geophysical Research, Volume 97, Issue D3, pp. 2677-2686, American Geophysical Union.
- Drury, S.A. (2001): Image interpretation in geology, Routledge.
- Eagleson, P.S. (1978): Climate, soil and vegetation: 3. A simplified model of soil movement in the liquid phase. Water Resources Research, Volume 14, Issue 5, pp. 722-730, American Geophysical Union.
- Easa, S. and Chan, Y. (2000): Urban Planning and development applications of GIS. American Society of Civil Engineers.
- Eastman, J.R. (2006): IDRISI Andes: Guide to GIS and Image Processing. Worcester, USA. Clark University.
- Edwards-Jones, G. (2001): Final Report on Agricultural Policy and the environment in Syria: An examination of impacts and suggestions for policy reform.
- El Nadi, A.H. and Hudson, J.P. (1965): Effects of Crop Height on Evaporation from Lucerne and Wheat Grown in Lysimeters under Advective Conditions in the Sudan. Experimental Agriculture, Volume 1, Issue 4, pp. 289- 298, Cambridge University Press.
- ERDAS (2006) : ERDAS Imagine Tour Guides. Leica Geosystems Geospatial Imaging, LLC, USA
- Ernst, W.G. (2000): Earth systems: processes and issues, Cambridge University Press.
- ESRI (2005): ArcGIS Desktop Help. Environmental Systems Research Institute, Inc.
- Fageria, N.K. and Baligar, V.C. and Clark, R.B. and Clark, RB. (2006): Physiology of crop production, CRC.
- Fan, L. and Gao, Y. and Brück, H. and Bernhofer, C. (2009): Investigating the relationship between NDVI and LAI in semi-arid grassland in Inner Mongolia using in-situ measurements. Theoretical and Applied Climatology, Volume 95, Issue 1, pp. 151-156, Springer.
- FAO / ISRIC, (2001): Major Landforms in (semi) arid regions. Published in conjunction with the book "Lecture Notes on the Major Soils of the World"
- FAO ECOCROP database: <http://ecocrop.fao.org/ecocrop/srv/en/cropSearchForm>
- Farquhar, G.D. and Caemmerer, S. and Berry, J.A. (1980): A biochemical model of photosynthetic CO₂ assimilation in leaves of C3 species. Planta, Volume 149, Issue 1, pp. 78-90, Springer.
- Froukh, L.J. (2002): Groundwater Modelling in Aquifers with highly Karstic and Heterogeneous Characteristics (KHC) in Palestine. Water Resources Management, Volume 16, Issue 5, pp. 369 -379, Springer.
- Gao, J. (2009): Digital analysis of remotely sensed imagery. McGraw-Hill Professional.
- Garbrecht J. and Martz, L.W. (1999): TOPAZ: An Automated Digital Landscape Analysis Tool for Topographic Evaluation, Drainage Identification, Watershed

- Segmentation and Subcatchment Parameterization: TOPAZ Overview. United States Department of Agriculture, Agricultural Research Service.
- Garbrecht, J. and Martz, L.W. (2000): Digital elevation model issues in water resources modeling. Hydrologic and hydraulic modeling support with geographic information systems, pp. 1-28, Redlands, CA: ESRI Press.
- Garbrecht, J., and Martz, L.W. (1997): The assignment of drainage direction over flat surfaces in raster digital elevation models. *Journal of Hydrology*, Volume 193, Issue 204-213, Elsevier.
- Gerard, K. (1998): Environmental engineering. International Edn. McGraw-Hill.
- Gibson, P.J. and Power, C.H. (2000): Introductory Remote Sensing: Digital Image Processing and Applications, Routledge, 249 pages.
- Glowa-Danube, (2009): <<http://www.GLOWA-danube.de>>
- Gonzalez-Sanpedro, M.C. and Le Toan, T. and Moreno, J. and Kergoat, L. and Rubio, E. (2008): Seasonal variations of leaf area index of agricultural fields retrieved from Landsat data. *Remote Sensing of Environment*, Volume 112, Issue 3, pp. 810-824, Elsevier.
- Goodchild, M.F. and Parks, B.O. and Steyaert, L.T. (1993): Environmental modelling with GIS. Oxford University Press, USA.
- Goudie, A. (2001): The nature of the environment, Wiley-Blackwell.
- Gowda, P.H. and Chavez, J.L. and Colaizzi, P.D. and Howell, T.A. and Schwartz, R.C. and Marek, T.H. (2007): Relationship between LAI and Landsat TM Spectral Vegetation Indices in the Texas Panhandle, ASABE Annual International Meeting, Minneapolis, Minnesota.
- Gratton, D.J. and Howarth, P.J. and Marceau, D.J. (1993): Using Landsat-5 Thematic Mapper and digital elevation data to determine the net radiation field of a mountain glacier. *Remote Sensing of Environment*, Volume 43, Issue 3, pp. 315-331, Elsevier.
- Gregorio, A.D. and Jansen, L. J.M. (1998) Land Cover Classification System (LCCS): Classification Concepts and User Manual. Food and Agriculture Organization of the United Nations (FAO), Rome.
- Gupta, R.P. (2003): Remote sensing geology. Springer, 655 pages.
- Han, F.X. and Singer, A. (2007): Biogeochemistry of trace elements in arid environments, Springer.
- Hank, T.B. (2008): A biophysically based coupled model approach for the assessment of canopy processes under climate change conditions. Ludwig-Maximilians-Universität München.
- Harbaugh, A.W. Banta, E.R. Hill, M.C. McDonald, M.G. (2000): MODFLOW-2000. The US Geological Survey Modular Ground-Water Model–User Guide to Modularization Concepts and the Ground-Water Flow Process. US Geological Survey.
- Harpstead, M.I. and Sauer, T.J. and Bennett, W.F. (2001): Soil science simplified. Wiley-Blackwell.

- Haude, W. (1955): Zur Bestimmung der Potentiellen Verdunstung auf möglichst einfache Weise. Mitteilungen des Deutschen Wetterdienstes, Volume 2, Issue 11, pp.1-24.
- Healy, R. and Scanlon, B. (2010): Estimating groundwater recharge, Cambridge University Press.
- Higano, Y. and Melhem, R. (2002): Endogenous derivation of the optimal policy measures to improve the water quality in Barada Basin, Syria. ERSA conference papers, European Regional Science Association.
- Hillel, D. (1998): Environmental soil physics, Academic Press.
- Hodges, T. (1991): Predicting crop phenology, CRC.
- Hoekstra, T.W. and Shachak, M. (1999): Arid lands management: toward ecological sustainability, University of Illinois Press.
- Hoffman, R.R. and Markman, A.B. (2001): Interpreting remote sensing imagery: human factors. CRC Press, 289 pages.
- Hoffmann, F. Köppen, M. Klawonn, F. and Roy R. (2005): Soft computing: methodologies and applications. Advances in Soft Computing, Volume 32, Springer.
- Holben, B. and Justice, C. (1981): An examination of spectral band ratioing to reduce the topographic effect on remotely sensed data. International Journal of Remote Sensing, Volume 2, Issue 2, pp. 115-133, Taylor & Francis.
- Holden, J. (2005): An introduction to physical geography and the environment. Pearson Education.
- Huang, C. Wylie, B. Homer, C. Yang, L. and Zylstra, G. (2002): Derivation of a Tasseled cap transformation based on Landsat 7 at-satellite reflectance. International Journal of Remote Sensing, Volume 23, Issue 8, pp. 1741-1748, Taylor and Francis.
- Hudak, P.F. (2005): Principles of hydrogeology, CRC
- Huggett, R.J. and Cheesman, J. (2002): Topography and the Environment. Pearson Education.
- Huston, M.A. (1994): Biological diversity: the coexistence of species on changing landscapes, Cambridge University Press.
- Ilaiwi, M. (2001): Soil of the Syrian Arab Republic. Soil Resources of Southern and Eastern Mediterranean countries, pp. 227 -243.
- Irish, R.R. (2000): Landsat 7 automatic cloud cover assessment. Proceedings-SPIE the International Society for Optical Engineering, pp. 348-355.
- Jackson, J.E. (2003): Biology of apples and pears, Cambridge University Press.
- Jacobs, J.J. and Jacobs, J.A. and Guertin, J. and Herron, C. (2001): Effects on soil and groundwater resources. CRC Press.
- Jain, S.K. and Agarwal, P.K. and Singh, V.P. (2007): Hydrology and water resources of India. Volume 57, Springer.
- Jarvis, P.G. (1976): The interpretation of the variations in leaf water potential and stomatal conductance found in canopies in the field. Philosophical Transactions

- of the Royal Society of London. Series B, Biological Sciences, Volume 273, Issue 927, pp. 593-610, The Royal Society.
- Jenny, H. (1994): Factors of soil formation: a system of quantitative pedology. Courier Dover Publications.
- Jensen, J.R. (1986): Introductory digital image processing: A remote sensing perspective. University of South Carolina, Columbus.
- Jenson, S.K., and Domingue, J.O. (1988): Extracting Topographic Structure from Digital Elevation Data for Geographical information System Analysis. Photogrammetric Engineering and Remote Sensing, Volume 54, Issue 11, pp. 1593-1600, CiteSeer.
- Jones, H.G. (1992): Plants and microclimate: a quantitative approach to environmental plant physiology, Cambridge University Press.
- Joseph, G. (2005): Fundamentals of Remote Sensing. Universities Press, 486 pages.
- Kappas, M. Kleinn, C. and Sloboda, B. (2007): Global Change Issues in Developing and Emerging Countries: Proceedings of the 2nd Göttingen GIS and Remote Sensing Days, Universitätsverlag Göttingen.
- Karimi, H.A. and Hammad, A. (2004): Telegeoinformatics: location-based computing and services. CRC Press.
- Kattan, Z. (1997): Environmental isotope study of the major karst springs in Damascus limestone aquifer systems: case of the Figeheh and Barada springs. Journal of Hydrology, Volume 193, Issue 1-4, pp. 161-182, Elsevier.
- Kelliher, F.M. and Leuning, R. and Raupach, M.R. and Schulze, E.D. (1995): Maximum conductances for evaporation from global vegetation types. Agricultural and Forest Meteorology, Volume 73, Issue 1-2, pp. 1-16, Elsevier.
- Kennedy, M. (2006): Introducing Geographic Information Systems with ArcGIS: featuring GIS software from environmental systems research institute, Wiley.
- Kirkham, M.B. (1999): Water use in crop production, CRC.
- Kirkham, M.B. (2005): Principles of soil and plant water relations, Academic Press.
- Kite, G.W. and Droogers, P. (2000): Integrated basin modeling, Iwmi.
- Kolay, A.K. (2007): Soil Genesis, Classification Survey and Evaluation. Volume 2, Atlantic Publishers & Distributors.
- Körner, C. (1994): Leaf diffusive conductances in the major vegetation types of the globe. In: Schulze, E-D. and Caldwell, M.M. (1995): Ecophysiology of Photosynthesis. Springer.
- Kotlarski, S. and Block, A. and BAhm, U. and Jacob, D. and others, (2005): Regional climate model simulations as input for hydrological applications: evaluation of uncertainties. Advances in Geosciences, Volume 5, pp. 119-125, CiteSeer.
- Kraak, M.J. and Ormeling, F. (2003): Cartography: visualization of geospatial data, Pearson Education.
- Kuligowski, R. and Parihar, J. and Saito, G. (2006): Agriculture and hydrology applications of remote sensing. Society of Photo-Optical Instrumentation Engineers (SPIE) Conference Series.

- Lagacherie, P. and McBratney, A.B. and Voltz, M. (2007): Digital soil mapping: an introductory perspective. Volume 31, Elsevier Science.
- Lal, R. (2006): Encyclopedia of soil science, Taylor and Francis.
- Lambers, H. and Chapin, F.S. and Pons, T.L. (2008): Plant physiological ecology, Springer.
- Latham, J. (1998): FAO Land Cover Mapping Initiatives. Environment and Natural Resources Service, Food and Agriculture Organization of the United Nations (FAO).
- Lavelle, P. and Spain, A.V. (2002): Soil ecology. Springer Netherlands.
- Lazaridis, M. (2010): First Principles of Meteorology and Air Pollution. Volume 19, Springer.
- Legros, J.P. (2006): Mapping of the soil. Science Publishers, Inc.
- Lillesand, T. and Kiefer, R.W. (1994): Remote Sensing and Image Interpretation. John Wiley and Sons Inc., New York.
- Lindgren, D.T. (1985): Land use planning and remote sensing. Springer.
- Liston, G.E. and Elder, K. (2006): A meteorological distribution system for high-resolution terrestrial modelling (MicroMet). Journal of Hydrometeorology, Volume 7, Issue 2, pages 217-234, American Meteorological Society.
- Lo, C.P. (1986): Applied remote sensing. John Wiley and Sons Inc., New York, NY.
- Loelkes, G.L. (1983): Land Use / Land Cover and Environmental Photointerpretation Keys. US Geological Survey.
- Lu, L. and Li, X. and Ma, MG and Che, T. and others, (2004): Investigating relationship between Landsat ETM+ data and LAI in a semi-arid grassland of Northwest China. IEEE International Geoscience and Remote Sensing Symposium, Volume 6.
- Ludwig, R. (2000): Die flächenverteilte Modellierung von Wasserhaushalt und Abflußbildung im Einzugsgebiet der Ammer [Spatially Distributed Modelling of Water Balance and Runoff Formation in the Ammer Catchment]. In: Münchener Geographische Abhandlungen, Series B, Volume 32, pp. 173.
- Ludwig, R. and Mauser, W. (2000): Modelling catchment hydrology within a GIS based SVAT-model framework. Hydrology and Earth System Sciences, Volume 4, Issue 2, pp.239-249.
- Ludwig, R. and Mauser, W. and Niemeyer, S. and Colgan, A. and others, (2003): Web-based modelling of energy, water and matter fluxes to support decision making in mesoscale catchments- the integrative perspective of GLOWA-Danube. Physics and chemistry of the Earth, Parts A/B/C, Volume 28, Issue 14-15, pp. 621-634, Elsevier.
- Lydolph, P.E. (1985): Weather and climate. Rowman & Littlefield Publishers, Inc.
- Lyon, J.G. (2003): GIS for Water Resources and Watershed Management. CRC Press.
- Ma, M. and Veroustraete, F. and Lu, L. and Li, X. (2007): Validating the MODIS LAI product by scaling up LAI measurements at a VALERI alpine meadow site in

- China. Proceedings of SPIE, Volume 6742, International Society for Optical Engineering.
- Maidment, D.R. (2002): Arc Hydro: GIS for Water Resources. Redlands, CA: ESRI Press.
- Maidment, D.R. and Djokic, D. (2000): Hydrologic and Hydraulic Modeling Support with Geographic Information Systems. Environmental Systems Research Institute, Inc., Redlands California.
- Marke, T. (2008): Development and Application of a Model Interface to couple Land Surface Models with Regional Climate Models for Climate Change Risk Assessment in the Upper Danube Watershed. Ludwig-Maximilians-Universität München.
- Marke, T. Mauser, W. (2008): SCALMET- a tool for bidirectional coupling of climate models with physically-based simulations of land surface processes. In: Borsdorf, A. Stötter, J. Veulliet, E. (Eds.), Managing Alpine Future- IGF Forschungsberichte, Volume 2, Verlag der Österreichischen Akademie der Wissenschaften, Innsbruck, Austria, pp. 216-225.
- Markham, B.L. and Barker, J.L. (1986): Landsat MSS and TM post-calibration dynamic ranges, exoatmospheric reflectances and at-satellite temperatures. EOSAT Landsat Technical Notes, Volume 1.
- Martin-Duque, J.F. and Brebbia, C.A. and Godfrey, A.E. (2004): Geo-environment. WIT Press, Computational Mechanics.
- Martz, L.W. and Garbrecht, J. (1992): Numerical definition of drainage network and subcatchment areas from digital elevation models. Computers and Geosciences, Volume 18, Issue 6, pp. 747-761, Elsevier.
- Martz, L.W. Garbrecht, J. (1999): An outlet breaching algorithm for the treatment of closed depressions in a raster DEM. Computers and Geosciences, Volume 25, Issue 7, pp. 835-844, Elsevier.
- Mather, P.M. (2004): Computer processing of remotely-sensed images: an introduction. Wiley and Sons.
- Mauser, W. (2002): GLOWA-Danube Papers Technical Release No. 3 (MeteoStationsData), Software-Release-No.: 0.9, Documentation Version: 0.9_01, Release Date: Jan 2002. Tech. rep., GLOWA-Danube Project.
- Mauser, W. and Bach, H. (2009): PROMET-Large scale distributed hydrological modelling to study the impact of climate change on the water flows of mountain watersheds. Journal of Hydrology, Volume 376, Issue 3-4, pp. 362-377, Elsevier.
- Mauser, W. and Prasch, M. and Strasser, U. (2007): Physically based modelling of climate change impact on snow cover dynamics in Alpine Regions using a stochastic weather generator. MODSIM 2007 International Congress on Modelling and Simulation. Modelling and Simulation Society of Australia and New Zealand, pp. 2138- 2145.

- Mauser, W. and Schädlich, S. (1998): Modelling the spatial distribution of evapotranspiration on different scales using remote sensing data. *Journal of Hydrology*, Volume 212, pp. 250-267, Elsevier.
- McBratney, A.B. and Minasny, B. and Cattle, S.R. and Vervoort, R.W. (2002): From pedotransfer functions to soil inference systems. *Geoderma*, Volume 109, Issue 1-2, pp. 41-73, Elsevier.
- McClatchey, R.A. Fenn, R.W. Selley, E.A. Volz, F.E. Garing, J.S. (1972): *Optical Properties of the Atmosphere*, third ed. Air-Force Cambridge Research Laboratories, Environmental Research Paper No. 411.
- McGinnies, W.G. and Goldman, B.J. (1968): *Deserts of the World*. Tucson: The University of Arizona Press.
- Meigs, P. (1953): World distribution of the arid and semiarid homoclimates. In: *Review of research of arid zone hydrology*, Volume 1, UNSECO, Paris, pp. 203-209.
- Meyers, T. and Tha Paw U.K. (1986): Testing of a higher-order closure model for modeling airflow within and above plant canopies. *Boundary-Layer Meteorology*, Volume 37, Issue 3, pp. 297-311, Springer.
- Miller, D.A. and White, R.A. (1998): A conterminous United States multilayer soil characteristics dataset for regional climate and hydrology modelling. *Earth Interactions*, Volume 2, Issue 2, pp. 1-26.
- Ministry of State for Environment Affairs- Syria, (2003): *Strategy and National Environmental Action Plan for the Syrian Arab Republic*.
- Mohamed, A.M.O. and Antia, H.E. (1998): *Geoenvironmental engineering*. Elsevier Science.
- Monteith, J.L. (1965): Evaporation and environment. *Symp. Soc. Exp. Biol*, Volume 19, pp. 205-234.
- Monteith, J.L. (1973): *Principles of Environmental Physics*. Elsevier, New York.
- Monteith, J.L. and Unsworth, M.H. (2008): *Principles of environmental physics*. Academic Press. .
- Moore I.D. Grayson R.B. Ladson A.R. (1991): Digital terrain modeling: a review of hydrological, geomorphological and biological application. *Hydrological processes*, Volume 5, Issue 1, pp. 3-30, Wiley Online Library.
- Möser, W. Raschke, E. (1983): Mapping of Global Radiation and Cloudiness from METEOSAT Image Data. *Meteorologische Rundschau*, Volume 36, pp. 33-37.
- Muerth, M. (2008): A soil temperature and energy balance model for integrated assessment of Global change impacts at the regional scale, Ludwig-Maximilians-Universität München.
- Nag, P. and Kudrat, M. (1998): *Digital remote sensing*, Concept Publishing Company.
- Nash, J.E. and Sutcliffe, J.V. (1970): River flow forecasting through conceptual models, a discussion of principles. *Journal of hydrology*, Volume 10, Issue 3, pp. 282-290, Elsevier.
- Navulur, K. (2006): *Multispectral Image analysis using the object-oriented paradigm*. CRC Press, 165 pages.

- Nemani, R. and Pierce, L. and Running, S. and Band, L. (1993): Forest ecosystem processes at the watershed scale: sensitivity to remotely-sensed leaf area index estimates. *International Journal of Remote Sensing*, Volume 14, Issue 13, pp. 2519-2534, Taylor & Francis.
- Nemani, R.R. and Running, S.W. (1989): Testing a theoretical climate-soil-leaf area hydrologic equilibrium of forests using satellite data and ecosystem simulation. *Agricultural and Forest Meteorology*, Volume 44, Issue 3-4, pp. 245-260, Elsevier.
- Newton, A.C. (2007): *Forest ecology and conservation: a handbook of techniques*. Oxford University Press, USA.
- Nichols, J.D. and Brown, P.L. and Grant, W.J. (1984): Erosion and productivity of soils containing rock fragments: proceedings of a symposium, American Society of Agronomy.
- Norman, J.M. (1979): Modelling the complete plant canopy. In: *Modification of the Areal Environment of Plants*, American Society of Agricultural Engineers, pp. 248-277.
- Nützmann, G. and Viotti, P. and Aagaard, P. (2005): *Reactive transport in soil and groundwater: Processes and models*. Springer.
- O'Callaghan J.F. Mark D.M. (1984): The extraction of drainage networks from digital elevation data. *Computer vision, Graphics and Image Processing*, Volume 28, Issue 3, pp.323-344, Elsevier.
- Ojima, D.S. and Svensson, B.H. (1992): *Trace gas exchange in a global perspective*. Wiley-Blackwell, 206 pages.
- Pachepsky, Y. and Radcliffe, D.E. and Selim, H.M.E. (2003): *Scaling methods in soil physics*, CRC.
- Pachepsky, Y. and Rawls, W.J. (2004): *Development of pedotransfer functions in soil hydrology*. Elsevier Science.
- Packham, J.R. and Harding, D.J. and Hilton, GM and Stuttard, RA. (1992): *Functional ecology of woodland and forests*, Springer.
- Pandey, B.W. (2002): *Geoenvironmental hazards in Himalaya: assessment and mapping: the Upper Beas Basin*. Mittal Publications.
- Park, C.C. (2001): *The environment: principles and applications*, Routledge.
- Peckham, R.J. and Jordan, G. (2007): *Digital Terrain Modelling: Development and Applications in a Policy Support Environment*. Springer.
- Peixoto, J.P. and Oort, A.H. (1992): *Physics of climate*, Springer.
- Peng, G. and Leslie, L.M. and Shao, Y. (2002): *Environmental modelling and prediction*. Springer.
- Perera, A. and Euler, D. and Thompson, I. (2001): *Ecology of a managed terrestrial landscape: patterns and processes of forest landscapes in Ontario*. University of British Columbia Press.
- Philip, J.R. (1957): The theory of infiltration: 1.The infiltration equation and its solution. *Soil Science*, Volume 83, Issue 5.

- Pilgrim, D.H. and Chapman, T.G. and Doran, D.G. (1988): Problems of rainfall-runoff modelling in arid and semiarid regions. *Hydrological Sciences Journal*, Volume 33, Issue 4, pp. 379-400, Taylor & Francis.
- Pontauiller, J.Y. and Hymus, G.J. and Drake, B.G. (2003): Estimation of leaf area index using ground-based remote sensed NDVI measurements: validation and comparison with two indirect techniques. *Canadian Journal of Remote Sensing*, Volume 29, Issue 3, pp. 381-387, Ottawa: Canadian Aeronautics and Space Institute.
- Pouncey, R. Swanson, K. and Hart, K. (1999): *ERDAS Field Guide*, Fifth Edition, ERDAS, Inc. Atlanta, Georgia.
- Prasch, M. Strasser, U. Mauser, W. (2007): Validation of a physically based snow model for the simulation of the accumulation and ablation of snow (ESCIMO). In: *Proceedings of the Alpine Snow Workshop 2006*, Germany. Berchtesgaden National Park Research Report No. 53, pp. 78-91.
- Price, J.C. (1989): Quantitative aspects of remote sensing in the thermal infrared. *Theory and applications of optical remote sensing*, pp. 578- 603, New York: John Wiley and Sons.
- Propastin, P. and Kappas, M. (2009): Mapping Leaf Area Index over semi-desert and steppe biomes in Kazakhstan using satellite imagery and ground measurements. *EARSel eProceedings*, Volume 8, Issue 1, pp. 75-92.
- Quinn, P. Beven, K. Chevallier, P. and Planchon, O. (1991): The prediction of hillslope flow paths for distributed hydrological modelling using digital terrain models. *Hydrological Processes*, Volume 5, Issue 1, pp. 59 -79, Wiley Online Library.
- Rajan, S.S. (2002): *Plant Physiology*. Anmol Publications PVT. LTD, 532 pages.
- Ramsey, R.D. and Wright, D.L. and McGinty, C. (2004): Evaluating the use of Landsat 30m Enhanced Thematic Mapper to monitor vegetation cover in shrub-steppe environments. *Geocarto international*, Volume 19, Issue 2, pp. 39-47, Taylor & Francis.
- Ranzi, R. and Rosso, R. (1995): Distributed estimation of incoming direct solar radiation over a drainage basin. *Journal of Hydrology*, Volume 166, Issue 3-4, pp. 461-478, Elsevier.
- Raupach, M.R. (1995): Vegetation-atmosphere interaction and surface conductance at leaf, canopy and regional scales. *Agricultural and Forest Meteorology*, Volume 73, Issue 3-4, pp. 151-179, Elsevier.
- Rawls, W.J. Brakensiek, D.L. (1989): Estimation of soil water retention and hydraulic properties. In: Morel-Seytoux, H.J. (Ed.), *Unsaturated Flow in Hydrologic Modelling: Theory and Practice*. Kluwer Academic Publishers, pp. 275-300.
- Razvalyaev, A.V. and Ponikarov, V.P. (1966): *The Geological Map of Syria*, Scale 1:200,000, Sheets I-37-VII (Dimashq) I-36-XII (Beirout), Explanatory Notes.
- Reddy, K.R. and Hodges, H.F. (2000): *Climate change and global crop productivity*, CABI.

- Refsgaard, J.C. and Abbott, M.B. (1996): The role of distributed hydrological modelling in water resources management. *Distributed Hydrological Modelling*, Kluwer, The Netherlands.
- Richards, J.A. and Jia, X. (2006): *Remote sensing digital image analysis: an introduction*, Springer.
- Richardson, A.J. and Wiegand, D.F. (1992): Multisite analyses of spectral-biophysical data for sorghum. *Remote Sensing of Environment*, Volume 41, Issue 1, pp. 71-82, Elsevier.
- Roberts, M.B.V. (1986): *Biology: a functional approach*. Nelson Thornes.
- Rofail, N. and Al-Koudmani, S. E. (1986): Evaluation of the groundwater observation network of Damascus plain (Case Study). UNDP/WMO/ACSAD regional training workshop on design of groundwater networks, Ryadh, Saudi Arabia.
- Rosenberg, N.J. and Blad, B.L. and Verma, S.B. (1983): *Microclimate: the biological environment*. Wiley-Interscience.
- Roy, J. and Aronson, J. and Di Castri, F. (1995): Time scales of biological responses to water constraints. The case of Mediterranean biota, SPB Academic Publishing.
- Sahu, K.C. (2007): *Textbook of Remote Sensing and Geographical Information Systems*. Atlantic Publishers & Distributors.
- Schädlich, S.(1998): Regionalisierung von aktueller Verdunstung mit Flächenparametern aus Fernerkundungsdaten [Regionalization of actual evaporation using surface parameters derived from remote sensing data]. In: *Münchener Geographische Abhandlungen, Series B, Band 27, München*.
- Schaetzl, R.J. and Anderson, S. (2005): *Soils: Genesis and geomorphology*. Cambridge University Press.
- Schowengerdt, R.A. (2007): *Remote sensing: models and methods for image processing*. Academic Press, 515 pages.
- Schröder, P. and Pfadenhauer, J. and Munch, J.C. (2008): *Perspectives for agroecosystem management: balancing environmental and socio-economic demands*. Elsevier Science Ltd.
- Seiler, K.P. and Gat, J. (2007): *Groundwater recharge from run-off, infiltration and percolation*. Volume 55, Springer.
- Sellers, P.J. (1985): Canopy reflectance, Photosynthesis, and transpiration. *International Journal of Remote Sensing*, Volume 6, Issue 8, pp. 1335-1372, Taylor & Francis.
- Sellers, P.J. (1987): Canopy reflectance, photosynthesis, and transpiration, II. The role of biophysical in the linearity of their interdependence. *Remote Sensing of Environment*, Volume 21, Issue 2, pp. 143-183, Elsevier.
- Sellers, P.J. and Dickinson, R.E. and Randall, D.A. and Betts, A.K. and others, (1997): Modelling the exchanges of energy, water, and carbon between continents and the atmosphere. *Science*, Volume 275, Issue 5299, American Association for the Advancement of Science.

- Shahaideh, A. and Nahas, B. and Shhadeh, W. and others, (2001): Territorial and structural differentiation of Syrian agriculture: case studies. Research Training Report, Project GCP/SYR/066/ITA. Damascus, FAO.
- Shamsi, U.M. (2005): GIS application for water, wastewater, and stormwater systems. CRC Press.
- Shaw D.A. and Martz, L.W. and Pietroniro, A. (2005): A methodology for preserving channel flow networks and connectivity patterns in large-scale distributed hydrological models. *Hydrological Processes*, Volume 19, Issue 1, pp. 149-168.
- Shipman, J.T. and Wilson, J.D. and Todd, A.W. (1983): An introduction to physical science.
- Shuttleworth, W.J. and Wallace, J.S. (1985): Evaporation from sparse crops-an energy combination theory. *Quarterly Journal of the Royal Meteorological Society*, Volume 111, Issue 469, pp. 839-855, John Wiley & Sons.
- Shuval, H.I. and Dwiek, H. (2007): Water resources in the Middle East: the Israeli-Palestinian water issues: from conflict to cooperation. Springer.
- Singh, V.P. (1989): Hydrologic systems: watershed modeling, Prentice Hall.
- Singh, V.P. and Frevert, D.K. (2002): Mathematical models of large watershed hydrology. Water Resources Publications.
- Singh, Y.K. (2006): Environmental Science, New Age International, 320 pages.
- Slabbers, P.J. (1977): Surface roughness of crops and potential evapotranspiration. *Journal of Hydrology*, Volume 34, Issue 1-2, pp. 181-191, Elsevier.
- Smith, W.K. (1980): Importance of aerodynamic resistance to water use efficiency in three conifers under field conditions. *Plant Physiology*, Volume 65, Issue 1, American Society of Plant Biology.
- Solomon, A.M. and Shugart, H.H. (1993): Vegetation dynamics and global change, Chapman and Hall.
- Somani, L.L. (1989): Dictionary of plant sciences (including horticulture). Mittal Publications.
- Spanner, M.A. and Pierce, L.L. and Peterson, D.L. and Running, S.W. (1990): Remote sensing of temperate coniferous forest leaf area index: The influence of canopy closure, understory vegetation and background reflectance. *International Journal of Remote Sensing*, Volume 11, Issue 1, pp. 95-111, Taylor & Francis.
- Sperry, J.S. (2000): Hydraulic constraints on plant gas exchange. *Agricultural and Forest Meteorology*, Volume 104, Issue 1, pp. 13-23, Elsevier.
- Steffen, W.L. and Sanderson, A. (2005): Global change and the earth system: a planet under pressure, Springer.
- Steiner, F.R. and Butler, K.S. and American Planning Association, (2007): Planning and urban design standards. John Wiley.
- Stensrud, D.J. (2007): Parameterization schemes: key to understanding numerical weather prediction models. Cambridge University Press.
- Stephenson, D. and Shemang, E.M. and Chaoka, T.R. (2004): Water Resources of Arid Areas: Proceedings of the International Conference on Water. Taylor & Francis.

- Strasser, U. (1998): Regionalisierung des Wasserkreislaufs mit einem SVAT- Modell am Beispiel des Weser-Einzugsgebiets [Regionalization of the Water Cycle using a SVAT Model, Exemplary for the Weser Catchment]. In: Münchener Geographische Abhandlungen, Series B, Volume 28, pp. 146.
- Strasser, U. and Mauser, W. (2001): Modelling the spatial and temporal variations of the water balance for the Weser catchment 1965-1994. *Journal of Hydrology*, Volume 254, Issue 1-4, pp. 199-214, Elsevier.
- Strasser, U. Franz, H. Mauser, W. (2007): Distributed modelling of snow processes in the Berchtesgaden National Park (Germany). In: Proceeding of the Alpine Snow Workshop, Munich, Germany. Berchtesgaden National Park Research Report No. 53, pp. 117-130, Berchtesgaden. <<http://www.alpinesnowworkshop.org>>.
- Sun, W. (1999): A New Information Fusion Method for Land-use Classification Using High Resolution Satellite Imagery: An Application in Landau, Germany. Dissertation at the Geosciences Department of the Johannes Gutenberg University in Mainz.
- Taschner, S. (1997): Sensitivitätsanalyse des Verdunstungsmodells PROMET, [Sensitivity analysis of the evapotranspiration model PROMET]. In: Strasser, U. (1998): Regionalisierung des Wasserkreislaufs mit einem SVAT- Modell am Beispiel des Weser-Einzugsgebiets [Regionalization of the Water Cycle using a SVAT Model, Exemplary for the Weser Catchment]. In: Münchener Geographische Abhandlungen, Series B, Volume 28, pp. 146.
- Teh, C. (2006): Introduction to mathematical modelling of crop growth: How the equations are derived and assembled into a computer model. Brown Walker Press, 280 pages.
- Thomas, I.L. and Benning, V.M. and Ching, N.P. (1987): Classification of Remotely Sensed Images. Adam Hilger, 268 pages.
- Todini, E. (2007): A mass conservative and water storage consistent variable parameter Muskingum-Cunge approach. *Hydrology and Earth System Sciences Discussions*, Volume 4, Issue 3, pp. 1549-1592.
- Torrecillas, A. and Galego, R. and Perez-Pastor, A. and Ruiz-Sanchez, M.C. (1999): Gas exchange and water relations of young apricot plants under drought conditions. *The Journal of Agricultural Science*, Volume 132, Issue 04, pp. 445-452, Cambridge University Press.
- Torrecillas, A. and Ruiz-Sanchez, M.C. and Leon, A. and Garcia, A.L. (1988): Stomatal response to leaf water potential in almond trees under drip irrigated and non-irrigated conditions. *Plant and Soil*, Volume 112, Issue 1, pp.151-153, Springer.
- Troeh, F.R. and Thompson, L.M. (2005): Soils and soil fertility. Wiley-Blackwell, 489 pages.
- Tso, B. and Mather, P.M. (2001): Classification methods for remotely sensed data, Taylor and Francis, 332 pages.
- Tucker, C.J. and Grant, D.M. and Dykstra, J.D. (2004): NASA's global orthorectified Landsat data set. *Photogrammetric Engineering and Remote Sensing*, Volume

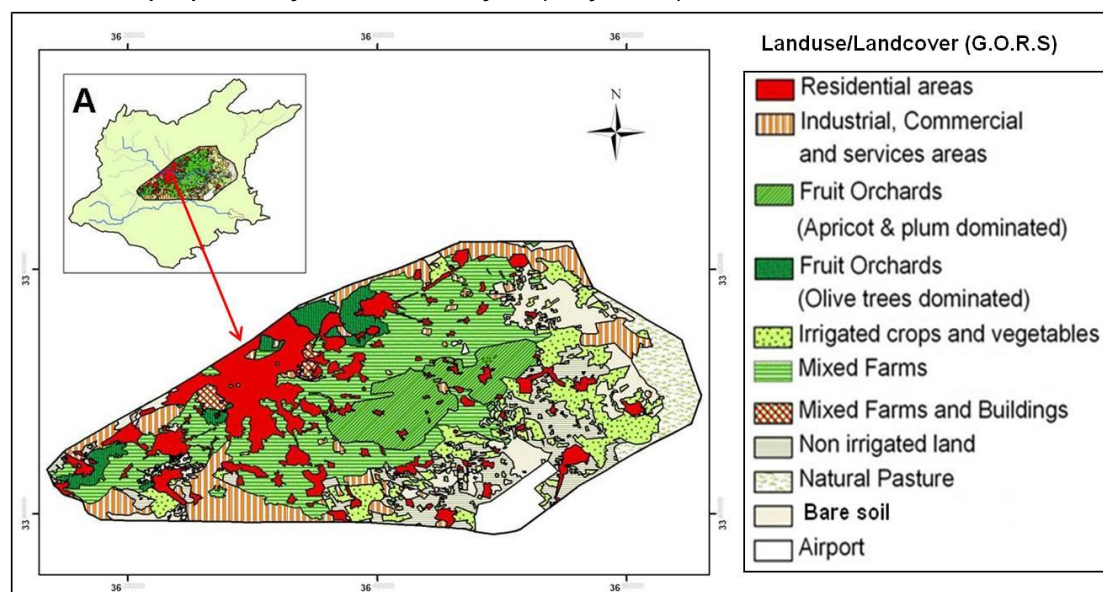
- 70, Issue 3, pp. 313-322, ASPRS- American Society for Photogrammetry and Remote Sensing.
- Turner, D.P. and Cohen, W.B. and Kennedy, R.E. and Fassnacht, K.S. and Briggs, J.M. (1999): Relationships between leaf area index and Landsat TM spectral vegetation indices across three temperate zone sites. *Remote Sensing of Environment*, Volume 70, Issue 1, pp. 52-86, Elsevier.
- Tyree, M.T. and Sperry, J.S. (1989): Vulnerability of xylem to cavitation and embolism. *Annual Review of Plant Biology*, Volume 40, Issue 1, pp. 19-36.
- UNEP (1992): *World Atlas of Desertification*. Edward Arnold, London.
- USDA Soil Survey Staff, (1975): *Soil Taxonomy*. United States Department of Agriculture Handbook, 436, Washington, D.C.
- USDA Soil Survey Staff, (1999): *Soil Taxonomy: A Basic System of Soil Classification for Making and Interpreting Soil surveys*, 2nd ed. Agric. Handbook No. 436, U.S. Government Printing Office, Washington, D.C.
- USGS (2010): MODFLOW and Related Programs.
<<http://water.usgs.gov/nrp/gwsoftware /modeflow.html>>
- Valentini, R. (2003): Fluxes of carbon, water and energy of European forests. Volume 163, Springer.
- Varshney, P.K. and Arora, M.K. (2004): *Advanced image processing techniques for remotely sensed Hyperspectral data*. Springer, 322 pages.
- Verma, V.K. (2003): *High Altitude Geo-Environment and Resources. Perspectives in resource management in developing countries*, Concept Publishing Company.
- Vieux, E.B. (2004): *Distributed hydrological modeling using GIS*. Springer, 289 pages.
- Wagner, B. and Tranawski, V.R. and Hennings, V. and others, (2001): Evaluation of pedo-transfer functions for unsaturated soil hydraulic conductivity using an independent data set. *Geoderma*, Volume 102, Issue 3-4, pp. 275-297, Elsevier.
- Wakeman, R.J. and Tarleton, E.S. (1999): *Filtration: Equipment selection, modelling and process simulation*. Elsevier Science Ltd.
- Wang, J. and Rich, P.M. and Price, K.P. (2003): Temporal responses of NDVI to precipitation and temperature in the central Great Plains, USA. *International Journal of Remote Sensing*, Volume 24, Issue 11, pp. 2345-2364, Taylor & Francis.
- Weiner, E.R. (2000): *Applications of environmental chemistry: a practical guide for environmental professionals*. CRC press.
- Weiss, M. (2009): *Modelling of Global Change Impacts on Hydrology with focus on Europe and Africa*. Kassel University Press GmbH.
- Weng, Q. (2008): *Remote sensing of impervious surfaces*. CRC Press, 454 pages.
- Whalen, J.K. and Sampedro, L. (2010): *Soil Ecology and Management*. CABI Publishing, 296 pages.
- White, R.E. (2006): *Principles and practice of soil science: the soil as a natural resource*. Wiley-Blackwell.

- Wiegand, C.L. and Maas, S.J. and Aase, J.K. and Hatfield, J.L. and others, (1992): Multisite analyses of spectral-biophysical data for wheat. *Remote Sensing of Environment*, Volume 42, Issue 1, pp. 1-21, Elsevier.
- Wilson, J.P. and Gallant, J.C. (2000): *Terrain Analysis: Principles and Applications*. John Wiley and Sons.
- Wolfart, R. (1964): *Hydrogeology of the Damascus Basin (southwest-Syria)*. General Assembly of Berkeley Publications.
- Wösten, J.H.M. and Lilly, A. and Nemes, A. and Le Bas, C. (1999): Development and use of hydraulic properties of European soils. *Geoderma*, Volume 90, Issue 3-4, pp. 169-185, Elsevier.
- Wulder, M.A. and Franklin, S.E. (2003): *Remote sensing of forest environments: concepts and case studies*. Springer Netherlands.
- Wulder, M.A. and Franklin, S.E. (2007): *Understanding forest disturbance and spatial pattern: remote sensing and GIS approaches*. CRC Press.
- Xavier, A.C. and Vettorazzi, C.A. (2004): Monitoring leaf area index at watershed level through NDVI from Landsat-7 / ETM+ data. *Scientia Agricola*, Volume 61, Issue 3, pp. 243-252, SciELO Brasil.
- Zavala, L.M. and Jordan, A. and Bellinfante, N. and Gil, J. (2010): Relationships between rock fragment and cover and soil hydrological response in a Mediterranean environment. *Soil Science & Plant Nutrition*, Volume 56, Issue 1, pp. 95-104, John Wiley & Sons.
- Zereini, F. and Hötzl, H. (2008): *Climatic Changes and Water Resources in the Middle East and North Africa*. Springer, 552 pages.
- Zhou, Q. and Liu, X. (2002): Error assessment of grid-based flow routing algorithms used in hydrological models. *International Journal of Geographical Information Science*, Volume 16, Issue 8, pp. 819-842, Taylor and Francis.

12. Appendix

Appendix 1

The Land use/Land cover map of the central part of the study area (Al-Ghouta), which was prepared by G.O.R.S in Syria (May 2001).



Appendix 2

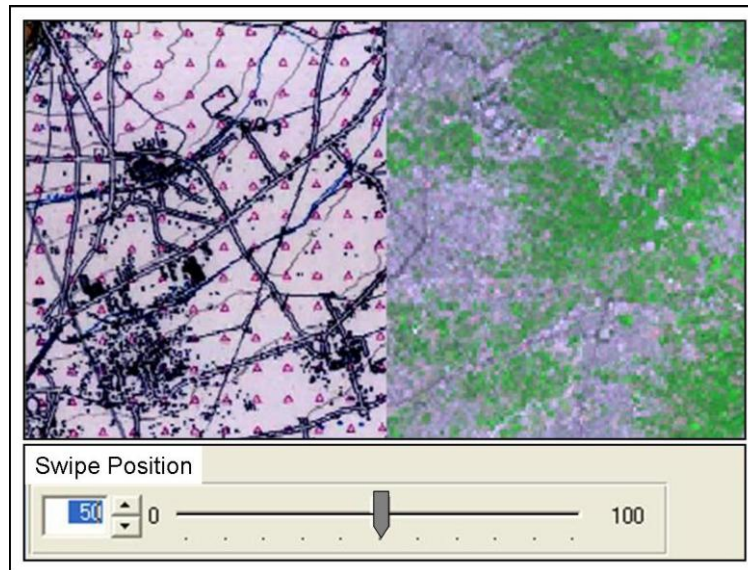
Characteristics of Landsat 7 ETM bands

Band	Wavelength (μm)	Nominal Spectral Location	Principal Applications	Ground Resolution (m)
1	0.45 – 0.52	Visible Blue	Useful for coastal water mapping, Soil/Vegetation differentiation, and deciduous /conifer difference	30
2	0.52 -0.60	Visible Green	Green reflectance by healthy vegetation and vigour assessment; important for discriminating vegetation types.	30
3	0.63 – 0.69	Visible Red	Chlorophyll absorption for plant species differentiation.	30
4	0.76 /0.90	Near infrared	Useful for determining vegetation types, vigour, and biomass content.	30
5	1.55 -1.75	Mid-infrared	Vegetation moisture measurement, snow/ cloud differentiation, soil moisture measurement.	30
6	10.4 -12.5	Thermal infrared	Useful in vegetation stress analysis, soil moisture discrimination.	60
7	2.08 - 2.35	Mid-infrared	Useful for discrimination of mineral and rock types.	30
PAN	0.52 -0.90	Green to infrared	Panchromatic (gray scale). Co-registered with other bands to obtain better spatial resolution.	15

Landsat 7 has a swath width of 185 km. The repeat coverage interval is 16 days. (Adapted from Lillesand and Kiefer, 1994; Pouncey et al., 1999).

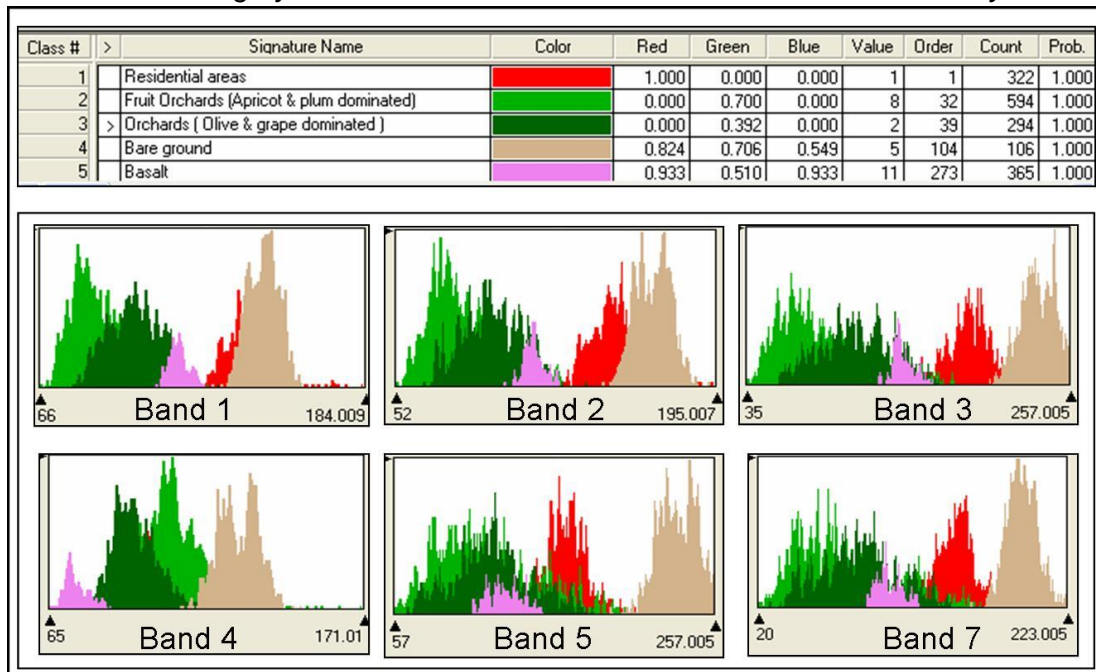
Appendix 3

The viewer shows a comparison between a sub-scene of the Landsat ETM+ image, which was used for derivation of land use/land cover classes of the study area, with its corresponding topographic map (using the Swipe tool in ERDAS IMAGINE-9.1).



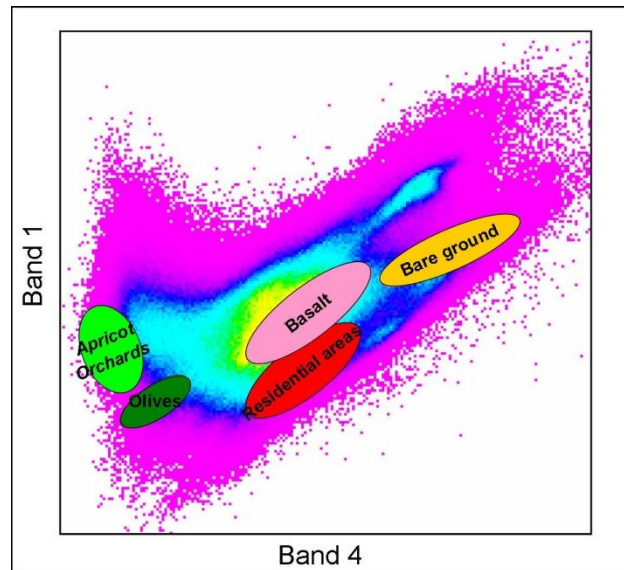
Appendix 4

Histograms for multiple signatures in each of the six non-thermal bands of the Landsat ETM imagery used for land use/land cover classification in this study.



Appendix 5

Ellipses for several land use/land cover types in a feature space image (scatterplot), where values of band-1 have been plotted versus values of band-4.



Appendix 6-a

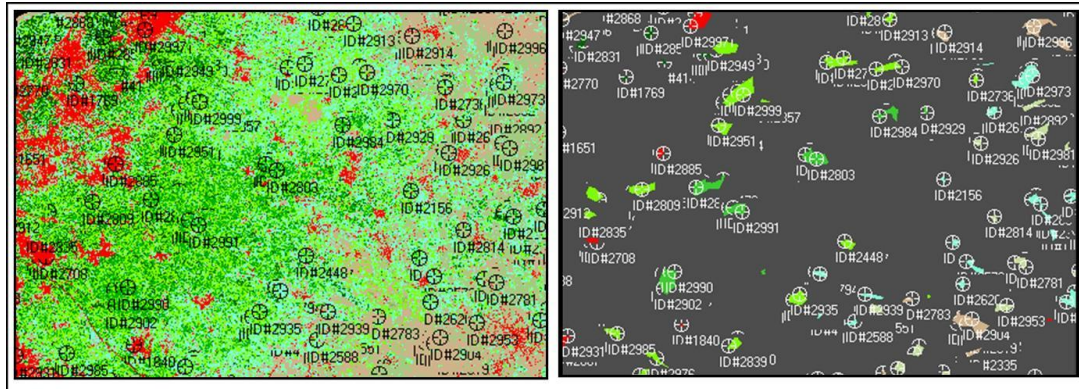
A section of the CellArray created for the purpose of classification accuracy assessment. It lists the exact geographic locations of the testing points (X, Y), the class values for the pixels to be checked, and the class values for the ground truth pixels.

Accuracy Assessment CellArray

Name	X	Y	Class	Reference
ID#1	827750.8	3705300.7	5	5
ID#2	835660.8	3717710.7	3	3
ID#3	799470.8	3710285.7	5	5
ID#4	821020.8	3706825.7	3	3
ID#5	813075.8	3701120.7	6	6
ID#6	808690.8	3706465.7	4	3
ID#7	814180.8	3708520.7	8	8
ID#8	811415.8	3720260.7	5	5
ID#9	807665.8	3712865.7	1	1
.....
ID#3000	828045.8	3725875.7	5	5

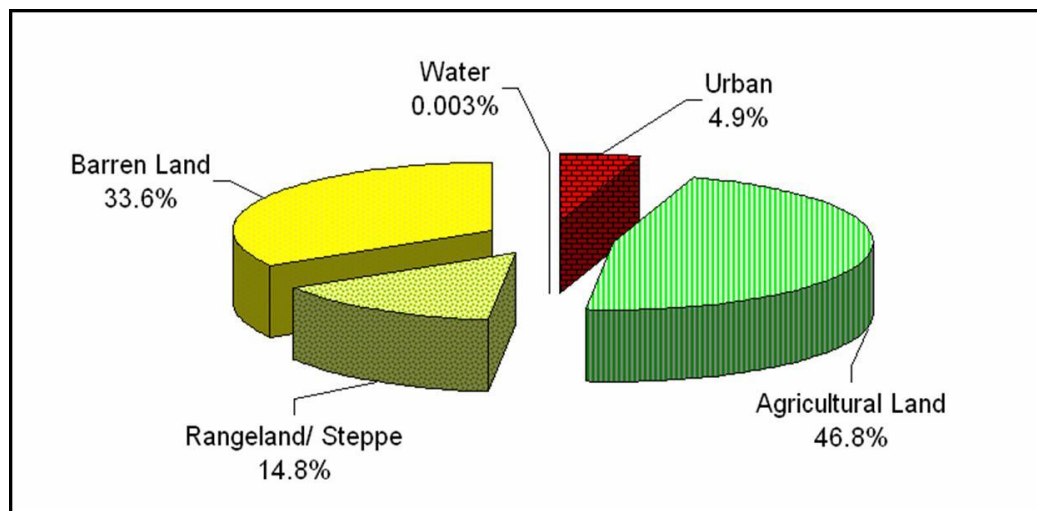
Appendix 6-b

The figure shows the geographic locations of some random points (testing points) in a subset of the classified image (left) and in its corresponding testing samples image (right).



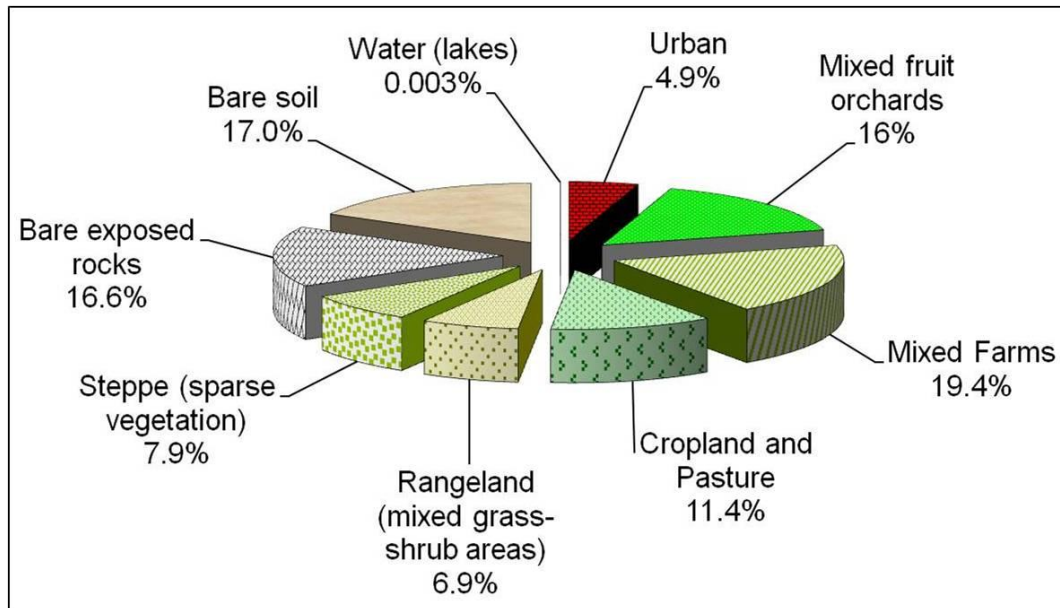
Appendix 7

The figure shows estimated proportion for each land cover type at level-I of the adopted classification scheme.



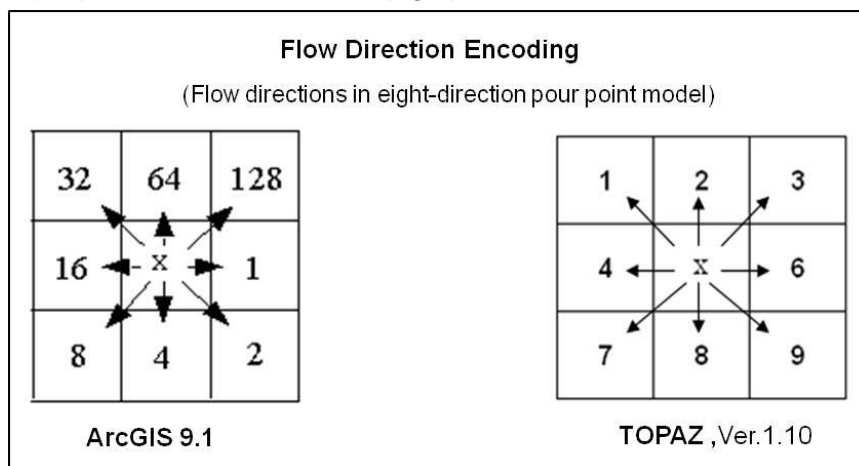
Appendix 8

The figure shows estimated proportion for each land use / land cover type at level-(II) of the adopted classification scheme.



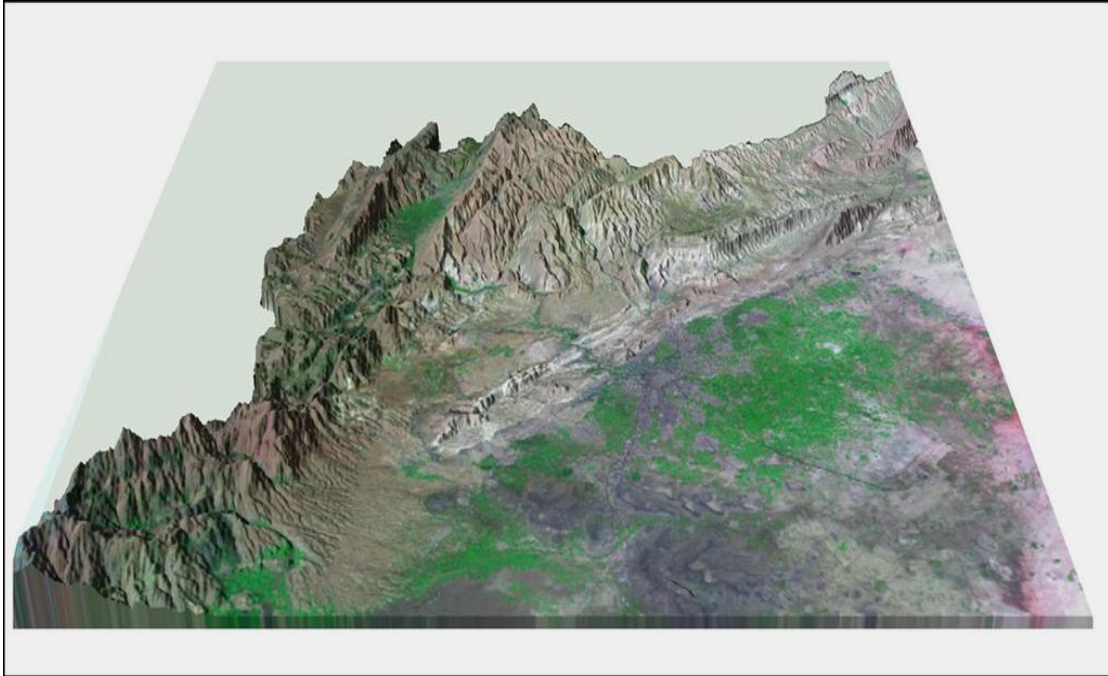
Appendix 9

The figure shows a comparison between two different flow-direction encoding schemes that have been adopted by the software packages used in this study: ArcGIS 9.1 (left) and TOPAZ, ver.1.10 (right).



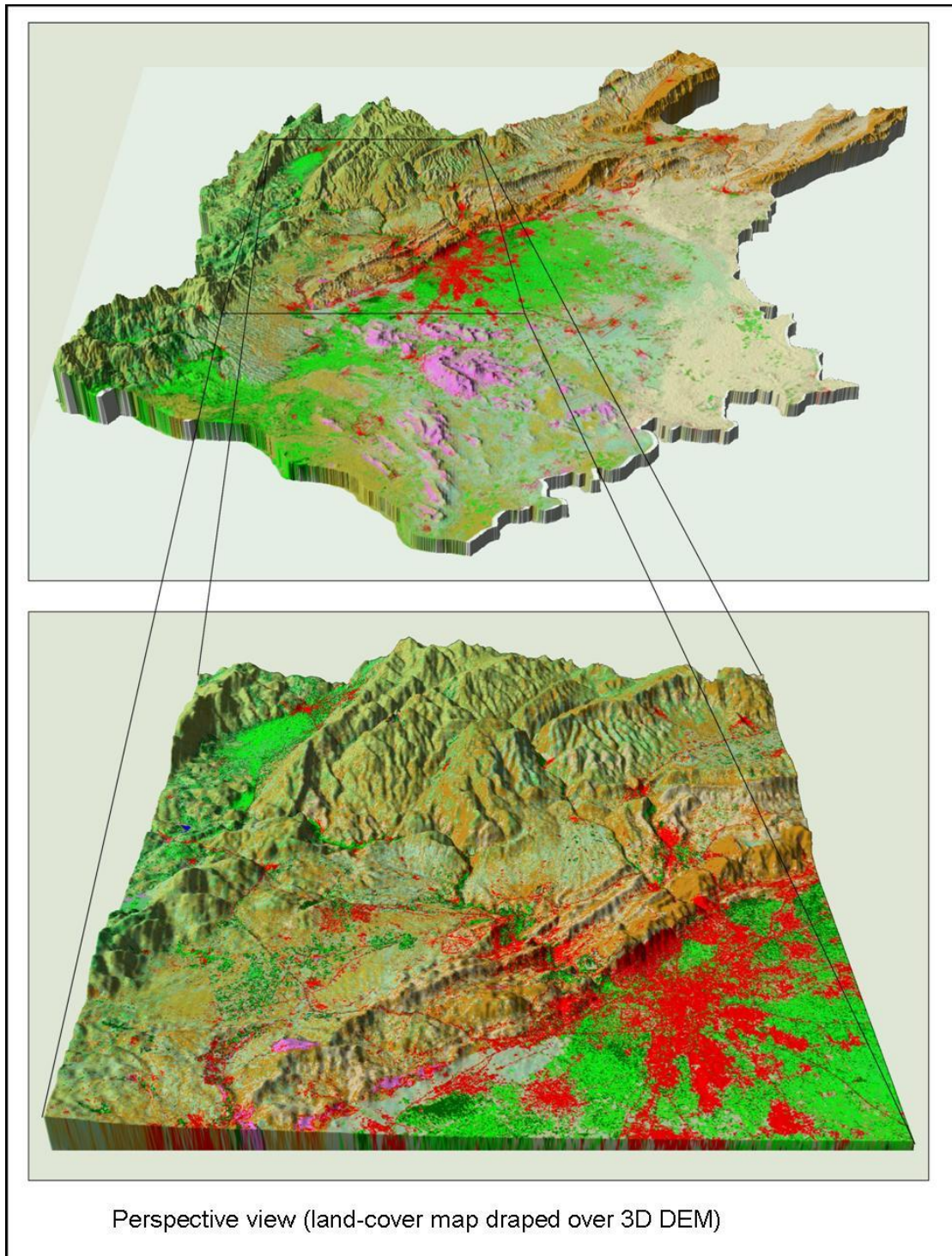
Appendix 10

Perspective view of the north-western part of the study area produced by draping Landsat ETM+ image (bands 2, 4, 5 =B, G, R respectively) over the 3D digital elevation model and viewing from the south.



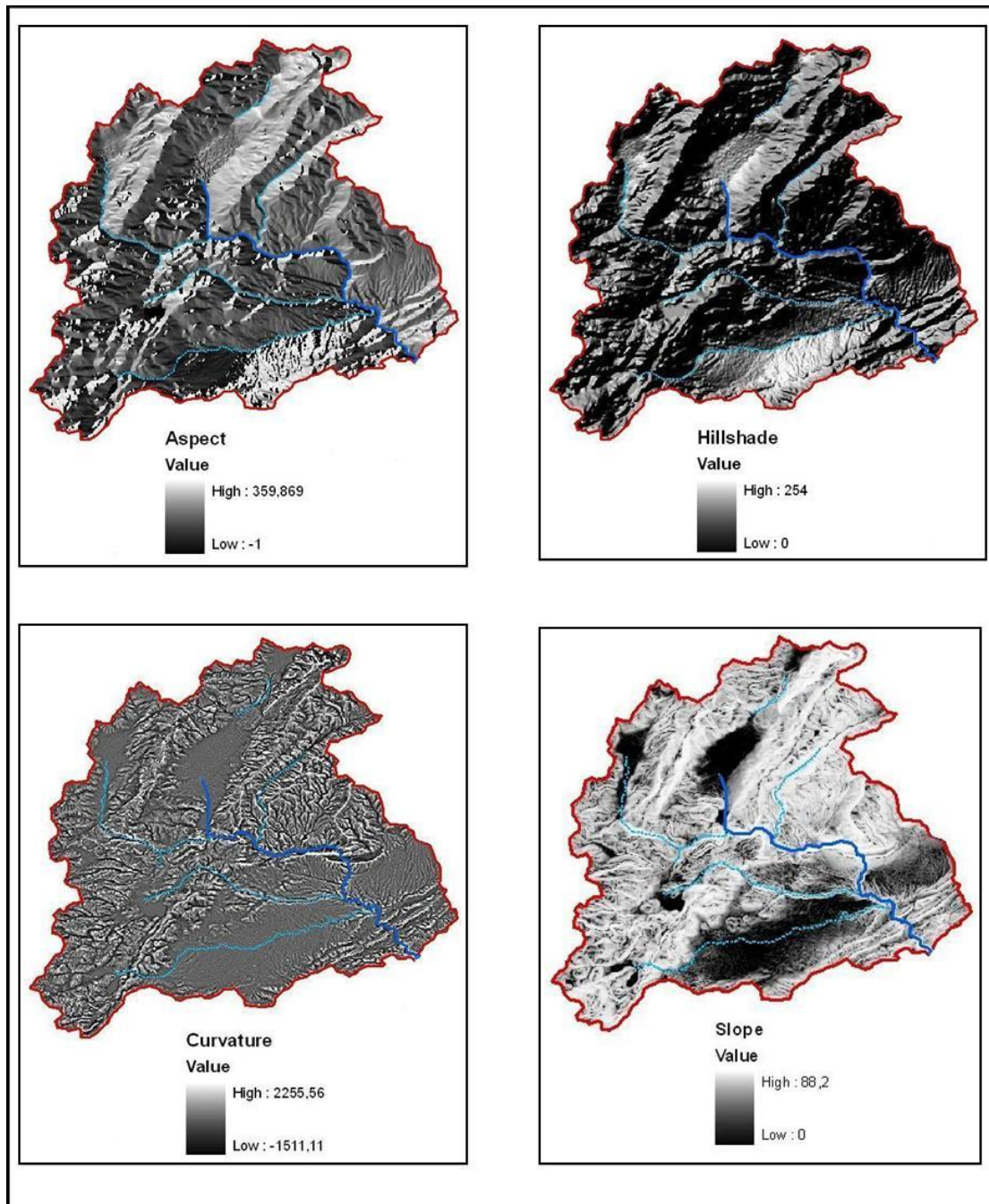
Appendix 11

Perspective view of the study area produced by draping the resulting land use/land cover map over the 3D digital elevation model and viewing from the south.



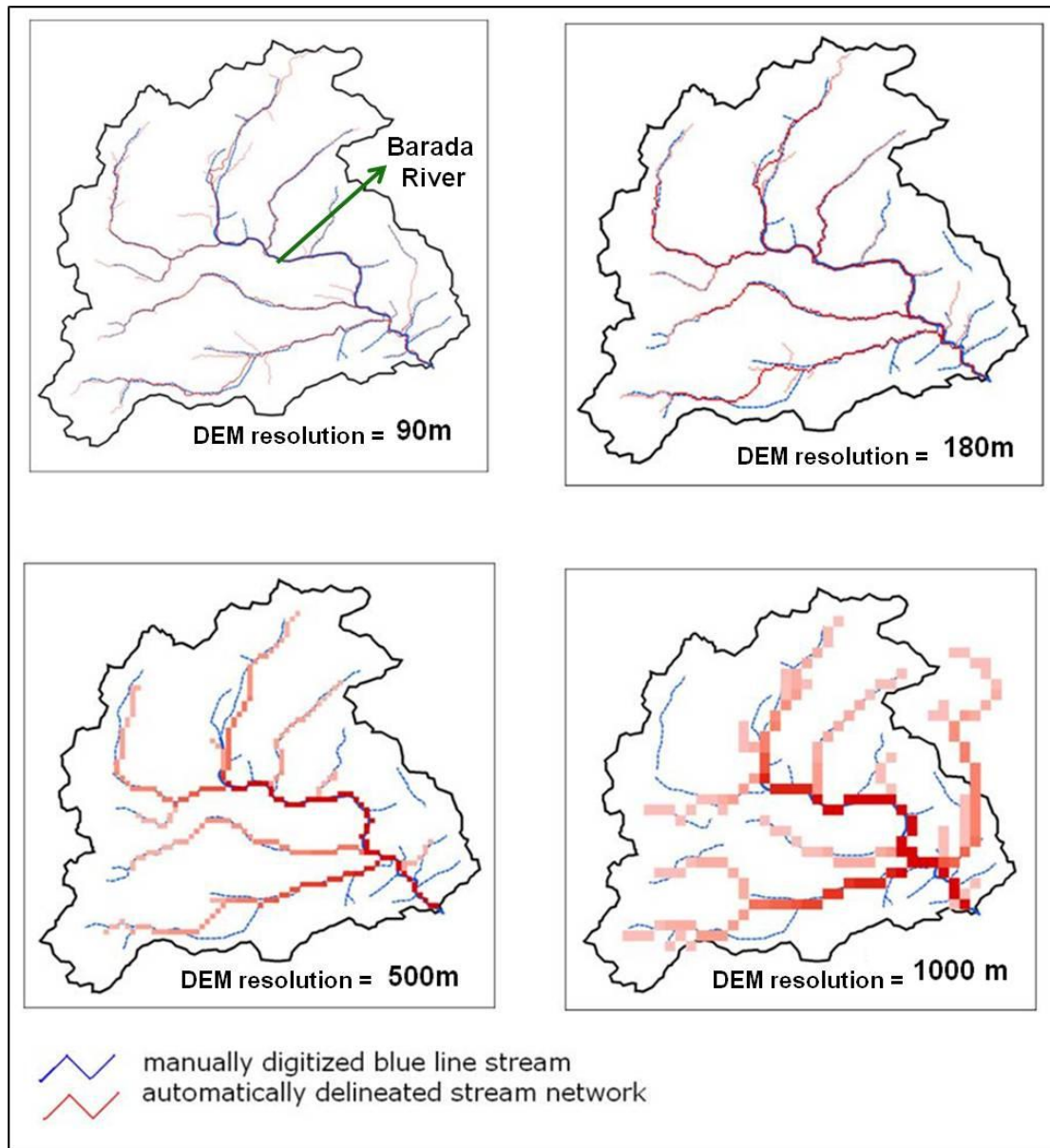
Appendix 12

Aspect, Hillshade, curvature, and slope raster calculated for a mountainous subwatershed within the study area. The blue lines are the main streams draped over each of them.



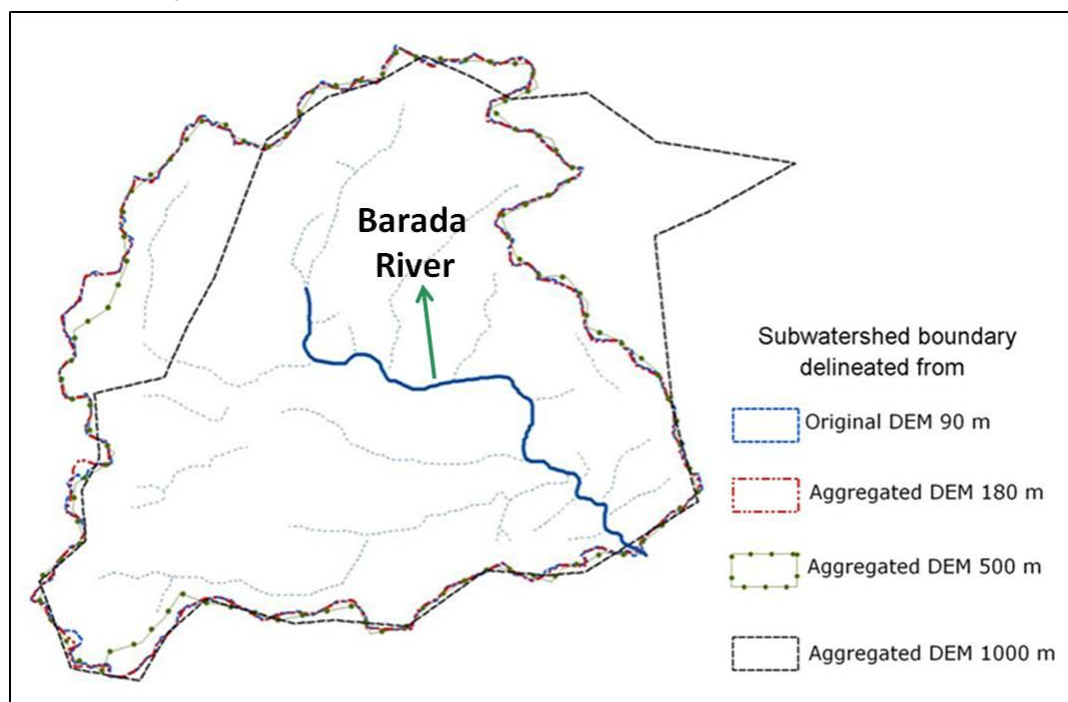
Appendix 13

A comparison between the manually digitized and automatically delineated drainage network at different DEM resolutions (for subwatershed within the study area).



Appendix 14

A comparison between the automatically delineated boundaries of subwatershed within the study area at different DEM resolutions.



Appendix 15

The names, geographical locations and elevations of the rain-gauge stations used in this study.

Station Name	Longitude	Latitude	Elevation m
Al-demayer	36,69	33,64	670,00
Al-konetera	35,86	33,26	941,00
Mazze Al-markazi	36,26	33,51	750,00
Mazze Airport	36,22	33,48	730,00
Damascus Airport	36,52	33,43	610,00
Al-nabek	36,73	34,02	1329,00
Kharabo	36,46	33,51	620,00
Mazraa'et bayet Jen	35,92	33,31	980,00
Maysaloun	36,06	33,59	1156,00
Katana	36,08	33,44	880,00
Madaya	36,10	33,69	1240,00
Al-Zabadani	36,09	33,72	1145,00
Al-Saboura	36,13	33,52	935,00
Maa'ret Saydenaya	36,39	33,67	1380,00
Sorgaya	36,14	33,79	1409,00
Mashtal Dower Al-Herajee	36,42	33,46	635,00
Al-Keswa	36,24	33,36	720,00
Al-Tal	36,31	33,60	940,00
Saydenaya	36,39	33,68	1400,00
Rankous	36,39	33,75	1620,00

Douma	36,39	33,57	660,00
Hela	36,53	33,73	1070,00
Dayer al-Hajar	36,46	33,36	620,00
Al-Nashabeya	36,49	33,51	615,00
Karahta	36,43	33,41	633,00
Maa'lola	36,55	33,86	1409,00
Qutafa	36,60	33,74	930,00
Khelkhola	36,53	33,07	706,00
Urna	35,88	33,36	1400,00
A'yen Al-Fejeh	36,18	33,61	878,00
Al-Mesherfa(AlNabek)	36,58	34,03	1810,00
Om Al-Sharatet	36,07	33,31	850,00
Naba' al-Sakher	35,95	33,17	990,00
Sa'Sa'	36,03	33,29	897,00
Rakhla	35,98	33,54	1600,00
Doureen	35,97	33,26	925,00
Dumar	36,24	33,55	860,00
Daraya	36,24	33,46	700,00
Jedaydet Yabous	35,96	33,66	1272,00
Ma'raba	36,30	33,58	840,00
Kafar Shamis	36,11	33,12	720,00
Ya'four	36,07	33,53	961,00
Bakasam	35,93	33,40	1400,00
Al-Tekeya	36,08	33,63	1150,00
Al-Deymas	36,09	33,59	1100,00
Al-Hama	36,22	33,56	860,00
Gabageb	36,23	33,18	696,00
A'rtoos	36,15	33,42	765,00
Al-Rawda Betrone	36,02	33,65	1275,00
Maa'roneh	36,40	33,64	985,00
Halboun	36,24	33,66	1350,00
Khabakheb	36,28	33,01	610,00
Zakeya	36,16	33,33	770,00
A'yen Menen	36,30	33,64	1100,00
Maydaa'a	36,53	33,56	608,00
Barzi al-Balad	36,33	33,56	682,00
A'sal Al-Wared	36,42	33,86	1604,00
Harasta	36,36	33,56	680,00
Jedaydet A'rtoos	36,15	33,44	715,00
A'dra	36,51	33,61	609,00
Al-hayjani	36,56	33,36	610,00
Jawbar	36,33	33,53	700,00
Jaramana	36,35	33,49	660,00
Yabroud	36,65	33,96	1400,00
Jayroud	36,74	33,81	810,00
Bayet Jen	35,88	33,31	1150,00

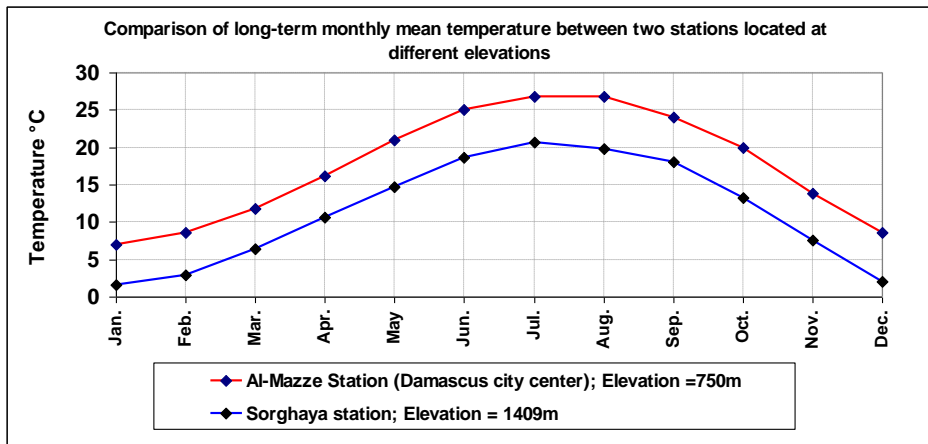
Appendix 16

The table lists the meteorological parameters which were used in this study to generate the required meteorological input data fields (MET-file).

column	parameter
1 – 7	station number
8 – 11	year
12 – 13	month
14 – 15	day
16 – 19	air temperature 7:00 [deg C *10]
20 – 23	air temperature 14:00 [deg C *10]
24 – 27	air temperature 21:00 [deg C *10]
28 – 30	relative humidity 7:00 [%]
31 – 33	relative humidity 14:00 [%]
34 – 36	relative humidity 21:00 [%]
37 – 38	windspeed 7:00 [beaufort]
39 – 40	windspeed 14:00 [beaufort]
41 – 42	windspeed 21:00 [beaufort]
43 – 45	average windspeed [beaufort*10]
46 – 47	cloudiness 7:00 [1/8th]
48 – 49	cloudiness 14:00 [1/8th]
50 – 51	cloudiness 21:00 [1/8th]
52 – 54	sunshine hours [h*10]
55 – 56	visibility 7:00
57 – 58	visibility 14:00
59 – 60	visibility 21:00
61 – 64	rainfall 7:00 [mm/h *10]
65 – 65	precipitation type 7:00
66 – 69	rainfall 14:00 [mm/h *10]
70 – 70	precipitation type 14:00
71 – 74	rainfall 21:00 [mm/h *10]
75 – 75	precipitation type 21:00
76 – 79	daily rainfall sum [mm/d]
80 – 80	daily precipitation type

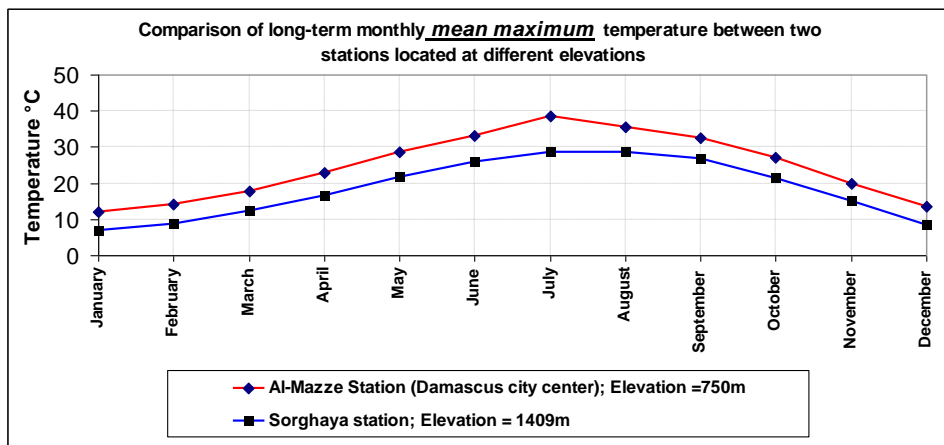
Appendix 17

A comparison of the long-term monthly mean temperature between “Al-Mazze” station (750m) and “Sorghaya” station (1409m).



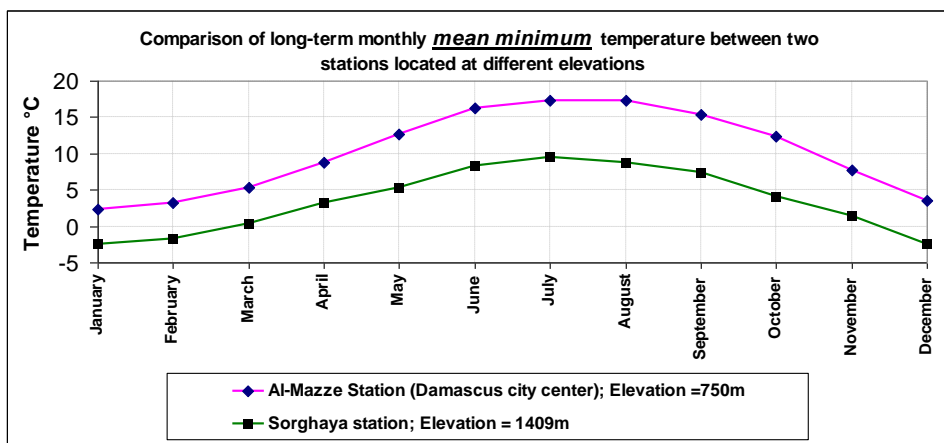
Appendix 18

A comparison of the long-term monthly mean maximum temperature between “Al-Mazze” station (750m) and “Sorghaya” station (1409m).



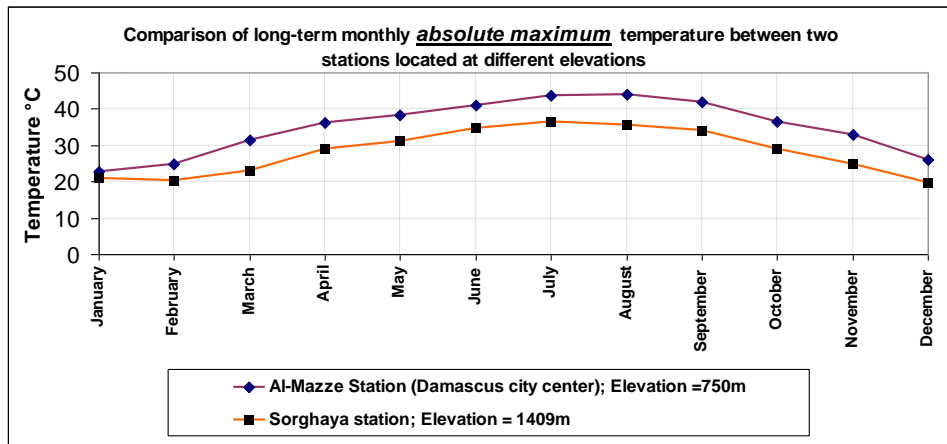
Appendix 19

A comparison of the long-term monthly mean minimum temperature between “Al-Mazze” station (750m) and “Sorghaya” station (1409m).



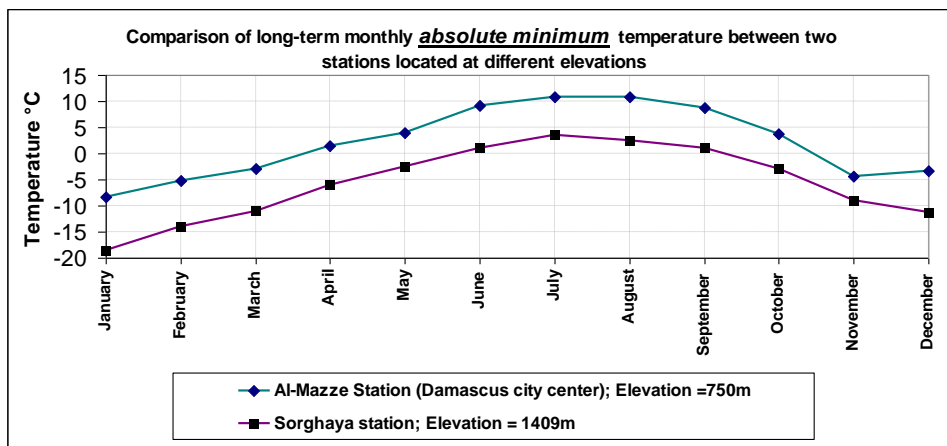
Appendix 20

A comparison of the long-term monthly **absolute maximum** temperature between “Al-Mazze” station (750m) and “Sorghaya” station (1409m).



Appendix 21

A comparison of the long-term monthly **absolute minimum** temperature between “Al-Mazze” station (750m) and “Sorghaya” station (1409m).



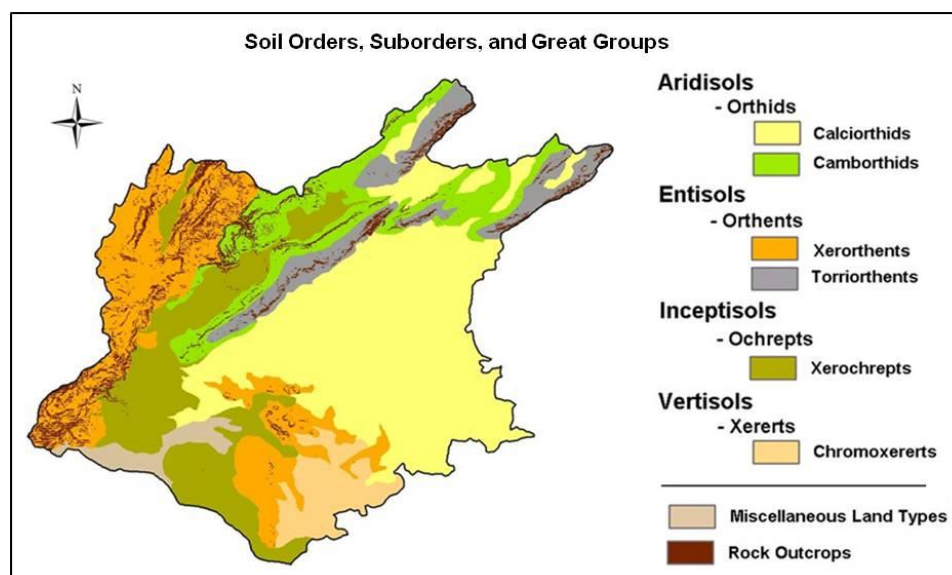
Appendix 22

Monthly lapse rates for the station pair “Al-Mazze – Sorghaya”.

Al-Mazze -Sorghaya			
Month	Mean monthly temperature		Temperature lapse rate
	Al-Mazze (750 m.a.s.l)	Sorghaya (1409 m.a.s.l)	
Jan.	7	1,6	-0,0082
Feb.	8,6	2,9	-0,0087
Mar.	11,8	6,4	-0,0082
Apr.	16,1	10,6	-0,0084
May	21	14,7	-0,0096
Jun	25,1	18,7	-0,0098
Jul	26,8	20,7	-0,0093
Aug	26,8	19,8	-0,0107
Sep	24,1	18	-0,0093
Oct	20	13,2	-0,0104
Nov	13,9	7,6	-0,0096
Dec	8,6	2,1	-0,0099
Mean Annual	17,5	11,3	-0,0095

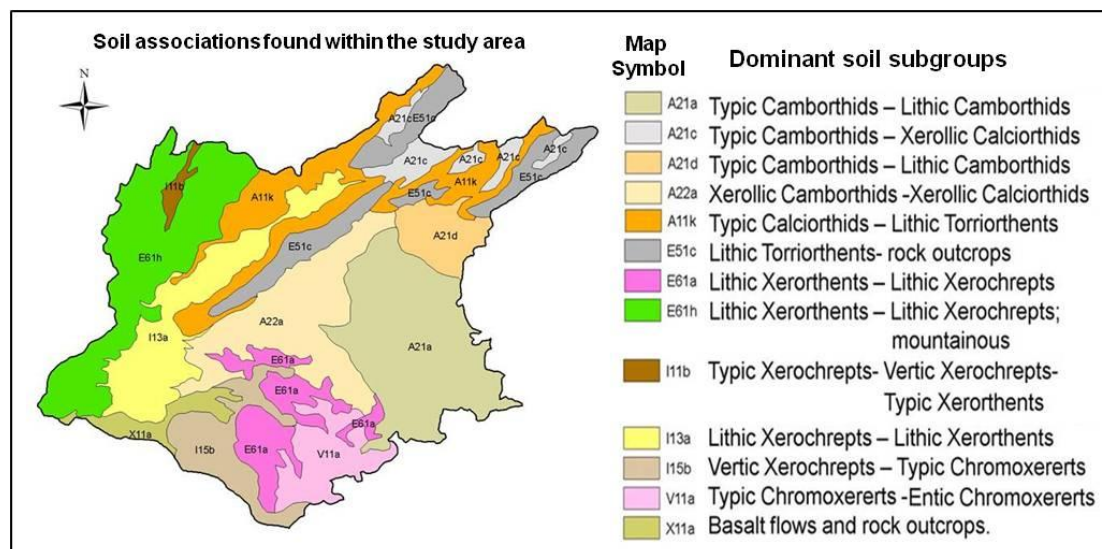
Appendix 23

The spatial distribution of soils of the study area at the level of Suborder and Great-Group (digitized from the soil map of Syria at a scale of 1:500,000, USAID, 1982).



Appendix 24

The spatial distribution of the soil associations found within the study area (digitized from the soil map of Syria at a scale of 1:500,000). The legend includes the dominant soil subgroups in each soil associations.



Appendix 25

The estimated values of the hydraulic parameters for each soil type found within the study area, as derived from basic soil characteristics using the pedotransfer function of Rawls and Brakensiek (1989) and Wösten et al (1999).

soil type class	soil name	soil layer	soil depth [cm]	texture	pore size distribution index	bubbling pressure head [cm]	effective porosity [m3/m3]	saturated hydraulic conductivity [cm/s]
1	Lithic Torriorthents	1	0 - 3	Loam	0.27	27.7	0.34	0.000141
1		2	3- 12	Clay Loam	0.18	40.5	0.26	0.000203
1		3	12 -33	Clay Loam	0.21	34.1	0.29	0.000208
1		4	33-42	Clay Loam	0.17	62.9	0.25	0.000142
2	Lithic Xerorthents	1	0-12	clay Loam	0.18	50.8	0.25	0.000155
2		2	12-21	clay Loam	0.17	60.5	0.26	0.000158
2		3	21-38	Clay	0.17	68.7	0.23	0.000120
2		4	38-50	Clay	0.16	69.3	0.22	0.000115
3	Typic Camborthids	1	0-6	Sand Clay Loam	0.21	22.8	0.32	0.000337
3		2	6- 17	Clay Loam	0.22	33.8	0.27	0.000272
3		3	17-49	Clay Loam	0.21	38.4	0.28	0.000205
3		4	49-115	Clay	0.11	108.2	0.21	0.000103
4	Lithic Xerochrepts	1	0-3	Clay Loam	0.22	52.4	0.28	0.000132
4		2	3-21	Clay Loam	0.22	38.4	0.29	0.000190
4		3	21-42	Clay	0.13	65.6	0.20	0.000136
4		4	42-55	Clay	0.13	67.8	0.21	0.000130

5	Lithic Camborthids	1	0-14	Loam	0.22	30.9	0.30	0.000260
5		2	14-23	Clay	0.13	50.2	0.20	0.000173
5		3	23-34	Clay Loam	0.21	40.7	0.28	0.000181
5		4	34-48	Clay Loam	0.21	41.5	0.27	0.000190
6	Xerollic Camborthids	1	0-4	Clay	0.13	97.1	0.20	0.000092
6		2	4-54	Clay	0.13	70.1	0.20	0.000126
6		3	54-93	Clay	0.15	54.7	0.22	0.000153
6		4	93-135	Clay	0.14	68.4	0.21	0.000126
7	Xerollic Calciorthids	1	0-25	Loam	0.21	36.1	0.28	0.000208
7		2	25-67	Loam	0.19	38.1	0.27	0.000201
7		3	67-90	Clay loam	0.19	43.6	0.26	0.000176
7		4	90-140	Clay loam	0.17	47.5	0.24	0.000168
8	Typic Chromoxererts	1	0-20	Clay	0.11	134.8	0.17	0.000071
8		2	20-50	Clay	0.11	128.5	0.17	0.000075
8		3	50-90	Clay	0.14	105.4	0.20	0.000087
8		4	90-145	Clay	0.12	109.3	0.18	0.000088
9	Typic Xerochrepts	1	0-18	Clay Loam	0.21	34.3	0.29	0.000221
9		2	18-60	Clay Loam	0.22	33.9	0.30	0.000222
9		3	60-95	Clay	0.16	49.9	0.23	0.000164
9		4	95-130	Clay	0.13	42.3	0.21	0.000204
10	Vertic Xerochrepts	1	0-12	Clay	0.11	82.8	0.18	0.000113
10		2	12-36	Clay	0.16	59.1	0.23	0.000141
10		3	36-106	Clay	0.09	111.8	0.13	0.000092
10		4	106-145	Clay	0.10	82.3	0.17	0.000116
11	Lithic Calciorthids	1	0-9	Clay Loam	0.2	36.0	0.28	0.000211
11		2	9-25	Clay Loam	0.21	34.5	0.29	0.000218
11		3	25-40	Clay	0.15	50.6	0.22	0.000165
11		4	40-53	Clay	0.13	42.0	0.21	0.000203
12	Typic Calciorthids	1	0-12	Clay	0.10	132.2	0.16	0.000071
12		2	12-56	Clay	0.12	105.6	0.18	0.000087
12		3	56-93	Clay	0.09	129.3	0.15	0.000075
12		4	93-155	Clay	0.10	92.8	0.17	0.000103
13	Typic Torriorthents	1	0-18	Clay Loam	0.18	30.8	0.27	0.000264
13		2	18-35	Clay Loam	0.2	32.5	0.29	0.000239
13		3	35-62	Sand Clay Loam	0.16	24.1	0.28	0.000568
13		4	62-108	Sand Clay Loam	0.17	26.1	0.29	0.000565
14	Entic Chromoxererts	1	0-21	Clay	0.14	87.7	0.20	0.000100
14		2	21-55	Clay	0.12	105.6	0.18	0.000087
14		3	55-95	Clay	0.12	67.3	0.19	0.000135
14		4	95-140	Clay	0.15	62.0	0.22	0.000136
15	Petrocalcic Xerochrepts	1	0-17	Clay Loam	0.21	35.1	0.28	0.000216
15		2	17-45	Clay Loam	0.18	32.6	0.27	0.000244
15		3	45-108	Clay Loam	0.18	32.5	0.26	0.000247
15		4	108-145	Clay Loam	0.18	35.6	0.26	0.000222

Appendix 26

The values of the maximum stomatal conductance ($\text{mmol m}^{-2} \text{s}^{-1}$) along with their corresponding calculated minimum stomatal resistance (s.m^{-1}) for some vegetation categories selected (from other types of vegetation reported by Körner (1994)) to be correlated with the vegetation of the study area.

Type of vegetation	Mean \pm SD [$\text{mmol m}^{-2} \text{s}^{-1}$]	The corresponding calculated Minimum stomatal resistance [s.m^{-1}]
Woody vegetation		
Mediterranean deciduous shrubs / tress	235 \pm 87	175
Mediterranean evergreen shrubs / tress	203 \pm 108	202
Hot desert shrubs, drought deciduous	202 \pm 83	203
Hot desert shrubs, evergreen	222 \pm 86	185
Semi-arid shrub and woodland vegetation	198 \pm 58	207
Non-woody vegetation		
Grassland (prairie, steppe)	326 \pm 163	126
Anthropogenic vegetation		
Cereals	ca. 450	91
Broadleaved herbaceous crops	ca. 500	82

Appendix 27

The mean values of the minimum stomatal resistance for the three aggregated vegetation super-classes at both leaf (r_s) and canopy (R_s) scales, as provided by Kelliher et al., (1995).

Super-class	r_s (at leaf-scale) [s.m^{-1}]	R_s (at canopy-scale) [s.m^{-1}]
Woody vegetations	182	51
Natural herbaceous	125	59
Agricultural crops	86	32

Appendix 28

The values of the minimum canopy resistance (R_s), together with their respective LAI for some types of agricultural crops, as determined by Kelliher et al., (1995).

Agricultural crop	Leaf Area Index (LAI)	R_s (at canopy-scale) [s.m^{-1}]
Wheat	3.2	45
	5.5	40
	6.5	30
	9	20
Corn	3.4	50
Soybeans	3.8	33
Alfalfa	-----	20

Appendix 29

The plant-specific physiological parameters derived from the various sources mentioned below for the different vegetation types of the study region.

Vegetation Type (Land use /Land cover classes)	$r_{s(min)}$ s.m ⁻¹	b_{rs} W/m ²	Ψ_0 MPa	T_{min} °C	T_{opt} °C	T_{max} °C
Orchards (Olive dominated)	200	25	-2.5	5	27	40
Mixed Fruit orchards (Apricot & plum dominated)	195	22	-2,4	6	25	40
Mixed Farms (Vegetables & forage dominated)	140	40	-0.7	6	21	35
Cropland (Cereals and Legumes)	90	55	-1	3	20	35
Natural Pasture	125	81	-1	3	22	39
Rangeland (Mixed Grass-Shrub)	135	50	-1.5	4	18	34
Steppe (Sparse vegetation)	130	65	-1.6	3	26	40

Parameter

Source (based on correlations with)

$r_{s(min)}$ minimum stomatal resistance

Körner (1994) and Kelliher et al., (1995).

b_{rs} slope of the stomatal resistance with PAR

Baldocchi et al.,(1987) and Strasser (1998).

Ψ_0 threshold value of leaf water potential

Kirkham (1999), Jackson (2003), Torrecillas et al, (1999), Torrecillas et al., (1988), Baldocchi et al., (1987), Strasser (1998) and Ludwig (2000).

T_{min} , T_{opt} , T_{max} cardinal temperatures

FAO ECOCROP database

Appendix 30

The values of the slope parameter of the stomatal resistance with solar irradiance for some types of vegetation available in literature.

Vegetation	Conifer (Spruce)	Deciduous (Oak)	Corn	Soy- bean	Winter wheat	Summer wheat	Summer barley	Potato	pasture
b_{rs} W/m ²	25	22	66	10	60	38	38	66	81

Values for spruce, oak, corn and soybean are presented by Baldocchi et al., (1987), whereas values for wheat, barley, potato and pasture are reported by (Strasser, 1998) and (Ludwig, 2000).

Appendix 31

Threshold values of leaf water potential for some vegetation types as reported in literature.

Vegetation	Ψ_o [MPa]	Source
Olive (evergreen)	-2.5	Kirkham (1999)
Apple (deciduous)	-2.3	Jackson (2003)
Apricot (deciduous)	-2.5	Torrecillas et al, (1999)
Almond (deciduous)	-2.7	Torrecillas et al., (1988)
Spruce (conifer)	-2.1	Baldocchi et al., (1987),
Oak (deciduous)	-2	Baldocchi et al., (1987),
Corn (grass)	-0.8	Baldocchi et al., (1987),
Soybean (legume)	-1.1	Baldocchi et al., (1987),
Wheat (cereal)	-1	(Strasser, 1998) and (Ludwig, 2000)
Pasture	-1	(Strasser, 1998) and (Ludwig, 2000)

Appendix 32

The approximate values of cardinal temperatures for some plant species present within the area under investigation. Data source: FAO ECOCROP database.

Life form	species	T_{min} °C	T_{opt} °C	T_{max} °C	Life form	species	T_{min} °C	T_{opt} °C	T_{max} °C
tree	Olive	5	27	40	herb	Alfalfa	5	24	45
	Apple	8	21	33		Beans	13	22	34
	Apricot	7	25	40		Chickpea	7	22	35
	Almond	10	23	40		Lentil	5	22	32
	Cherry	6	23	40		Potato	7	20	30
	Walnut	7	22	40		Lettuce	5	17	30
	Grape	10	24	38		Tomato	7	20	35
	Cedrus	4	27	38		Astragalus	12	27	40
grass	Wheat	5	20	30	Sub-shrub	Artemisia	4	16	26
	Barley	2	19	40		Atriplex	5	15	33

Appendix 33

The lower (L_{min}) and upper (L_{max}) limits of the post-calibration spectral radiance range for each spectral band of each LANDSAT ETM+ image used in this study (measured in $Wm^{-2} sr^{-1} \mu m^{-1}$), as provided by its corresponding metadata file.

Band	06.11.2000 (Autumn)		08.03.2002 (Winter)		21.05.2000 (Spring)		22.06.2000 (Early summer)		07.08.1999 (Mid summer)	
	L_{min}	L_{max}	L_{min}	L_{max}	L_{min}	L_{max}	L_{min}	L_{max}	L_{min}	L_{max}
1	-6.2	191.6	-6.2	293.7	-6.2	191.6	-6.2	191.6	-6.2	191.6
2	-6.4	196.5	-6.4	300.9	-6.4	196.5	-6.4	196.5	-6.4	196.5
3	-5.0	152.9	-5.0	234.4	-5.0	152.9	-5.0	152.9	-5.0	152.9
4	-5.1	157.4	-5.1	241.1	-5.1	241.1	-5.1	157.4	-5.1	157.4
5	-1.0	31.06	-1.0	47.57	-1.0	31.0	-1.0	31.0	-1.0	31.0
7	-0.35	10.8	-0.35	16.54	-0.35	10.8	-0.35	10.8	-0.35	10.8

Appendix 34

The general length for each growth stage along with the planting (or green up) date for some plant species grown in the study basin, as derived from a comprehensive database provided by Allen et al., (1998).

Plant species	Planting (or green up) date	Initial stage (days)	Development stage (days)	Mid-season stage (days)	Late season stage (days)
Deciduous Trees	March	20	70	105	45
Olives *	March	30	90	60	90
Grapes	April	20	40	120	60
Winter – wheat/barley	November	30	130	40	30
Summer- wheat/barley	March	20	25	60	30
Lentil	November	25	35	70	40
Chickpea	March	25	25	35	30

Olives *: Olive trees gain new leaves in March.

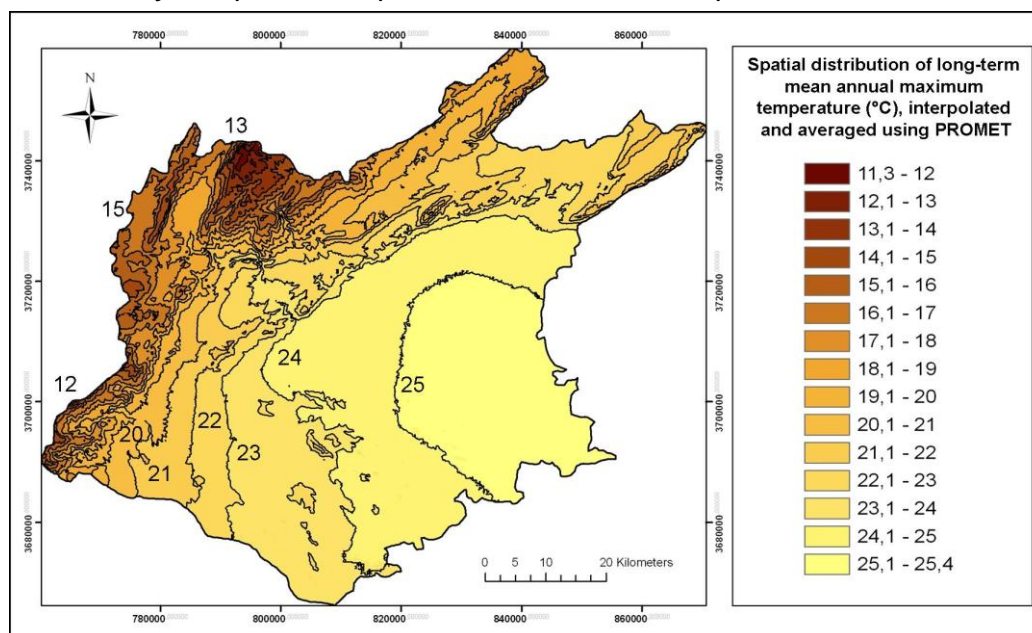
Appendix 35

The Table lists the mean maximum height, together with the range of maximum root depth for some plant species existing in the study region, as given in a comprehensive database reported by Allen et al., (1998).

Plant species	Mean Maximum Plant Height (m)	Maximum Root Depth (m)
Olives	3-5	1.2-1.7
Apricots, Peaches,	3	1.0-2.0
Apples, Cherries, Pears	4	1.0-2.0
Almonds	5	1.0-2.0
Walnut	4-5	1.7-2.4
Grapes	2	1.0-2.0
Barley	1	1.0-1.5
Summer Wheat	1	1.0-1.5
Winter Wheat	1	1.5-1.8
Chick pea	0.4	0.6-1.0
Lentil	0.5	0.6-0.8
Tomato	0.6	0.7-1.5
Potato	0.6	0.4-0.6
Beans	0.4	0.5-0.7
Alfalfa Hay	0.7	1.0-2.0
Grazing Pasture	0.10-0.30	0.5-1.0

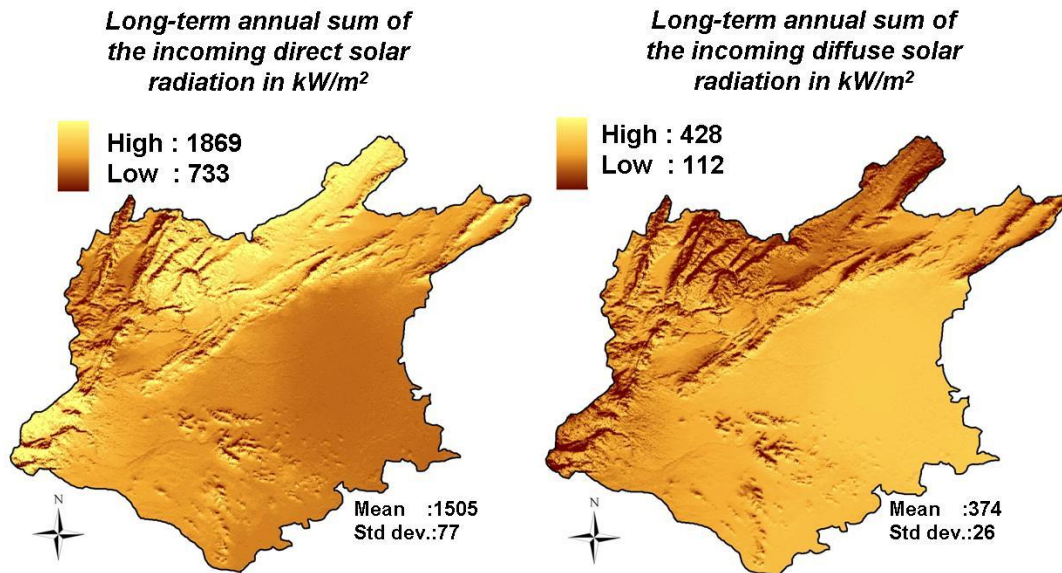
Appendix 36

The spatial distribution of long-term mean annual maximum temperature in the study area derived by interpolation of point observations for the period 1990-2005.



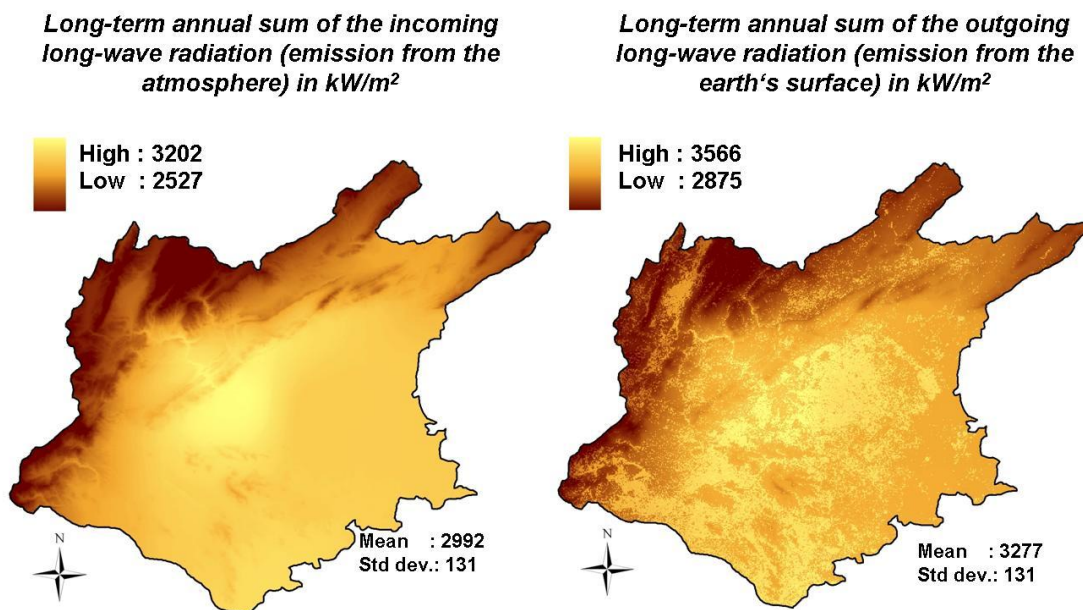
Appendix 37

Spatial distribution of the long-term (1991-2005) annual sum of incoming shortwave - direct radiation (left), and - diffuse radiation (right), as simulated by the model PROMET in kW/m².



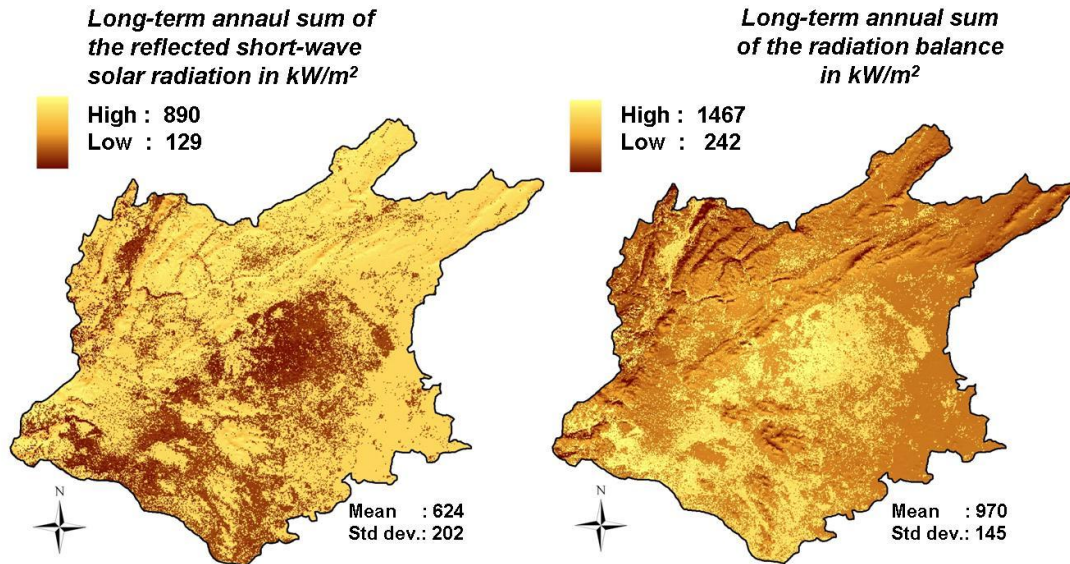
Appendix 38

Spatial distribution of the long-term (1991-2005) annual sum of incoming longwave radiation (left), and outgoing longwave radiation (right), as simulated by the model PROMET in kW/m².



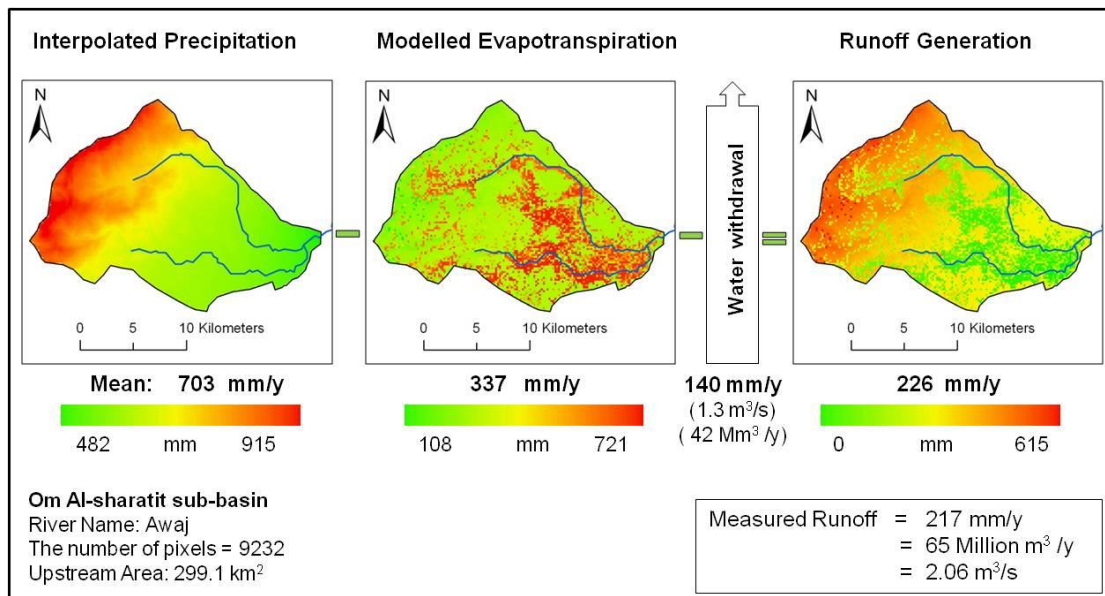
Appendix 39

Spatial distribution of the long-term (1991-2005) annual sum of reflected shortwave radiation (left), and the radiation balance (right), as simulated by the model PROMET in kW/m²



Appendix 40

The average modelled water balance in “Om Al-sharatit” subcatchment over the period from 1992 to 2005. The simulated mean annual runoff from this subcatchment (226 mm/ y) compares well with the runoff measured at its respective outlet gauge station (217 mm/y).



Appendix 41

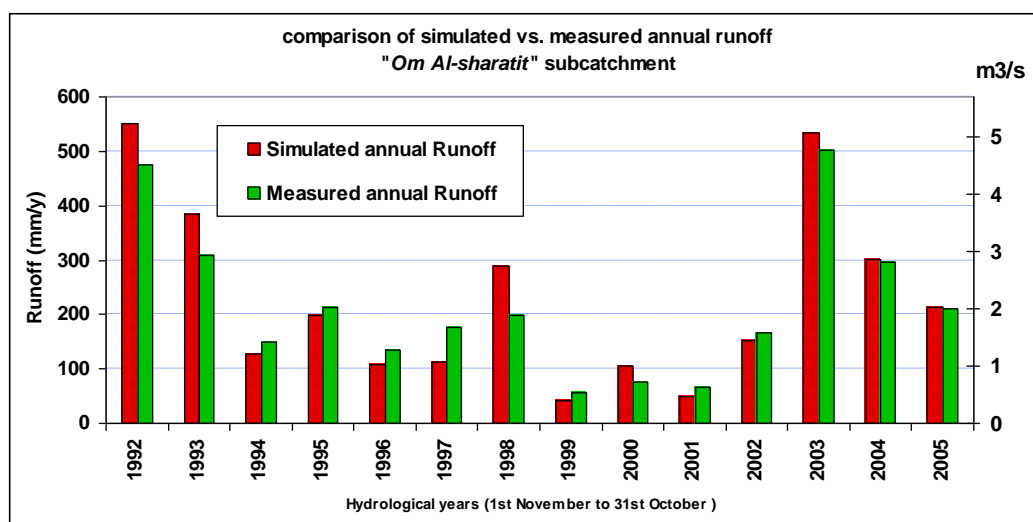
The modelled annual water balance components (in mm/y) for “Om Al-sharatit” subcatchment as simulated by PROMET for each of the 14 hydrological years (1992-2005).

Om Al-sharatit sub-basin							
River Name: Awaj							
Upstream Area: 299.1 km²							
P: Interpolated Precipitation (mm/y)							
ETa: Modelled actual Evapotranspiration (mm/y)							
Hydrological year 1.Nov.- 31.Oct	P mm/y	ETa mm/y	WW (withdrawal) mm/y	Q = P-ETa – WU (Calculated Runoff) mm/y	Measured Runoff mm/y	Deviation	
						mm/y	(%)
1992	1071	378	140	552	475	77	16
1993	861	336		385	309	76	25
1994	624	358		127	150	-24	-16
1995	691	351		199	213	-13	-6
1996	582	334		108	135	-27	-20
1997	575	323		113	177	-64	-36
1998	781	353		288	199	89	45
1999	421	240		41	57	-16	-28
2000	612	367		105	76	29	38
2001	440	250		50	65	-15	-23
2002	650	359		151	166	-14	-9
2003	1060	387		533	503	30	6
2004	775	334		301	297	3	1
2005	698	345		213	210	3	1
Mean	703	337	140	226	217	10	4 %

WW: water withdrawal (water use) from Om Al-sharatit sub-basin is estimated to be 140 mm/y (42 Million Cubic Meters/year or mean annual withdrawal rate of **1.3 m³/s**).

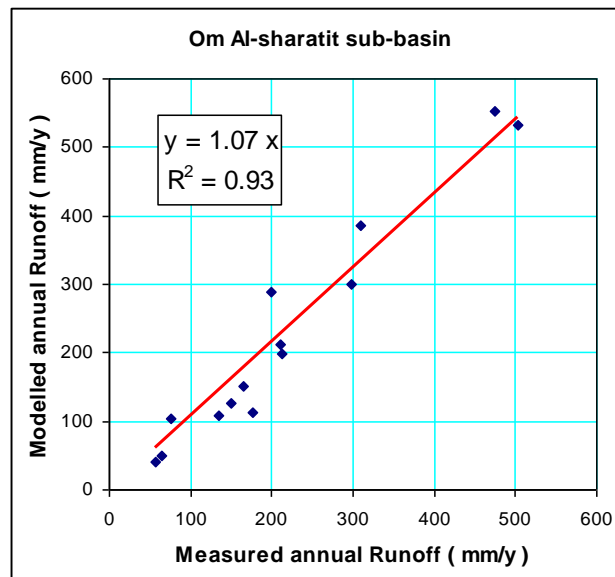
Appendix 42

A comparison between the modelled annual runoff volumes from “Om Al-sharatit” subcatchment (in mm/y and in m³/s) and those annual discharges measured at its outlet gauge station for the hydrological years from 1992-2005.



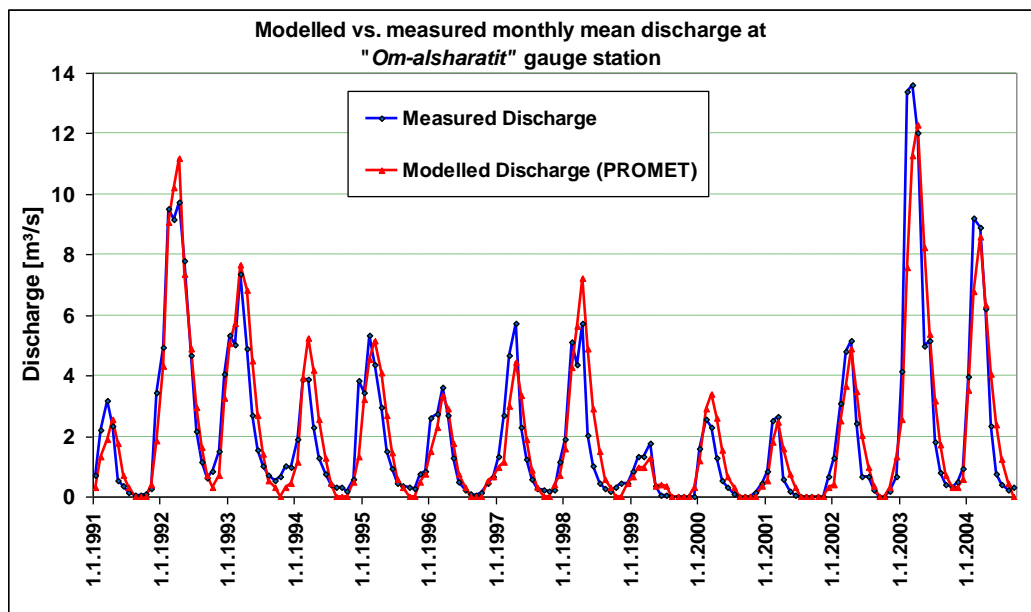
Appendix 43

The linear regression line (forced through the origin) between the modelled and measured annual runoff volumes (in mm/y) at “Om Al-sharaitit” outlet gauge station.



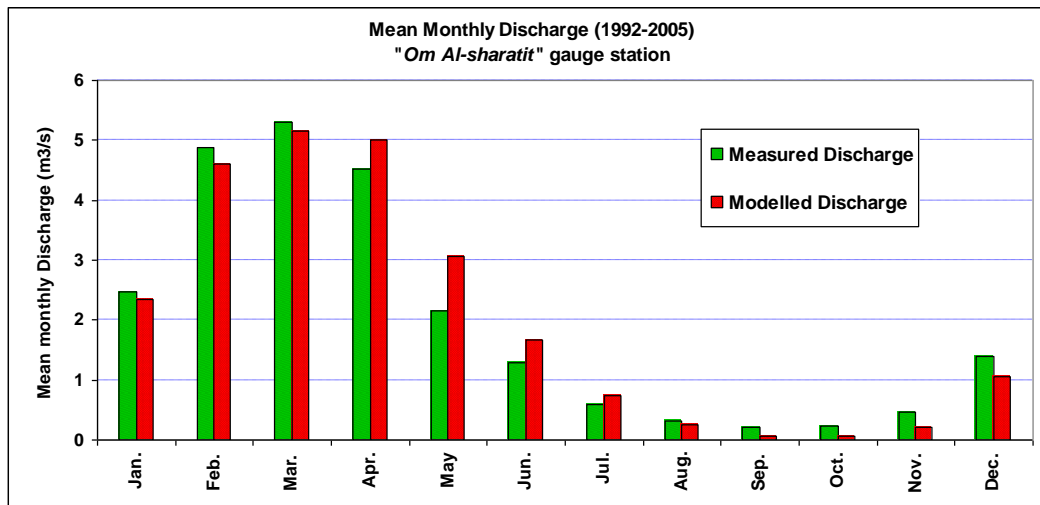
Appendix 44

The temporal course of modelled and measured monthly mean discharge at “Om Al-sharaitit” gauge station for the period (1991-2005).



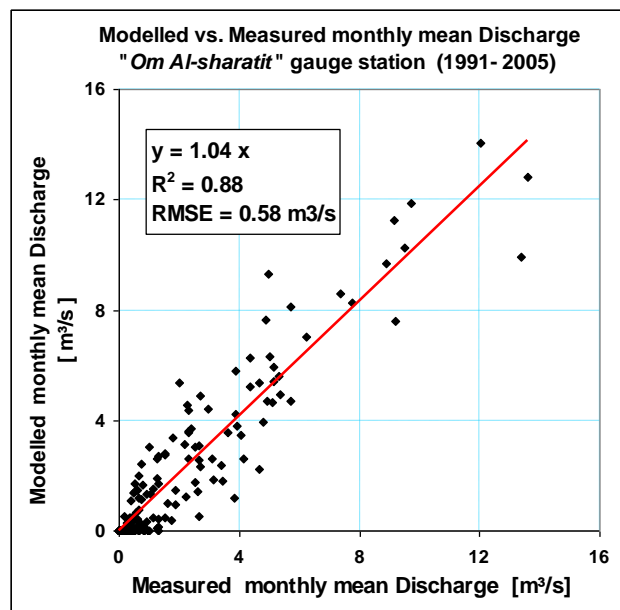
Appendix 45

A comparison between simulated and observed mean monthly discharge at "Om Al-sharait" gauge for the period (1991-2005).



Appendix 46

The linear regression line (forced through the origin) between the modelled and measured monthly mean discharge volumes (in m³/s) at "Om Al-sharait" outlet gauge station for the period 1991-2005.



13. Curriculum Vitae

Personal

Name: Khaled Haider

Date of Birth: 21.05.1979

Place of Birth: Damascus-Suburb / Syria

Nationality: Syrian

Email: khaled_haider@hotmail.de

Doctoral Thesis

2006-2011: Ph.D. research, Ludwig-Maximilians-University (LMU) Munich (Germany)

Learning German

2005(4months): TestDaF (Test Deutsch als Fremdsprache) certificate at the
"Zentraleinrichtung Moderne Sprachen (ZEMS)" of the TU Berlin

2004(8months): Zertifikat Deutsch (ZD, "Certificate German") at the language
learning institute, Damascus, Syria.

Study of Geosciences

2002-2003: Post Graduate Diploma in Hydrogeology at the University of Damascus,
Syria, grade "Excellent"

2000-2002: Study of Geophysics, Damascus University, Syria, grade "very good"

1998-2000: Study of Geology, Damascus University, Syria, grade "very good"

Education

1998 -1995: Upper Secondary Education (High school), Damascus-Suburb, Syria

1995 -1992: Lower Secondary Education, Damascus-Suburb, Syria

1992 -1986: Primary Education, Damascus-Suburb, Syria

Scholarships/Awards

-Scholarship for PhD Degree in Germany, 2006-2011, Ministry of Higher Education,
Syria.

-Basel Al-Assad Award for Academic Excellence, First Rank, 2000, 2001, 2002,
Damascus University, Syria.